Thèse n°9531

Mechanics of Physical Knots: From Filaments in Contact to Surgical Suturing

Présentée le 10 février 2023

Faculté des sciences et techniques de l'ingénieur
Laboratoire des Structures Flexibles
Programme doctoral en mécanique

pour l'obtention du grade de Docteur ès Sciences

par

Paul JOHANNS

Acceptée sur proposition du jury

Prof. J. M. Kolinski, président du jury
Prof. P. M. Nunes Pereira de Almeida Reis, directeur de thèse
Prof. B. Audoly, rapporteur
Prof. E. Grinspun, rapporteur
Prof. T. Schneider, rapporteur

École
polytechnique
fédérale
de Lausanne

2023

For since the fabric of the universe is most perfect, and is the work of a most wise Creator,
nothing whatsoever takes place in the universe in which some relation of
maximum and minimum does not appear.
— Leonhard Euler, 1744, introducing his seminal work on elastic curves

EMOTION, MOTION
There is the excitement of knowing a number of knots,
followed by the satisfaction of choosing the right one for a specific task,
and finally the joy of tying and tightening, which is the result of setting the rope in motion,
arranging, conducting, orchestrating its parts.
— Philippe Petit, 2013

To my family

Acknowledgements

I am extremely grateful to Pedro for giving me this fantastic opportunity more than four years ago. Your guidance, encouragement, and advice shaped me during this memorable experience. Your passion for research, and inspiring analogies during uncountable research meetings were always an important driving force to me. I am very thankful to Prof. Tobias Schneider, Prof. Basile Audoly, and Prof. Eitan Grinspun for having evaluated this work and for having read in great detail this thesis. I deeply appreciated the constructive discussion during the thesis defense. My gratitude also goes to Prof. John Kolinski for kindly accepting to preside over the jury. I am very thankful to Prof. John H. Maddocks for having shared his immense knowledge on the theory of rods and knots in lectures and collaborations throughout my thesis. During the last few years, I have had the chance to meet and work with many interesting people, inside and outside of the *fleXLab*. First of all, I would like to thank all the members of the original *Knot Team* – Grandgeorge, Changyeob, Tomohiko, and Alastair – it was an amazing experience to work together with you, uniting various fields of expertise, and sharing the enthusiasm for knotted rods. I am proud of what we have achieved in these few years, considering that we started from scratch in 2018. I am glad that a couple of rod-and knot-related projects are bearing fruits and will continue to thrive after my departure, with Fani and Michael bringing new momentum into the field. I like to nostalgically remember the first two years of my Ph.D.: surrounded by a group of charismatic and helpful post-docs, I enjoyed setting up the labs together, progressing in my research, and doing fun activities in our free-time. Dinners, drinks, skiing, hiking, and salsa dancing were only a few of our 'team-building' activities. At this place, I would like to express my huge gratitude to Grandgeorge for all the support and advice related to research and on a personal level, as well as for the countless moments we spent together! Thank you, Sam, Matteo, and Tim, for having always been up to listen to my concerns and joys over a drink, pizza, or tartar steak. Thank you, Fani, for having been such a patient office-mate, fully supporting me and my mood changes in the final run of my Ph.D.! Dong, thank you so much for your unconditional help with any IT-related issues and, completely unrelated, the Boston lobster! I will never forget the following phrases, which accompanied me through this adventure: 'Everything will be fine!' (Tim, 2019); '#GonnaHappen' (Matteo, 2020); 'You can do this!' (Fani, 2021). I wish a wonderful Ph.D. adventure to Eduardo, and a successful

wrapping-up for Arefeh – you can do this! I would also like to express my gratitude to Noelia, for her precious support during my thesis; whatever my question was, you have always had a solution. Finally, from the bottom of my heart, I want to say that all this would not have been possible without my family in Switzerland, who supported me all the way. Thank you, Yuliethe, for your tireless comfort and unconditional support over the last three years. The time with you and Dieguito has been extremely precious to me to resource myself after long days at work. Merci infiniment! Thank you to my family in Luxembourg, who I have not visited enough during the pandemic time, and in the final push of my thesis. Visiting you has always been an important source of energy to me. Villmols merci! Thank you to all the people who believed in me!

Lausanne, January 21, 2023 Paul Johanns

Abstract

In this thesis, we study the mechanics of tight physical knots. Knots are omnipresent in surgery, climbing, and sailing, with disastrous consequences when the filament or the rope fails to perform its function. Even if the importance of mechanical analysis of knots has long been recognized, established guidelines for best practices typically rely primarily on empirical data gained from historical experience, not structural analysis.

Existing models in knot theory or Kirchhoff's theory for elastic rods are often insufficient to describe the functional behavior of tight physical knots due to the intricate three-dimensional nonlinear geometries, large elastic (and sometimes plastic) deformations, and frictional interactions. A few past studies reported stability and knot quality measurements, which, however, are specific and difficult to generalize.

We tackle the study of the mechanics of physical knots by combining topological and geometric arguments, precision-model experiments, and high-fidelity numerical simulations using the finite element method. An elaborate toolbox is developed for volumetric imaging of X-ray micro-computed tomography data. Our investigation is centered on the shape of physical trefoil knots, the performance of stopper knots, and the strength of surgical knots.

First, we perform a compare-and-contrast investigation between the equilibrium shapes of physical and ideal trefoil knots, in closed and open configurations. We construct physical realizations of tight trefoil knots tied in an elastomeric rod. X-ray tomography and 3D finite element simulation allow for evaluating the role of elasticity in dictating the physical knot's overall shape, self-contact regions, curvature profile, and cross-section deformation. The results suggest that regions of localized elastic deformation, not captured by the geometric models, act as precursors for the weak spots that could compromise the strength of knotted filaments.

Second, we investigate the performance of stopper knots, which prevent the rod end from retracing through a narrow passage. We develop a physical model involving an inextensible elastomeric rod, onto which a figure-eight knot is tied and pulled against a rigid stopper plate. A complex interplay of frictional interactions and friction-induced twist leads to capsizing, a mechanism that rearranges the knot configuration while keeping its topology. In contrast to isotropic rods, we find that the decoupling of bending and twisting rigidities in rope-like structures penalizes rod twisting, which impedes the knot from capsizing.

Third, we study the operational and safety limits of surgical sliding knots, highlighting the previously overlooked but crucial effect of plastic deformation. The relevant range of applied tensions, geometric features, and the resulting knot strengths are characterized using experimental and numerical model systems. Finally, we find that all the experimental and numerical data, involving all the knot configurations we investigated and a wide range of friction coefficients, collapse onto a master curve.

The acquisition and study of unprecedented experimental data, combined with FEM simulations, has enabled us to systematically explore the different ingredients dictating the mechanical performance of knotted structures with highly nonlinear geometrical features and material properties.

Key words: Mechanics of knots, knots, physical knots, contact mechanics, friction, plasticity, surgical suturing, mechanical testing, X-ray tomography, Finite Element Modeling.

Résumé

Dans cette thèse, nous étudions la mécanique des nœuds physiques serrés. Les nœuds sont omniprésents en chirurgie, en escalade et en voile, avec des conséquences désastreuses lorsque le filament ou la corde ne remplit pas sa fonction. Même si l'importance de l'analyse mécanique des nœuds est reconnue depuis longtemps, les directives établies pour les meilleures pratiques s'appuient généralement sur des données empiriques issues de l'expérience historique, et non sur une analyse structurelle.

Les modèles existants de la théorie des nœuds ou de la théorie de Kirchhoff pour les tiges élastiques sont souvent insuffisants pour décrire le comportement fonctionnel des nœuds physiques serrés en raison des géométries tridimensionnelles non linéaires complexes, des grandes déformations élastiques (et parfois plastiques) et des interactions de frottement. Quelques études antérieures ont rapporté des mesures de stabilité et de qualité des nœuds, qui sont toutefois spécifiques et difficiles à généraliser.

Nous abordons l'étude de la mécanique des nœuds physiques en combinant des arguments topologiques et géométriques, des expériences sur des modèles de précision et des simulations numériques à haute-fidélité utilisant la méthode des éléments finis. Une boîte à outil méthodologique élaborée est développée pour l'imagerie volumétrique des données de la tomographie à rayons X. Notre étude est centrée sur la forme des nœuds de trèfle physiques, la performance des nœuds d'arrêt et la résistance des nœuds chirurgicaux.

Tout d'abord, nous effectuons une étude comparative entre les formes d'équilibre des nœuds de trèfle physiques et idéaux, dans des configurations fermées et ouvertes. Nous construisons des réalisations physiques de nœuds trilobés serrés dans une tige élastomère. La tomographie à rayons X et la simulation par éléments finis en 3D permettent d'évaluer le rôle de l'élasticité dans la détermination de la forme globale du nœud physique, des régions d'auto-contact, du profil de courbure et de la déformation de la section transversale. Les résultats suggèrent que les régions de déformation élastique localisée, non prises en compte par les modèles géométriques, sont les précurseurs des points faibles qui pourraient compromettre la résistance des filaments noués.

Deuxièmement, nous étudions la performance des nœuds d'arrêt, qui empêchent l'extrémité de la tige de retraverser un passage étroit. Nous développons un modèle physique impliquant une tige élastomère inextensible, sur laquelle un nœud en huit est noué et tiré contre une plaque d'arrêt rigide. Une interaction complexe entre les interactions de frottement et la torsion induite par le frottement conduit au 'chavirement', un mécanisme qui réarrange la configuration du nœud tout en conservant sa topologie. Contrairement aux tiges isotropes, nous constatons que le découplage des rigidités de flexion et de torsion dans les structures de type corde pénalise la torsion de la tige, ce qui empêche le nœud de chavirer.

Troisièmement, nous étudions les limites opérationnelles et de sécurité des nœuds coulissants chirurgicaux, en mettant en évidence l'effet crucial, mais jusqu'ici négligé, de la déformation plastique. La gamme pertinente des tensions appliquées, les caractéristiques géométriques et les résistances des nœuds qui en résultent sont caractérisées à l'aide de systèmes de modèles expérimentaux et numériques. Enfin, nous proposons une loi d'échelle générale qui permet de regrouper les données expérimentales et numériques sur une unique courbe maîtresse. Cette description capture la force des nœuds chirurgicaux serrés, couvrant toutes les conformations de nœuds coulissants considérées sur une large gamme de coefficients de frottement.

L'acquisition et l'étude de données expérimentales sans précédent, combinées à des simulations FEM, nous ont permis d'explorer systématiquement les différents ingrédients dictant la performance mécanique de structures nouées présentant des caractéristiques géométriques et des propriétés matérielles hautement non linéaires.

Zusammenfassung

In dieser Arbeit untersuchen wir die Mechanik von festen physikalischen Knoten. Knoten sind in der Chirurgie, beim Klettern und Segeln allgegenwärtig und haben katastrophale Folgen, wenn der Faden oder das Seil seine Funktion nicht erfüllt. Obwohl die Bedeutung der mechanischen Analyse von Knoten seit langem anerkannt ist, stützen sich die etablierten Richtlinien für bewährte Verfahren in der Regel in erster Linie auf empirische Daten, die aus historischen Erfahrungen gewonnen wurden, und nicht auf strukturelle Analysen.

Bestehende Modelle aus der Knotentheorie oder der Kirchhoff'schen Theorie für elastische Filamente reichen oft nicht aus, um das funktionelle Verhalten fester physikalischer Knoten zu beschreiben, da es sich um komplizierte dreidimensionale nichtlineare Geometrien, große elastische (und manchmal plastische) Verformungen und Reibungswechselwirkungen handelt. Einige frühere Studien berichteten über Stabilitäts- und Knotenqualitätsmessungen, die jedoch spezifisch und schwer zu verallgemeinern sind.

Wir befassen uns mit der Untersuchung der Mechanik physikalischer Knoten, indem wir topologische und geometrische Argumente, Präzisionsmodellexperimente und numerische Simulationen mit hoher Genauigkeit unter Verwendung der Finite-Elemente-Methode kombinieren. Für die volumetrische Darstellung von Röntgen-Mikro-Computertomographie-Daten wird ein umfangreicher Methodik-Werkzeugkasten entwickelt. Unsere Untersuchung konzentriert sich auf die Form von physikalischen Kleeblattknoten, die Leistung von Stopfenknoten und die Festigkeit von chirurgischen Knoten.

Zunächst vergleichen wir die Gleichgewichtsformen von physikalischen und idealen Kleeblattknoten in geschlossenen und offenen Konfigurationen. Wir konstruieren physikalische Realisierungen von engen Kleeblattknoten, die in ein Elastomerfilament eingebunden sind. Mit Hilfe von Röntgentomografie und 3D-Finite-Elemente-Simulationen lässt sich die Rolle der Elastizität bei der Bestimmung der Gesamtform des Knotens, der Selbstkontaktbereiche, des Krümmungsprofils und der Querschnittsverformung bewerten. Die Ergebnisse deuten darauf hin, dass Regionen mit lokaler elastischer Verformung, die von den geometrischen Modellen nicht erfasst werden, als Vorläufer für die Schwachstellen fungieren, die die Festigkeit der Knotenfilamente beeinträchtigen könnten.

Zweitens untersuchen wir die Leistung von Stopperknoten, die verhindern, dass das Filamentende durch einen engen Kanal zurückläuft. Wir entwickeln ein physikalisches Modell mit einem nicht dehnbaren Elastomerfilament, an den ein Achterknoten gebunden und gegen eine starre Stopperplatte gezogen wird. Ein komplexes Zusammenspiel von Reibungswechselwirkungen und reibungsinduzierter Verdrehung führt zum ‘Kentern’, einem Mechanismus, der die Konfiguration des Knotens unter Beibehaltung seiner Topologie umgestaltet. Im Gegensatz zu isotropen Stäben stellen wir fest, dass die Entkopplung von Biege- und Torsionssteifigkeit in seilähnlichen Strukturen die Verdrehung der Stäbe hemmt, was ein Kentern des Knotens verhindert.

Drittens untersuchen wir die Operations- und Sicherheitsgrenzen von chirurgischen Gleitknoten, wobei wir den bisher übersehenen, aber entscheidenden Effekt der plastischen Verformung hervorheben. Der relevante Bereich angewandter Spannungen, geometrischer Merkmale und der daraus resultierenden Knotenfestigkeit wird anhand experimenteller und numerischer Modellsysteme charakterisiert. Abschließend schlagen wir ein allgemeines Skalierungsgesetz vor, das es ermöglicht, experimentelle und numerische Daten auf einer Masterkurve zusammenzufassen. Diese Beschreibung erfasst die Knotenfestigkeit chirurgischer Knoten und deckt alle betrachteten Gleitknotenkonformationen über einen weiten Bereich von Reibungskoeffizienten ab.

Die Erfassung und Untersuchung noch nie dagewesener experimenteller Daten in Kombination mit FEM-Simulationen hat es uns ermöglicht, die verschiedenen Faktoren systematisch zu untersuchen, die die mechanische Leistung von Knotenstrukturen mit stark nichtlinearen geometrischen Merkmalen und Materialeigenschaften bestimmen.

Contents

Acknowledgements **i**

Abstract (English/Français/Deutsch) **iii**

1 Introduction **1**

1.1 Functional Applications of Knots Across Ages and Length Scales 2
1.2 Frameworks to describe the mechanics and geometry of rods 4
  1.2.1 Frictional Contact in the Capstan System 5
  1.2.2 Kinematics of Framed Curves 7
  1.2.3 Discrete Differential Geometry of curves in 3D space 8
1.3 A (Very Brief) Primer on Topology and Knot Theory 10
  1.3.1 The Beginnings of Knot Theory 10
  1.3.2 Basic Concepts in Topological Knot Theory 11
1.4 Tightest Tangles and Knots Tied in Geometric Rods 13
1.5 Loose Knots Described by Kirchhoff's Theory for Elastic Rods 15
1.6 Numerical Simulations on Elastic Knots 17
1.7 Knot Quality and Stability 19
1.8 Summary and Research Niche 22
1.9 Outline of the Thesis 25

2 Methodology: Experimental Toolbox **27**

2.1 Motivation 28
2.2 Fabrication of Composite Rods for μCT Imaging 29
  2.2.1 Bulk Core Rod Produced by Injection Molding 29
  2.2.2 Physical Fiber and Eccentric Inset 32
  2.2.3 Outer Coating Using Dip-Coating Technique 33
  2.2.4 Quality Control of the Rod Fabrication 37
  2.2.5 Mechanical Properties of the Rod 39
2.3 X-Ray Tomographic Imaging and Image Analysis 42
  2.3.1 X-Ray μCT Principles and Scanning Settings 42

2.3.2 Centerline Coordinates and the Contact Regions From μCT Data 45
2.3.3 Adaptations to Use the Geometric Centerline Definition *minCS* 50
2.3.4 Parameter-Tuning to Handle Extreme Geometries and Their Limitations 54
2.4 Geometric Quantification of the Rod Deformation 55
2.4.1 Discrete Curvature Based on Cosserat Framework 55
2.4.2 Discrete Curvature Associated With Vertices 56
2.4.3 Smoothing of The Raw Data to Reduce 'Noise' in The Curvature Computation 56
2.4.4 Cross-Sectional Area and Flattening 57
2.4.5 Shape of the Contact Region Between the Two Rods 57
2.5 Protocols for Characterization of Rods 58
2.5.1 Characterization of the Material Properties of VPS 58
2.5.2 Frictional Behavior of Powder-Treated VPS Surfaces 60
2.6 Summary and Outlook 62

3 Methodology: Computational Toolbox 63
3.1 Modelling of Elastic Rods and Tubes 64
3.2 Procedure for Tying Elastic Knots 66
3.2.1 Tying Process of the Open Trefoil Knot 66
3.2.2 Validation of Numerical Model 68
3.2.3 Tying Process of the Closed Trefoil Knot 70
3.2.4 Tying Process of the Figure-Eight Knot 71
3.2.5 Tying Process of the Sliding Granny Knot 73
3.3 Comparison Between *minCS* and *matCL* 74
3.4 Summary and Outlook 77

4 From Ideal to Elastic Knots: The Shapes of Physical Trefoil Knots 79
4.1 Literature Review and Motivation 80
4.2 Physical Realization of Trefoil Knots 84
4.2.1 Experimental Protocols 84
4.2.2 Finite Element Simulations 87
4.3 Ideal Versus Elastic *Closed* Trefoil Knots 87
4.4 Ideal Versus Elastic *Open* Trefoil Knots 90
4.5 Homotopy in the Physical Closed Trefoil Knot 93
4.6 Summary and Outlook 94

5 To Stop or Not to Stop: Capsizing Mechanism in Stopper Knots 97
5.1 Literature Review and Motivation 98

5.2 Experimental and Numerical Methodology 100

5.2.1 Fabrication of the Composite Rods 100

5.2.2 Characterization of Frictional Properties 101

5.2.3 Apparatus and Setting of the Initial Configuration 102

5.2.4 Protocol for the Experimental Mechanical Tests 102

5.2.5 Finite Element Simulations 103

5.3 Initial Knotted Configuration Prior to Testing 105

5.4 Mechanical Testing of the Figure-Eight Stopper Knots 106

5.5 The Role of Friction in Dictating Knot Performance 108

5.6 Friction-Induced Twist Triggers Capsizing 110

5.7 Resistance to Capsizing in Braided Ropes 112

5.8 Summary and Outlook 115

6 Strength of Surgical Knots **117**

6.1 Literature Review and Motivation 118

6.2 Failure of Surgical Sliding Knots 120

6.2.1 Procedure to Tie Surgical Knots 120

6.2.2 Mechanical Testing to Measure the Knot Strength 122

6.3 Effect of Experience of the Surgeon on Strength of Knots 122

6.4 Definition of a Tight Knot 124

6.5 Material Testing and Fracture 127

6.6 Dependence of the Knot Strength on Pre-Tension and Topology 130

6.6.1 Intermediate Tightness Regime 130

6.6.2 Mapping the Operating range of the Surgeon 131

6.6.3 Enhancing Knot Safety with Additional Number of Throws 131

6.6.4 Effect of Topology on Knot Strength 133

6.7 Characterization of the Frictional-Contact Interactions 134

6.8 Modeling of Surgical Filaments 135

6.8.1 Constitutive Elasto-Plastic Model 136

6.8.2 Residual Stresses to Describe Unknown Deformation History 137

6.9 Calibration of the Material Model 138

6.9.1 Uniaxial tensile tests for Model Calibration 139

6.9.2 Plastic Capstan Configuration to Calibrate the Residual Stress 141

6.10 Knot Strength Established by Normal Contact Forces 142

6.11 Summary and Outlook 146

7 Conclusion and Perspectives **147**

7.1 Summary of Findings 147

7.2 Opportunities for Future Works 150
    7.2.1 Mechanics of the Bowline Knot 150
    7.2.2 Mechanics of Knotted Umbilical Cords 152
7.3 Final Remarks 154

Bibliography **155**

Curriculum Vitae **169**

1 Introduction

From polymer chains to the shipping industry, knots are omnipresent across length scales. Overall, functional knots can be described as mechanical links used to establish kinematic constraints between filaments. For centuries, extensive practical knowledge of knotted filamentary structures has been acquired in applications including sailing, climbing and surgery. Still, the predictive understanding of the underlying physical mechanisms in knots remains crude. Knot theory, an important branch of topology, has primarily been limited to the realm of pure mathematics and idealized knots are too abstract for practical settings. Beyond their topology, physical knots also involve elasticity (bending, torsion, and stretching) of the rod, a finite diameter of the rod with deformable cross section, and frictional interactions at points of self-contact. Furthermore, knotted rods can also exhibit more complex inelastic constitutive behavior (e.g., elasto-plastic filaments in surgery), or, in the case of braided filaments or ropes, could be structured, with intricate internal frictional interactions.

This introductory chapter is structured as follows. In Section 1.1, we first describe how knots have been used through historical times before focusing on knots that spontaneously form or that are voluntarily tied to fulfill a function. In Section 1.2, we introduce several fundamental concepts (both classic and recent) pertaining to the mechanical description of rods that we will require in our investigations of physical knots. More specifically, we focus on the classic capstan problem and its limitations and on the kinematics describing framed curves in 3D space. In Section 1.3, we describe concepts in topological knot theory, required for the work in thesis. In Section 1.4, we then focus on geometric rod models, a sub-field of knot theory that is largely concerned with the computation of tightest knot configurations tied in perfectly flexible and frictionless strings. Studies applying Kirchhoff's theory to describe knotted elastic rods are summarized in Section 1.5. Next, in Section 1.6, we focus on works involving reduced- and full-3D simulations of elastic knots using the Finite Element Method. Lastly, we report relevant studies on evaluating knot quality and stability in Section 1.7. Finally, we summarize the existing literature on physical knots and describe our research niche, as well as the research questions that we have devised to address it (Section 1.8), before presenting the outline of this thesis in Section 1.9.

1.1 Functional Applications of Knots Across Ages and Length Scales

Even if knots have been used across the ages, a detailed historical account of their development remains vague. Attributing the oldest knot in the world to a specific civilization or purpose is probably not possible due to the lack of records and findings. As Turner and van de Griend [1] wrote in their comprehensive book on the '*History and Science of Knots*', the materials used to tie knots were inevitably organic, thus, subject to decay. It has been speculated that knots predate the use of fire and the invention of the wheel [1, 2]. Fortunately, there are some archaeological discoveries included well-preserved knot samples that shed some light on how prehistoric and ancient civilizations used knotted filaments.

In 1922, during the discovery of the tomb of the Egyptian pharaoh Tutankhamun, the doors of one of the shrines were secured by a knotted rope (see Figure 1.1**a1**), consisting of coiled loops and half-hitches. Egypt's desert conditions made the preservation of organic rope structures possible. The Egyptian civilization was familiar with knotting and even had a hieroglyph for the word 'knot' ('tjeset'), as shown in Figure 1.1**a2** [1].

Beyond binding applications, the Peruvian Inca civilization also used knots in counting operations for the bookkeeping of tax obligations or to store calendrical information. These knots are called '*quipu*' and were mostly based on overhand knots with different numbers of throws (see Figure 1.1**b1-b2**) [1]. Moreover, knots were used for decorative and religious purposes by the Celts, as shown in Figure 1.1**c1** and **c2**. Knot diagrams were drawn, mapping the three-dimensional knot geometry into a plane, and visualizing over- and under-crossings. Knot features symbolize time, life, seasonal changes, night and day, among others [1].

In a different context, unlike measuring distance on the ground with the units of kilometers or miles, sailors at sea use the nautical mile and the corresponding speed called 'knot' (ISO: kn, for nautical mile per hour). The origin of this unit dates back to the 16th century when mariners would gauge the speed of their ships by using a chip log. This device consisted of a piece of floatable wood (called 'chip') and an attached coil of rope with uniformly spaced knots (47 feet and 3 inches) tied in it. By throwing the chip into the water, the rope line followed freely at the back of the boat. The speed was then measured by counting the number of knots that were pulled into the water, using time intervals of 28 seconds, measured with an

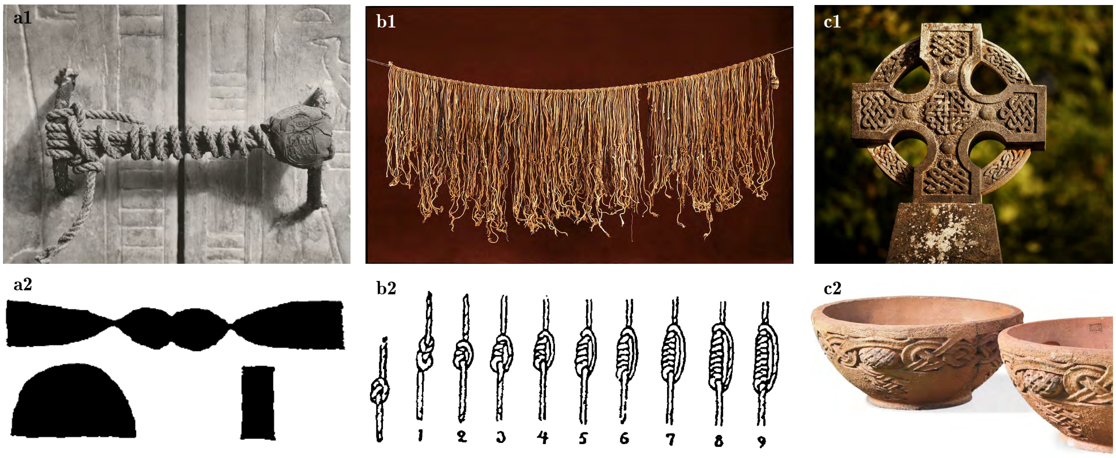

Figure 1.1: **Historical usage of knots. a1**, Shrine doors of the tomb of Tutankhamun secured by a knotted rope. Image adapted from Ref. [3]. **a2**, Hieroglyph of the word '*knot*'. Image adapted from Ref. [1]. **b1**, Photograph of a preserved '*quipu*'-device, used by Incas for counting operations. Image adapted from Ref. [4]. **b2**, Overhand knots of different numbers of throws used as '*quipu*'. Image adapted from Ref. [1]. **c1**, Celtic cross with religious knot diagrams. Image adapted from Ref. [5]. **c2**, Celtic pottery with decorative knot drawings. Image adapted from Ref. [6].

hourglass. Nowadays, the speed measurement has been vastly upgraded and standardized but the name of the unit stayed 'knot' [7]. One nautical mile corresponds to 1.15 miles, thus, 1 knot corresponds to 1.15 miles per hour.

Despite some of the historical functional purposes of knots described above, their involuntary formation can also be regarded as a nuisance during knitting [8] (Figure 1.2**a**) and in hair (Figure 1.2**b**). Raymer and Smith [9] performed tumbling experiments of rods contained in a box. The authors measured the probability of knotting as a function of rod lengths and found that almost all of the formed knots were prime knots (which will be explained in the next Section). Further, knots can form spontaneously in various natural contexts across a wide range of length scales, including, but not limited to, polymer (Figure 1.2**c**) and DNA strands [10, 11, 12], and in plasma and fluid flows [13, 14, 15], as shown in Figure 1.2**d**. During pregnancy in humans, fetal activity can spontaneously lead to the knotting of the umbilical cord. Knotted umbilical cords are observed only in around 1% of pregnancies [16], but have been shown to increase the probability of fetal death by almost a factor of four [17].

The seminal book by Ashley [22], is regarded as the first comprehensive reference manual on knots, containing 3857 numbered knot types used in innumerable applications, such as fishing [23], sailing, and climbing activities. For example, and as shown in Figure 1.2**e**, a mooring line is knotted on a mooring bollard on the dock to attach a boat. During climbing,

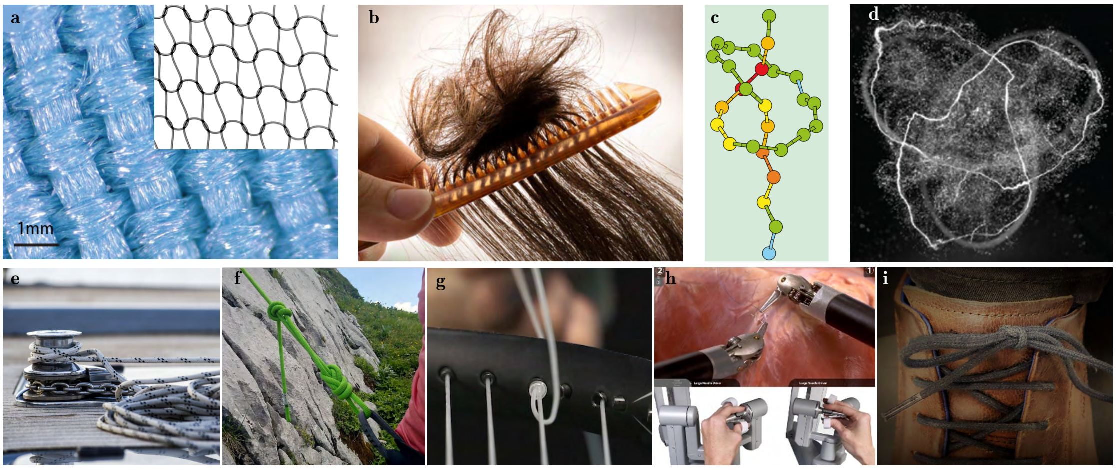

Figure 1.2: **Involuntary knot formation and applied knots.** **a**, Microscopic image of a knitted tissue. The inset shows a close-up view of the individual stitches of knitted fabric and is adapted from Poincloux et al. [8]. **b**, Tangles and knots are considered a nuisance in hair. Image adapted from Ref. [18]. **c**, Model of an overhand knot in a polymer strand. Image adapted from Saitta et al. [10]. **d**, Knotted vortex of a closed trefoil topology. Image adapted from Kleckner and Irvine [13]. **e**, Mooring line attached to a mooring bollard on a dock. Image adapted from Ref. [19]. **f**, Figure-eight bend and termination knot during climbing. Image curtesy of P. Reis. **g**, Stopper knot used tie filament off during tennis racket stringing. Image adapted from Ref. [20]. **h**, Knots used in surgical applications on mono- and multi-filamentary sutures. Image adapted from Ref. [21]. **i**, Shoelace knot based on the binding square knot topology.

the rope is typically tied to the climber's harness by a double figure-eight knot (see Figure 1.2**f**). Further, a stopper knot at the end of the rope on the belayer's side prevents the rope from completely sliding through the rappelling device, which could have fatal consequences. Similarly, a termination knot is used during tennis racket stringing, as shown in Figure 1.2**g**. In surgery, sutures and ligatures are utilized for the closure of wounds [24, 25, 26] (Figure 1.2**h**). Shoelaces are tied with binding knots (see Figure 1.2**i**) and are subject to failure due to cyclic impact loading and inertial effects [27].

1.2 Frameworks to describe the mechanics and geometry of rods

Before focusing on existing models describing loose or tight knots, we will first outline classic and more recent concepts derived for elastic rods but, in some limiting conditions, also potentially applicable to knotted rods. From a mechanical point of view, physical knots involve frictional interactions between the touching strands, or between a rod and a rigid object (typically a cylindrical post), as in the case of hitch-knots. Therefore, we focus on studies that challenge the classic capstan problem to evaluate its applicability for tight, physical knots.

From a geometric point of view, knots comprise a single or multiple rods that are entangled in 3D space. Next, we summarize some existing frameworks commonly used to describe the kinematics of framed curves, also focusing on a discrete approach.

1.2.1 Frictional Contact in the Capstan System

As we will show throughout this thesis, *friction* is key in functional knots. The capstan problem is a classic setting that has recently drawn attention in the context of tight filaments in contact. The word ‘*capstan*’ originated from the Latin "pulley cord" designating a mechanical device used on sailing ships to attach, raise, or lower anchors or other heavy equipment by ropes or chains (see Figure 1.3**a**). If the frictional contact between a rope and a cylindrical capstan is sufficiently large, the rope can be in equilibrium for a high loading force, T_1, on one extremity, and a vanishing loading force on the other end. A prediction, describing this tension drop was first derived by Euler [28] and Eytelwein [29],

$$\frac{T_1}{T_0} = e^{\mu \Delta \alpha}, \tag{1.1}$$

where $\Delta\alpha$ is the wrapping angle of the filament or rope around the cylinder, and μ is the dynamic friction coefficient. According to Eq. (1.1), the tension in the filament increases exponentially along the contact region. During the derivation of this equation, it is assumed that the filament is (1) perfectly thin and (2) perfectly flexible. Despite these non-physical requirements of the idealized capstan equation, Eq. (1.1) accurately predicts the tension difference for filaments with low bending rigidity, such as ropes, and when the diameter of the filament is much smaller than the cylinder diameter.

In textiles and tight knots, the filaments wind around themselves; the underlying filament acts as the cylindrical capstan, albeit with the same diameter as the contacting filament, which violates the assumption (1) mentioned above, required for the derivation of Eq. (1.1). In pulley systems involving belts, the assumption (2) of negligible bending stiffness is also compromised. The theoretical study by Stuart [31] analyzed the effect of finite bending stiffness of the filament on the tension ratio, while keeping the condition on the vanishing cross section of the filament (1). They reported concentrated forces at the locations of touch-down and lift-off of the filament (see Figure 1.3**b**). Further, they defined critical limits for the minimum wrapping angle, $\Delta\alpha$, and minimum applied loads on the filament extremities, above which the classic capstan equation is applicable. Later, Jung et al. [34, 32] investigated the effect of finite thickness (and bending stiffness) of the filaments winding around rigid cylinders of varying diameters. In addition to the local force balance, the moment balance was included in the analytical method (see Figure 1.3**c**). The theoretical prediction suggested

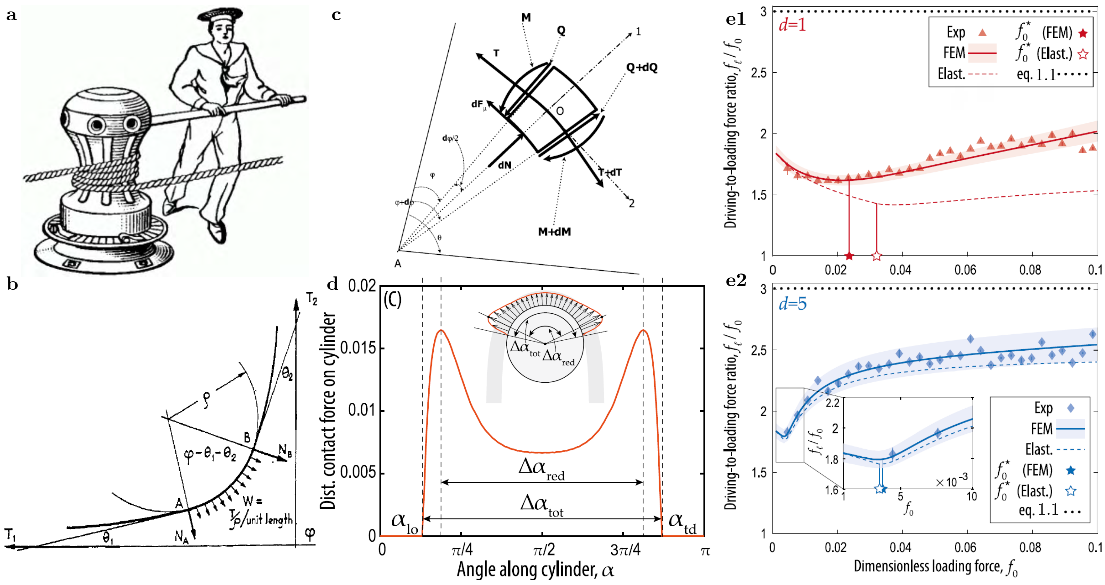

Figure 1.3: **The capstan problem.** **a**, Schematics of a sailor using the capstan device on a boat to lift heavy weights. Image adapted from Ref. [30]. **b**, Force distribution with localized point forces at the touch-down and lift-off locations of a stiff but thin filament in contact with a rigid capstan. Image adapted from Ref. [31]. **c**, Free-body diagram on a curved filament with finite thickness and bending rigidity. Image adapted from Ref. [32]. **d**, Distributed contact force on the cylinder as a function of the wrapping angle, $\Delta\alpha$. Image adapted from Ref. [33]. **e**, Experimental and numerical results with the theoretical prediction of the force ratio, T_1/T_0, as a function of the loading force, T_0. The wrapping angle is $\Delta\alpha = \pi$, and the friction coefficient, $\mu = 0.35$. The classic capstan prediction is shown by the horizontal dotted line, and the predictions by the elastica model are represented by the dashed curves. The cylinder to filament ratio of diameters is, $d = 1$, in **e1**, and $d = 5$, in **e2**. Image adapted from Ref. [33].

.

that the force ratio, T_1/T_0, decreases for smaller diameters of the rigid capstan, but does not consider local contact forces, as previously suggested by Stuart [31].

The previous studies by Stuart [31] and Jung et al. [34, 32] report the significant impact on tension ratio given by Eq. (1.1) if one ideality condition, (1) or (2), is not met. In an effort to better understand the underlying mechanics of the problem, Grandgeorge et al. [33] have recently combined precision model experiments, numerical simulations, and theoretical analyses. Specifically, the authors focused on the contact region (wrapping angle, $\Delta\alpha$) and the distribution of the contact pressure in a static and a sliding model system. In the static case, where there is no relative displacement between the filament and the capstan, it was found that a localized contact region transitions to a double-peaked contact force distribution (see Figure 1.3**d**) for increasing symmetric loading forces, $T_1 = T_0$. In the sliding case, a local minimum was observed in the force ratio, T_1/T_0, as a function of the loading force, T_0 (see

Figure 1.3**d**), which is not captured by the classic capstan prediction. This behavior is shown in Figure 1.3**e** for the cylinder-to-filament ratio of diameters, $d = \{1, 5\}$. Note that derived solutions of the elastica equations (dashed lines in Figure 1.3**e**) are able to predict the results for large d but cannot capture the tension ratio when $d \approx 1$.

The contacting regions of physical knots can be seen as a modified capstan problem but where the rigid cylindrical capstan is replaced by an underlying, non-straight, non-rigid filament, and with $d \approx 1$. Consequently, the filament crossings are in general non-orthogonal and involve tight contacts, with non-negligible bending stiffness. Thus, the idealized capstan equation, Eq. (1.1), as suggested by Euler [28] and Eytelwein [29], is of limited applicability in the context of physical knots with tight filaments in contact.

1.2.2 Kinematics of Framed Curves

As reported by O'Reilly [35], the Cosserat brothers were the first to formulate a rod theory based on director vectors, $(\hat{\mathbf{d}}_1, \hat{\mathbf{d}}_2, \hat{\mathbf{d}}_3)$, describing a three-dimensional curve, that deforms rigidly. This framework, called Kirchhoff's rod theory in recognition of the contribution of Gustav Kirchhoff, is capable of modeling bending and torsion in rods, though typically keeping the inextensibility constraint. Extensible versions of Kirchhoff's rod theory have also been proposed [35]. We refer to the comprehensive book by O'Reilly [35] for the derivation of the rod model and focus next on providing a brief description of the kinematics of rods, which will be need later in this thesis.

Assuming negligible cross-sectional and local shear deformations, slender rods can be approximated as curves in 3D space. The orientation of the local orthogonal basis of a rod can be described by the Cosserat frame $(\hat{\mathbf{d}}_1, \hat{\mathbf{d}}_2, \hat{\mathbf{d}}_3)$ along its physical centerline [36]. This orthogonal basis is an adapted frame, moving according to the deformation of the rod, including twist (contrary to the Frenet frame). The unit vector $\hat{\mathbf{d}}_3(s)$ is defined as the tangent to the physical centerline, such that $\hat{\mathbf{d}}_3 \equiv \mathbf{r}'(s)$, where $\mathbf{r}(s)$ corresponds to the coordinates of the physical centerline curve parametrized along the arc length s. The $[\cdot]'$ notation represents derivatives with respect to s. The unit vectors $\hat{\mathbf{d}}_1$ and $\hat{\mathbf{d}}_2$ form the basis of the plane normal to the tangent vector $\hat{\mathbf{d}}_3$, and satisfy the kinematic relation:

$$\hat{\mathbf{d}}'_a = \Omega \times \hat{\mathbf{d}}_a \quad (a = 1, 2, 3), \tag{1.2}$$

$$\text{where } \Omega = \sum_{a=1,2,3} \Omega_a \hat{\mathbf{d}}_a \tag{1.3}$$

is the Darboux vector $\Omega(s)$ describing the rotation of the Cosserat frame along the arc length. More precisely, the ath component of the Darboux vector, Ω_a, corresponds to the rotation rate of the Cosserat frame around the axis $\hat{\mathbf{d}}_a$[36, 35].

The total curvature of the centerline is then:

$$K(s) \equiv \sqrt{\Omega_1^2 + \Omega_2^2}. \tag{1.4}$$

The framework of the Cosserat frame is not limited to curly rods or tangles but can be applied on any knot topology in its loose and tight configurations. For this reason, the concept of using framed curves to describe properties like curvature or twist will be essential in this thesis. In Chapter 2, we will fabricate rods including geometric features, that allow to experimentally extract the Cosserat frame (used in Ref. [37]). In Chapter 2, we will also implement specific node sets in fully 3D rods in order to extract the director vectors in FEM (used in Chapter 5 and Ref. [37]).

1.2.3 Discrete Differential Geometry of curves in 3D space

Experimental and numerical measurements of the geometric configurations of rod systems are intrinsically discrete, not continuous. Typically used in the context of computer graphics [38], Discrete Differential Geometry (DDG) is valuable tool to describe rod-like structures as discrete curves in 3D space. Here, we briefly describe the advantages and challenges of using DDG, as highlighted in Ref. [38].

On the one hand, geometric properties of *discrete* objects can easily be measured, and their discrete nature matches computational data structures. On the other hand, mathematical theorems are typically well-defined for *continuous* objects. Transferring the geometric information from the discrete to the continuous domain is less trivial than it might appear. To illustrate, the curvature computation is a geometric key property in knots and is well-defined in the case of a smooth, continuous curve. In a planar setting, it was shown that convergence of geometric properties of discrete curves with the analog smooth curves could be achieved by refining the discrete curves using inscribed polygonal geometry [38]. In Figure 1.4**a**, the procedure of mapping the various vertices and edges of an open polygon onto a unit circle by using a Gaussian map is visualized. Each edge maps to a single point on the unit circle, while the vertices are described by an arc to smooth the change in direction.

It was recognized that the DDG framework could be applied to rods because the centerline describes a curve in 3D space. Bergou et al. [39] extended the DDG approach of curves to thin elastic rods. Using the Kirchhoff equations to describe the elastic energy of rods, a discrete form of these equations is derived to describe the centerline of a rod parametrized by an arc

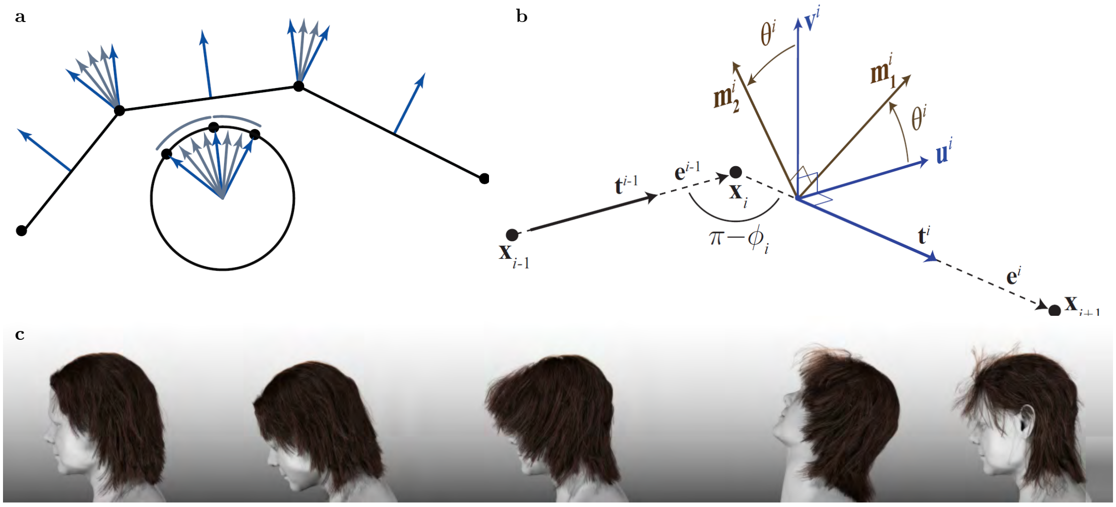

Figure 1.4: **Underlying principals of Discrete Elastic Rod theory.** **a**, Polygone constituting of edges and vertices. The edges and vertices can be mapped onto the unit circle (a single point for edges, an arc for vertices). Image adapted from Grinspun and Secord [38]. **b**, Representation of a discrete framed curve consisting of a centerline, described by vertices and edges, and a material frame per edge. Image adapted from Bergou et al. [39]. **c**, Simulation of hair using Discrete Elastic Rod theory. Image adapted from Bergou et al. [40].

length and a material frame (Cosserat frame), as represented in Figure 1.4**b**.

Bergou et al. [39] introduced the discrete curvature defined as:

$$\kappa_i = 2\tan\frac{\phi_i}{2} = 2\frac{\sin\phi_i/2}{\cos\phi_i/2}, \tag{1.5}$$

where ϕ_i is the angle between two consecutive edges along a discrete curve. Note that the curvature at i uses the combined information from two consecutive $(i-1)$ and i edges. To avoid the use of turning angles ϕ_i, Eq. (1.5) can be converted such that it only includes vector edges $\mathbf{e}_i = \mathbf{r}(s_{i+1}) - \mathbf{r}(s_i)$, where $\mathbf{r}(s_i)$ are the discrete vertices of the curve. To this end, we consider that the angle $\phi_i/2$ is spanned as follows:

$$\text{Span}\{\phi_i/2\} = \left\{\frac{(\mathbf{e}_i/|\mathbf{e}_i| + \mathbf{e}_{i-1}/|\mathbf{e}_{i-1}|)}{|(\mathbf{e}_i/|\mathbf{e}_i| + \mathbf{e}_{i-1}/|\mathbf{e}_{i-1}|)|}, \frac{\mathbf{e}_i}{|\mathbf{e}_i|}\right\} \tag{1.6}$$

After some algebra steps, the explicit expression from Bergou et al. [39] for the definition of the discrete curvature is derived, only making use of the vector edges $\mathbf{e}_i$:

$$\kappa_i = 2\frac{\mathbf{e}_{i-1}\times\mathbf{e}_i}{|\mathbf{e}_{i-1}||\mathbf{e}_i| + \mathbf{e}_{i-1}\cdot\mathbf{e}_i}. \tag{1.7}$$

While the curvature computation based on the Darboux vectors needs the information of the whole Cosserat frame (used in Chapter 5), Bergou et al. [39] provides a method to compute the discrete curvatures of knotted rods only relying on the tangent vectors of the centerline (applied in Chapter 4). The described kinematics of Discrete Elastic Rods (DER) is explained in detail in the comprehensive book by Jawed et al. [41], and is at the basis of simulations that closely reproduce physical phenomena of rod-like structures, *e.g.* hair, as shown in Figure 1.4**c** [40].

1.3 A (Very Brief) Primer on Topology and Knot Theory

Compared to the long history of the practical usage of knots in ropes and threads, the origins of the mathematical theory of knots in the 1860s are quite recent [42]. Even though the emphasis of this thesis is on physical knots, the knowledge gathered in the field of topology and its sub-field of knot theory in the last century is extensive. In this Section, we will comment on the origins of mathematical knot descriptions before focusing on terminology and basic concepts in topological knot theory.

1.3.1 The Beginnings of Knot Theory

In the comprehensive "*Knot Book*" [42], Adams describes the historical origins of the mathematical field of knot theory. In 1867, the theory proposed by Lord Kelvin (William Thomson), where atoms were regarded knotted vortices, raised significant interest in the study of knots. Kelvin hypothesized that atoms were knots, which make up a substance, called ‘ether’ (see Figure 1.5**a**). Shortly after the presentation of this model for atoms, the field of knot theory was kicked off by the Scottish physicist Peter Guthrie Tait, who was able to tabulate and classify knots up to 10 crossings (as detailed in the next paragraph). The corresponding publication in the year 1885 is known as the ‘Tait conjectures’ [42]. In 1887, the Michelson-Morley experiments demonstrated that Kelvin’s model for atoms was wrong [42]. Nevertheless, the mathematical community had already caught interest in knot theory and continued their studies. Over the decades that followed, knot theory became a sub-field of the mathematical field of topology. Interestingly, a century after the field of knot theory originated from a misguided theory, it became useful in chemistry and biology. In the 1980s, biochemists discovered that DNA molecules form knots [43, 44], and that the topology of knotted molecules determines their properties [45, 46].

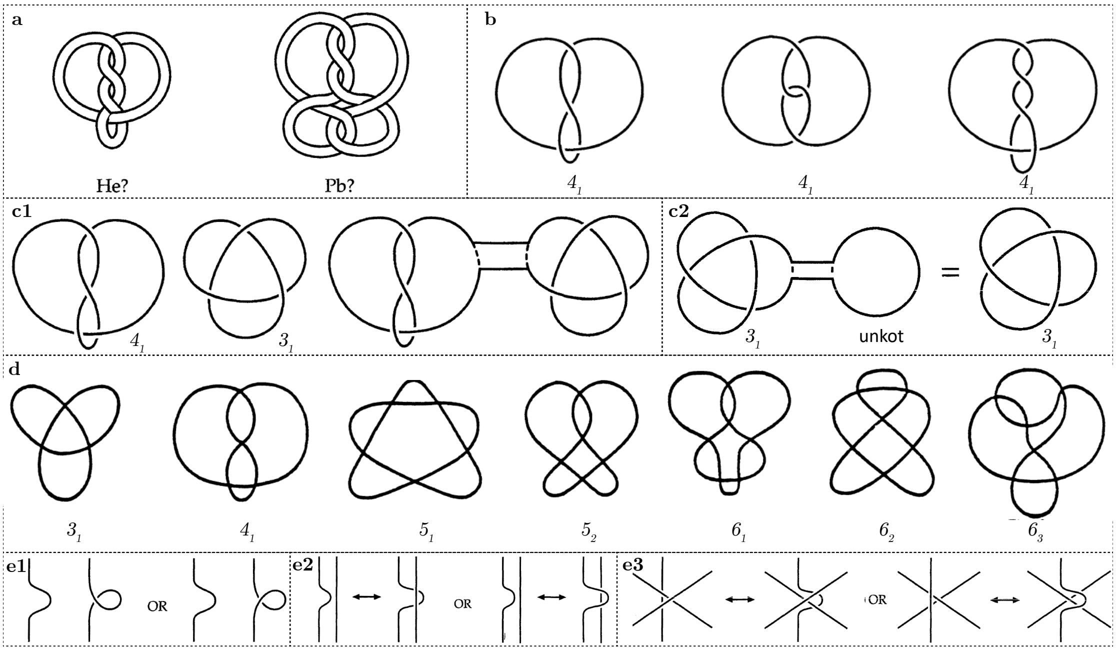

Figure 1.5: **Concepts of mathematical knot theory.** **a**, According to a misguided theory, atoms were described as knotted vortices. **b**, Three projections of the figure-eight knot. **c1**, Joining the figure-eight with the trefoil knot leads to a composed knot. **c2**, The trefoil knot is a prime knot and cannot be decomposed further. **d**, Projections of all the prime knots with less or equal to six crossings. The knots are described using the Alexander-Briggs notation. Image adapted from Ref. [47]. **e**, The three types of Reidemeister moves (type I in **e1**, type II in **e2** and type III in **e3**). The images in **a**, **b**, **c** and **e** are adapted from Ref. [42].

1.3.2 Basic Concepts in Topological Knot Theory

Mathematical knots are typically closed knots (with joined ends), as opposed to applied physical knots tied in ropes. In two dimensions, knots can be pictured by *projections*. Each of the three depicted projections, shown in Figure 1.5**b**, represents the figure-eight knot, which has a minimum of four crossings. Any knot can be drawn with an infinite amount of *crossings*, but there is a minimum number of crossings for each knot. The simplest knot is the unknotted circle, called the *unknot*, or the *trivial knot*.

Knot theory is largely concerned with classifying knots, and showing if knots are different or not, *i.e.* if it is possible to find the same projection just by rearranging the string segments of a closed knot without undoing its crossings. In this context, a *composite knot* can be decomposed in multiple non-trivial knots, called *factor knots*. In Figure 1.5**c1**, the decomposition of a composite knot is shown, resulting in a figure-eight and a trefoil knot. Eventually, if a knot cannot be written as the sum of two non-trivial knots, it is called a *prime knot*. For instance, in Figure 1.5**c2**, the closed trefoil knot cannot be decomposed further into non-trivial factor knots. Consequently, the trefoil knot is a prime knot. In Figure 1.5**d**, the first prime knots up to six crossings are listed. For a positive integer of crossings, n, a finite number of prime knots exist.

The most traditional notation to describe the knot topology dates back to the year 1926 and is called the *Alexander-Briggs notation* [47]. The knots are organized according to their crossing number, n, with an arbitrary subscript that underlies the condition that torus knots (see below) are listed first. In Figure 1.5**d**, we used the Alexander-Briggs notation for the labeling of each of the knots shown. The Dowker and the Conway notations as well as the Gauss code, are more sophisticated since they include knot properties. However, in this thesis, the Alexander-Briggs notation is sufficient to denote the different knot topologies considered.

To check whether two projections are *equivalent* (corresponding to the same knot), the mathematician Kurt Reidemeister provided the so-called *Reidemeister moves*, which do not change the knot topology. The first Reidemeister move introduces or takes out a simple twist in the string, as shown in Figure 1.5**e1**. If two crossings are added or removed (see Figure 1.5**e2**), it is called type II Reidemeister move. The third and last move allows to slide a string completely from one side of the crossing to the other side, see Figure 1.5**e3**.

Each knot can be classified into one of the following three knot types: torus knots, satellite knots, and hyperbolic knots. The torus knots (ex. the trefoil knot) lie on an unknotted (from the trivial unknot) torus, as depicted in Figure 1.6**a**. A satellite knot constitutes a first knot inside an unknotted torus. The latter is then tied itself into a second knot, resulting in the satellite knot (see Figure 1.6**b**). Finally, in 1974, Thurston [48] defined the hyperbolic knot type as a knot that has a complement that can be given a metric of constant negative curvature. In Figure 1.6**c**, the hyperbolic figure-eight knot is shown together with the space-filling surface that spans the figure-eight knot. We refer to Ref. [48] for further explanations since this is out of the scope of this thesis.

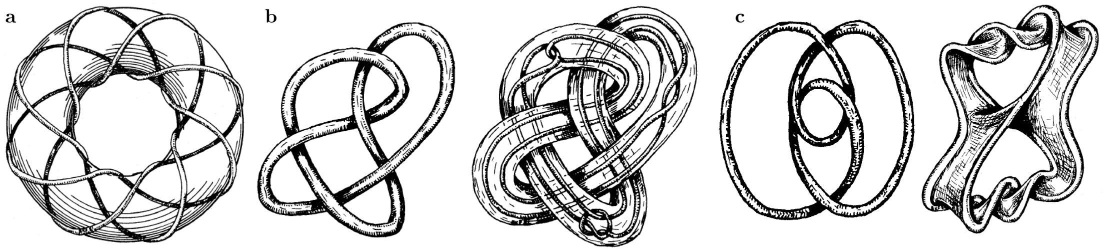

Figure 1.6: **Classification in three knot types.** **a**, Torus knots depicted with the unknotted torus surface. **b**, Non-trivial knot (left) and its satellite (right). **c**, The figure-eight knot (left) and the same knot spanned by a surface in three-dimensional space. The images in **a**, **b** and **c** are adapted from Ref. [48].

1.4 Tightest Tangles and Knots Tied in Geometric Rods

While knot theory is largely concerned with the tabulation and classification of knots, independent of their tightness, a smaller sub-field has developed in the mathematical knot theory community, studying knots tied in *idealized ropes* [49, 50]. An idealized rope of finite diameter assumes an inextensible centerline, undeformable cross section, and no bending energy of the centerline. Also, the self-contact of the rods is modeled as perfectly slippery. In this context of a purely geometric rope model, complex algorithms have been developed to compute the tightest knot configurations. Cantarella et al. [51] developed a geometric model based on the minimization of the rope length and allowing for the modeling and visualization of the tightening of knots.

Pierański [52] performed computations of ideal knot shapes and developed the SONO (Shrink On No Overlap) algorithm for knot tightening. This algorithm operates on a piece-wise linear (polygonal) curve with a hard sphere inscribed at each vertex. If two spheres are found to overlap, they are shifted apart, and if the average overlap value is small enough, the knot is shrunk by scaling it (while keeping the radius of the spheres fixed). However, piecewise linear curves are not continuously differentiable and have zero thickness because they have sharp corners, so the normal injectivity radius of SONO configurations is zero. The *normal injectivity radius* of a curve is the radius of the largest tube such that the surface of the tube is smooth and the tube does not intersect itself [53].

An important milestone was achieved when Rawdon [54] showed that a non-continuously differentiable curve could be constructed with a finite thickness from a piece-wise linear curve. The authors proved that by inscribing arcs in polygonal curves, and as the number of edges tends to infinity, the polygonal thickness converges to the true thickness of the inscribed curve. Thus, the use of piece-wise linear discretization in searching for ideal knots is justified and gives a notion for the thickness of a polygonal curve. This additional construction made SONO configurations very useful as it is a fast algorithm when initialized with a far-from-ideal shape. Based on non-zero polygonal thickness, another code for tightening knots, called *RidgeRunner*, was developed by Ashton et al. [55]. The authors combine the polygonal thickness with a Constrained Gradient Descent (CGD). The constrained gradient of the polygonal rope length is calculated in addition to a penalty term that encourages the polygon to remain close to equilateral, which is not implemented in the previously-described SONO algorithm.

All these computations of ideal knot shapes have produced configurations that are very accurate for smooth topological curves, but none are particularly good at resolving derivatives. In the following, we illustrate the difficulty of evaluating properties involving first and second derivatives, such as curvature. Baranska et al. [56] studied torsional features and details of the curvature profile of tight, closed trefoil knots using the SONO algorithm. Since the simulated rope consists of discrete spheres, the rope is corrugated, as visualized for a small number of spheres in Figure 1.7**a1**. Consequently, the zoom into the curvature profile (see Figure 1.7**a2**) reveals numerous sharp deeps. On the one hand, these peaks reduce for a large number of spheres, while, on the other hand, the sensitivity of corrugation increases when the knot approaches its tightest configuration. Note that the characteristic double-peaks in the curvature profile are visible as singularities in the rope surface (see Figure 1.7**a3**, and described further by Smutny, Jana [57]. In Chapter 4 of this thesis, we comment on the existence of the double-peaks in a physical, closed trefoil knot.

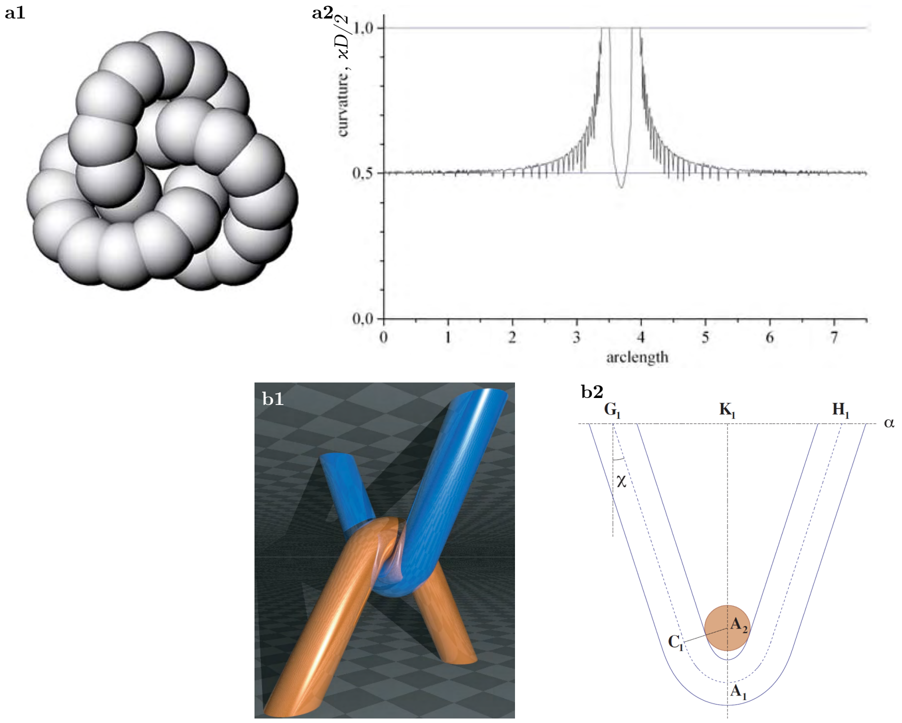

Figure 1.7: **Ideal knot shapes based on purely geometric rod models.** **a1**, Visualization of the SONO algorithm applied on a closed trefoil knot. Hard spheres are inscribed on the vertices of the centerline, which corrugate the tube. **a2**, Detailed view on one of the double-peaks in the curvature profile of the closed trefoil knot, displaying numerous sharp deeps. **a3**, Close-up view on the 3D closed trefoil knot, showing a loop and the piece of rope passing through it. Singularities can be observed at the arc length locations of the double-peaks in **a2**. **a1-a3**, Images are adapted from Baranska et al. [56]. **b1**, Two linked pieces of ideal rope attached to parallel planes. **b2**, The central section of the two clasped ropes showing the double contact. **b1-b2**, Images are adapted from Starostin [58].

It has been observed by various authors, for example by Oscar Gonzalez and Smutny [59], that two diametrically opposed infinite helices can have single or double contact. Therefore, the question was raised whether there exist finite length configurations of two curves in double contact everywhere. One such configuration is the orthogonal clasp, computed, for example, by [58], and shown in Figure 1.4**b1-b2**. Comparison with contact maps from ideal knots and links, such as the collection presented in Ref. [60], suggests that physical knots may be composed of non-symmetric versions of such interwound configurations.

1.5 Loose Knots Described by Kirchhoff's Theory for Elastic Rods

In the previous Section, the ideal knot model assumes a perfectly flexible string, which does not necessarily describe physical knots. The purely geometric rods do not include a constitutive material model, meaning that they offer no resistance to bending or torsion, nor can they include cross-sectional or shear deformations. All of these ingredients are, however, crucial in physical and functional knots, *e.g.* stopper knots (Chapter 5) and surgical knots (Chapter 6).

Audoly et al. [61] took on the problem of relating the topology of a physical knot to its mechanical behavior, developing a framework for the mechanical response of loose elastic overhand knots based on the theory of Kirchhoff rods (see Figure 1.8**a**). The kinematics of a Kirchhoff rods were summarized previously, in Section 1.2.2. Kirchhoff's theory for elastic rods makes the assumption that the three characteristic lengths of the knot, the radius of the rod, $D_{\text{Rod}}/2$, the braided length l and the characteristic radius of curvature $D_{\text{Loop}}/2$, are all of different orders of magnitude. In other words, the separation of length scales assumes that $D_{\text{Rod}}/2 \ll l \ll D_{\text{Loop}}/2$, as shown in Figure 1.8**b**.

In general, by minimizing the sum of bending and potential energies in the tensioned overhand knot, as well as accounting for Coulomb friction, Audoly et al. [61] reported that the tensile force, T, can be expressed as:

$$\frac{TD^2}{4B} = \frac{\pi^2}{2\bar{e}^2} \pm \frac{0.492\mu\pi^{1.5}}{\bar{e}^{1.5}}, \tag{1.8}$$

where $B = \pi ED^4/64$ is the bending stiffness (with Young's modulus, E, the undeformed diameter D), $\bar{e} = e/D = (L_0 - L)/D$ is the normalized end-to-end shortening (with the undeformed length L_0, and the end-to-end distance between the extremities, L), and μ denotes the dynamic Coulomb friction coefficient for self-contact. The first term in Eq. (1.8) represents the elastic bending contribution, and the second term arises due to dynamic friction in the regions of self-contact. The positive (or negative) sign of the second term corresponds to the tying (or untying) of the knot when $\dot{\bar{e}} < 0$ (or when $\dot{\bar{e}} > 0$). Note that Eq. (1.8) was reported in Ref. [62], where it was rewritten from the original one, presented in Ref. [61].

Interestingly, the model developed by Audoly et al. [61] also accounts for *weak* friction in the braid, such that the effect of friction remains small compared to the other traction and pulling forces in the knot system. The simple dynamic Coulomb friction law describes friction and alters the relation between the applied tension and the end-to-end distance. Moreover, for loose overhand knots, the predicted contact topology was validated by close-up photographs of the braided region. The same theory was also verified for cinquefoil knots (two throws: unknotting number, $n = 2$), a variation of the overhand knot (one throw: unknotting number, $n = 1$) in Ref. [61, 63].

Subsequent experiments by Jawed et al. [64] with loose knots of higher unknotting numbers (number of times the knot must be passed through itself to untie it) highlighted limitations of the previous theory by Audoly et al. [61]. The longer frictional contact region in the braid in long elastic overhand knots ($n \leq 2$) leads to large traction forces during the tightening process. Consequently, Jawed et al. [64] derived an analytic model, incorporating a *strong* effect of friction, to describe the topology and mechanics of long elastic overhand knots (see Figure 1.8**b**), up to unknotting number $n = 10$. Excellent agreement was found between theory and experiments for overhand knots in their loose configurations, collapsing the experimental traction curves on the master curve (dashed line) predicted by the theory [64].

The previously presented frameworks describing simple and long overhand knots were based on Kirchhoff's theory for elastic rods, assuming a separation of length scales, as mentioned earlier. Indeed, Audoly et al. [61] reported that Eq. (1.8) is valid for loose overhand knots, in the $\bar{e} \gtrsim 100$ regime. In the limit of $\bar{e} \to 0$, Eq. (1.8) predicts the divergence of T, which is a manifestation of the inextensibility constraint of the underlying Kirchhoff rod theory.

Despite these limitations, Audoly et al. [61] attempted to compare their results of the analytic model, considering a tighter configuration of the overhand knot ($\bar{e} = 9.58$), with the geometrical prediction of the curvature by Pierański et al. [65] in Figure 1.8**a**. Although similar levels of tightness were considered, the simulations based on the elastic model were in contradiction with the geometric model. Whereas the geometric model in Ref. [65] gives the maximal curvature at the entrance of the knot, the analytical model [61], developed for loose configurations, yields that the curvature reaches a maximal value in the outer segment of the knot, denoted by **a** and **c** in Figure 1.8**a**. Recently, Baek et al. [62] showed that the Kirchhoff rod model in Ref. [61] predicts well the qualitative centerline curvature obtained through experiments and Finite Element simulations on purely elastic rods tied in an overhand knot with end-to-end shortening, $\bar{e} = 9.58$ (see Figure 1.8**c**). Quantitative differences were expected, given the tight knot configuration.

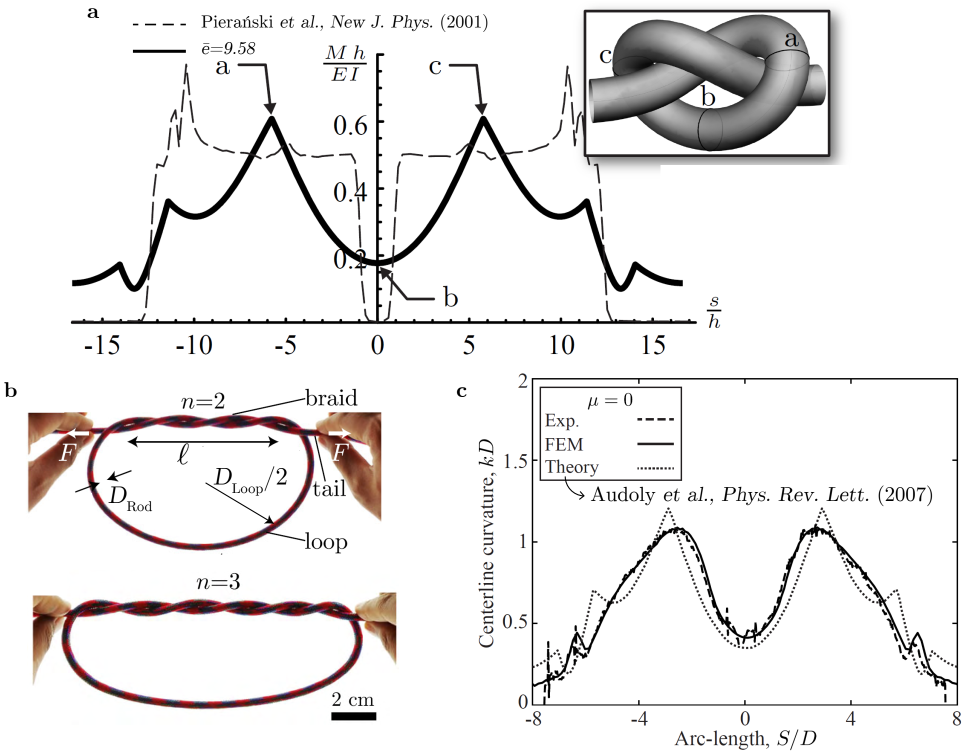

Figure 1.8: **Knots described by the Kirchhoff rod model for elastic rods.** **a**, Comparison of curvature profiles of tight open trefoil knots between a model based on Kirchhoff rods and purely geometric rope model according to Ref. [65]. Image is adapted from Audoly et al. [61]. **b**, Photographs of overhand knots with different unknotting numbers n. Images adapted from Jawed et al. [64]. **c**, Centerline curvature profiles for an overhand knot obtained from FEM simulations, experiments, and the theoretical prediction from Eq. (1.8). Image is adapted from Baek et al. [62].

1.6 Numerical Simulations on Elastic Knots

The capability of using the kinmeatics of Discrete Elastic Rod (DER) theory, introduced in Section 1.2.3, on knots has been recognized in the mechanics community. In the context of rods with contact interactions, the physical ingredient of friction needs to be accounted for. Typically, the friction is considered as constraints for the equations of motions. Using the constraint-based method to describe the frictional effects together with DER theory, Tong et al. [66] successfully simulated snap buckling in overhand knots. The authors reported an excellent match between the numerics and experiments, even for the dynamic event of snap buckling (called ‘inversion’). Their framework enabled the extraction and interpretation of the physical properties of long overhand knots.

Since the implementation of the constraint-based contact handling method slows down simulations significantly, Choi et al. [67] developed a fully implicit penalty-based frictional contact method (IMC), which decreased the computational cost of DER-based simulations by converging faster. The authors validated the IMC contact model by incorporating it in the DER algorithm and comparing it to the results of existing contact models, using the long overhand knot as a test case. Recently, Tong et al. [68] applied the combination of DER theory with the IMC contact model on flagella bundling. In addition, the authors showed that their model is capable of predicting the experimental force-displacement behavior of long overhand knots by Ref. [64].

Since we are dealing with elasto-plastic deformation in Chapter 6, the study by Li et al. [69] should not miss in this literature review. Based on discrete differential geometry, the authors developed a framework that is able to simulate elasto-plastic rods by meshing the cross section of the rod with fiber-like elements. A nonlinear constitutive model is applied to the discrete elements which are associated with a flow rule. The simple test cases of uniaxial stretching and a simply supported beam yielded good agreement between the numerical simulations and the analytical solutions.

Durville [70] developed a finite element approach to simulate the mechanical behavior of beam assemblies by point-wise beam-to-beam contact elements. Contrary to the assumption of rigid cross sections in typical beam models, this customized beam model includes additional degrees of freedom, enabling the description of the kinematics of cross sections. The tying process of an overhand knot is displayed sequentially in Figure 1.9**a1-a8**, involving two rigid bars to prevent a rotation of the loop. Emphasis was put on the contact-friction interactions at self-contact or between different beams (as shown in Figure 1.9**b**). To this end, the closest points between two curves were locally predicted, assuming point-wise contact. An adaptive adjustment of the penalty coefficient was implemented allowing the treatment not only of monofilaments but also of several contact elements, *e.g.* fibrous materials (see Figure 1.9**c**). Still, acute angles between the contacting beams and parallel beam assemblies were not treated, as reported by Litewka [71]. This includes configurations of curves that have double contact (introduced in Section 1.4) and would not be represented correctly by this model.

Finite element (FE) simulations that include the *full* 3D-elasticity model have been performed by Alden et al. [72]. A simple overhand knot was tightened in an FE simulation using a homogeneous isotropic elastic material. While one rod extremity was fixed (displacement and rotation), the other one was subjected to an imposed displacement. Even though the numerical results match the overall experimental force-displacement curve, it is questionable if it represents well the local geometric and mechanical features in the knot itself since the elasto-plastically-deforming nylon fishing line can hardly be described by an isotropic elastic

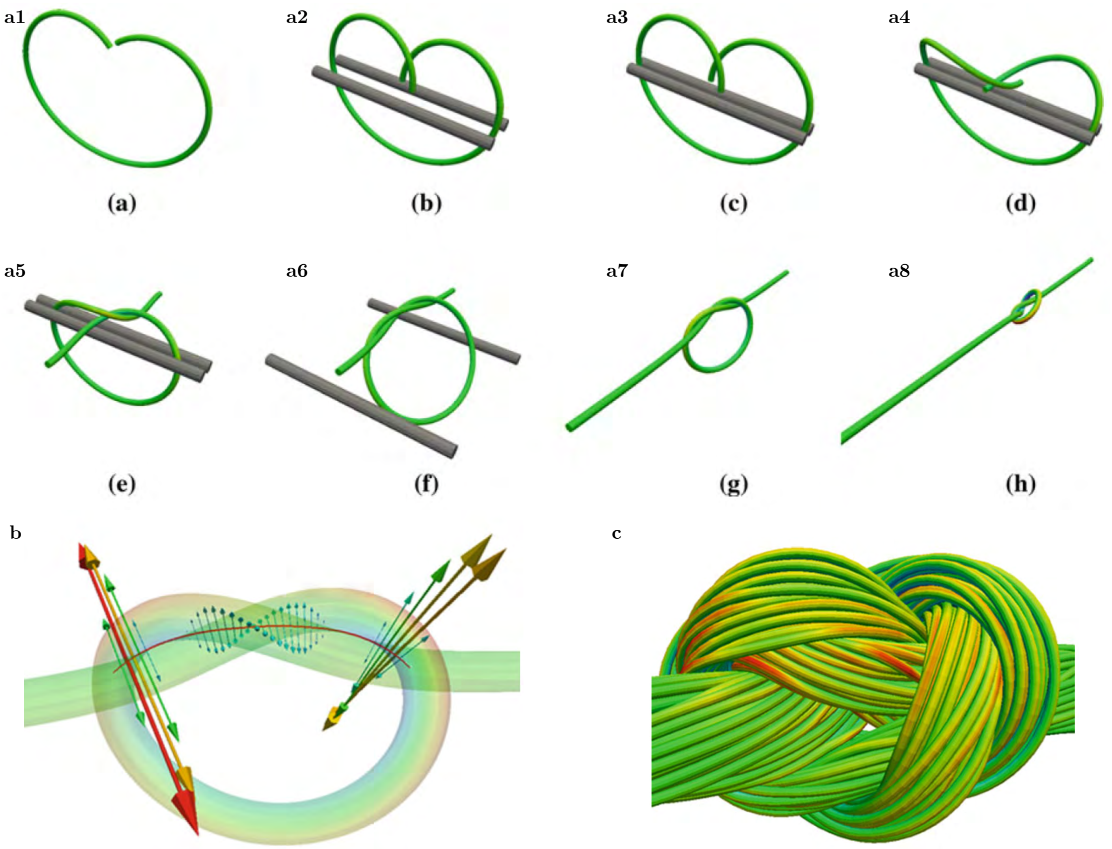

Figure 1.9: **Finite Element simulations of knots.** **a1-a8**, Tying process of the overhand knot tied in a beam including kinematics of cross sections. Two rigid bars (grey) avoid a rotation of the loop. **b**, Normal contact reactions of the point-wise contact. **c**, Tight overhand knot tied in 27 filaments with point-wise beam-to-beam contact elements. The images are adapted from Ref. [70].

constitutive model (see Chapter 6).

Recently, Baek et al. [62], together with the author of this thesis, reported a detailed validation of a Finite Element framework to model purely elastic knots, *e.g.* the overhand knots and the figure-eight knot. Parts of this publication are described in Chapter 3, 3.2.1

1.7 Knot Quality and Stability

Since general descriptions and formulations for the mechanical performance of tight physical knots are challenging, the studies described next have involved the development of testing and counting schemes to evaluate the quality and stability of knots. Knots can fail by fracture of the filament but also through unraveling, sliding, or capsizing (without fracture), as we will demonstrate in the Chapters 5 and 6.

Hanna et al. [73] defined the *Knot Quality Score* (KQS) in the context of measuring the mechanical performance of the surgeon's knot as:

$$KQS = \frac{\text{(Knot breaking or slipping force)} \times \text{(Integrated force for the knot)}}{\text{(Thread breaking force)} \times \text{(Integrated force for the thread)}} \tag{1.9}$$

Using a universal testing machine, the breaking force of a simple thread and that of a thread containing a knot were related to their displacement. Consequently, a value of $KQS \approx 1$ corresponds to a strong knot since the strength of the knotted thread is close to the strength thread alone (without a knot). In contrast, the knot is weak if $KQS \ll 1$. The KQS system has been used in other studies (Lee et al. [74], Goldenberg and Chatterjee [75]), although it is based on integrated magnitudes of forces and does not consider internal stress concentration. In addition, this characterization approach is purely empirical and unique to a particular thread diameter and material. So, the KQS system is a way of characterizing the mechanical performance of knots; however, the previously mentioned deficiencies are very restrictive to formulating generalizations.

Daily-Diamond et al. [27] investigated the accidental untying of shoelace knots through dynamic events; a common event in our daily life. Through controlled testing on cyclic impacts, the authors observed that knot loosening results from the repeated shoe impact, with a subsequent slipping of the laces due to the whipping motion of the swinging leg. A systematic change of parameters allowed to rationalize the effect of various ingredients in the untying process. Specifically, side impacts were found to accelerate knot failure compared to rear-impacted knots. It was also found that an inertial imbalance between the loops and the free ends during the leg-swinging phase favors the slippage of the rod ends, leading to a rapid failure. Finally, the authors observed that the granny knot fails quicker and more often than the square knot. However, the underlying mechanism that leads to the difference in stability, was not addressed. Moreover, the effect of the shoelace material and their frictional behavior on the untying mechanism was not addressed.

In one of few prior theoretical analyses of physical knots, Maddocks and Keller [76], beyond pure geometry, introduced more physical ingredients into their knot model. These authors analyzed the mechanical equilibrium of ropes in contact, taking into account tension and friction using the classical capstan equation (Eq. (1.1)), described in Section 1.2.1. The tension was assumed to jump from zero at the loose end to some non-zero value at a point where the rope is squeezed by another part of the knot, called the nip region. Each crossing in a knot results in a jump in tension. The authors showed a critical value of friction above which such a knot will hold. Moreover, a theory for ropes lying on surfaces was developed and extended to interwound ropes. In all cases, the shape was assumed to be given. This model, however, was developed under the assumption that each point on one rope is in contact with just one point on the other rope. It was only later that the double-contact feature between two contacting curves was observed, as discussed in Section 1.4.

Maddocks and Keller [76] predicted that the clove hitch knot should slip when subjected to a tension at one rod extremity, independent of the cylinder or rod diameters. Sano et al. [37], together with the author of this thesis, challenged this theoretical prediction by experimentally and numerically studying the kinematics and the mechanical stability of the common clove hitch knot. FEM simulations of this knot were validated using Darboux vector components (introduced in Section 2.4.1) obtained from X-ray micro-computed tomography. The numerical results gave access to the internal tension profile along the arc length of the rod centerline. In the knotted rod segments that are in frictional contact with a cylinder, an exponential decay of the internal tension was observed, according to [34] (see Section 1.2.1). The other frictional contact interaction in the clove hitch knot is the pinching of the self-contacting rod, which leads to discontinuous drops in the internal tension profile (see Figure 1.10**a1**). Still in the work by Sano et al. [37], an experimental stability analysis was carried out by applying a traction force, T_{high}, on one rod end while the other one was free, $T_{\text{low}} = 0$, for varying rod-to-cylinder diameter ratios. The resulting phase diagram, shown in Figure 1.10**a2** has a phase boundary between a region of stable behavior (no slippage) and failure (knot becomes undone) that depends on the diameters of the rod and the cylinder. Thus, the theoretical prediction suggested by Maddocks and Keller [76] could not be confirmed.

In the study by Patil et al. [2], topological counting rules were applied to 2-tangles to predict their relative mechanical stability. In Figure 1.10**b1**, the topological diagram of the granny and the square knot (reef knot) are shown with the fibers oriented by a pulling direction. The twist direction of the fiber depends on the handedness of the crossing, as shown in Figure 1.10**b2**. Thus, the authors assigned a discrete *twist charge* at each fiber crossing. The self-torque data, together with other topological parameters, allowed to rationalize the stability of numerous 2-tangles. Remarkably, the numerical simulations and experiments agree with the stability analysis regarding the untying force. Still, the latter could not be generalized further since the model is limited to 2-tangles and does not include a constitutive model nor contact geometry or frictional interactions.

Lastly, Moestopo et al. [77] developed architected materials using interwoven fibers. By using arrays of unit cells, woven lattices were achieved, which could be subjected to large tensile and compressive strains (> 50%). The high mechanical performance was made possible by a new design of the beam junctions. Instead of using classic monolithic junctions between fibers, the

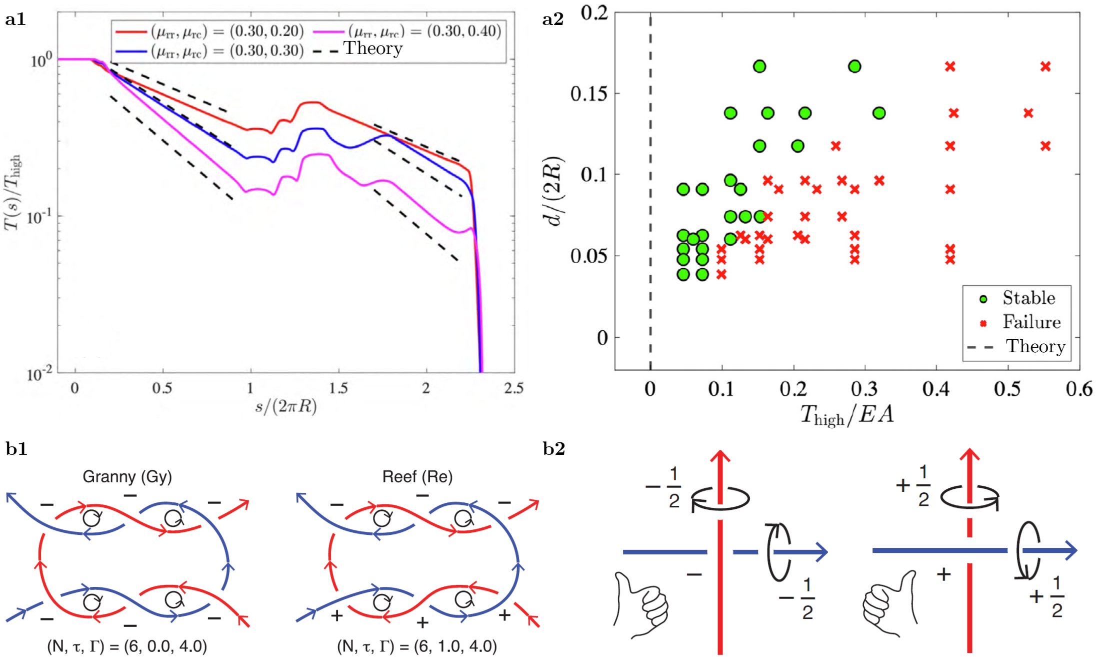

Figure 1.10: **Stability analysis on a hitch knot and 2-tangles.** **a1**, Internal tension as a function of the rod arc length in a clove hitch knot. The theoretical prediction of the tension decay is based on Ref. [34]. The image is adapted from Ref. [37]. **a2**, Stability diagram for clove hitch knots tied on cylinders of varying diameters, d, and as a function of applied traction forces, T_{high}, on one rod end. The theoretical prediction is given by Ref. [76]. The image is adapted from Ref. [37]. **b1**, Topological diagram of the granny and the reef knots, with applied topological counting rules. The image is adapted from Ref. [2]. **b2**, Schematics of the rule to determine the handedness of each crossing. The image is adapted from Ref. [2].

authors reported interwoven fibers at the effective junction location. The new design allows for the reduction of stress concentration in the junctions of woven microfibers.

1.8 Summary and Research Niche

In all the examples of knots used throughout history (excluding decorative knots) and applications, the characteristic length-scales in *physical* knots are of the same order. According to the definition of tightness given in Section 1.5, these knots, therefore, qualify as *tight*. The importance of tightness and the three-dimensional nature of tight contacts will be highlighted throughout this thesis. In the following paragraphs, we will summarize the previously presented theories, models, and tools to describe knotted filaments and evaluate their applicability on tight, physical knots.

The field of **knot theory** is largely concerned with the tabulation of (closed) knots and their unique topological properties. In this context, the rod is idealized as a curve or a perfectly flexible string without self-contacts. Despite its topological importance, knot theory does not describe tight, physical knot properties. The knot theory sub-branch of **geometric rods**, however, deals with the tightest knot configurations, tied in rods with finite thickness. Perfectly flexible and slippery rods are assumed, thus, they cannot resist to bending or torsion, nor do they take into account cross-sectional or shear deformation. In Chapter 4, we challenge these geometric frameworks by comparing characteristic features between ideal knots to knotted elastic rods.

Next, analytic models based on the **Kirchhoff theory of rods** incorporate important physical ingredients to describe the mechanics of real-life knots (in contrast to ideal knots). However, these models assume a separation of the characteristic length scales and are therefore limited to *loose* knot configurations. We conclude that these descriptions are still too academic for practical relevance, as functioning knots are typically tight.

Further, the **discrete elastic rod theory** allows for the description of elastic (so physical) and also tight knots. However, it does not take into account the cross-sectional deformation of the rod, nor does it provide a detailed contact model, including friction. Still, the discrete descriptions presented in Ref. [39] provide a useful framework to describe the centerline of framed curves (*e.g.* discrete curvature), applicable as well to tight knots.

Moreover, full 3D **Finite Element Modeling** of knotted rods seems very promising to simulate the full mechanics of physical and tight knots. While full 3D simulations were computationally very expensive until recently, optimized numerical solvers and high-performance computing nowadays reduce the simulation time significantly. Inspired by the tying procedure by Durville [70], we will use a similar tying procedure but different contact mechanics in Chapter 3.

Finally, the literature addressing the **quality and stability of knots** does not provide analytic models predicting knot performance. Instead, they characterize knot behaviors, which are then rationalized. Since these tools could be applied to both physical and tight knots, these studies are of great interest to this thesis.

Research niche: To date, successful models that can accurately predict the mechanical response of knots based on the theory of elasticity are restricted to the simple overhand knot and only in loose configurations. The most critical factor precluding progress in this field is the difficulty in capturing the nonlinear geometry of physical knots tied on filaments with frictional interactions at self-contacts. Moreover, there is a striking lack of precision experiments to enable systematic exploration of knotted structures, provide physical insight into the nontrivial behavior of these systems and yield high-quality data that can be used to motivate and validate different theoretical and computational models.

Given that the geometry of tightly knotted structures cannot be accessed through 2D imaging, 3D volumetric imaging will be performed. We combine state-of-the-art X-ray micro-computed tomographic imaging, mechanical testing, and Finite Element simulations to understand the intricate three-dimensional geometries, large deformations, and frictional interactions of tight, physical knots.

In the context of characterizing the global and local geometry and mechanics, we will investigate three physical knot problems: the shapes of physical (closed and open) trefoil knots (Chapter 4); capsizing due to friction-induced twist in the failure of stopper knots (Chapter 5); and the interplay between plasticity and friction dictating the strength of surgical knots. We will tackle the following research questions:

- Could the ideal geometric model act as a scaffold to (fully or partially) describe the shape of physical knots, including elasticity? (Chapter 4)
- Which key features in simple knots are not captured by the purely geometric rods? And vice versa, which purely geometric characteristics are potentially smoothed by the presence of elasticity? (Chapter 4)
- What causes knots to break at their entrance and exit points? Is this structural weakening purely geometric, as reported by Pierański et al. [65]? (Chapter 4)
- How do common stopper knots resist applied loads? Besides filament fracture, do common stopper knots demonstrate another failure mechanism? (Chapter 5)
- What is the effect of frictional interactions (self-contacting rod and rod versus stopper plate) on the capsizing mechanism in stopper knots? (Chapter 5)
- Which mechanism is at the source of capsizing, and how can the rearrangement of rod segments be impeded (tightness, friction, rod stiffness)? (Chapter 5)
- How does the topology of half-hitches influence the resistance to sliding (called *knot strength*) in surgical sliding knots? (Chapter 6)
- How do friction, plasticity, and the number of throws affect the mechanical knot strength? Can we rationalize the underlying mechanism to guarantee secure surgical knots? (Chapter 6)
- Can we establish physics-based operational and safety guidelines on the mechanical strength of surgical sliding knots? (Chapter 6)

1.9 Outline of the Thesis

This thesis is divided into two parts. The first part is dedicated to experimental and numerical methodology (Chapters 2 and 3, respectively). Then, in the second part, we focus on three knot problems: physical trefoil knots (Chapter 4), stopper knots (Chapter 5), and surgical knots (Chapter 6).

In **Chapter 2**, we will develop and validate the experimental toolbox involving the fabrication of composite rods for X-ray tomographic imaging and the required image processing techniques, including the framework we devised to quantify geometric rod deformation. In **Chapter 3**, the computational toolbox is described. It involves Finite Element Modeling of extensible and inextensible elastic rods and tubes, the tying procedure of various knot topologies, and the validation with experiments.

In Section 1.4, we described the geometric rod model based on idealized ropes. In **Chapter 4**, We use this well-defined tightest geometric configuration to investigate its applicability to physical knots in the absence of friction. In a compare-and-contrast study on the basic trefoil knot in an open and closed configuration, we analyze the similarities and differences between the physical knots and their geometric counterpart.

In **Chapter 5**, we then turn to more functional knots, including frictional interactions, by studying the performance of stopper knots. In a model system, we study the resistance of figure-eight knots against the capsizing mechanism, as well as the differences between our homogeneous elastomeric rod system and structured systems like ropes. We realize that purely elastic systems are physical but rarely applied in practice for a reason.

Lastly, in **Chapter 6**, we investigate the performance of surgical knots tied, as in real-life, into elasto-plastic monofilaments by combining data gathered from surgeon-tied knots with precision experiments and numerical simulations based on a plasticity model. The results enable us to understand the underlying mechanism based on frictional interactions and plastic filament deformation and to formulate a practice guide on the operation for tying safe surgical knots.

Finally, in **Chapter 7**, we summarize the main findings in this thesis and comment on possible avenues for future research opened by this thesis.

2 Methodology: Experimental Toolbox

In general, realistic physical knots are tight, with no separation of length scales; the overall size of the knot, the diameter of the rod, and its characteristic radii of curvature are all of the same order. Analytical models based on Kirchhoff's theory exist for elastic rods [61, 63, 64]. However, these descriptions are however limited to simple knots in loose configurations, and consequently, too abstract for practical settings. The goal of this Thesis is to study *functional* and *tight* tangles and knot systems that typically involve the following characteristics: highly nonlinear elastic and/or plastic rod deformations (stretching, bending and twist, cross-sectional deformation), intricate contact geometry, and nontrivial frictional interactions. These systems, studied in the follow-up chapters, are two filaments in tight orthogonal contact (clasp configuration) [78], the open and closed trefoil knots (Chapter 4), the clove hitch knot [37], stopper knots (Chapter 5), and surgical knots (Chapter 6). To get insight and a deeper understanding of the geometry and mechanics of these tangles and knots, we decided to use a combination of experiments (3D imaging and mechanical testing) and finite element modeling. A lack of these tools allowed us to set up our research niche by developing and applying them on knotted systems.

This chapter describes the experimental toolbox that we developed to study simple and complex physical knots tied in silicone-based elastomeric rods. The reader may want to skip this chapter in a first read and come back to it as needed in the later chapters. In Section 2.1, we give an overview of the experimental tools that needed to be developed and what they will be used for. First, in Section 2.2, we detail the fabrication protocol we developed to produce composite (coaxial) elastomeric rods. These rods were made compatible with X-ray micro-computed tomographic (μCT) imaging for the geometrical characterization of tangles and knots. Secondly, in Section 2.3, we describe the procedure to capture the μCT images of the clasp configuration and of knotted structures with the subsequent image-processing algorithm developed in-house. Then, in Section 2.4, we present the most useful post-processing strategies that are applied in the follow-up chapters. Finally, in Section 2.5, we determine material properties and evaluate the frictional contact behavior between powder-treated VPS surfaces.

2.1 Motivation

To generalize our results across length scales using scaling laws, we decided to conduct model experiments, at the desktop scale, using homogeneous elastomeric rods. On the one hand, the length of cylindrical rods scales with its diameter only, due to the slender nature of the rods. On the other hand, the Neo-Hookean material model of incompressible elastomers only depends on the Young's modulus, scaling the traction force on the rod with the modulus of elasticity and the cross-sectional area. In tangled and knotted systems, we seek to access the following two sets of information: geometry (centerline coordinates, curvature, contact shape, etc.) and forces (reaction forces at rod ends, contact pressure profiles). Next, we briefly describe which toolboxes need to be developed to extract the desired information in experiments.

In Section 1.5, we introduced an existing model developed by Audoly et al. [61], predicting the mechanical response of loose elastic overhand knots based on the theory of Kirchhoff rods. The author used digital photography to capture most of the geometry in loose overhand knots. The 2D imaging was sufficient and allowed the authors to include frictional interactions in the analytical predictive model. However, this imaging technique could not capture the third dimension of the depth in tight overhand or more complex knots. Inspired by this study, the goal was to use non-destructive 3D imaging (μCT) to extract information on out-of-plane deformation and contact regions. Firstly, we had to determine the method to fabricate the bulk core rod (Section 2.2.1). Secondly, due to the working principles of μCT scanners (Section 2.3.1), we needed to turn the elastomeric rods into composite rods including various features: a thin and uniform coating (Section 2.2.3) and physical insets incorporated inside the bulk core rod (Section 2.2.2). After imaging the tangled and knotted systems, the reconstructed volumetric data needed to be treated. To this end, we developed a powerful image post-processing toolbox (described in Section 2.3.2) that is fully-automatized to extract accurate centerline coordinates, 3D contact regions, and the subsequent curvature profiles and contact maps (Section 2.4).

Finally, experimental tests were necessary to determine the parameters of the material model (Section 2.5.1) and to find the static and kinematic friction coefficients (Section 2.5.2).

2.2 Fabrication of Composite Rods for μCT Imaging

This section describes the protocol we developed to fabricate the composite elastomeric rods in a way that made them compatible with μCT volumetric imaging of tangles and knots (described in Section 2.3). The main goals of this fabrication technique were twofold. First, we seek to extract the physical centerline coordinates of the rods. Second, we want to quantify the contact geometry at self-contact or between two touching rods.

To achieve the above goals, our composite rods comprised three different regions: (i) a bulk core rod embedded within (ii) a physical centerline fiber, and (iii) an outer coating layer. The physical centerline fiber and the outer coating layer were required to be made of a material with a sufficiently lower density than the density of the bulk core rod to differentiate two touching volumes using tomographic imaging (further details can be found in Section 2.3.1).

In the schematics of Figure 2.1), we depict the various steps of the composite rod fabrication protocol. First, the bulk core rod was cast inside a stainless steel cylindrical tube by injecting the liquid polymer through the lower inlet of the mold. A weight of mass $M = 200\,\mathrm{g}$, together with machined aligners, ensured coaxiality of the nylon filament (see Figure 2.1**a**). The demolding step of the bulk core rod from the mold is shown in Figure 2.1**b**, involving the extraction of the nylon fiber yielding a monolithic polymeric rod with a void along its centerline. A different liquid polymer is then injected inside the void generating the material centerline (Figure 2.1**c**). Lastly, and depicted in Figure 2.1**d**, the application of a dip-coating technique [79] allowed for an outer polymeric coating layer to be deposited uniformly on the bulk core rod; the latter is pulled out vertically from a circular bath containing uncured liquid polymer, at a constant velocity U.

In the following subsections, we describe the steps necessary to fabricate parts (i), (ii) and (iii), in more detail. Parts of the text and figures in this section are adapted from the supplementary information in Ref. [78], which resulted from a collaboration with Paul Grandgeorge, Changyeob Baek, Harmeet Singh, Tomohiko G. Sano, Alastair Flynn, John H. Maddocks and Pedro M. Reis.

2.2.1 Bulk Core Rod Produced by Injection Molding

The bulk core rod was cast with Vinylpolysiloxane (VPS-16, Zhermack) using a stainless-steel cylindrical mold (stainless-steel pipes, part number PSTS12A-400, Misumi). This casting tube had length $L_\mathrm{m} = 400\,\mathrm{mm}$ and inner diameter $D_\mathrm{m} = 8.3\,\mathrm{mm}$, which set the outer diameter of the bulk core rod upon demolding (Figure 2.1**a**). The drawing in Figure 2.2**a-b** shows the dimensions of the cylindrical mold. To guarantee a high precision of the location of

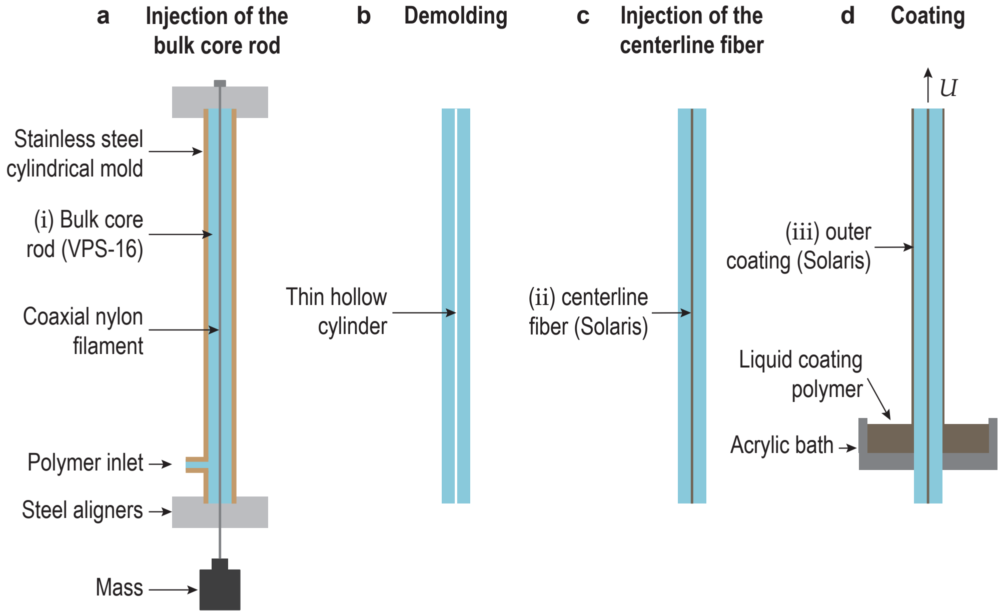
a
Injection of the bulk core rod
b
Demolding
c
Injection of the centerline fiber
d
Coating
Stainless steel cylindrical mold
(i) Bulk core rod (VPS-16)
Coaxial nylon filament
Polymer inlet
Steel aligners
Mass
Thin hollow cylinder
(ii) centerline fiber (Solaris)
U
(iii) outer coating (Solaris)
Liquid coating polymer
Acrylic bath

Figure 2.1: **Schematics of the fabrication protocol of the coaxial composite VPS rods used for μCT imaging. a**, The bulk core rod was cast inside a stainless steel cylindrical tube by injecting the liquid polymer (VPS-16) through the lower inlet of the mold. A weight of mass $M = 200\,\mathrm{g}$, together with machined aligners, ensured coaxiality of the nylon filament. **b**, Demolding of the bulk core rod from the mold and extraction of the nylon fiber yielded a monolithic polymeric rod with a void along its centerline. **c**, Injection of liquid polymer (Solaris) inside the void generated the material centerline. **d**, A dip-coating technique [79] was used to uniformly deposit an outer polymeric coating layer on the bulk core rod; the bulk core rod is pulled out vertically from a circular bath containing uncured Solaris at a constant velocity U.

the physical fiber and the eccentric inset (described in Section 2.2.2, and as analyzed in Section 2.2.4), it is essential that the mold is perfectly straight and not intrinsically bent, which would have been the case had we used simple acrylic tubes.

The stainless steel cylinder was mounted vertically to allow the remaining air bubbles to escape to the free surface thanks to gravity. The commercially available cylinder was customized by adding a tapped hole in its wall, acting as the inlet for the liquid polymeric mixture. Further, on both sides of the tube, a notch dedicated to an O-ring was lathed. The rubber O-rings allow a tight fit between the cylinder and aligners that close the open ends of the mold. These aligners, shown in Figure 2.2**c-d**, were machined to high precision (±0.05 mm) as they include boreholes that guide slender fibers through the cylinder (see Section 2.2.2).

The photo in Figure 2.3 shows the fabrication setup of the core rod, including the vertically aligned stainless steel cylinders, the aligners, and an in-house fabricated compressed air

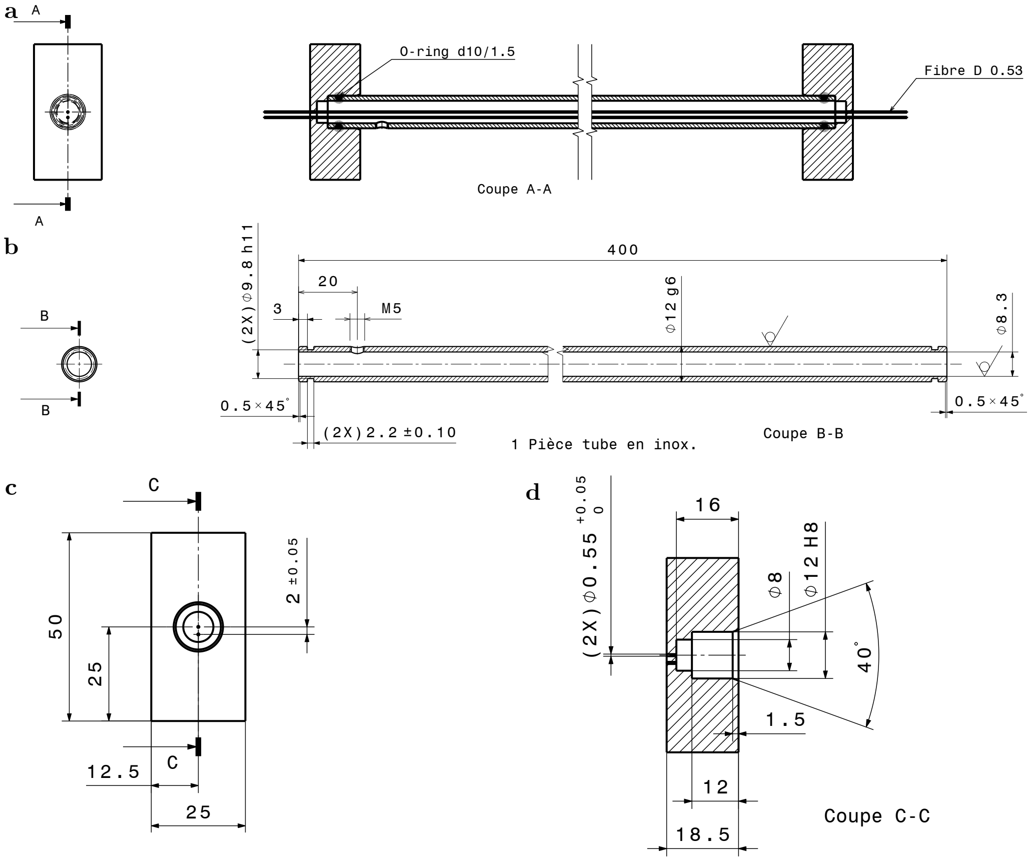
a
A
O-ring d10/1.5
Fibre D 0.53
Coupe A-A
A
b
B
B
(2X)Φ9.8 h11
400
20
3
M5
Φ12 g6
Φ8.3
0.5×45°
0.5×45°
(2X)2.2 ±0.10
1 Pièce tube en inox.
Coupe B-B
c
C
50
25
2 ±0.05
C
12.5
25
d
(2X)Φ0.55 +0.05 0
16
Φ8
Φ12 H8
40°
1.5
12
18.5
Coupe C-C

Figure 2.2: **Drawing of the cylindrical mold and the aligners.** **a**, Overall view on stainless steel cylinder, two aligner pieces, and the slender fibers. **b**, Geometric measures of the cylindrical mold, including a tap machined hole on one side and a notch for an adapted O-ring lathed on both ends. **c**, Top view on the so-called aligners that close the open ends of the cylinder while allowing slender nylon fibers to pass by. **d**, Side view on the aligner with geometric measures, showing the 4 mm gap between the end of the cylinder and the aligners wall that facilitates the demolding procedure.

pump (on the right side in Figure 2.3). By injecting compressed air in the cup filled with liquid silicone-based polymer, a positive pressure is created in the pump. Consequently, the polymer is pushed up the tube towards the inlet of the mold. This design avoided the generation of air bubbles in the elastomer because the liquid polymer did not need to be transferred to another container (*e.g.* a syringe) after mixing.

The polymer for the bulk core rod, VPS-16, is prepared using base and catalyst components. The density of cured VPS-16 was measured to be $\rho_{\text{VPS16}} = 1160\ \text{kg/m}^3$ using a pycnometer (25 mL Gay-Lussac Pycnometer, Milian) and its Young's modulus was $E = 520\,\text{kPa}$ (see Section 2.5.1 for details on the mechanical characterization). During the injection molding process, particular care was taken to avoid air bubbles by defoaming the mixed solution using

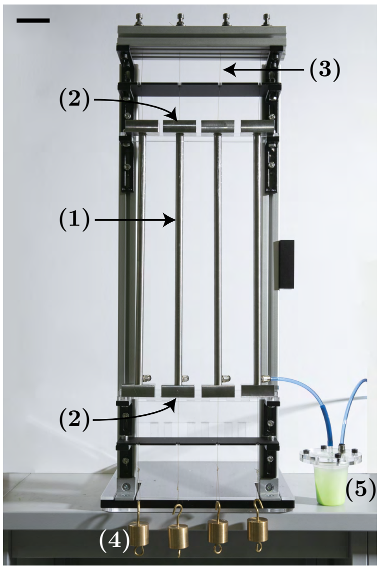

Figure 2.3: **The rod fabrication setup** consists of vertically aligned stainless steel cylinders (1), machined stainless steel aligners (2) for fiber (3) guidance, weights (4), and an in-house fabricated compressed air pump (5). The length of the scale bar is 5 cm.

a centrifugal mixer including degassing functionality (ARE-250, Thinky), and subsequently applying vacuum for 30 seconds to the mixed solution using a vacuum chamber. Including the same cup in the compressed air pump minimizes the injection of air into the polymer. The flow of compressed air starts the injection molding process, which should happen between the following speed limits: the introduction of the liquid polymer mixture should happen at a low rate to give the potential air bubbles time to move up to the surface and to escape the vertically placed mold, while not exceeding the working time of the polymer (working time: 5 minutes; setting time: 10 minutes). For a tube length of $L_\mathrm{m} = 400\,\mathrm{mm}$, we chose a (vertical) speed of 1 mm/s, resulting in a total casting time of 40 seconds.

2.2.2 Physical Fiber and Eccentric Inset

A physical fiber needed to be embedded into the bulk of the rod, acting as a thin material centerline, to enable the extraction of the material centerline coordinates from volumetric CT-imaging (see Section 2.3). Access to the twist along the arc length of the rod will be useful to construct closed knots avoiding excess-twist (see Chapter 4) or to compute curvatures using the Darboux vectors from the Cosserat frame [37]. To this end, we use an eccentric inset fiber, which is offset of the centerline by half of the rod's radius: 2 mm (see the geometry of the aligners in Figure 2.2**c**). Since the fabrication of the eccentric inset fiber is equivalent to the one of the physical fiber, we focus only on the fabrication method of the centerline fiber in the following paragraphs.

First, custom-machined steel aligners, shown in Figure 2.2**c-d**, were placed at both ends of the casting tube to align a straight nylon filament (diameter $D_\mathrm{n} = 0.5\,\mathrm{mm}$) concentrically. During casting, we kept the nylon filament under tension by hanging a weight of mass $M = 200\,\mathrm{g}$ at its lower extremity (see Figure 2.1**a**). Liquid-phase VPS-16 was injected into the assembly to cast the bulk core rod (as described in Section 2.2.1). After curing of the core rod, the nylon thread was pulled out, leaving a thin hollow cylindrical void (of diameter $D_\mathrm{n} = 0.5\,\mathrm{mm}$) along its central axis of the rod (Figure 2.1**b**). The core rod could simply be pulled out of the cylindrical mold as it is standing out of the latter one thanks to the design of a 4 mm gap between the end of the cylinder and the aligners wall (see Figure 2.2**d**). The axial stretch of the rod while pulling, together with the Poisson effect leads to shrinkage in the radial direction and consequently to delamination between the core rod and the tube.

Next, we filled up the void inside the core rod by injecting still-liquid platinum cure silicone rubber (Solaris, Smooth-On), (Figure 2.1**c**). The Solaris polymer cured in approximately 24 hours after injection, with a final Young's modulus of $E_\mathrm{solaris} = 320\,\mathrm{kPa}$ and density $\rho_\mathrm{solaris} = 1001\,\mathrm{kg/m^3}$ (see Section 2.5.1 for mechanical characterization). It is important to highlight that the density difference of 13 % between the cured Solaris and VPS-16 polymers was sufficiently large to enable the differentiation and segmentation of the material centerline fiber from the bulk core rod during μCT imaging (see Section 2.3). This alignment procedure ensured a satisfactory concentricity of the material centerline and the rod (see case study on material centerline accuracy in Section 2.2.4).

2.2.3 Outer Coating Using Dip-Coating Technique

We aim to easily fabricate straight elastomeric rods with a thin, uniform, and constant coating to enable the quantification of the contact regions during the μCT imaging (see Section 2.3.1). Since larger samples need to be placed in larger μCT sample holders, leading to a reduction of the effective scanning resolution (see Section 2.3.1), we seek to use a method and develop a model that allows tuning parameters to easily adapt the coating thickness. A homogeneous thin film of uniform thickness along the rods was achieved with the dip-coating technique [80], also called free coating or unobstructed coating, which is based on Landau and Levich [79].

The photograph of our experimental coating setup is shown in Figure 2.4**a**. The VPS-16 core rod, including the centerline fiber, was pulled vertically out of a bath of liquid Solaris, at a constant velocity U, yielding a coating of thickness $e = 150\,\mu\mathrm{m}$ (see Figure 2.1**d**) and Figure 2.4**b**). To avoid using a large liquid bath, the bulk core rod was passed through a concentric hole at the bottom of a shallow cylindrical acrylic bath of liquid Solaris (depth of the bath ≈ 5 mm). The hole at the bottom of the bath had the same diameter as the bulk core rod (8.3 mm), thus avoiding leakage. The bath container was cylindrical (inner diameter 40 mm) to ensure an axisymmetric flow and, hence, a homogeneous deposition during coating.

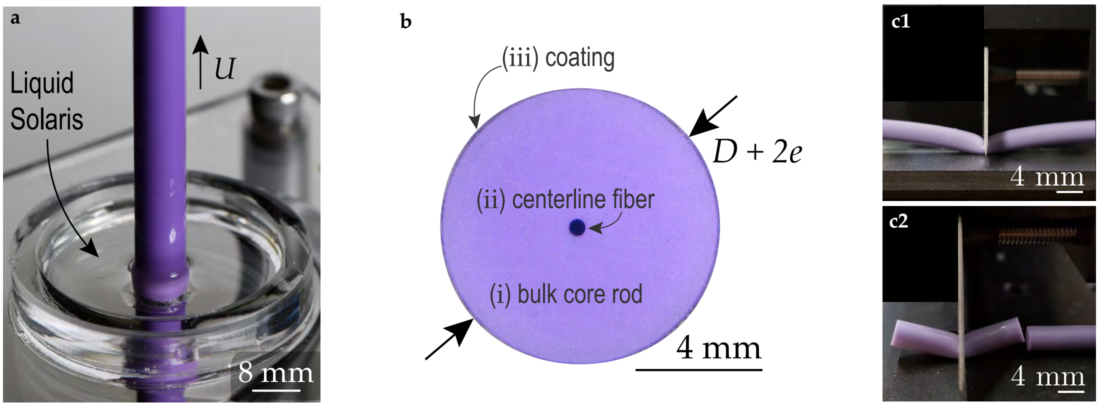

Figure 2.4: **Coating thickness profile analysis. a**, Experimental apparatus for dip-coating the VPS-16 rods with the liquid coating polymer Solaris. **b**, Micrograph of a cross-sectional cut of the coated rod embedded with the physical centerline fiber (image obtained using a VHX 5000 digital microscope, Keyence). **c1-c2**, Cutting procedure bisecting each rod piece in several iterations using a sharp cutting blade.

In an effort to achieve reproducible and predictable coating layers, we systematically investigated the dependence of the withdrawal speed, U, on the coating thickness, e. To this end, we coated multiple identical bulk core rods of diameter $D = 4$ mm at different withdrawal velocities, $U = \{20, 50, 100, 200, 400, 1000\}$ μm/s. After curing, the resulting coating thickness was measured by analyzing digital microscope images (Keyence VHX 5000) of cross-sectional cuts (see Figure 2.4**b**). Achieving planar cuts turned out to be more challenging than anticipated. Opting for a bisecting procedure by keeping symmetry on the left and the right side of the cutting blade yielded satisfactory planar cuts: the first cutting step is shown in Figure 2.4**c1**, and the subsequent cut is depicted in Figure 2.4**c2**. The rod was cut in 10 mm pieces to analyze the average coating thickness, e, and the standard deviation of every cross section along the axial direction, z, of the rod.

Existing models describing the dip-coating technique [81, 82, 83, 79, 84, 85] predict that after an initial square root distribution of the coating thickness, e, the latter one reaches a plateau where the coating thickness is constant. The schematics in Figure 2.5**a** and **b** show the different coating zones (wetting zone, constant film thickness zone, dynamic and static meniscus) in the case of plate and fiber coating, respectively. In Figure 2.5**c**, we present experimental results for the thickness profile, e, (as a function of its axial length z) of the outer film of Solaris on a VPS16 rod ($R = 2$ mm radius) pulled from the polymer bath at a speed $U = 100$ μm/s. After an initial nonlinear evolution, the coating thickness, e, reaches a nearly constant value (slight thickness increase for rod length larger than 300 mm due to a viscosity increase, see below).

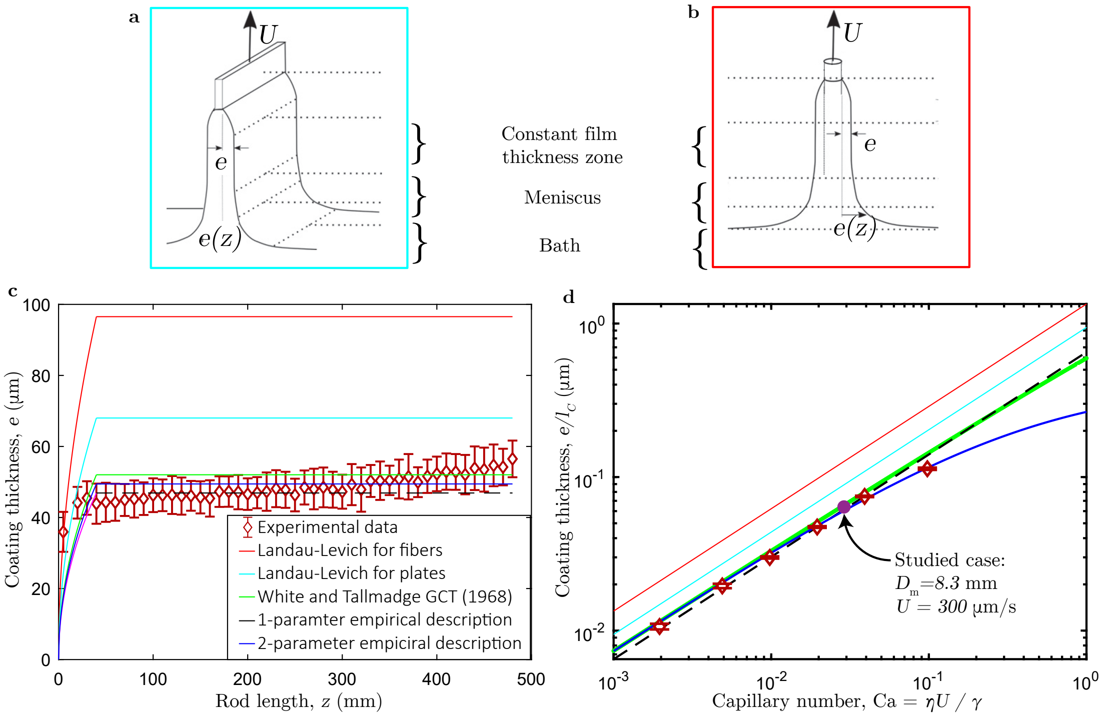

Figure 2.5: **Empirical fits based on coating thickness descriptions. a-b**, Schematics adapted from Rio and Boulogne [85] depicting characteristic zones during the dip-coating process of plates (**a**) and fibers (**b**). **c**, Coating thickness of a rod of diameter $D = 4\,\text{mm}$ and a withdrawal speed of $U = 100\,\mu\text{m/s}$. **d**, Coating thickness measurements for multiple cross sections and on four rods, coated using different withdrawal speeds, U. The experimental data is overlapped with models describing the relation between the dimensionless coating thickness, e/l_c as a function of the Capillary number, Ca (see text for the definitions of l_c and Ca). The purple datapoint refers to the selected coating conditions (velocity $U = 300\,\mu\text{m/s}$) to achieve a coating thickness of $e = 150\,\mu\text{m}$. The legend in **d** is the same as for **c**.

The average values of the coating thickness in the constant film thickness zone, as well as the corresponding standard deviations, were computed from the angular component of each cross section. First, the coating thickness was averaged over the cross sections, and second, another averaging step was executed for four rod samples. In Figure 2.5**d**, we present the experimental results (datapoints) for the coating thickness normalized by the capillary length, l_c, as a function of the non-dimensional capillary number, Ca. Next, we introduce the parameters and their measured quantities, that were required to define the capillary length and number: the density of the coating polymer (as mentioned in Section 2.2.2) is $\rho_{\text{solaris}} = 1001\,\text{kg/m}^3$, the liquid-air surface tension of Solaris is $\gamma = 23\,\text{mN/m}$ [86] and $g = 9.81\,\text{m/s}^2$ is the gravitational acceleration. Rheological measurements were carried out (rheometer Discovery HR-2, TA-

Instruments) to determine the viscosity of Solaris, $\eta = 2.19\,\mathrm{Pa\cdot s}$, the time dependence of which was found to be negligible during the entire coating process (the viscosity increases by 5.6 % during the coating process of 25 min). This slow time evolution of η ensured a nearly constant thickness of the coating layer along the rod. From the experimental results in Figure 2.5**d**, we find that the coating thickness increases monotonically with the extraction velocity, U. Having measured the necessary quantities allowed to determine the capillary length, $l_c = \sqrt{\gamma/\rho g}$, and the non-dimensional capillary number, $\mathrm{Ca} = \eta U/\gamma$.

Next, we briefly review existing descriptions of the film thickness obtained from dip-coating technique and test them against our experimental results. After an initial transient, the coating thickness, e, reaches a plateau value, which scales with the capillary length, l_c, and the capillary number, Ca [82, 79, 84, 85]. According to the classic Landau-Levich theory [79], the predicted thickness of the film coating is,

$$\frac{e}{l_c} = \Delta\,\mathrm{Ca}^{2/3}, \tag{2.1}$$

with the prefactor $\Delta_{\mathrm{Plates}} = 0.944$ for plates, and $\Delta_{\mathrm{Fibers}} = 1.34$ for fibers [85]. The relationship in Eq. (2.1) has been found to accurately predict the constant coating thickness for the withdrawal of plates and fibers from a viscous bath with pure Newtonian liquids [85].

In Figure 2.5**c** and **d**, we observe a significant mismatch between this model (plates and fibers) and our experimental data. Since our rods have diameter $D_{\mathrm{m}} = 4-8\,\mathrm{mm}$, the theoretical prediction reaches its limitations, as pointed out by Rio and Boulogne [85]. Firstly, the Goucher number, $\mathrm{Go} = (D_{\mathrm{m}}/2)/l_c$, physically quantifies the relative importance between the two curvatures, vertical and azimuthal, set by the capillary length and the fiber radius, respectively. The plate limit (zero azimuthal curvature) gives $\mathrm{Go} \to \infty$, whereas $\mathrm{Go} \ll 1$ corresponds to the fiber limit. In the conditions of our experiments, $\mathrm{Go} \approx 2.7$, so the coating experiment is close to the crossover between the plate and the fiber regimes [85]. Secondly, the Landau-Levich theory neglects gravity and, therefore, is only valid for $\mathrm{Ca} < 10^{-3}$ (the visco-capillary regime or Landau-Levich regime). In our case, gravity cannot be neglected since our velocity range, $U \in [100; 1000]\,\mu\mathrm{m/s}$, corresponds to capillary numbers $\mathrm{Ca} \in [0.01; 0.95]$. Also, more sophisticated models like the gravity-corrected theory (GCT) by White and Tallmadge [82], that is applicable for higher capillary numbers in the Derjaguin regime (hydrodynamics limit in presence of gravity, as opposed to the visco-capillary regime), still predict a coating thickness that is larger than the experimentally measured one, especially in the first coating segment ($z < 300\,\mathrm{mm}$, see the green curve in Figure 2.5**c**).

Nevertheless, we observed that the scaling law from Eq. (2.1) based on the Landau-Levich model was still appropriate to describe the experimental coating thickness profiles, albeit with a prefactor, $\Delta_{\mathrm{Rod}} = 0.651 \pm 0.004$, that we had to determine through the fitting of the experimental results. In Figure 2.5**c** and **d**, we juxtapose Eq. (2.1) with Δ_{Rod} (black dashed line) onto the experimental data, finding excellent agreement.

Further, we also applied a semi-empirical scaling based on Aussillous *et al.* [84] which includes a saturating mechanism that is important for large capillary numbers and results in a convergence of the coating thickness.

$$\frac{e}{l_c} = \frac{\alpha \mathrm{Ca}^{2/3}}{1 + \alpha\beta \mathrm{Ca}^{2/3}} \tag{2.2}$$

Eq. (2.2) involves a 2-parametric fitting (with $\alpha = 0.749 \pm 0.009$ and $\beta = 2.428 \pm 0.009$), and is represented by the blue curve in Figure 2.5**c** and **d**.

We conclude that we are most interested in the range of coating thicknesses of $40 - 200\mu$m, corresponding to capillary numbers $\mathrm{Ca} \approx 10^{-2}$. Thus, it is appropriate to use the simpler, adapted Landau-Levich model rather than considering the saturating mechanism in Eq. (2.2) for larger capillary numbers. The coating thickness of $e = 150\,\mu$m is selected for bulk core rods of diameter $D_{\mathrm{m}} = 8.3\,$mm such that the coating layer was sufficiently thick to be captured in the μCT images (see Section 2.3), while sufficiently small not to affect the overall mechanical behavior of the VPS rods. The small cross-sectional areas of both the Solaris centerline fiber and the outer coating, with respect to the VPS-16 bulk core, allowed us to assume a homogeneous mechanical behavior of the composite rod (see Section 2.2.5). This semi-empirical scaling allowed us to achieve the desired coating thickness of $e = 150\,\mu$m by imposing a withdrawal velocity $U = 300\,\mu$m/s (purple point in Figure 2.5**d**).

2.2.4 Quality Control of the Rod Fabrication

Determining the accuracy of the centerline location will be crucial to get reliable results; the centerline coordinates themselves, curvature, and contact maps (see Section 2.3.2 and Section 2.4) depend on the exact location. In addition, these quantities will be used to validate numerical simulations in ABAQUS CAE. In Chapter 3, we will describe the procedure of modeling knotted rods using the finite element method (FEM) in more detail. The FEM involves 3D solid elements defined on the initially straight rod and giving access to its full 3D deformation. In the same manner, the nodes constituting the *material* centerline are defined in the reference configuration of the straight, undeformed rod, and their location can be extracted easily in the deformed (*e.g.* tangled or knotted) configurations (see Chapter 3).

To do comparisons with confidence between results from FEM and experimental data, the concentricity of the physical fiber incorporated in the core rod is analyzed in the subsequent paragraphs. We chose to fabricate the rods with a central void, which allowed us to improve the contrast during microscopic imaging. More specifically, we used the configuration prior to injecting Solaris that forms the physical fiber, as described in Section 2.2.2. Four rods were cast using a setup including precision-manufactured stainless steel parts as introduced in Section 2.2 (rod diameter $D_\mathrm{m} = 8.3\,\mathrm{mm}$, central void diameter $D_\mathrm{n} = 0.5\,\mathrm{mm}$), and one rod was fabricated with the previous setup constituting of an acrylic cylindrical mold and 3D-printed aligners ($D_\mathrm{m} = 8.0\,\mathrm{mm}$, $D_\mathrm{n} = 0.5\,\mathrm{mm}$). Second, using a VHX 5000 digital microscope (Keyence) after cutting the rods into pieces following the bisecting procedure described in Section 2.2.3, we measured the distance, Δ, between the centroid of the circle fitting the rod edge and the one fitting the edge of the void. A characteristic rod cross section can be seen in Figure 2.6**a1** and a close-up view on the measurement of Δ is shown in Figure 2.6**a2**.

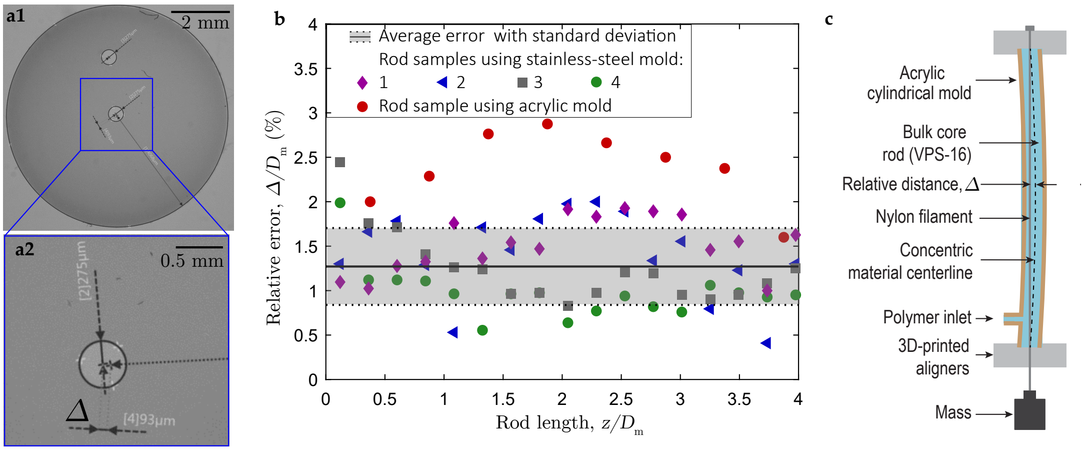

Figure 2.6: **Concentricity of the central void in the core rod. a1-a2**, High-resolution microscopic image of the cross section with three measurements: outer rod edge and inner void edge with corresponding centroids, as well as the relative distance, Δ, between the centroids. **b**, Relative distance, Δ, between the centroids as a function of normalize rod length, l/D_m. The shaded region depicts the average error with the standard deviation at all rod locations, z, of all rod samples combined that were cast in stainless steel cylindrical molds using machined stainless steel aligners. The red data points show the relative error, Δ/D_m, of a rod sample cast in an acrylic cylindrical mold using 3D-printed aligners. **c**, Schematics of the rod casting setup using an acrylic cylindrical mold. The intrinsically-curved tube leads to the offset, Δ, between the physical fiber and the concentric material centerline.

In Figure 2.6**b**, the concentricity of the central void in the core rod, Δ/D_m, is plotted as a function of the axial rod length, z. We observe that the use of precision-manufactured stainless steel parts allows for achieving a very low average relative error of $\Delta/D_\mathrm{m} \approx 1.3 \pm 0.4\%$ for the concentricity of the experimental material centerline of the rod. In contrast, the red data points are based on in-house fabricated casting parts and show that the use of 3D printed aligners and acrylic cylindrical molds do not yield the precision of the stainless steel parts.

Especially, the central region of the rod ($0.5 < z/D_{\mathrm{m}} < 3.5$) shows a pronounced offset distance, Δ, despite small deviations at both rod ends. We identified that the acrylic cylinders are slightly intrinsically curved. As a consequence, and as shown schematically in Figure 2.6**c**, the central rod region is facing low concentricity of the nylon fiber location relative to the centerline of the curved cylindrical mold. In contrast, the precision-manufactured stainless steel parts with quasi-straight cylindrical molds (as shown in Figure 2.1) allow preventing this effect.

The *material* centerline is used in all the studies presented in this thesis involving model systems based on purely elastic rods that are fabricated according to the protocols described in Section 2.2. In Chapter 6, however, we will make use of purchased surgical suturing monofilaments and have to sidestep to a *geometric* centerline. There is no unique definition of a geometric centerline of a deformed (bent, twisted, sheared, cross-sectional deformation) rod, *i.e.* both the following definitions are plausible: taking the centroids of planes that are oriented in a way that the cross-sectional area at each iteration is minimized or in a way that circularity of the sections is maximized. Therefore, in Chapter 3, Section 3.3, we will do a compare-and-contrast investigation between a geometric centerline definition and the material centerline.

2.2.5 Mechanical Properties of the Rod

Adding a physical fiber, an eccentric inset, and an outer coating layer of a different material to the rod could alter the material behavior of the core rod compared to a monolithic rod made of a single material. In this subsection, we compute the relative stiffness change, δ^{β}, (with $\beta = \{\text{axial, bending, torsional}\}$) and discuss if a homogeneous mechanical behavior of the composite rod can be assumed.

In Figure 2.7**a**, we depict the cross-sectional cut as if the rod only consisted of a monolithic core rod (without coating nor insets) with stiffness $K^{\beta}_{\mathrm{Mono}}$, and in Figure 2.7**b**, of the actual composite rod with stiffness $K^{\beta}_{\mathrm{Comp}}$, including insets and a thin coating layer. The quantitative geometric and material parameters as mentioned earlier in Section 2.2 are the core rod diameter, $D_{\mathrm{m}} = 8.3\,\mathrm{mm}$, the outer rod diameter $D_{\mathrm{out}} = 8.5\,\mathrm{mm}$, the inset (physical fiber and eccentric inset) diameters, $D_{\mathrm{n}} = 0.5\,\mathrm{mm}$, the offset between the physical fiber and the eccentric inset, $d = 2\,\mathrm{mm}$, the Young's modulus of the core rod material, $E_{\mathrm{VPS}} = 0.52\,\mathrm{MPa}$, and of the coating and inset material, $E_{\mathrm{Solaris}} = 0.32\,\mathrm{MPa}$. Similarly, I_{α} and J_{α} denote the second moment of area and the polar moment of inertia, respectively, with $\alpha = \{\text{Mono, coating}\}$. Further, we define the orthonormal coordinate system, $(\mathbf{e}_1, \mathbf{e}_2)$, that will be used below.

Next, we compute the resistance to (i) axial, (ii) bending and (iii) torsional deformation of both

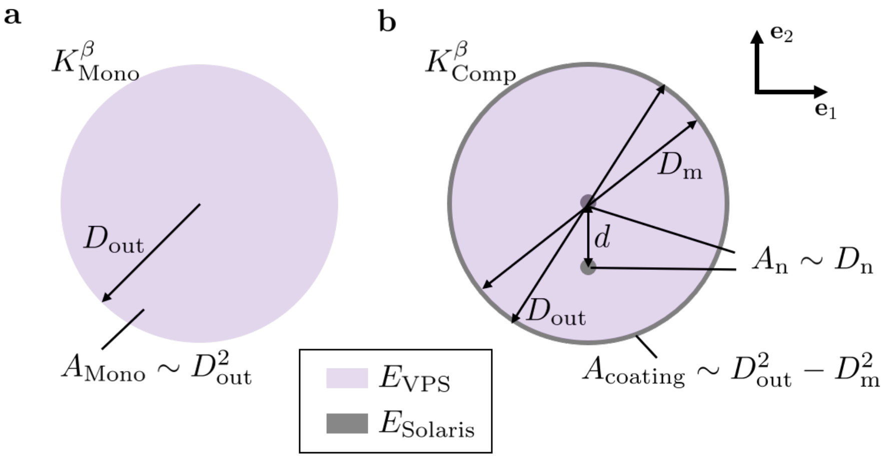
a
$K^{\beta}_{\mathrm{Mono}}$
D_{out}
$A_{\mathrm{Mono}} \sim D^2_{\mathrm{out}}$
b
$K^{\beta}_{\mathrm{Comp}}$
$\mathbf{e}_2$
$\mathbf{e}_1$
D_{m}
d
$A_{\mathrm{n}} \sim D_{\mathrm{n}}$
D_{out}
$A_{\mathrm{coating}} \sim D^2_{\mathrm{out}} - D^2_{\mathrm{m}}$
E_{VPS}
E_{Solaris}

Figure 2.7: **Schematics of monolithic versus composite rod cross sections.** **a**, Cross-sectional cut of monolithic rod out of VPS material with stiffness, $K^{\beta}_{\mathrm{Mono}}$, cross-sectional area, A_{Mono}, and diameter, D_{out}. **b**, View of the cross section of the composite rod with stiffness $K^{\beta}_{\mathrm{Comp}}$, including the VPS core rod of diameter, D_{m}, the physical fiber and the eccentric insets out of Solaris polymer of diameters, D_{n}, and cross-sectional areas, A_{n}, and a thin Solaris coating layer of area, A_{coating}, and thickness: $1/2(D_{\mathrm{out}} - D_{\mathrm{m}})$. For both schematics, we use the orthonormal coordinate system, $(\mathbf{e}_1, \mathbf{e}_2)$.

the monolithic and the composite rod (as shown in Figure 2.7**a** and **b**, respectively). Then, we determine the relative stiffness change, δ^{β}, between the actual composite rod and the monolithic counterpart.

(i) **Axial stiffness:**

$$K^{\mathrm{axial}}_{\mathrm{Mono}} = E_{\mathrm{VPS}} A_{\mathrm{Mono}} \tag{2.3}$$

$$K^{\mathrm{axial}}_{\mathrm{Comp}} = E_{\mathrm{VPS}}(A_{\mathrm{Mono}} - A_{\mathrm{coating}} - 2A_{\mathrm{n}}) + E_{\mathrm{Solaris}}(A_{\mathrm{coating}} + 2A_{\mathrm{n}}) \tag{2.4}$$

Combining Eq. (2.3) and Eq. (2.4) yields:

$$K^{\mathrm{axial}}_{\mathrm{Comp}} = K^{\mathrm{axial}}_{\mathrm{Mono}} - E_{\mathrm{VPS}}(A_{\mathrm{coating}} + 2A_{\mathrm{n}}) + E_{\mathrm{Solaris}}(A_{\mathrm{coating}} + 2A_{\mathrm{n}}) \tag{2.5}$$

Then, the relative axial stiffness change can be expressed as:

$$\delta^{\text{axial}} = \left| \frac{K^{\text{axial}}_{\text{Comp}} - K^{\text{axial}}_{\text{Mono}}}{K^{\text{axial}}_{\text{Mono}}} \right| \tag{2.6}$$

$$= \frac{A_{\text{coating}} + 2A_{\text{n}}}{A_{\text{Mono}}} \left| 1 - \frac{E_{\text{Solaris}}}{E_{\text{VPS}}} \right| \tag{2.7}$$

$$= \frac{(D^2_{\text{out}} - D^2_{\text{m}}) + 2D^2_{\text{n}}}{D^2_{\text{out}}} \left| 1 - \frac{E_{\text{Solaris}}}{E_{\text{VPS}}} \right| = 3.0\% \tag{2.8}$$

(ii) **Bending rigidity or bending stiffness:** We can skip a couple of steps by taking Eq. (2.7), in which we replace the cross-sectional area with the second moment of area. Using the theorem of parallel axis, $I^*_{\text{n}} = I_{\text{n}} + A_{\text{n}} d^2$, gives the relative bending rigidity change w.r.t. the $\mathbf{e}_1$-axis:

$$\delta^{\text{bending 1}} = \left| \frac{K^{\text{bending}}_{\text{Comp}} - K^{\text{bending}}_{\text{Mono}}}{K^{\text{bending}}_{\text{Mono}}} \right| = \frac{I_{\text{coating}} + I^*_{\text{n}} + I_{\text{n}}}{I_{\text{Mono}}} \left| 1 - \frac{E_{\text{Solaris}}}{E_{\text{VPS}}} \right| = 5.4\% \tag{2.9}$$

and the relative bending rigidity change w.r.t. the $\mathbf{e}_2$-axis:

$$\delta^{\text{bending 2}} = \left| \frac{K^{\text{bending}}_{\text{Comp}} - K^{\text{bending}}_{\text{Mono}}}{K^{\text{bending}}_{\text{Mono}}} \right| = \frac{I_{\text{coating}} + 2I_{\text{n}}}{I_{\text{Mono}}} |1 - \frac{E_{\text{Solaris}}}{E_{\text{VPS}}}| = 5.3\% \tag{2.10}$$

(iii) **Torsional rigidity:** Again, we make use of Eq. (2.7) and replace the cross-sectional area by the polar second moment of area. Uisng the perpendicular axis theorem, $J^*_{\text{n}} = I^*_{\text{n}} + I_{\text{n}}$, yields the relative torsional rigidity change:

$$\delta^{\text{torsional}} = \left| \frac{K^{\text{torsional}}_{\text{Comp}} - K^{\text{torsional}}_{\text{Mono}}}{K^{\text{torsional}}_{\text{Mono}}} \right| = \frac{J_{\text{coating}} + J^*_{\text{n}} + J_{\text{n}}}{J_{\text{Mono}}} |1 - \frac{G_{\text{Solaris}}}{G_{\text{VPS}}}| = 5.3\% \tag{2.11}$$

We conclude that the relative stiffness changes, δ^{β}, between the composite rod and the monolithic counterpart are around ≈ 5% for axial, bending, and torsional deformations. Given the limit of sufficiently large features (coating layer and insets) in the composite rod for volumetric imaging purposes (see Section 2.3), the predicted stiffness change is regarded as adequate. We take the 5%-stiffness change as an upper threshold below which we consider the rod as homogeneous.

2.3 X-Ray Tomographic Imaging and Image Analysis

To extract geometric information from physical samples (tangles and knots), we used X-ray micro-computed tomography (μCT). Applying this non-destructive volumetric imaging technique on knotted rod samples, and harvesting useful information by post-processing the reconstructed data, was to the best of our knowledge not reported in the literature before. In this section, we give a detailed description of the imaging technique followed by post-processing steps of the volumetric reconstructed data. In Section 2.3.1, we describe the procedure to capture the μCT images of tangles and knots. The subsequent image-processing algorithm that we developed to track the coordinates of the centerlines of the touching rods, as well as their contacting region is presented in Section 2.3.2. Making use of the image-processing algorithm, in Section 2.4, we describe the geometric quantities that we are able to extract and compute from the experimental data. The development of these toolboxes was a substantial part of the present thesis and was published in Grandgeorge et al. [78]. Thus, portions of the text and figures in this section are adapted from the supplementary information in the latter publications.

2.3.1 X-Ray μCT Principles and Scanning Settings

To study the geometrical properties of knots, we make use of μCT, which is a non-destructive imaging technique based on volumetric differential X-ray absorption. An X-ray generator irradiates the sample of interest, which partially absorbs the incoming X-ray beam [87]. The X-ray fraction passing through the sample is projected onto a detector, producing a 2D snapshot. Then, a collection of 2D images is obtained from multiple viewpoints (we performed scans with 1,000 projections), from which the 3D volumetric (tomographic) image of the sample is reconstructed. The intensity I of an X-ray beam as it passes through a bulk material is expected to decrease exponentially with the following attenuation behavior [88]:

$$I = I_0 e^{-Ax} = I_0 e^{-\mu\rho x}, \tag{2.12}$$

where I_0 is the initial X-ray beam intensity, A is the material-specific absorption coefficient, and x is the depth of penetration. The mass absorption coefficient μ and the absorption coefficient A are related by the material density ρ as $\mu = A/\rho$. μCTs typically have a high spatial resolution, with voxel sizes down to 1 μm or smaller. The voxel size is the size of a 3D pixel in the rendered image.

We used the tomograph with an automatic sample changer, μCT 100 (Scanco Medical, Brütisellen, Switzerland), on tangled and knotted rod configurations, aspiring to differentiate between regions inside and outside of the knot sample thanks to contrast differences in the images. Further, we followed the ambitious goal to be able to segment the features introduced in the composite rod (as described in Section 2.2) to give us even further insights into the experimental samples. Determining the optimal μCT scanning settings was crucial to obtaining high-quality volumetric images of our scans. For all the configurations involving VPS material, we consistently performed the μCT scans at an X-ray source energy of 70 kV and intensity 200 μA. Each projection was produced with an acquisition time of 300 ms. Furthermore, we made use of the built-in 0.5 mm-thick aluminum filter to correct beam hardening effects [87]. The total scanning time of each configuration highly depends on the desired resolution and scanning height and typically ranged from 1 hour to 4 hours. The spatial resolution of knotted and tangled configurations typically ranged from 25 to 35 μm (size of the voxels).

After the scanning process, the data was reconstructed (GPU accelerated) using the built-in commercial software package. Subsequently, the raw tomographic images were further post-processed following the scheme presented in Section 2.3.2. To illustrate the different steps of volumetric scanning, we make use of two examples, a knot, and a tangle. A simple figure-eight knot tied in a homogeneous elastomeric rod (see image in Figure 2.8**a**), and two elastomeric rods in orthogonal contact (also called: the elastic clasp, see optical photograph in Figure 2.9**a**). These two configurations allow demonstrating that the methodology works for both cases, one single rod with self-contact, and two different rods in contact.

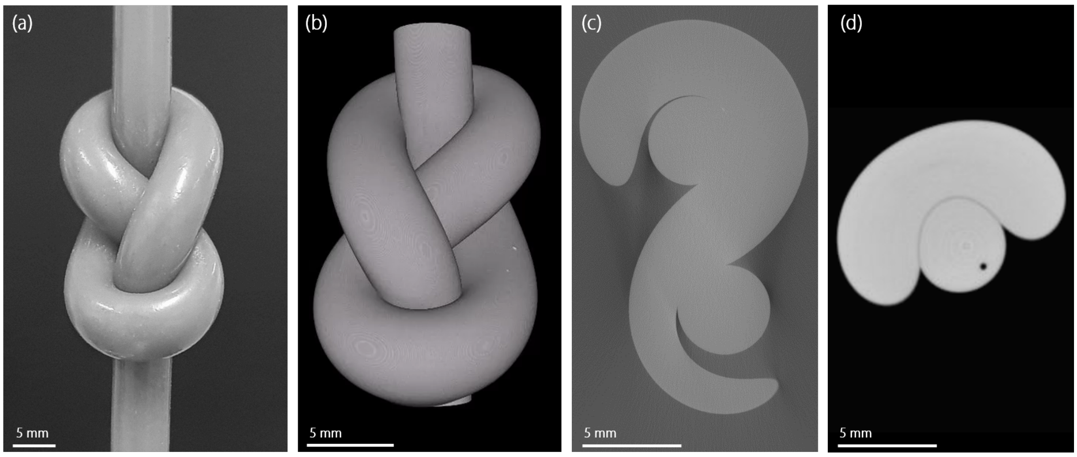

Figure 2.8: **Volumetric μCT imaging of the figure-eight knot.** **a**, Optical image of a figure-eight knot tied in a homogeneous elastomeric rod; **b**, 3D reconstructed μCT data; **c**, Cross-sectional cut image of the stack of images generated by the μCT; the contact regions are not visible; **d**, Cross-sectional cut image by the μCT with information on contact interface between different parts of the rod (dark grey region).

The μCT generates a stack of images, specifically, cross-sectional cuts (see raw μCT image in Figure 2.8**c** and Figure 2.9**c**), that can be reconstructed into a 3D image of the knot (see Figure 2.8**b** and Figure 2.9**b**). In the cross-sectional cut in Figure 2.8**c** and Figure 2.9**c**, it is observed that the different parts of the rod cannot be told apart. In other words, scanning the perfectly homogeneous knot leads to a loss of contact information because there is no differential absorption across the contact interface of a homogeneous material.

Distinguishing the two touching rods and their contact regions will be central to the subsequent image analysis presented in Section 2.3.2. Empirically, we found that a density difference of at least $10-15\%$ was sufficient to differentiate the two touching volumes. That is why we use the composite rods, introduced in Section 2.2, to visualize the contact regions and the material centerlines. Also, a minimum size of $3-5$ pixels of one material volume is required to be accurately captured in the subsequent image analysis. Combined with the finite resolution of the volumetric images (typically $\sim 30\,\mu$m/voxel), the above requirements set the limit thickness of both the outer coating and the physical centerline fiber. These constraints justify our choices of $e = 150\,\mu$m for the coating thickness and $D_\mathrm{n} = 500\,\mu$m for the diameter of the centerline fiber. With these parameters, as demonstrated in the cross-sectional cut of the knot in Figure 2.8**d** and of the clasp shown in Figure 2.9**d**, we were able to achieve a clear visualization of both the contact region and the material centerline.

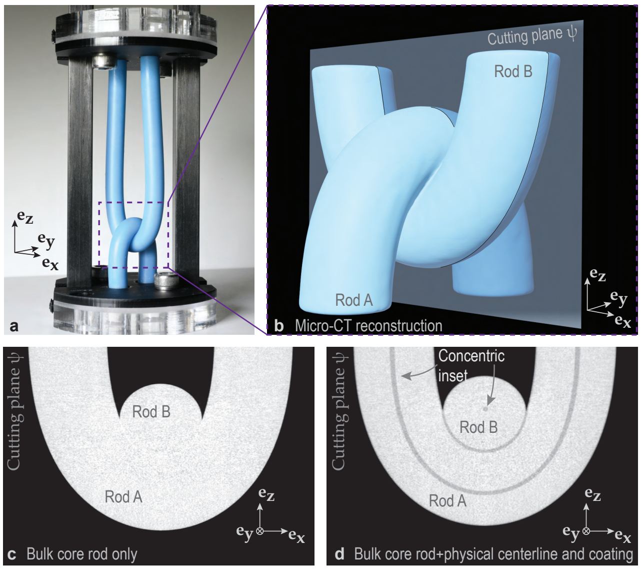

Figure 2.9: **Volumetric μCT imaging of the static elastic clasp. a**, Optical photograph of an elastic clasp. **b**, X-ray tomographic reconstruction of the configuration in **a**. **c-d**, Images of a cut (along the plane ψ defined in **b**) of a 3D volumetric image for a **c** monolithic elastomeric VPS-16 rod (the contact regions are not visible) and **d** for a VPS-16 bulk core rod coated with Solaris polymer and including the material centerline (also made out of Solaris). In (**d**), the contact interface at the crossing of the two rods (dark gray region) is clearly visible, whereas not so in **c**. The rest diameter of the rods composing the elastic clasps in **a**, **b** and **c** is $D = 8.3$ mm and in **d**, it is $D = 8.5$ mm (the extra thickness is due to the presence of the outer coating).

2.3.2 Centerline Coordinates and the Contact Regions From μCT Data

Once the tomographic data of the sample was acquired using the μCT and reconstructed into 3D volumetric images (Section 2.3.1), it was necessary to process them further to digitize the material centerline coordinates and locate the contact region. We did not use existing commercial segmentation software to fully control all the parameters and to avoid switching between multiple software during image-processing. For example, the extraction of the Darboux vectors of the Cosserat frame is not defined in commercial segmentation software. In this section, we describe the image post-processing algorithm we developed in-house to extract relevant geometric quantities. Specifically, this algorithm will enable us to relate the location of the contact regions to the corresponding arc length coordinates of the centerlines of the respective rods.

The reconstructed 3D images obtained from the μCT data comprise a stack of grayscale images. We convert the original *DICOM* file into a compact *TIFF* format that is readable by Matlab (Matlab 2019b, MathWorks), in which the main post-processing will be done. First, the *DICOM* images were treated using the open-source image analysis platform ImageJ 1.52b (National

Institutes of Health [89]) for contrast enhancement; voxels corresponding to the surrounding air down were shifted down to black (0) and the brightest regions to white (255). The 16-bit data was then downscaled to 8-bit to reduce the file sizes and further alleviate the computational load of the subsequent image post-processing routine (detailed below). Secondly, Matlab's Imaging Processing Toolbox was used to convert the 8-bit stack of images into a dense 3D matrix, whose voxels had values ranging from 0 to 1, representing the local material density. The voxel values were ≈ 0.9 and ≈ 0.8 for the VPS and Solaris regions, respectively. As a reminder, VPS-16 was used for the bulk core rod and Solaris for the centerline fiber and the outer coating layer.

Next, to extract the centerline coordinates of the rod, we need to apply one of the following two approaches: if we are dealing with purely elastic rods that are fabricated according to the protocols described in Section 2.2, we make use of the incorporated **material centerline**. Since this approach is based on the material centerline, we call it *matCL*. However, we have to sidestep to a **geometric centerline** in the case of purchased surgical suturing monofilaments due to the absence of a physical centerline inset. The geometric centerline is extracted by determining the centroid of a plane that is oriented in such a way that the cross-sectional area at each iteration is minimized and referred to as *minCS*. In Section 3.3, we evaluate this technique by doing a compare-and-contrast investigation between this geometric centerline definition and the material centerline.

The subsequent post-processing algorithm aims to digitize the centerlines and the contact surface between two rods. The code is based on the presence of a material centerline (*matCL*) and involves the following two stages. In *Stage (I)*, we extract a set of coordinates that follows the knotted rod and coarsely describes the centerline coordinates. Taking the coarse set of centerline locations found in *Stage (I)*, as a scaffold, and iterating between them, the centerline is refined, and the contact surfaces are digitized in *Stage (II)*. Next, we present *Stage (I)* and *Stage (II)* in more detail.

Stage (I) – Coarse discretization of the rod centerline: The goal of this first step is to build a coarse (approximate) discrete centerline, $\mathbf{p} = \{\mathbf{p}_k\}$, where $k = 1, 2, \cdots$ represents the index of a point along the discrete centerline. Each point $\mathbf{p}_k$ is obtained from cross-sectional cuts of the 3D volumetric image. To better illustrate the methodology, we make use of the elastic clasp configuration (see Figure 2.10). We iterate through the centerline by following these steps:

(I).1 Initial ansatzes for both the starting point of the centerline ($\mathbf{p}_1^{\text{guess}}$) and the tangent of the centerline at that point ($\hat{\mathbf{t}}_1^{\text{guess}}$) are input by the user. A square cross-sectional view of size $1.5D \times 1.5D$ (D is the rest diameter of the rod), normal to $\hat{\mathbf{t}}_1^{\text{guess}}$ at $\mathbf{p}_1^{\text{guess}}$ is investigated (see Figure 2.10**a**). A Gaussian filter was applied to this frame using Matlab's `imgaussfilt` function, with the standard deviation `SIGMA=3`. This smoothing allowed us to decrease the noise of the grayscale material frame without the loss of fine details.

(I).2 From the cross-sectional view at $\mathbf{p}_1^{\text{guess}}$, and along $\hat{\mathbf{t}}_1^{\text{guess}}$, the user is prompted to input the refined position of $\mathbf{p}_1$ by locating the darker area (see inset of Figure 2.10**a**) corresponding to the physical material centerline.

(I).3 The second point of the material centerline ($\mathbf{p}_2$) is now to be determined. The cross-sectional view at the projected second point, $\mathbf{p}_2^{\text{proj}} = \mathbf{p}_1 + \xi\,\hat{\mathbf{t}}_1^{\text{guess}}$, with a normal $\hat{\mathbf{t}}_1^{\text{guess}}$, is investigated (see Figure 2.10**b**). We typically took the incremental distance between two successive coarsely distributed centerline locations $\xi = D/10$.

(I).4 The user is prompted to input the position of $\mathbf{p_2}$ by locating the dark area of the cross-sectional view. From $\mathbf{p}_1$ and $\mathbf{p}_2$, the first tangent vector is updated by $\hat{\mathbf{t}}_1 = (\mathbf{p}_2 - \mathbf{p}_1)/\|\mathbf{p}_2 - \mathbf{p}_1\|$.

(I).5 The iterative loop runs automatically without further user input from this step onward. For point indices $k \geq 3$, the kth point is projected from the $(k-1)^{\text{th}}$ point such that $\mathbf{p}_k^{\text{proj}} = \mathbf{p}_{k-1} + \xi\,\hat{\mathbf{t}}_{k-1}$ and $\hat{\mathbf{t}}_{k-1} = (\mathbf{p}_k - \mathbf{p}_{k-1})/\|\mathbf{p}_k - \mathbf{p}_{k-1}\|$. Since the 2D cross-sectional cuts are in close proximity ($\xi = 0.1D$), the image generated at $\mathbf{p}_k^{\text{proj}}$, at each step, is sufficiently similar to the previous one, such that the dark region of the physical centerline can be tracked automatically by locating the small darker region of the physical centerline in the close vicinity of the center of the generated 2D image (as shown in Figure 2.10**c**). To track this darker region, we first binarize the image of the cross-sectional cut and then use the Matlab 2019 function `regionprops` to locate the centroid of the dark centerline region.

(I).6 Iteration on k, step (I).5., is repeated until the other rod extremity is reached. In Figure 2.10 **d**, we show the iteration process at $k = 14$.

The final output of Stage I of the algorithm is a discrete set of 3D points $\mathbf{p} = \{\mathbf{p}_k\}$ and a corresponding set of unit tangent vectors $\hat{\mathbf{t}} = \{\hat{\mathbf{t}}_k\}$, representing the material centerline of the rod. We define the unit normal $\hat{\mathbf{n}}$ and binormal vectors $\hat{\mathbf{b}}$ such that

$$\hat{\mathbf{b}} = \frac{(\mathbf{e}_z \times \hat{\mathbf{t}})}{\|\mathbf{e_z} \times \hat{\mathbf{t}}\|}, \tag{2.13}$$

and

$$\hat{\mathbf{n}} = \hat{\mathbf{b}} \times \hat{\mathbf{t}}, \tag{2.14}$$

where $\mathbf{e}_z$ is the unit vector along the z-axis. We used the plane spanned by $\hat{\mathbf{n}}$ and $\hat{\mathbf{b}}$ to construct

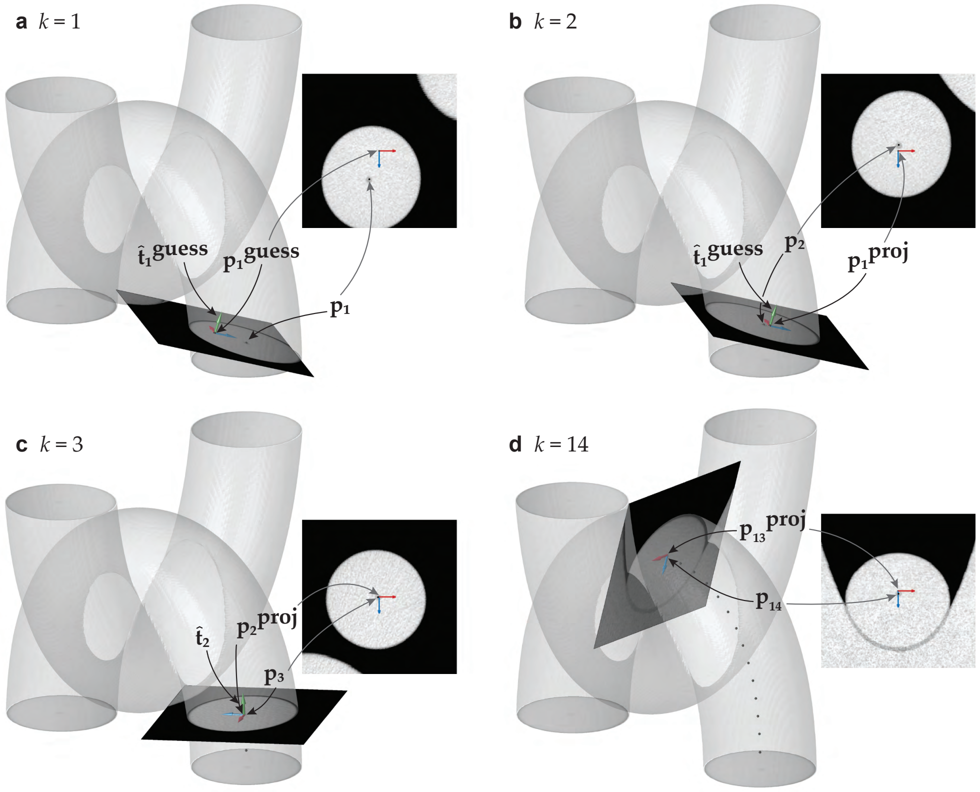

Figure 2.10: **Procedures for digitizing the coarse centerline (*Stage (I)*). a.** Initialization. The user inputs guesses for a point in the 3D laboratory frame and the tangent ($k = 1$). The resulting 2D material frame showing the rod cross section is presented in the inset. **b.** Identification of the second point on the centerline ($k = 2$) by projection to construct the second cross-sectional view. **c.** Beyond the third point on the centerline ($k \geq 3$), the centerline tracking is fully automated; the centerline fiber is tracked by isolating the darker (less dense) regions in the material frame. The tangent vector is constructed at each step using the two previous centerline points. **d.** The 14 first coarse centerline coordinates are represented by the black dots in the image. In all four panels, the unit binormal ($\hat{\mathbf{b}}$) and normal ($\hat{\mathbf{n}}$) vectors are respectively represented as red and blue arrows.

a material frame using only a central point $\mathbf{p}$ and a tangent vector $\hat{\mathbf{t}}$ (allowing us to construct the unit normal and binormal vectors) at each step.

Stage (II) – Refinement of the centerline coordinates and tracking of the rod surface: During this second stage of the algorithm, we refine the density of the discrete arc lengths at which we locate the centerline fiber coordinates. This second stage also allows us to compute a discrete set of 3D coordinates of the rod's surface boundaries at each discrete arc length. This *Stage (II)* is fully automated; the discrete centerline $\mathbf{p}_k$ and tangents $\hat{\mathbf{t}}_k$ determined previously in *Stage (I)* are now used to construct intermediary material frames in between the coarse data.

(II).1 The mth intermediary frame is constructed between the coarse centerline locations $\mathbf{p}_k$ and $\mathbf{p}_{k+1}$ determined in Stage (I), such that $1 \leq m \leq M$ where M is the number of intermediate centerline locations in between each coarse centerline location. To construct this m^{th} material frame, we linearly interpolate $\mathbf{p}_k$ to provide a guess for the location of the current centerline such that $\mathbf{p}_{k,m}^{\text{guess}} = (M - m + 1)/M \cdot \mathbf{p}_k + (m-1)/M \cdot \mathbf{p}_{k+1}$. We make use of the same linear interpolation scheme to generate the mth intermediary guessed tangent vector $\hat{\mathbf{t}}_{k,m}^{\text{guess}}$.

(II).2 The refinement of the centerline coordinates is implemented by automatically tracking the darker region of the centerline fiber in the intermediary frames (using the Matlab 2019 function `regionprops`). We obtain all the refined centerline coordinates $\mathbf{p}_n$, where n is the overall index of the finely distributed centerline coordinates such that $n = M(k-1) + m$, with $1 \leq n \leq N$ (where N is the total number of finely distributed locations of the centerline coordinates, typically we have $N \simeq 250$).

(II).3 At the end of this refinement step, we smoothed to the centerline coordinates by making use of the Matlab 2019 command `smoothdata` with a window size of $\simeq$ `round(`$N/7$`)`. These smoothed centerline locations allow us to generate the discrete $N-1$ final tangent vectors $\hat{\mathbf{t}}_n$ of the discrete centerline such that $\hat{\mathbf{t}}_n = (\mathbf{p}_{n+1} - \mathbf{p}_n)/\|\mathbf{p}_{n+1} - \mathbf{p}_n\|$. Without this smoothing step, the resulting tangent vectors would be too noisy to allow subsequent processing steps.

(II).4 In addition to the centerline refinement, we also developed an edge-detection algorithm to track the surface boundaries of the deformed rod, yielding the full 3D envelope (discrete) of the rod of interest. Note that locating the rod boundaries is straightforward in the absence of rod-rod contact. In this case, the material frame is binarized, and then the boundaries of the rod cross section are located using the Matlab function `regionprops`. By contrast, when there is rod-rod contact along some locations of its arc length (see example Figure 2.10**d**), the boundary of the rod must be determined in an alternative way. This edge-detection strategy is detailed next.

In Figure 2.11, we present the procedure for digitizing the rod surface in the case of contact and no contact. After constructing the intermediary 2D material frame of interest (shown in Figure 2.11**a**) that is centered at the centerline location $\mathbf{p}_n$), we analyze the gray values of this material frame along a *probing line* that emanates radially from the material centerline, with a specified angle φ. This angle was varied discretely within the range $0 \leq \varphi \leq 360°$, in 100 steps. In Figure 2.11**a**, we represent two representative probing lines at angles with the horizontal axis φ_1 and φ_2 (red and green solid lines, respectively). We also present the result of the rod-surface tracking procedure. The red points correspond to free rod surfaces (contact with surrounding air), and the green points correspond to contact location with another rod.

Finally, in Figure 2.11**b**, the gray-scale values along the probing lines (1) and (2) and represented as a function of the radial distance to the centerline location (black point in Figure 2.11**a**). When the rod is in contact with air (probing line (1)), the gray values along this line will jump from a finite value (inside the rod) to zero (surrounding air). Therefore, we determine the location of the rod surface where the gray-scale profile measured along this probing line drops below a threshold value (determined dynamically using the average of the gray value of the bulk rod at each frame). On the other hand, when the rod is in contact with another rod (probing line (2)), the gray values along the probing line will not drop to zero, but they will be affected by the darker surface coating of the rod. Consequently, the gray values will exhibit a local minimum along the probing line, the location of which is attributed to the rod surface.

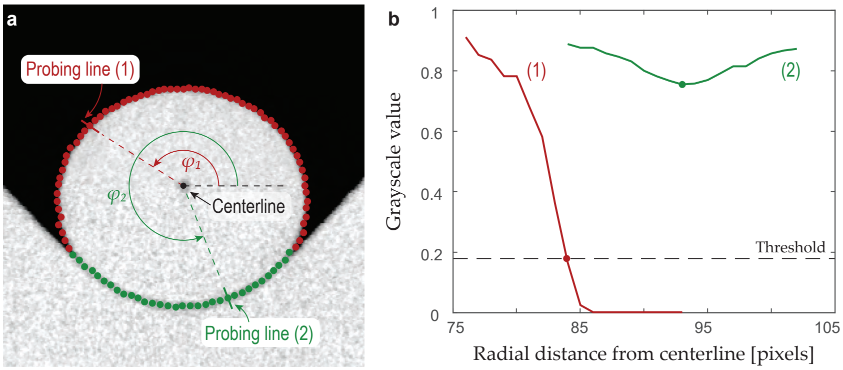

Figure 2.11: **Procedure for digitizing the rod surface from a cross-sectional cut. a,** We represent two representative probing lines on a cross-sectional cut at angles with the horizontal axis φ_1 and φ_2 (red and green solid lines, respectively). The red points correspond to free rod surfaces (contact with surrounding air), and the green points correspond to contact location with another rod. **b,** The gray-scale profiles along the probing lines (1) and (2) are represented as a function of the radial distance to the centerline location (black point in **a**). The rod surface is determined by a threshold value in case the rod is in contact with air (probing line (1)) or by the minimum of the grayscale profile when the rod is in contact with another rod (probing line (2)).

2.3.3 Adaptations to Use the Geometric Centerline Definition *minCS*

We do not always have the possibility to incorporate a physical fiber that acts as a *material* centerline. For instance, when studying the role of plasticity in surgical knots in Chapter 6, we use purchased suturing monofilaments and have to sidestep to a *geometric* centerline. However, there is no unique geometric centerline definition of a rod with varying cross section and shear deformation. We hypothesize that the centroids of planes that are oriented such that the cross-sectional area at each arc length location is minimized are a valid definition of a geometric centerline. In the following paragraphs, we will abbreviate this procedure as *minCS*. In this section, we first describe the process of extracting this geometric centerline and subsequently do a compare-and-contrast investigation between this geometric centerline definition and the material centerline.

Following the procedure for the material centerline extraction (described in Section 2.3.2), we split the post-processing in two steps: *Stage I* and *Stage II*. Similar to *matCL*, the goal of the first step is to coarsely extract centerline coordinates that act as a scaffold for the next step, *Stage II*, in which the centerline is refined. The schematics in Figure 2.12 show a two-dimensional curved rod and help to describe the various steps of the post-processing technique. Given the similarities between the techniques *matCL* and *minCS*, we will only focus on the differences and ask the reader to use the process steps (I).1-(I).6 and (II).1-(II).4 described in Section 2.3.2 as the basis.

Stage I – Coarse approximate geometric centerline discretization:
Step (I).1 remains unchanged to the one presented in Section 2.3.2. As shown in Figure 2.12**a**, $\{\mathbf{p}^{\mathrm{I}}_{n}, \mathbf{t}^{\mathrm{I}}_{n}\}$ denote the initial guess for the centerline point and the tangent vector, respectively. Here, $n = 1, 2, \cdots$ represents the index of a point along the discrete centerline. Omitting Step (I).2 leads to Step (I).3 which is the same than in *matCL*, and yields $\{\mathbf{p}^{\mathrm{proj}}_{n+1}, \mathbf{t}^{\mathrm{proj}}_{n+1}\}$. Then, in step (I).4, we draw the plane (blue line in Figure 2.12**a**) that passes through $\mathbf{p}^{\mathrm{proj}}_{n+1}$ and that is orthogonal to $\mathbf{t}^{\mathrm{proj}}_{n+1} = \mathbf{t}^{\mathrm{I}}_{n}$. Instead of locating the darker area of a physical fiber, the edge locations of the rod's cross section are used to determine the centroid location of the quasi-circular shape. This centroid is considered as an approximate centerline location, and denoted as $\mathbf{p}^{\mathrm{I}}_{n+1}$. The orientation of the tangent vector $\mathbf{t}^{\mathrm{I}}_{n+1}$ is set by connecting the two approximate centerline points, $\mathbf{p}^{\mathrm{I}}_{n}$ and $\mathbf{p}^{\mathrm{I}}_{n+1}$ (see drawing in Figure 2.12**a**). In Step (I).5, the algorithm repeats the Steps (I).3 and (I).4 until the end of the rod is reached, yielding the complete coarse approximate geometric centerline as shown in Figure 2.12**b**.

Stage II – Fine accurate geometric centerline:
Next, we start again at the initial point from *Stage I*, and as described in Step (II).1, m intermediary frames between $\mathbf{p}^{\mathrm{I}}_{n}$ and $\mathbf{p}^{\mathrm{I}}_{n+1}$ are constructed by linear interpolations. To simplify the description, we only focus on the frames n, but the same procedure is applied to the intermediary frames of the refined centerline.

Then, in Step (II).2, we apply the minimization of the cross-sectional area procedure described next. A plane is constructed that passes through the approximate centerline location from *Stage I*, $\mathbf{p}^{\mathrm{I}}_{n}$, and whose orientation depends on two variable angles, α_n and β_n describing the

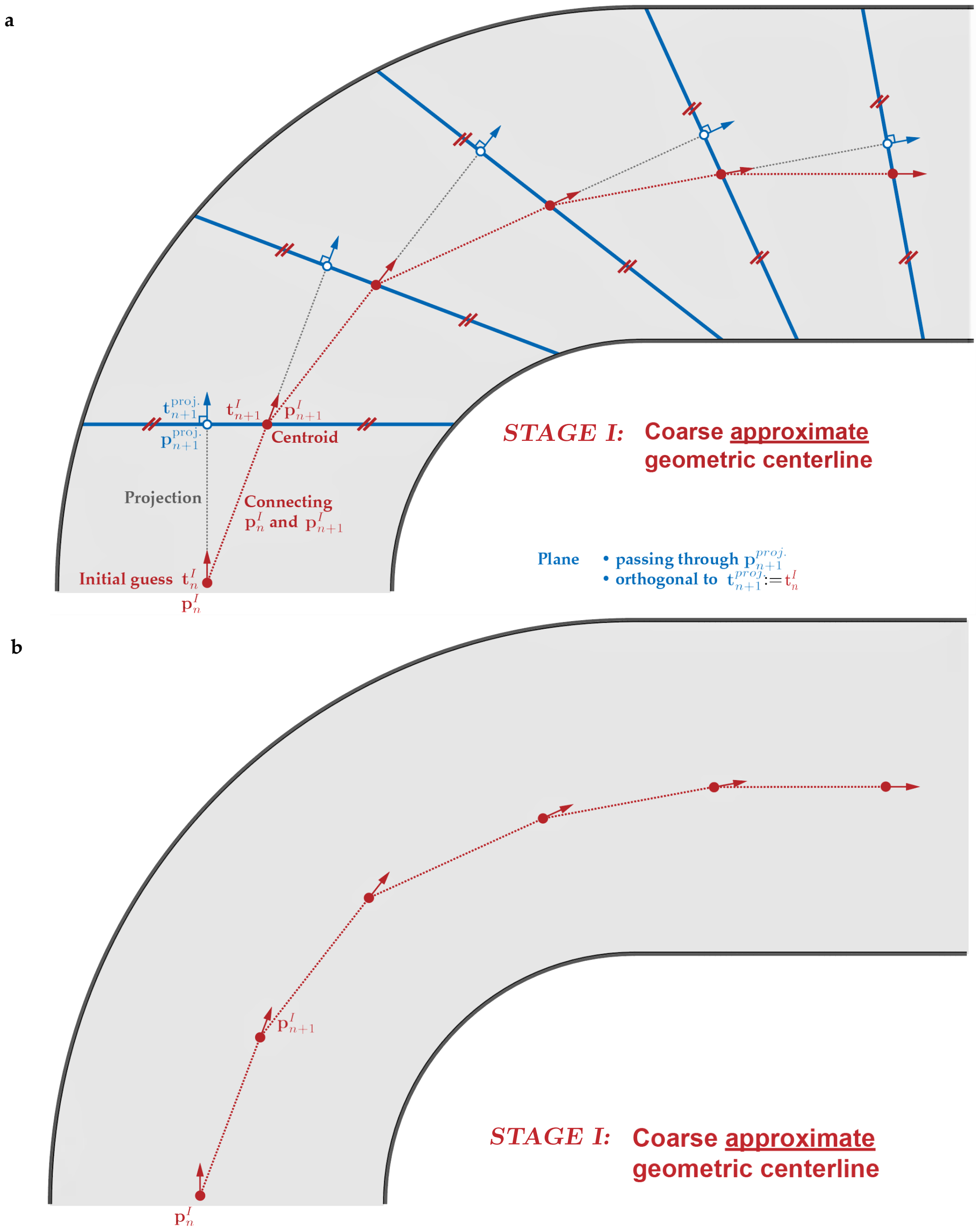
a
$\mathrm{t}^{\text{proj.}}_{n+1}$
t^{I}_{n+1}
p^{I}_{n+1}
$\mathrm{p}^{\text{proj.}}_{n+1}$
Centroid
Projection
Connecting p^{I}_{n} and p^{I}_{n+1}
Initial guess t^{I}_{n}
p^{I}_{n}
STAGE I: Coarse approximate geometric centerline
Plane
• passing through $\mathrm{p}^{proj.}_{n+1}$
• orthogonal to $\mathrm{t}^{proj.}_{n+1} := \mathrm{t}^{I}_{n}$
b
p^{I}_{n+1}
STAGE I: Coarse approximate geometric centerline
p^{I}_{n}

Figure 2.12: ***Stage I* of procedure for digitizing the rod surface from a cross-sectional cut using the *minCS* technique. a,** Iterative approach to determine a coarse approximate geometric centerline using projections and the centroid method. **b,** The coarse and approximate centerline coordinates and tangent vectors constitute the final output of *Stage I* and will serve as an input to *Stage II*.

orientation of the tangent vector $\mathbf{t}^{\mathrm{II}}_{n}(\alpha_n, \beta_n)$. By applying the derivative-free minimization function in Matlab 2019 `fminsearch`, α_n and β_n are determined such that the cross-sectional area – determined from the rod edge-points of the current cross-sectional cut – reaches its

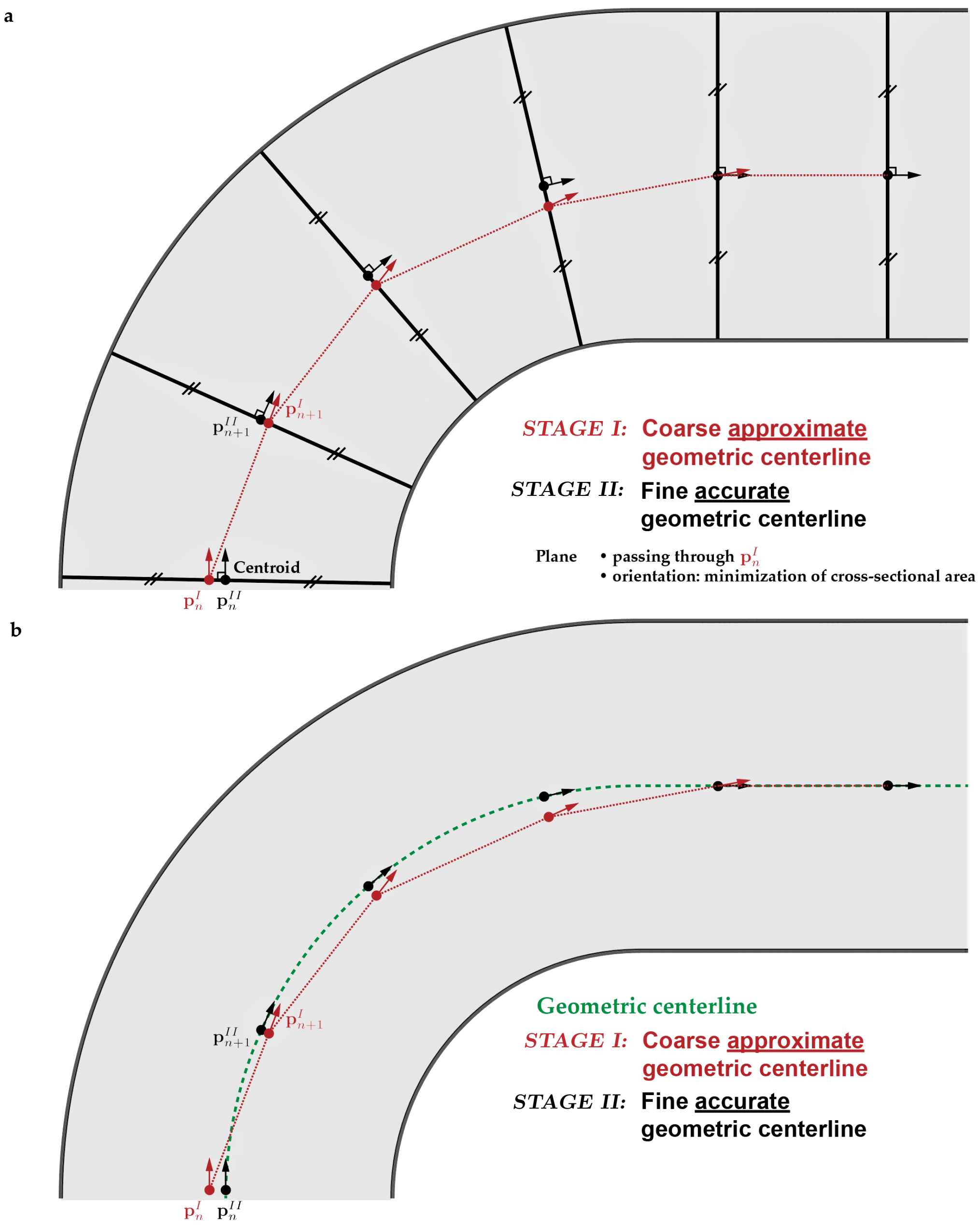
a
p^{II}_{n+1}
p^{I}_{n+1}
Centroid
p^{I}_{n} p^{II}_{n}
STAGE I: Coarse approximate geometric centerline
STAGE II: Fine accurate geometric centerline
Plane
• passing through p^{I}_{n}
• orientation: minimization of cross-sectional area
b
p^{II}_{n+1}
p^{I}_{n+1}
p^{I}_{n} p^{II}_{n}
Geometric centerline
STAGE I: Coarse approximate geometric centerline
STAGE II: Fine accurate geometric centerline

Figure 2.13: ***Stage II* of procedure for digitizing the rod surface from a cross-sectional cut using the *minCS* technique. a,** Determination of the fine and accurate geometric centerline information by applying the strategy of minimizing the cross-sectional area at each iterative step. **b,** Final *fine-discretized* geometric centerline from the procedure *minCS* (green dashed curve) in comparison to the output from *Stage I*.

minimum. Once the cutting plane is found, the centroid of the polygon forming the edge of the rod cross section is defined as a point on the geometric centerline, $\mathbf{p}_n^{\mathrm{II}}$. The final tangent vector is determined from the minimization procedure of α_n and β_n. This procedure is repeated for the other approximate centerline locations, and shown in a 2D setting in Figure 2.13**b**. Steps (II).3 and (II).4 are identical to the ones described in the context of the material centerline. Finally, in Figure 2.13**b**, we show the resulting geometric centerline for a fine-discretized centerline (green dashed curve).

2.3.4 Parameter-Tuning to Handle Extreme Geometries and Their Limitations

Even rods with severe cross-sectional deformation can be processed by tuning the key parameters right. By increasing the search area for rod surface detection, also regions closer to the centerline are included. The condition for this solution to work is that the rod does not include any defects like voids of air incorporated during rod fabrication.

The algorithm also manages to follow the centerline of rods with moderate-high curvatures (normalized curvature $\kappa D \sim 1.25$). By decreasing the incremental distance between two successive coarsely distributed centerline locations ξ, the material frame can still capture the entire rod cross section without exiting the rod. Decreasing the incremental distance leads to larger angles of the tangent vectors. Since these vectors are not final and only serve as rough guesses in the refinement step (*Stage (II)*), a simple smoothing of the data is sufficient to move on to *Stage (II)*.

However, if the curvatures reach extreme local values (normalized curvature $\kappa D > 1.5$), usually combined with large cross-sectional deformation, the post-processing toolbox might fail. To avoid the material frame from shooting out of the rod, the incremental distance between two successive coarsely distributed centerline locations ξ would need to be decreased significantly, leading to unstable variations of the tangent vectors. Thus, the material frame does not capture the whole rod cross section and cannot capture the correct information.

The previously described procedure allows us to experimentally extract rod features with high precision. This toolbox is a novelty in the experimental analysis of physical rod-like structures. With the experimental centerline coordinates and rod surface locations at hand, we will be able to make use of the Cosserat frame to compute curvature, twist, cross-sectional flattening, and other useful properties that lead to more understanding of knotted configurations in the Chapters 4, 5 and 6 (as well as in [62, 78, 37]). This second post-processing step quantifying the rod deformation will be described next, in Section 2.4.

2.4 Geometric Quantification of the Rod Deformation

Once the locations of the material centerline and the contact surface have been extracted, we can quantify the deformation of the rods in tangles and knots. The data gathered during the previously described post-processing steps (Section 2.3.2) is saved such that every arc length location is related to a centerline coordinate, a tangent vector, the corresponding rod surface points (with and without contact), and if an eccentric inset exists, a vector connecting the latter one to the centerline position.

This section describes the framework we employed to quantify the kinematics and centerline curvature profiles of tangled and knotted elastomeric rods for CT scans. First, we will focus on the case of a rod, including an eccentric inset. Second, we describe another framework to compute discretized curvature of the rod centerline even in the absence of information on the material frame orientation. Finally, we will explain the procedures applied on CT and numerical data to extract the cross-sectional area and flattening of the rod and the contact region parametrized by the arc length coordinate of the rod.

2.4.1 Discrete Curvature Based on Cosserat Framework

Based on the volumetric μCT data, our procedure consists in computing the rotation of the rod local orthogonal basis, the Cosserat frame $(\hat{\mathbf{d}}_1, \hat{\mathbf{d}}_2, \hat{\mathbf{d}}_3)$ along its physical centerline [36, 35]. Note that, in Section 2.3.2, we used the Frenet-Serret framework $(\hat{\mathbf{t}}, \hat{\mathbf{n}}, \hat{\mathbf{b}})$ to describe the post-processing technique, not tracking the local rotation of the material frame. Here, we apply the Cosserat framework and notation introduced in Chapter 1, Section 1.2.2 to describe the framed curve. describe the steps we follow to compute the discretized curvature of the rod centerline. The composite nature of our custom-fabricated elastomeric rods (Section 2.2), coupled with X-ray tomography (Section 2.3), allows us to extract a discrete set of the locations of the centerline coordinates, $\mathbf{r}(s_i)$ and the corresponding discrete set of locations of the eccentric fiber inset, $\boldsymbol{\xi}(s_i)$. The integer i corresponds to the index of the centerline locations with $1 \leq i \leq N$ (where N is the total number of centerline points). We first construct the discrete set of tangent vectors $\hat{\mathbf{d}}_3$ at $s = s_i$ such that

$$\hat{\mathbf{d}}_3(s_i) \simeq \frac{\mathbf{r}(s_i + \delta s) - \mathbf{r}(s_i)}{\|\mathbf{r}(s_i + \delta s) - \mathbf{r}(s_i)\|}, \tag{2.15}$$

with the increment $\delta s \equiv \|\mathbf{r}(s_{i+1}) - \mathbf{r}(s_i)\|$. Next, we compute the unit director vector $\hat{\mathbf{d}}_1(s)$. To obtain this unit vector, we first construct the plane normal to $\hat{\mathbf{d}}_3(s_i)$ and determine the location $\boldsymbol{\xi}(s_i)$ at which the eccentric fiber crosses this plane. The vector $\hat{\mathbf{d}}_1(s)$ is then constructed from the coordinates $\boldsymbol{\xi}(s_i)$ using the relation

$$\hat{\mathbf{d}}_1(s_i) \equiv \frac{\boldsymbol{\xi}(s_i) - \mathbf{r}(s_i)}{\|\boldsymbol{\xi}(s_i) - \mathbf{r}(s_i)\|}. \tag{2.16}$$

Having $\hat{\mathbf{d}}_1$, the binormal vector $\hat{\mathbf{d}}_2$ is readily computed as $\hat{\mathbf{d}}_2 = \hat{\mathbf{d}}_3 \times \hat{\mathbf{d}}_1$, thus completing the discrete set of the Cosserat basis $(\hat{\mathbf{d}}_1(s_i), \hat{\mathbf{d}}_2(s_i), \hat{\mathbf{d}}_3(s_i))$. We further compute Ω_i; by taking the inner product between Eq. (1.2) and $\hat{\mathbf{d}}_b$ ($b = 1,2,3$), we find $\Omega_1 = \hat{\mathbf{d}}_2' \cdot \hat{\mathbf{d}}_3 = -\hat{\mathbf{d}}_3' \cdot \hat{\mathbf{d}}_2$, $\Omega_2 = \hat{\mathbf{d}}_3' \cdot \hat{\mathbf{d}}_1 = -\hat{\mathbf{d}}_1' \cdot \hat{\mathbf{d}}_3$, and $\Omega_3 = \hat{\mathbf{d}}_1' \cdot \hat{\mathbf{d}}_2 = -\hat{\mathbf{d}}_2' \cdot \hat{\mathbf{d}}_1$, which we discretize using the discrete derivatives

$$\Omega_1(s_i) \simeq \frac{\hat{\mathbf{d}}_2(s_i + \delta s) - \hat{\mathbf{d}}_2(s_i)}{\delta s} \cdot \hat{\mathbf{d}}_3(s_i), \tag{2.17}$$

$$\Omega_2(s_i) \simeq \frac{\hat{\mathbf{d}}_3(s_i + \delta s) - \hat{\mathbf{d}}_3(s_i)}{\delta s} \cdot \hat{\mathbf{d}}_1(s_i), \tag{2.18}$$

$$\Omega_3(s_i) \simeq \frac{\hat{\mathbf{d}}_1(s_i + \delta s) - \hat{\mathbf{d}}_1(s_i)}{\delta s} \cdot \hat{\mathbf{d}}_2(s_i). \tag{2.19}$$

Based on this discretized version of the Darboux vector, we finally compute the total curvature of the centerline as

$$K(s_i) \equiv \sqrt{\Omega_1^2(s_i) + \Omega_2^2(s_i)}. \tag{2.20}$$

2.4.2 Discrete Curvature Associated With Vertices

In case we do not have access to the eccentric inset, *e.g.* if we are using the geometric centerline definition *minCS* (described in Section 2.3.3) on surgical monofilaments (in Chapter 6), we cannot make use of the Cosserat frame. As introduced in the context of Discrete Differential Geometry in Chapter 1, Section 1.2.3, the curvature of a discrete curve can be computed by Eq. (1.7), which only relies on the tangent vectors of the centerline curve [39].

2.4.3 Smoothing of The Raw Data to Reduce 'Noise' in The Curvature Computation

Prior to computing the curvature profiles of the rod centerline by the method presented in Section 2.4.1 or Section 2.4.2, we applied a Gaussian-weighted moving average filter (command `smoothdata` in Matlab 2019) to $\boldsymbol{r}(s)$, with a window size defined by $\sigma = \texttt{round}(N_\text{b}/N_\text{gauss})$. To test the fidelity of the computed curvature data, given the discrete nature of the raw data, we performed a parametric test of the filter on the closed trefoil knot (studied in Chapter 4). In this test, we fixed the total number of discrete centerline points $N_\text{b} = 984$ for the closed trefoil knot, and systematically varied $N_\text{gauss} = \{15, 25, 50\}$. Without the filter (*i.e.*, $\sigma = 1$, corresponding $N_\text{gauss} = 984$), the data would be far too noisy for analysis. In Fig. 2.14, we present profiles for normalized curvatures, $\kappa(s)$, for decreasing values of N_gauss (the data is increasingly smoothed as N_{gauss} decreases). We selected the window size of $\sigma = 39$ (*i.e.*, $N_{\text{gauss}} = 25$), which reasonably suppresses noise while not over-smoothing the curvature features.

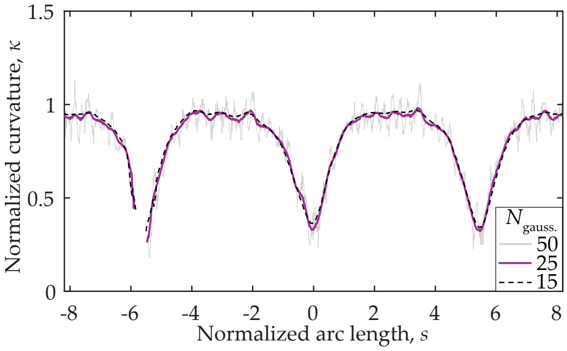

Figure 2.14: **Test for the smoothing of the curvature computed from the centerline data for the experimental closed trefoil knot.** A Gaussian-weighted moving average filter with changing size of the smoothing window allowed to find the trade-off value between noisy and over-smoothed curves. The selected value for the window size used for the data presented in the main text is $N_{\text{gauss}} = 25$ (*i.e.*, $\sigma = 39$).

2.4.4 Cross-Sectional Area and Flattening

The protocol described above allows us to extract the shape of the rod cross section at each constructed material frame, from which we quantify the cross-sectional area and flattening of the rod along its physical centerline. The extraction of the cross-sectional area is straightforward using the `regionprops` Matlab function. We define the flattening using the geometric quantity $1 - b/a$, where a and b are the major and minor axes of the rod cross section, respectively. The length of the minor axis, b, is determined in the 2D material frame by the shortest distance between the centerline coordinate to the closest rod-surface location. Similarly, the major axis, a, is the radial length between the centerline location to the furthest rod-edge coordinate. The quantification of the cross-sectional area and the flattening of the rod is applied in various studies (see Chapter 4 and Chapter 6) including Grandgeorge et al. [78] and Johanns et al. [90].

2.4.5 Shape of the Contact Region Between the Two Rods

Having access to the rod-surface coordinates and their state of contact or no contact, we can perform comparisons of the contact region between different tangle or knot configurations. To this end, we project the experimental contact surface onto a plane by assigning each discrete contact point detected in step (II).4 of Section 2.3.2 to the closest discrete centerline locations along the arc length s_1 and s_2 of the rod (or of the two rods in case of a 2-tangle).

This mapping of the contact shape is used in Chapters 4 and 6, as well as in Refs. Grandgeorge et al. [78], Johanns et al. [90].

2.5 Protocols for Characterization of Rods

In this section, we present the experimental procedure for the mechanical testing of knots. To rationalize and model the behavior of the elastomeric rods, we need to determine the underlying material model and the corresponding material parameters. In Section 2.5.1, we report the material characterization of the polymers used to fabricate the rods. Since knotted rods involve contact regions, we characterize the frictional behavior of the polymeric rods in Section 2.5.2.

2.5.1 Characterization of the Material Properties of VPS

We characterize the mechanical properties of VPS-16 and VPS-32, which form the bulk core of our elastic rods (see Section 2.2). We observed a non-negligible time-dependence of these polymers, and first, try to determine the time interval after which the material properties stabilize. A quick and reliable experiment to determine the evolution of the elastic modulus over a period of time is the resonance test, which consists on measuring the natural frequencies, ω_n, (with the natural mode shapes n) of a beam to determine the Young's modulus, E. In Figure 2.15**a1**, we show the schematic diagram of a vertically clamped VPS-16 beam. The beam of length $L_0 = 31.5\,\mathrm{mm}$ has a rectangular cross section of area $A = wd$ and a second moment of area $I = dw^3/12$, of width $w = 3\,\mathrm{mm}$ and depth $d = 5\,\mathrm{mm}$. The material density of VPS-16 is $\rho_{\mathrm{VPS16}} = 1160\ \mathrm{kg/m^3}$. The photograph in Figure 2.15**a2** shows the procedure of imposing a deflection, $\Delta \approx 15\,\mathrm{mm}$, of the beam centerline using a screwdriver. Releasing the beam leads to an oscillatory motion that is recorded and processed in MatLab to determine the natural frequency. The dynamic Young's modulus can be extracted from the relation between this frequency and the bending stiffness, EI. The first natural frequency, $\omega_{\mathrm{n=1}}$ can be written as:

$$\omega_{\mathrm{n=1}} = \frac{\beta_{\mathrm{n=1}}^2}{2\pi L_0^2}\sqrt{\frac{EI}{\rho A}}, \qquad (2.21)$$

with $\beta_{\mathrm{n=1}} = 0.597\pi$. Applying the Fast Fourier Transform (FFT) of the time series of the tip position allows to extract the fundamental frequency, and compute E of the material with Eq. (2.21). In Figure 2.15**a3**, we plot the evolution of the Young's modulus over time, observing a significant increase in the first week before reaching a plateau level at $E_{\mathrm{VPS\text{-}16}} = 0.52\,\mathrm{MPa}$. Similar behavior was observed for the other polymers, *i.e.* VPS-32. Consequently, we leave the bulk rod samples to rest for one week after curing to ensure their mechanical properties reach a steady state before performing any additional experimental tests.

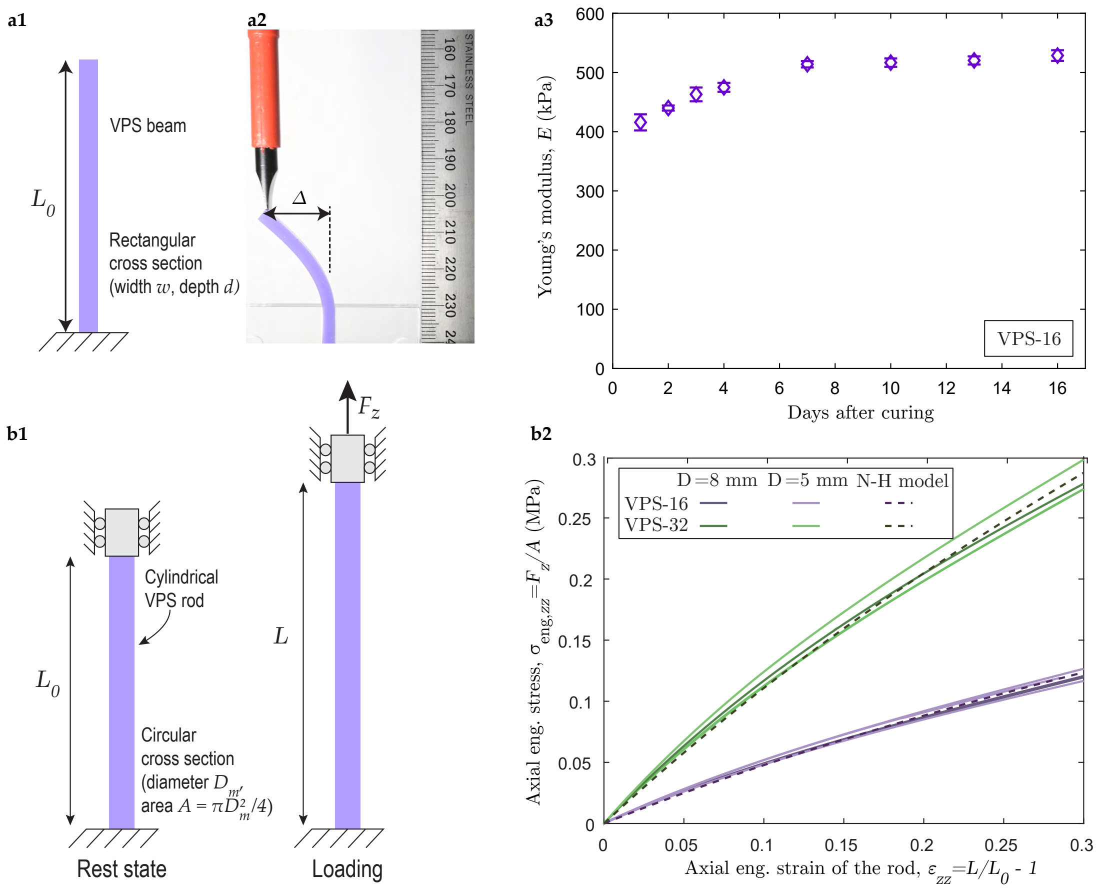

Figure 2.15: **Mechanical testing of the VPS-16 and VPS-32 rods. a1-a2**, Schematic diagram and a photograph of the resonance test on a vertically clamped VPS beam with a rectangular cross section; **a2** is at the initial moment of maximal deflection of the VPS-16 beam. **a3**, Evolution of the Young's modulus of a VPS-16 strip over 16 days. **b1**, Schematic diagram of the tensile test of the experimental VPS rods with a circular cross section in their rest state and their axially stretched state. **b2**, Engineering stress-strain curves (solid lines) of the cylindrical rods of different lengths and diameters (see legend). The dashed lines corresponds to the one-dimensional engineering stress-strain predicted for incompressible Neo-Hookean material; Eq. (2.22). The Figures in **b1-b2** were adapted from Ref. [78].

After a rest period of 7 days, we characterize the mechanical properties of VPS-16 and VPS-32 using a Universal Mechanical Testing Machine (Instron 5943) with cylindrical rods to determine the accurate material model for these elastomers. We performed the tests on rods of diameters $D = 5$ and $8\,\mathrm{mm}$, with a length chosen to preserve a constant aspect ratio $L_0/D_m = 20$; *i.e.* $L_0 = 100$ and $160\,\mathrm{mm}$, respectively. We measure the force F_z necessary to impose a distance $L > L_0$ between the rod extremities (see Figure 2.15**b1**) and relate the axial engineering stress $\sigma_{\mathrm{eng},zz} = F_z/A$ (where $A = \pi D^2/4$ is the cross-sectional area of the rod at rest) and the engineering strain $\epsilon_{zz} = L/L_0 - 1$. The corresponding experimental curves are reported in Figure 2.15**b2** (solid lines). As expected, no significant difference is observed between the two rod diameters. We then fitted each experimental curve with the one-dimensional engineering stress-strain prediction from the Neo-Hookean model for incompressible hyperelastic materials [91]:

$$\sigma_{\mathrm{eng},zz} = \frac{F_z}{A} = \frac{E}{3}\left(1 + \epsilon_{zz} - \frac{1}{(1+\epsilon_{zz})^2}\right). \tag{2.22}$$

Fitting the above expression to the experimental data yields the ground-state Young's modulus: $E = 520 \pm 0.02$ kPa for VPS-16 and $E = 1.25 \pm 0.05$ MPa for VPS-32. The dashed lines in Figure 2.15**b** correspond to Eq. (2.22) using the mean value of E across five experiments for VPS-16 and three experiments for VPS-32. The uncertainty corresponds to the standard deviation of the fitted parameter E across the different samples. The excellent match between the fitted material model and the tensile tests lets us conclude that the Neo-Hookean model is adapted to describe the VPS material. This information is important for rod modeling in Finite Element simulations described in Chapter 3.

2.5.2 Frictional Behavior of Powder-Treated VPS Surfaces

We observed that the Amontons-Coulomb friction could not describe the VPS-to-VPS contact; the tangential force F_t applied between the samples is not linearly proportional to the normal force, F_n, between them. However, in many real-life applications of filaments in frictional contact, the Amontons-Coulomb friction law is a reasonable description [92]. To ensure the Amontons-Coulomb friction throughout, we surface-treated our VPS rods by applying different types of powder, as described next.

The frictional behavior of the powder-treated VPS-16 and VPS-32 elastomers is characterized using an adapted version of the standard ASTM D1894-14 protocol [93], designed to measure the dynamic friction coefficient, μ, from the normal force F_n and tangential force F_t by the relation $F_\mathrm{t} = \mu F_\mathrm{n}$.

The original protocol involves a $60\times60\,\mathrm{mm}^2$ steel sleigh (self-weight: 213g) covered by a 1 mm thick VPS sheet which is dragged at a velocity of 3 mm/s on a second VPS layer of the same thickness (Figure 2.16**a** and **c1**). A calibrated weight imposes the normal force F_n between the two flat sheets of VPS on the sliding sleigh. The corresponding tangential force F_t is measured using a Universal Mechanical Testing Machine (Instron 5943). First, we explore two surface treatments applied on the VPS layers: talcum powder (Milette baby powder, Migros, Switzerland) and chalk powder (Sigma-Aldrich, Merck). The surfaces are conditioned with powder that was adsorbed by the VPS surface during 24 hours. Before each experimental run, the excess talcum powder was gently wiped off the surface with a fine cloth.

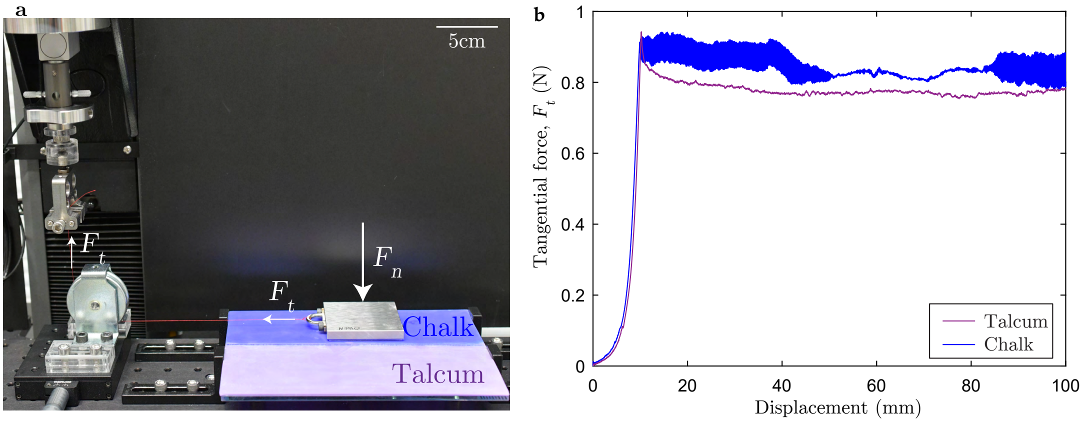

Figure 2.16: **Frictional behavior of powder-treated VPS surfaces.** **a**, Photograph of the adapted version of the ASTM D1894-14 protocol [93] to measure the friction coefficient between two surfaces. **b**, Characteristic curves for the measured tangential force, F_t, as a function of displacement, for talcum and chalk powder-treated substrates.

Figure 2.16**a** shows the setup with the sledge sliding on a chalk-treated path, next to a region on which talcum powder was applied. The typical curves for the measured tangential force, F_t, as a function of displacement for each type of surface treatment are plotted in Figure 2.16**b**. Since the talcum powder yields a ‘less noisy’ response than the surfaces treated with chalk powder, we choose to perform the experiments in Chapter 5 with talcum powder. We leave the quantitative characterization of the specific friction coefficient for the corresponding Chapter 5, Section 5.2.2.

We deactivate rod-rod friction by applying a few drops of liquid soap (Palmolive Original from Migros, Switzerland) in the contacting region (used in Grandgeorge et al. [78] and Chapter 4). The liquid soap generates a thin lubrication layer between the two rods, sufficient to reduce local tangential forces significantly. Care must be taken so that the soap layer does not dry and become sticky. An alternative solution is to apply a few drops of silicone oil (Bluesil 47V1000, Slitech, dynamic viscosity 1 Pa·s) to the contact regions. The disadvantage here is the swelling phenomenon of VPS in contact with silicon oil if the rod sample should be reused days after the application of the silicone oil [94].

2.6 Summary and Outlook

Due to the lack of an experimental toolbox to study tight physical knots (Section 2.1), the development of techniques and protocols described in this Section was extensive. An extra effort was put into the rod fabrication (Section 2.2); though the geometry of a straight elastomeric cylindrical rod seems trivial, their specialization to composite rods for compatibility with μCT-scanning involved a protracted process. We showed the high potential of X-ray micro-computed tomography combined with image-processing to study tight knot configurations in Section 2.3. We were able to extract the discrete centerline and contact information such that we could apply existing frameworks, *e.g.*, computing the Darboux vectors of the Cosserat frame or mapping the contact shape (as detailed in Section 2.4). Besides the geometric properties of the rods and the knot topology, the material properties were determined and a robust protocol to measure frictional contact properties was described in Section 2.5. The full toolbox will we applied in Chapter 4 and in Refs. [78, 62, 90, 37].

While developing the experimental toolbox, we learned of its capabilities, however, it also has its limitations. On the one hand, we are able to extract unprecedented experimental data from tight knots. On the other hand, we do not have access to local contact pressure or local strains in the rod. In addition, we understood the intricacy of the frictional contact behavior between VPS rods (Section 2.5.2); we found a surface treatment allowing a repeatable friction behavior between VPS surfaces. Unfortunately, the frictional case can only be achieved with one single friction coefficient. Understanding the impact of the friction coefficient will be crucial in the studies described in Chapters 5 and 6 as well as in Ref. [78, 37]. Consequently, we will introduce a computational toolbox in Chapter 3, which allows to accurately model tight knots, to gradually adapt the frictional behavior, and to give access to local stresses.

3 Methodology: Computational Toolbox

Knowing the capabilities and the limitations of the experimental toolbox described in Chapter 2, we aim to complement the mechanical and imaging experiments with numerical simulations. To this end, we develop a methodology to simulate knotted structures in filaments by employing the framework of fully three-dimensional (3D) Finite Element Modeling (FEM). The simulation allow us to access local stresses and strains, and study the influence of frictional rod contact in tangles and knots by systematically varying the friction coefficient. Since all the knot simulations start with straight rods, we first introduce the overall properties of the purely elastic rods as well as their specific features in Section 3.1. To show the potential of the numerical framework, we also describe the procedure to convert the solid rods to elastic tubes. Second, in Section 3.2, we focus on the numerical FEM procedure to tie knots. More specifically, we implement our simulation framework for the cases of open and closed trefoil, figure-eight and clove hitch knots. Moreover, the numerical results are validated against experiments using precise rod fabrication, mechanical testing, and tomographic imaging (introduced in Chapter 2, Section 2.3). In Section 3.2.2, we compare the numerical and experimental results to the theoretical prediction for open trefoil knots provided in [61]. Some of the following content is adapted from Refs. [62, 90, 37]. Throughout, we place more emphasis on the method that we have employed, rather than on the presentation and interpretation of results. Specific results will be discussed in subsequent chapters. Finally, in Section 3.3, the validated computational framework is used to test if the geometric centerline definition *minCS*, introduced in Chapter 2, Section 2.3.2, could be considered as equivalent to the well-defined material centerline. With this toolbox, we will be able to tackle the problems in the next Chapters by accessing local geometric and mechanical properties and tuning the friction coefficients.

3.1 Modelling of Elastic Rods and Tubes

Our simulation approach is based on the finite element method using nonlinear dynamic-implicit analysis in the commercially available software package `ABAQUS/STANDARD` [95]. The nonlinear dynamic-implicit option allows for obtaining the response by direct time integration, solving nonlinear equilibrium equations at time point $0 \leq t + \Delta t \leq T$, with the total step time, T. Importantly, we adapted the total time T of each step such that the nodes of the model were displaced with unit-speed, guaranteeing quasi-static behavior. By using the default automatic time stepping, the accuracy of the equilibrium solution is evaluated using the intermediate half-step residual error at time point $t + \Delta t/2$ [96]. Consequently, the time increment is increased or reduced by a factor of two in case of small or large error magnitudes, respectively [95]. We typically defined a small initial increment size (*e.g.* 10^{-3}), a maximum increment size of $\Delta t/T = 1/10$, and the smallest increment size as 10^{-15}.

To capture the geometrically nonlinear deformation of tight knots, the elastic rod is meshed with 3D solid elements of the type `C3D8RH`. The choice of the 8-node linear, hexahedral hybrid elements with reduced integration is motivated by the combination of the cylindrical geometry of the rods and the computational cost. As such, hexahedral elements are better suited to mesh cylindrical rod geometries than tetrahedral elements, allowing lower mesh density. Linear elements (instead of quadratic elements) were qualified as sufficient for more than 20 elements on the rod circumference. The hybrid nature of the elements is necessary to model the incompressible behavior of the elastomeric material.

The number of elements per cross section of the rod is typically between 50 and 100 (see meshed cross section in Figure 3.1**a1**). Along the axial direction, the discretization level varies depending on the aspect ratio of the rod to ensure that the elements maintain a regular cubic shape. Figure 3.1**a1** shows a part of the meshed rod with a node set (highlighted in red) defined along the axial direction at the outer rod surface. This node set acts like the eccentric fiber described in Chapter 2, Section 2.2.2. As described in Chapter 2, Section 2.4.1, these discrete coordinates, $\boldsymbol{\xi}(s_i)$, along the axial nodes i together with the material centerline nodes, $\boldsymbol{r}(s_i)$ (Figure 3.1**a2**), allow us to define the director vector $\hat{\mathbf{d}}_1(s)$ using Eq. (2.16). Then, the curvature of the deformed rods can be computed using the Darboux vectors (see Chapter 1, Section 1.2.2).

Here, we focus exclusively on elastic rods, as applied in Chapters 4 and 5. The elasto-plastic material model, used in Chapter 6, will be detailed in that corresponding Chapter. The rationale for this choice is twofold. First, the experimental results used to validate the simulations (presented in Section 3.2.2) were obtained using rods made out of vinylpolysiloxane (VPS-32,

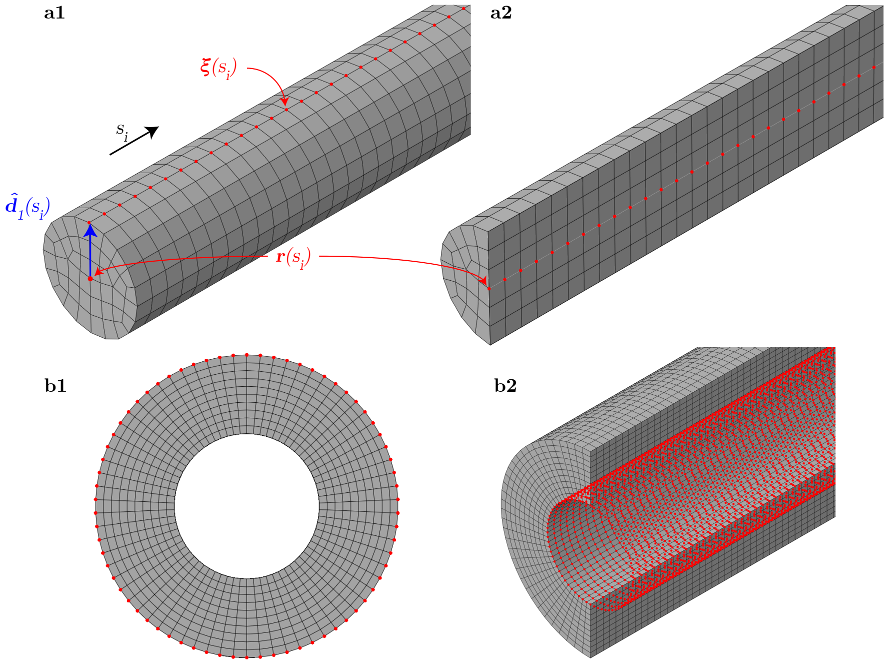

Figure 3.1: **Reference configurations of elastic rods and tubes in FEM. a1**, Elastic rod with a defined node set along the axial direction at the outer rod surface used for curvature calculations in Chapter 5 and in Ref. [37]. **a2**, Material centerline nodes, $\boldsymbol{r}(s_i)$. For better visualization, we show a longitudinal cut of the rod model. **b1**, View of the cross section of an elastic tube with radial meshing (used in Chapter 7). We highlight the nodes that form the outer rod surface. **b2**, Longitudinal cut along the tube with a visualization (red nodes) of the inner contact surface.

Zhermack), as described in Chapter 2, Section 2.2. Thus, modeling the elastomeric VPS material as a neo-Hookean incompressible solid (as detailed in Chapter 2, Section 2.5.1) permits us to have a direct map between the simulations and experiments for quantitative validation. Secondly, the focus on the elastic case allows us to emphasize the high-fidelity of the simulations in terms of the topological preparation protocol and the appropriateness of the frictional contact interactions without further complexifying the problem with additional constitutive ingredients.

Self-contact frictional interactions in the rod were taken into account by enforcing a normal penalty force combined with a tangential frictional force, with a prescribed dynamic Coulomb friction coefficient, $\mu = \bar{\mu} \pm \Delta\mu$. $\bar{\mu}$ denotes the average friction coefficient, and $\Delta\mu$, the standard deviation. Specifically, the *default basic Coulomb friction model* in `ABAQUS/STANDARD` [95] was applied, which are based on the concept that two contacting rod surfaces can carry shear stresses (through sticking) up to a certain magnitude before sliding occurs. The critical shear stress at the onset of sliding is defined as $\tau_{\text{crit}} = \mu p$, with the contact pressure p. Note that the simple implementation of the dynamic friction coefficient, measured experimentally (see Chapter 2, Section 2.5.2), was sufficient to achieve good agreement between the numerical simulations and experiments (as reported by Baek et al. [62]). Further, and as mentioned in Chapter 2, Section 2.5.2, we typically deal with either the frictionless case ($\mu = 0$) or the frictional case ($\mu = 0.30 \pm 0.02$, or $\mu = 0.35 \pm 0.02$, depending on the study) in experiments.

An adaptation of the full elastic rods is the introduction of a coaxial, cylindrical void. The resulting tube with a given wall thickness could be used to model a knotted tube system that transports a fluid through the internal channel, *e.g.* the biological system of a knotted umbilical cord (see Chapter 7, Section 7.2.2). In Figure 3.1**b1**, we show the cross-sectional view of the elastic tube model, on which we imposed a radial mesh. Various node sets can be defined, such that the outer tube surface (highlighted in Figure 3.1**b1**) and the inner tube surface which is visualized on the longitudinally-cut tube in Figure 3.1**b2**.

3.2 Procedure for Tying Elastic Knots

In this Section, we describe the strategy developed to tie the knot topology into the three-dimensional rods defined in their straight and undeformed reference state. Throughout the simulations, the extremities of the rod are kinematically tied to a pair of control nodes located at each end. The topology of the knotted rod is established by applying a sequence of prescribed displacements and rotations to these control nodes. We adopted a loading sequence from previous work on reduced FE modeling of knots [70].

In the subsequent Sections, we will describe the specific tying protocols for the knot topologies used in this Thesis. Specifically, we focus on the open and closed trefoil knots (studied in Chapter 4), the figure-eight knot (used in Chapter 5), and the sliding granny knot topology (investigated in Chapter 6).

3.2.1 Tying Process of the Open Trefoil Knot

The sequence of simulation snapshots presented in Figure 3.2 illustrates the tying process of an open trefoil knot, involving the following four steps (as reported in Ref. [62]):

(a) Firstly, we bend the rod into the configuration depicted in Figure 3.2**a**, while fixing the position of a pair of auxiliary nodes (denoted as x-shaped symbols in the figure) on the material centerline of the rod. At this stage, the extremities of the rod point to the negative x-direction.

(b) Secondly, the extremities of the rod were displaced inside the loop (see Figure 3.2**b**), now facing the $\pm z$-direction, thereby establishing the knotted configuration. During this second step, the positional constraints applied to the auxiliary nodes were still enforced so that those points lay on the xy-plane.

(c) Thirdly, we removed the imposed constraints on the auxiliary points to allow for the equilibrium configuration of the knot to be achieved (see Figure 3.2**c**).

(d) Finally, we tightened the knot (see Figure 3.2**d1-d3**) by continuously decreasing the normalized end-to-end shortening (introduced in Chapter 1, Section 1.5), $\bar{e}$, at the constant speed, $\dot{e} = -0.5\,\mathrm{mm/s}$, and measured the quantities of interest, including the tensile force, $T(\bar{e})$, and the configuration of the knot, $\mathbf{r}(s, \bar{e})$.

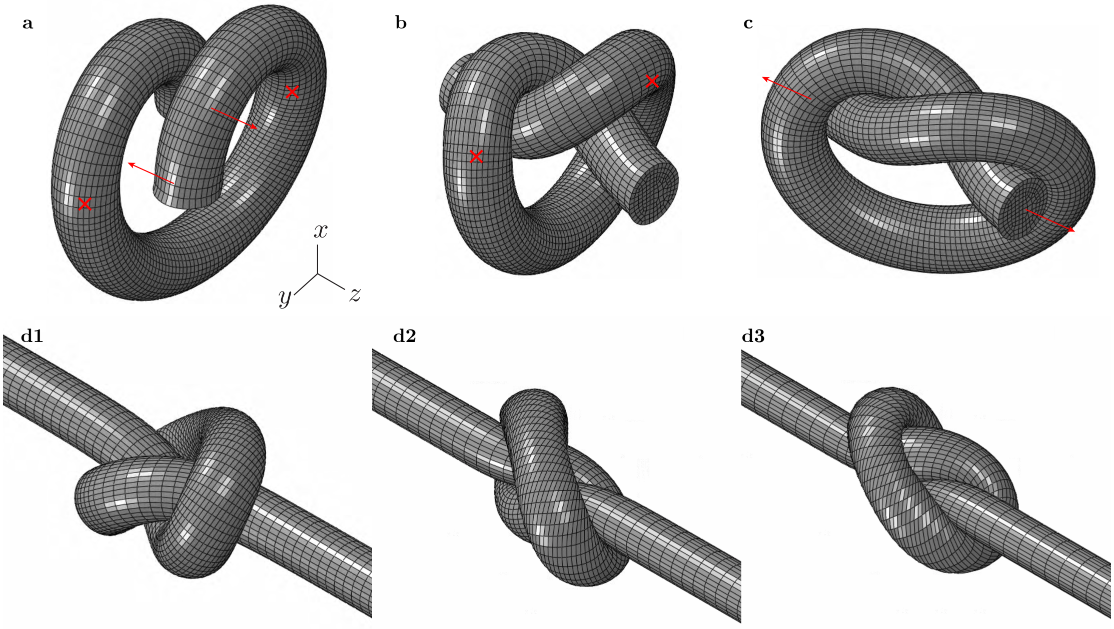

Figure 3.2: **Numerical protocol and pathing procedure to tie an open trefoil knot. a**, An originally straight rod is first bent to fix a pair of intermediary points (x-shaped symbols). Then, its extremities are pulled (red arrows) along the $\pm z$ directions. **b**, As a result, the topology of the knotted configuration is established. **c**, We then remove the positional constraints, formerly the x-shaped symbols in **a** and **b**, to obtain an equilibrium configuration. **d1-d3**, Having established the topology of the knot, we then tighten it by controlling the positions of the extremities to set a given value of the end-to-end shortening, e. Figure adapted from Ref. [62])

The typical computational cost for a full knot-tying simulations of an open trefoil knot, in which the normalized end-to-end shortening decreased gradually from $\bar{e} = 20$ to $\bar{e} = -10$ (in steps of $\Delta\bar{e} = 0.15$), is approximately 60 hours on a desktop workstation with an octa-core processor (Intel Xeon processor 6136 3.20 GHz) and 32 GB of RAM.

3.2.2 Validation of Numerical Model

We will validate the numerical protocol introduced above against precision experiments on the open trefoil knot, the details of which are provided next. To obtain the precision experimental data used for this validation, we measured the macroscopic mechanical response through the relation between the tensile force, T, and end-to-end shortening, e, and thoroughly quantified the coordinates of the centerline of the knotted polymeric rod.

Having introduced the computational framework for tying elastic open trefoil knots, we now quantify the applied tension required to tie this knot in the tight-knot regime. Here, we consider a rod with initial length, $L_0 = 350\,\text{mm}$. For comparison reasons with the data reported by Audoly et al. [61], we consider the dimensionless tensile force in the form, $\frac{TD^2}{4B}$. Note that the range of the values of end-to-end shortening considered in this tight regime is $-10 \le \bar{e} \le 30$, far below the threshold of validity of Eq. (1.8) ($\bar{e} \sim 500$), introduced in Chapter 1, 1.5.

In Figure 3.3**a**, we plot the dimensionless tensile force as a function of $\bar{e}$, from the experiments (dashed lines) and the FEM simulations (solid lines). The frictionless ($\mu = 0$; black lines) and frictional cases ($\mu = 0.3$; blue lines) of open trefoil knots are addressed and contrasted in both the experiments and simulations. The excellent agreement between the FEM results and the experimental data validates our numerical knot-tying procedure. By contrast, we observe a significant deviation between the numerical/experimental data and the prediction from Eq. (1.8), which assumes loose knots, regardless of whether friction is present or not. This discrepancy does not come as a surprise, given the significantly lower range of $\bar{e}$ that we have considered for our tight configurations compared to the regime of validity of the theory underlying Eq. (1.8). In Figure 3.3**b**, we present snapshots of three different configurations, **b1**, **b2** and **b3**, of the frictionless elastic knot ($\mu = 0$) from both experiments and FEM simulations, with $\bar{e} = \{-5, 5, 15\}$; the corresponding data points are presented by **B1**, **B2** and **B3** in Figure 3.3**a**.

Inspired by the success reported above in quantifying the tensile forces during knot-tying, we further quantify the shape of tight elastic open trefoil knots by contrasting the FEM simulations to precision X-ray micro-computed tomography. As detailed in Chapter 2, Section 2.3.2, the material centerline of the elastic knot, $\mathbf{r}(s)$, is digitized from the volumetric image acquired from the μCT, as well as from the FEM simulations. Again, we considered both the frictionless ($\mu = 0.0$) and frictional ($\mu = 0.3$) cases. The initial length of the rod was $L_0 = 130\,\text{mm}$, the initial diameter was $D_m = 8.3\,\text{mm}$, and the end-to-end shortening was $\bar{e} = 9.58$. The magnitude of the dimensionless curvature of the material centerline, $\kappa = KD$, is computed according to Eq. (1.7) (see Chapter 1, Section 1.2.3 and Chapter 2, Section 2.4.2), and plotted in Figure 3.3**c** and **d** as

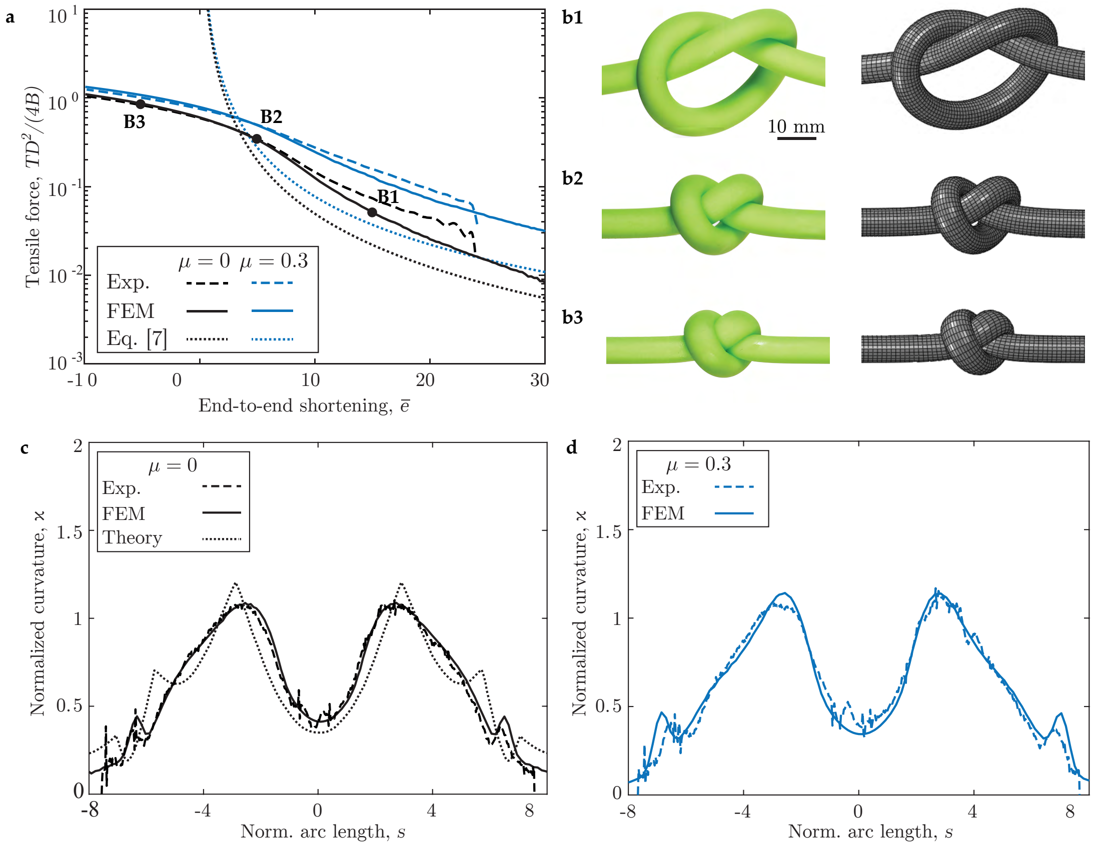

Figure 3.3: **Validation of the numerical model using the open trefoil knot configuration.** **a**, Normalized tensile force versus normalized end-to-end shortening for both frictionless ($\mu = 0$) and frictional ($\mu = 0.30$) elastic knots. The theoretical predictions (dotted lines) correspond to Eq. (1.8) from Ref. [61]. **b1-b3**, Snapshots obtained from the experiments (left) and FEM simulations (right) for open trefoil knots at different levels of tightness. The same points **B1**, **B2** and **B3** are marked in the plot in **a**. **c**, Profiles of the centerline curvature for an open trefoil knot with normalized end-to-end shortening, $\bar{e} = 9.58$, obtained from the FEM simulations (solid lines), the experiments (dotted lines), and the theoretical prediction from Eq. (1.8) (dashed line). The elastic rod onto which an open trefoil knot is tied has an initial length of $L_0 = 130\,\mathrm{mm}$ and a self-contact friction coefficient of $\mu = 0$. **d**, The same as in **c** but with a self-contact friction coefficient of $\mu = 0.3$.

a function of the dimensionless arc length coordinate, $s = S/D$. Again, an excellent agreement is found between the experiments (dotted lines) and FEM (solid lines), in both the frictionless (Figure 3.3**c**) and frictional cases (Figure 3.3**d**).

In Figure 3.3**c**, we also overlay the profile of the centerline curvature for the frictionless case (dashed line) predicted theoretically by the Kirchhoff rod model described by Eq. (1.8) in Chapter 1, Section 1.5 [61]. Surprisingly, the theoretical prediction yields a result that describes the experimental and simulation data remarkably well, albeit with small quantitative differences (the averaged difference in the curvature between the simulation data and the prediction is $\simeq 10\,\%$). Again, these deviations are expected, given the full 3D nature of our problem coupled to the fact that the theory in Ref. [61] was developed for loose knots, whereas we are considering tight configurations.

3.2.3 Tying Process of the Closed Trefoil Knot

The closed trefoil knot shares the same topology as its open counterpart, the previously described overhand knot. As described in more detail in Chapter 4, the numerical approximation to the ideal closed trefoil requires a length, L_0, to diameter, D_0, ratio of $L_0/D_0 = 16.37$ [97]. In FEM, multiple steps involving displacements and rotations are needed to tie an elastomeric rod into a *tight* closed trefoil knot. Given the application of this knot in Chapter 4 [90], we only focus on the frictionless case. The sequence of steps is shown in Figure 3.4, and described next:

(a) Firstly, we take the open trefoil configuration as the starting topology (see Figure 3.4**a**). The corresponding tying procedure is described in Section 3.2.1. The centerline mid-point node, located in the loop of the open trefoil knot, is fixed (denoted as x-shaped symbols in Figure 3.4). At this stage, the extremities of the rod face the $\pm x$-direction.

(b) Secondly, the extremities of the rod are displaced towards the $-y$-direction while being rotated by $\pi/4$ rad (see Figure 3.4**a**). The configuration shown in Figure 3.4**b** is achieved.

(c) The direction of the displacements of the extremities is changed to the $\pm x$-direction while the central centerline node is kept in place and the rotations at the extremities are continued (by $\pi/8$ rad). The resulting configuration is presented in Figure 3.4**c**. Note that the rod ends are not in contact. Since the 3D solid elements at the extremities are highly distorted at this stage, the knot cannot be closed with planar rod ends. A remedial approach is to add an intermediate step, in which we keep the extremities at their current position but remove the imposed constraint on the centerline mid-point node of the centerline.

(d) Figure 3.4**d** shows the relaxed state of the knot. To establish the closed knot configuration, we gradually bring the extremities of the rods in contact by applying a final rotation ($\pi/8$ rad) and displacement towards the $\pm x$-direction (see Figure 3.4**d**).

(e) The final equilibrium configuration of the closed trefoil knot is presented in Figure 3.4**e**. To prevent the extremities to have the rod diameter of the rest shape while the stretched rod is of a smaller diameter, the two extremities were constrained using the ABAQUS command `*COUPLING`. This enables the extremities to be displaced while allowing their cross-section to deform, thus allowing a constant rod cross section in the stitching region.

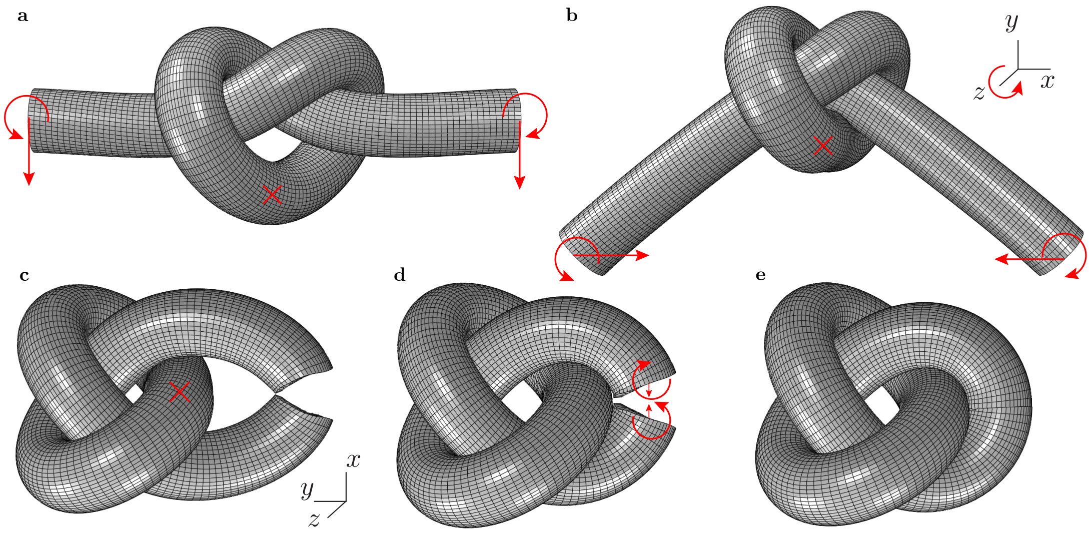

Figure 3.4: **Numerical protocol and pathing procedure to tie a closed trefoil knot.** **a**, The open trefoil knot forms the starting topology, on which we fix the centerline mid-point node. **b**, Aiming to bring the two extremities together, they are rotated and displaced. **c**, Then, the extremities are rotated and displaced to bring the rod ends close together, while preventing the rod ends from touching. **d**, Intermediate step releasing the fixed node in the loop. Then, a final rotation and displacement step allows bringing the extremities together. **e**, The closed knot topology is achieved in its equilibrium shape. The frictionless case is shown.

Since we are dealing with a closed knot, the mechanical response of the extremities is inaccessible experimentally. Consequently, the FEM model is validated by quantifying the shape of the tight elastic closed trefoil knot. Since this is part of the study on the shapes of physical trefoil knots in Ref. [90], we ask the reader to refer to Chapter 4 which contrasts the FEM simulations to precision X-ray micro-computed tomography on the closed trefoil configuration.

3.2.4 Tying Process of the Figure-Eight Knot

Another knot topology needed in Chapter 5 is the figure-eight knot. In Figure 3.5**a-d**, we present the sequence of four steps followed to tie this knot in FEM:

(a) Firstly, we bend a straight rod into the configuration depicted in Figure 3.5**a** while fixing the position of the centerline mid-point node (denoted as x-shaped symbols in the figure). At this stage, the extremities of the rod face the $\pm y$-direction.

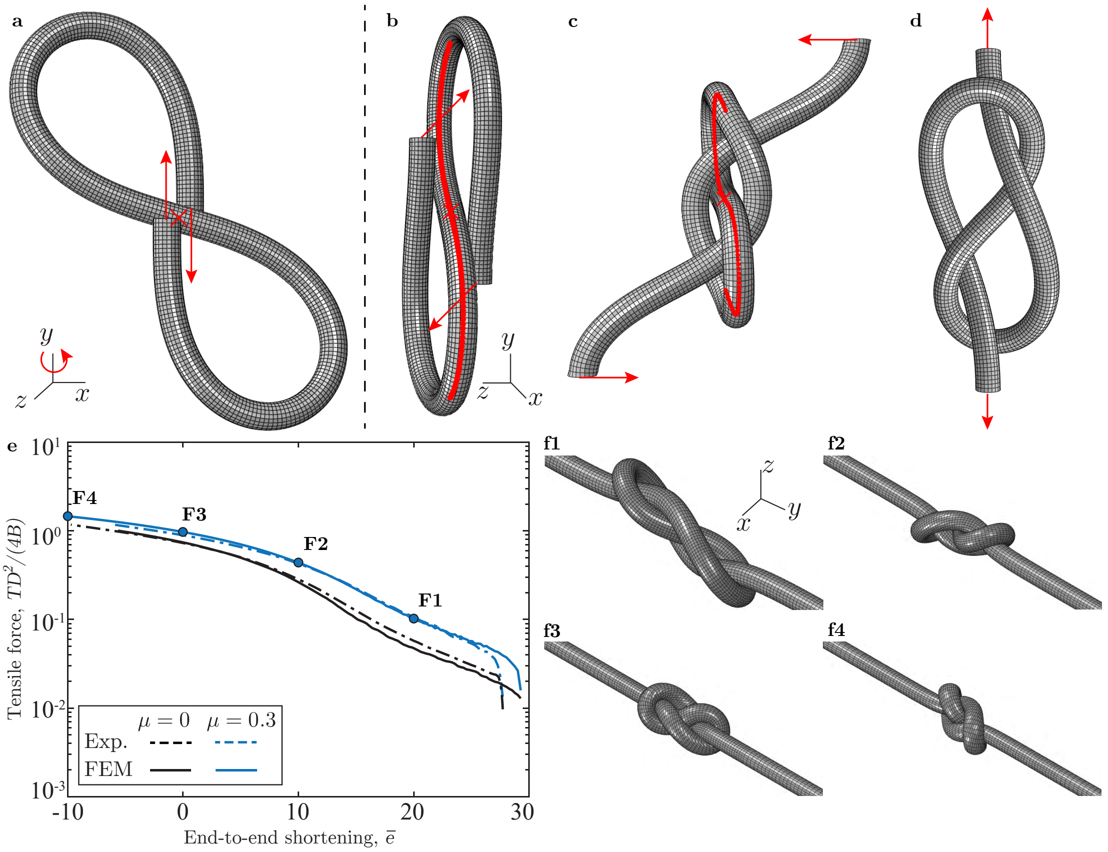

Figure 3.5: **Numerical protocol and pathing procedure to tie the figure-eight knot.** **a**, An originally straight rod is first bent while the centerline mid-point node is held in place. **b**, Preparation for the subsequent step by displacing extremities and fixing z-direction of the central centerline part (red line). **c**, By passing the extremities through the two loops, the figure-eight knot topology is established. **d**, Final alignment of extremities and all the fixed nodes are released to achieve the depicted equilibrium configuration. **e**, Validation of the numerical model by comparing the tensile force versus end-to-end shortening between FEM and experimental data (frictionless and frictional case). **f**, Snapshots of the configurations for consecutive values of the normalized end-to-end shortening, $\bar{e} = \{20, 10, 0, -10\}$. The corresponding data points, labeled as **F1**, **F2**, **F3** and **F4**, are indicated in **e**.

(b) Secondly, the extremities are displaced further in the $\pm y$-direction to be positioned well for the next step. In addition, the z-direction is fixed of the central part of the centerline $-L_0/4 < s < L_0/4$, shown as a red line in Figure 3.5**b**.

(c) Thirdly, to establish the knotted configuration, the extremities are displaced inside the respective loops (see Figure 3.5**b-c**) in the $\pm z$-direction, still facing the $\pm y$-direction.

(d) Finally, we align the two extremities by displacing them in $\pm z$-direction (see Figure 3.5**d-e**). At this stage, the fixed position of the central centerline node and the fixed z-direction of the central part of the centerline are released. Consequently, the equilibrium configuration of the loose figure-eight knot is achieved, as shown in Figure 3.5**d**. Having tied the figure-eight topology, the knot can be tightened by pulling on the extremities in the $\pm y$-direction.

In Figure 3.5**e**, we provide the mechanical response of the figure-eight knot with friction coefficients $\mu = \{0, 0.3\}$, plotting the dimensionless tensile force as a function of the dimensionless end-to-end shortening. The range of the end-to-end shortening explored in the FEM simulations is $-10 \leq \bar{e} \leq 29.5$. The corresponding experimental results for the same parameters are also included. The rod in the rest configuration has length $L_0 = 350\,\mathrm{mm}$ and diameter $D = 8.3\,\mathrm{mm}$. In Figure 3.5**f**, we present four representative configurations of the FEM knot for $\mu = 0.3$ and $\bar{e} = \{20, 10, 0, -10\}$. The data points corresponding to each configuration in Figure 3.5**f** are located on the loading curve in Figure 3.5**e** and denoted as **F1**, **F2**, **F3** and **F4**. Again, the agreement between the FEM and the experiment is remarkable for both the frictionless and the frictional cases, further confirming the validity and high-fidelity of our FEM knot-tying approach.

3.2.5 Tying Process of the Sliding Granny Knot

In Chapter 6, we will study sliding knot topologies and, more specifically, the sliding granny knot, which forms the basis during suturing. A similar tying protocol has been introduced in Sano et al. [37] in the context of the clove hitch knot. Both knots share the same topology but differentiate by their application: a clove hitch knot attaches a rod to a rigid cylinder (typically multiple times larger than the rod diameter), whereas the sliding granny knot is a binding knot, connecting two rods (of equal diameters). Here, we will make use of the tying algorithm used in Ref. [37], which only needed minor adaptations to tie the sliding granny knots in Chapter 6. To distinguish between the two rods in the subsequent description of the tying process, we denote the straight underlying rod as *cylinder* (in accordance with Ref. [37]) and the rod winding around the cylinder as *rod*. Next, and in Figure 3.6, we present the sequence of 6 steps followed to tie the sliding granny knot in FEM:

(a) Firstly, we place the center of mass of the rod above the rigid cylinder (Figure 3.6**a**).

(b) Secondly, the centerline mid-point is fixed and the two extremities are displaced to form an arch (Figure 3.6**b**).

(c) Thirdly, three points of the centerline are fixed, and the two extremities are moved horizontally to wrap the rod around the cylinder (Figure 3.6**c**).

(d) Next, the rod extremities are displaced upwards while fixing three node positions, one in the middle and the other two underneath the cylinder (Figure 3.6**d**).

(e) While fixing the three nodes of the previous step, the middle point is displaced upwards, and the two rod extremities are threaded underneath the opened gap to attain the clove hitch/sliding granny knot topology (Figure 3.6**e**).

(f) Finally, all nodes are released, except for the two rod extremities, which are loaded by two forces of the same magnitude but in opposite directions to yield a symmetric knot (Figure 3.6**f**).

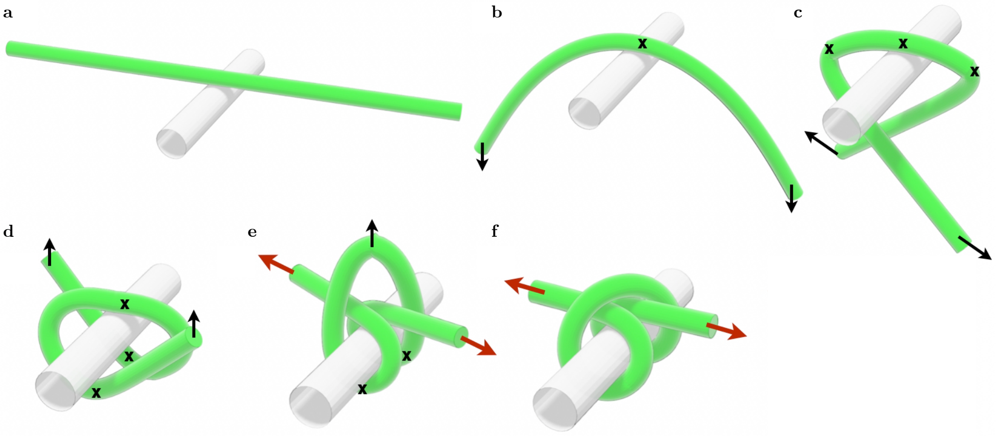

Figure 3.6: **Numerical protocol and pathing procedure to tie the clove hitch / sliding granny knot topology.** Nodes marked with **x** are fixed, whereas black and red arrows correspond to displaced and loaded nodes, respectively. **a**, Initial configuration involving a cylinder (gray) and a rod (green). **b**, Fixed centerline mid-point with displaced extremities such that the rod forms an arch. **c**, Three nodes of the rod centerline are fixed, and the extremities are displaced to wrap the cylinder. **d**, The extremities are displaced upwards while two fixed nodes hold the configuration in place. **e**, The centerline mid-point of the rod is pulled upwards, giving space to thread the extremities underneath the opened gap. This step establishes the topology of the clove hitch / sliding granny knot. **f**, All the fixed nodes are released, and a symmetric load is applied to the two rod extremities. Figure adapted from Ref. [37]

We refer the reader to Ref. [37], which contains a detailed validation of the numerical model based on the mechanical response and the curvature profiles.

3.3 Comparison Between *minCS* and *matCL*

In Chapter 2, Section 2.3.3, we describe the experimental protocoldeveloped for the extraction of the geometric centerline from CT data of a 2D rod (Figure 2.12). Since we did not consider cross-sectional deformation, the described algorithm *minCS* yielded identical centerline coordinates to the material centerline. Here, we consider a tight open trefoil knot tied in an elastic rod to test how the *minCS* algorithm handles more complex cases (*e.g.* normalized curvatures, $\kappa D > 1$, and cross-sectional deformation of the rod) by comparing the geometric centerline coordinates to the material centerline.

We choose to use the Finite Element data of a deformed rod since the nodal centerline definition (described in Section 3.1) gives access to the accurate material centerline. We aim to apply the *minCS* algorithm on a data set describing the outer rod edge. To this end, we developed the following procedure. First, a tight open trefoil knot is tied in FEM with normalized end-to-end shortening of $\bar{e} = e/D_m = -20.3\text{mm}/8\text{mm} \approx -2.5$. Second, a point-cloud (80′000 spatial points) describing the outer rod nodes is extracted from FEM. Given the symmetry of the knot, it is sufficient to only consider one-half of the rod. In Figure 3.7**a1**, we show the cut-off location on the full rod, resulting in the configuration depicted in Figure 3.7**a2**. Moreover, this change simplifies the case study by avoiding contact interactions.

A triangulated mesh is generated in Matlab, connecting the various vertices forming polygons. The Matlab function `Polygon2Voxel` is applied on these polygons, yielding a voxelized volume, as shown in Figure 3.7**a3**. This volume is created by choosing 1000 pixels in each of the three spatial directions. The largest direction (vertical distance in Figure 3.7**a2** is 43 mm) sets the spatial resolution which is $d_0 = 43\,\text{mm}/1000\,\text{px} = 43\,\mu\text{m}$ (size of the voxels). This value is close to the typical range of resolutions encountered in CT scans of knotted and tangled configurations (25 to 35 μm, see Section 2.3.1). This choice allows us to keep the post-processing parameters unchanged from the ones used in analyzing experimental knots and tangles.

Next, we apply the previously described *minCS* algorithm to the FEM-based open trefoil configuration and extract the geometric centerline coordinates. Regarding the material centerline coordinates, this information is readily available through the nodal information in FEM. In Figure 3.7**b1** and **b2**, we plot the 3D centerline coordinates for two different perspectives. We observe that in the region of high curvatures, the geometric centerline (purple line) tends to point radially toward the *inside* of the loop, compared to the material centerline (black dots). We quantify this difference in Figure 3.7**c** and **d**. First, we compute the normalized shortest distance $\bar{d} = d/D_m$, with the dimensional shortest distance, d, between the two sets of centerline coordinates (see Figure 3.7**c**). Indeed, the geometric centerline nearly coincides with the material one in the initial straight rod part and deviates by less than 6% in the curved part. The sub-resolution (below the voxel size defined by the spatial resolution) is represented by the shaded region and is bounded by the dashed horizontal line of $\bar{d} = d_0/D_m = 0.54\%$, with d_0 being the spatial resolution of the voxelized volume. Second, in Figure 3.7**d**, we show the curvature profiles along the arc length for both centerline sets. The curvature is computed

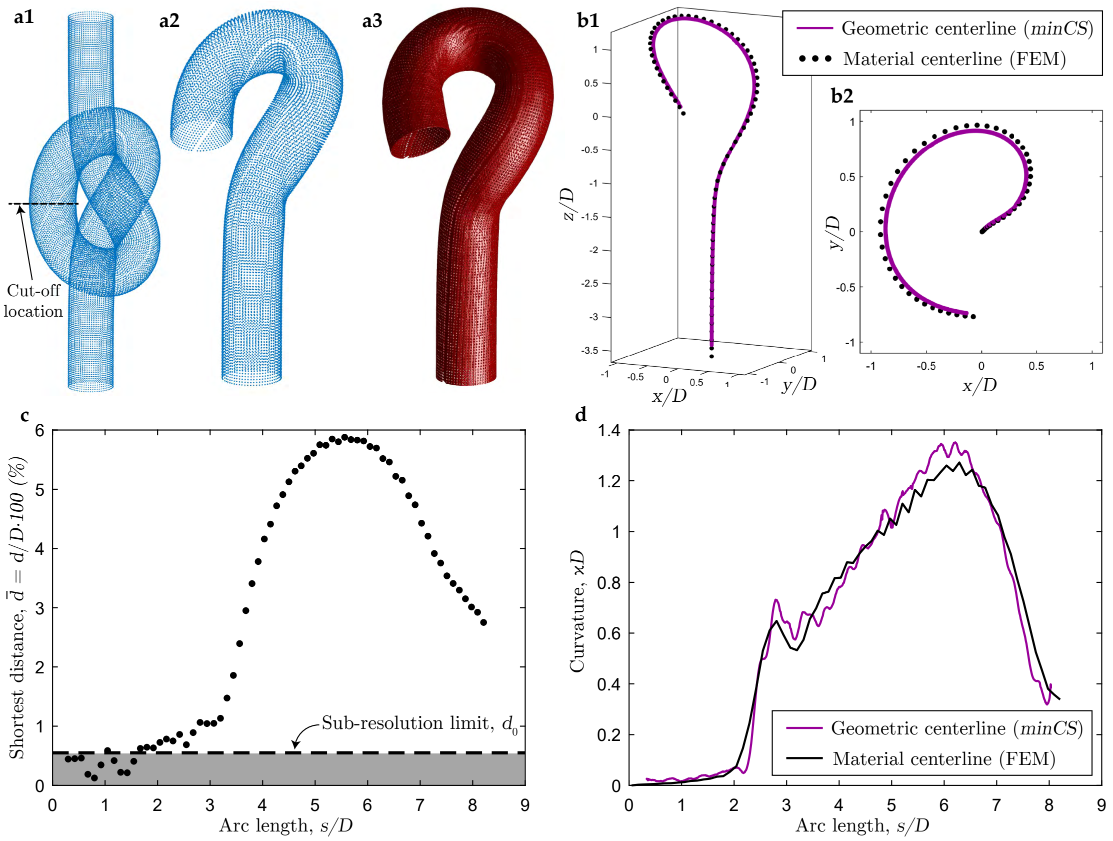

Figure 3.7: **Comparison between material and geometric centerline coordinates using FEM on a tight knot. a1-a3,** Procedure to convert a FEM-based point-cloud of the outer surface of the rod of an open trefoil knot into a voxelized volume (only considering half of the rod). **b1-b2,** 3D visualization of the rod centerline coordinates (material centerline vs. geometric centerline) in a side and a top view. **c,** Shortest distance δ between the two centerline curves as a function of the arc length s. The sub-resolution is shown by the shaded region and delimited by the horizontal dashed line. **d,** Curvature profiles of half of the tight open trefoil knot for both centerline definitions. The discrete curvature is computed following the method based on vertices by Bergou et al. [39], as discussed in Chapter 1, Section 1.2.3. and Chapter 2, Section 2.4.2

for the material as well as the geometric centerline with the same method based on vertices, as derived by Bergou et al. [39] (see Chapter 1, Section 1.2.3 and Chapter 2, Section 2.4.2). Both profiles are qualitatively similar, however, the geometric centerline tends to yield slightly higher curvatures (≈ 5%) in the bent region of the rod.

The case study investigated in this Section allows us to conclude that the geometric centerline definition *minCS* and the material centerline yield similar centerline coordinates and curvature profiles for small and moderate rod deformations. In the case of tight knots involving regions of normalized curvatures above unity, we expect a ≈ 5% deviation. This discrepancy should be considered when comparing centerline properties between FEM (based on the material centerline nodes) and processed CT data if we have to sidestep to the geometric centerline *minCS*.

3.4 Summary and Outlook

In this Chapter, we have presented a 3D FEM procedure to investigate tight elastic knots, with variable frictional contact interaction between the rods. The rods are modeled to give access to important geometric and mechanical properties, *e.g.*, centerline coordinates, director vectors, surface and contact information, as well as reaction forces (Section 3.1). We also described an adaptation of the rod to model knotted tubes. As illustrative examples, we focused on the tight configurations of the open and closed trefoil knots (Chapter 4), the figure-eight knot (Chapter 5), and the sliding granny knot (Chapter 6). In Section 3.2, we showed that an elaborated sequence of prescribed displacements and rotations to control nodes could set numerous knot topologies. Our numerical results were found to be in excellent agreement with precision model experiments while showing deviations from an existing 1D theory for loose elastic knots [61] (Section 3.2.2). Finally, in Section 3.3, our experimentally validated computational framework was used to quantify the difference between a geometric centerline definition and the material centerline, applying experimental image-processing tools previously developed in Chapter 2, Section 2.3.2.

For the subsequent Chapters, the versatility of the numerics will be of great importance to exploring large parameter spaces and to rationalize underlying mechanisms in physical knots. More specifically, we will make use of the methodology described above in the following settings:

- FEM allows for achieving perfectly slippery contact interactions. In Chapter 4, we will study **frictionless** knots to compare them to ideal geometric rod models, which do not include friction. In this context, the FEM also constitutes a way to verify if the equilibrium shape of the experimentally-tied knots is achieved using the soap lubrication technique (described in Chapter 2, Section 2.5.2).

- To evaluate the effect of the friction coefficients on the capsizing mechanism in Chapter 5 and the surgical knot strength in Chapter 6. A **friction sweep** in the experiments is challenging [98] and can be obviated by leveraging FEM.

- The **contact pressure** between rods in contact is an important mechanical property in physical, and especially in tight contact (see Grandgeorge et al. [78]). In knots, Finite

Element Modeling allows the extraction of contact pressure maps for various tightness. In Chapter 4, the contact pressure will be used to understand local elastic constrictions in the cross sections at the entrance and exit points of trefoil knots. Moreover, in Chapter 6, the importance of plastically deforming suture filaments will be rationalized thanks to the access to local contact forces between two rods in tight contact. We leave the description of the modeling of plastically-deforming filaments for Chapter 6.

- Extraction of contact forces enables the computation of **internal tensions**. This quantity was crucial to explain the functionality of the clove hitch knot, transforming high tension in a rod down to zero (see Sano et al. [37]).

Even though the Kirchhoff rod model is not applicable for tight elastic knots, we were able to numerically model tightly knotted rods in 3D. The convincing validations of the Finite Element Model with experimental data allow us to emphasize the high-fidelity of the simulations in terms of the topological preparation protocol, the material model, and the appropriateness of the frictional contact interactions. The experimental capabilities (Chapter 2) combined with this computational framework form a sophisticated and powerful toolbox to study tight, complex knots with different physical ingredients and practical relevance in the subsequent chapters.

4 From Ideal to Elastic Knots: The Shapes of Physical Trefoil Knots

In this Chapter, we perform a compare-and-contrast investigation between the equilibrium shapes of physical and ideal trefoil knots, both in *closed* and *open* configurations. Ideal knots are purely geometric abstractions for the tightest configuration tied in a perfectly flexible, self-avoiding tube with an inextensible centerline and undeformable cross-sections [99, 100]. Here, we construct physical realizations of tight trefoil knots tied in an elastomeric rod, and use X-ray tomography and 3D finite element simulation for detailed characterization. Representative examples are provided in the experimental photographs and FEM-snapshots of Figure 4.2. Specifically, we evaluate the role of elasticity in dictating the physical knot's overall shape, self-contact regions, curvature profile, and cross-section deformation.

The text and figures in this Chapter are adapted from the published manuscript in Ref. [90], which resulted from a collaboration with Paul Grandgeorge, Changyeob Baek, Tomohiko G. Sano, John H. Maddocks and Pedro M. Reis.

Firstly, we will focus on the *closed* trefoil knot, given its advantage of having a closed centerline with periodic boundary conditions; in particular, no external forces are required to attain equilibria. In its tight equilibrium configuration, we will show that the 2D mapping of the contact *surface* in the physical knot can be rationalized using the double-contact *lines* first computed by Carlen et al. [100] within the purely geometric model, forming an accurate outer skeleton for the contact surface patch observed in the elastic case. Secondly, we will study tight configurations of the *open* trefoil knot, where different levels of tightness can be systematically investigated by the application of a range of external forces, thereby elucidating the effects of elasticity. Our measured curvature profiles for knotted elastic filaments, both in the closed and open trefoils, are qualitatively different from those predicted by the ideal geometric models. Specifically, physical open knots exhibit curvature peaks inside the knot, instead of at their entrance/exit, contrary to previous predictions for the tightest ideal knot [99].

The excellent FEM-experimental agreement confirms the observed curvature profiles and enables us to extract and map the contact pressure distribution, thereby revealing significant rod constrictions at the entrance and exit of the tight open knot. Finally, we will characterize these regions of localized elastic deformation, which we speculate could act as precursors for the weak spots that compromise the strength of knotted filaments.

The structure of this Chapter is as follows. The motivation of this study is presented in Section 4.1, along with a literature review on the ideal shapes of closed and open trefoil knots in Section 4.1. In Section 4.2.2, we detail the fabrication procedure of our elastomeric rods, and the experimental protocol followed to knot them into *open* and *closed* trefoil configurations. In this Section, we also detail the procedure for image processing of the tomographic data to extract the relevant geometric data. Then, in Section 4.2.2, we present the corresponding numerical knot tying framework, where we compute the equilibrium shape of elastic open and closed trefoil knots using fully 3D finite element simulations. We ask the reader to refer to the detailed protocol descriptions in the Chapters 2 and 3 for further information on the methodologies of rod fabrication, volumetric imaging, and finite element simulations. In Section 4.3, we perform a detailed comparison between the ideal and the equivalent elastic closed trefoil knot. We then focus on the open trefoil configuration by contrasting ideal knot results to tight physical knot configurations in Section 4.4. We also discusses the potential role that localized deformation regions may have in acting as precursors for structural weakness spots. Furthermore, in Section 4.5, we detail on the topological feature, called homotopy, which is observed in the physical closed trefoil knot. Finally, in Section 4.6, we summarize our findings and provide a perspective for future work.

4.1 Literature Review and Motivation

The open trefoil knot, commonly known as the overhand knot, is the most elemental open knot, forming the basis of many, more complex, and functional knots. It is ubiquitous in practical applications, including fishing, climbing, sailing, and tying of shoelaces. The trefoil knot can be regarded as a building block in bend knots (*e.g.*, the fisherman's/English knot) [101], in binding knots (*e.g.*, square or reef, and granny knots) [76, 27], and in noose knots (lasso noose, honda knot, lariat loop) [22]. The classic overhand knot is also key in suturing procedures; *e.g.*, the surgeon's knot) [102, 24, 25, 103, 104, 72]. Overhand knots can form spontaneously in various natural contexts, across a wide range of length scales, from polymers and DNA strands [10, 11, 12] to the umbilical cord of human fetuses [16], and even in vortex loops in plasma and fluid flows [13, 14, 15].

The classic *mathematical theory of knots* is largely concerned with all possible topologies of knots tied in a closed loop, with no particular concern for any particular geometric configuration. For example, an unknot is any configuration of a closed loop that can be smoothly deformed to a circle without passing through itself. But any shape of a closed trefoil knot cannot be smoothly deformed to the circle, so it has a different topology; trefoil knots are in fact the simplest nontrivial knot type. Configurations of closed trefoil, or trinity, knots are also a common theme in Celtic art.

Ideal shapes: Recently, a mathematical literature of the *geometry* of so-called ideal knot shapes has developed, see e.g. Carlen et al. [100]. In this context, a knot is modeled as being tied in a closed loop of idealised rope approximated as a filament with an undeformable circular cross-section, and inextensible centerline (and vanishing bending stiffness so the problem has no mechanics only geometry). Within this geometric context, the ideal, or tightest, shape is the centerline configuration of the given knot type with shortest length L_0 (for prescribed cross-section diameter D_0, otherwise the problem is invariant under dilations). Ideal shapes are known to exist for all standard knot types [49] with centerlines that are $C^{1,1}$ curves, which means that the centerline has a continuously varying unit tangent at every point, and a curvature that is defined almost everywhere, but *not* everywhere. In particular, the curvature can be discontinuous.

For example a straight line segment joined to an arc of a circle with matching tangents, but a discontinuous curvature, can form part of an ideal shape, and numerics strongly suggest that straight line segments and discontinuities in curvature do arise in ideal shapes, for example on composite knots [105] (Knowing the fine detail of the precise smoothness or regularity of ideal knot shapes is important in designing good numerical algorithms to approximate them.). Unsurprisingly, the ideal shape of the unknot is a circle of circumference $L_0 = \pi D_0$. Surprisingly, the unknot is the only knot for which the ideal shape is known explicitly; all other ideal knot shapes have only been approximated numerically. (Other, comparatively simple, piece-wise planar, ideal shapes are known in the case of knotted *links*, *i.e.* knots with multi-component centerlines [51, 78], but we will not consider links here.

The ideal closed trefoil knot: Numerical approximations to the ideal closed trefoil are available, computed with a variety of algorithms, with the most accurate shape currently available probably being that provided by Przybyl *et al.* [97], with $L_0/D_0 = 16.3722\ldots$. The computed value of L_0/D_0 is a rigorous (to machine arithmetic precision) upper bound to the actual ideal value, and very probably the upper bound is rather close to the actual, unknown ideal value. However, rather than comparing many digits of accuracy in the ideal value of L_0/D_0 we seek to compare *features* of computed ideal trefoil shapes with both experiment and FEM simulation, which include a combination of elastic effects of bending and deformation of cross sections.

The first conditions for ideality of knot shapes were derived in Gonzalez and Maddocks [105] in terms of the *global radius of curvature*. Technically, these results depended on the slightly too strong assumption of a C^2 centerline. Extensions to the weaker and sharp hypothesis of a $C^{1,1}$ centerline were obtained in [106]. The necessary conditions that must be satisfied on an ideal shape include the three-way alternative that every point along an ideal centerline must be either part of a straight segment, or local curvature must achieve its maximal value $2/D_0$ (as is the case everywhere for the circular ideal shape for the unknot), or be at one end of a locally minimal distance, or contact, cord of length D_0 between two points on the centerline. The computations described in Carlen et al. [100] strongly suggested that for the ideal closed trefoil each point along the centerline was in fact at the end of *two* distinct contact cords, so that *double* contact arises at each point, and, moreover, that at some points the maximum local curvature of $2/D_0$ was additionally attained. However, no straight segments arise for the ideal trefoil knot case. These observations were confirmed and better visualized on improved simulation data, as fully described in Ref. [107, 108], from where we reproduced images in Figure 4.1, which we describe next in more detail.

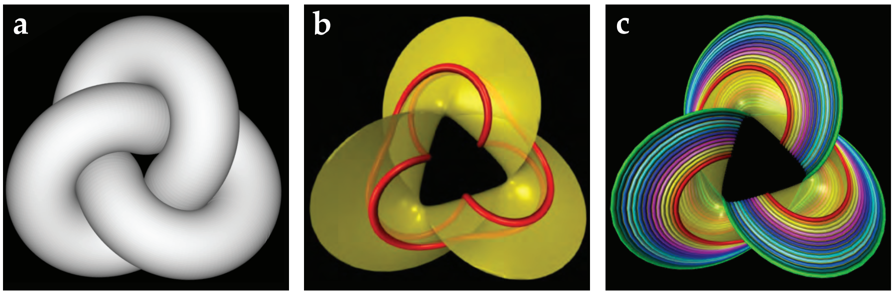

Figure 4.1: **3D Visualizations of the ideal closed trefoil knot**. (Adapted with permission from [107, 108].) **a**, a solid tube visualization, which obscures the inner structure of the one-parameter family of contact chords shown as a translucent yellow surface in panel **b**, at a slightly larger scale. The sharp edge of the surface is the centerline of the knot. The red curve traced out by the center points of the contact chords is the contact set where the tube of panel **a** touches itself. The contact curve can be seen to itself be a trefoil knot by the smooth homotopy from the contact curve (red) to knot center line (green) illustrated in panel **c**, where each of the non-intersecting multi-coloured closed curves lies on the yellow contact surface.

For the ideal closed trefoil, visualized as a solid tube in Figure 4.1**a**, each point along the tube centerline is in fact at the end of *two* distinct contact chords. The double-contact feature is present along the full arc length of the trefoil knot, which means that there is a one-parameter family of double contact chords which trace out a surface in 3D, as shown in Figure 4.1**b**, where the sharp edge of the translucent yellow surface is the centerline curve of the ideal trefoil shape. The 3D contact set for the ideal trefoil is a closed curve lying on the surface of the tubes visualized in Figure 4.1**a**, but is obscured. This contact line is also traced out by the mid-points of the contact chords (red curve in Figure 4.1**b**). The contact curve can be seen to itself be a trefoil knot by the homotopy illustrated in Figure 4.1**c**, where there is a family of non-intersecting multi-coloured closed curves that deform along the contact surface from the contact curve (red) to the knot center line (green).

Analogous double-contact phenomena had previously been reported for infinite double helices, depending on the pitch angle [109, 59], and in an ideal orthogonal clasp problem [58, 78]. Maritan et al. [110] and Ref. [109, 59] also showed that in an optimal packing problem, single helices frequently arise with both double contact cords and maximal curvature, and that the associated critical aspect ratio of this special helix arises for the C_α carbons in α helical segments of protein crystal structures. Thus the observed phenomena of double contact cords with additionally maximal curvature, is perhaps not as exceptional as it might first appear.

The ideal open trefoil knot: Ideal shapes of *open* knots can also be defined. Here, both the diameter and a (long) arc length of the filament are prescribed, and the ideal shape for a given knot type arises for the configuration with the maximal distance (in space, not arc length) between the two ends of the filament. This is a mathematically well-posed notion of open ideal configurations, which also closely corresponds to the physical process of tying a knot in a rope; one ties the knot and then pull the two ends apart until the knot is tight. For the unknot, the ideal configuration has a straight centerline, and the distance between the two ends is the arc length of the filament. However, for any nontrivial knot there must be an end shortening, *i.e.* a reduction in the maximal possible distance between the ends, with it to be expected that the more complicated the knot, the larger the end-shortening.

This sense of ideal shape for the open trefoil was first simulated by Pieranski et al. [99, 65]. These authors also sought to relate the equilibrium shape of a knotted filament to the decrease in its mechanical strength, induced by the knot itself. They reported peaks in the curvature profile, as a function of arc length, at both the entrance and exit points of the knot. Consequently, it was hypothesized that the weakening of knotted filaments was rooted in these geometric features. This observation has also been corroborated at the atomic scale by Saitta et al. [10], who performed molecular dynamic simulations on knotted polymer strands. These computations pointed to a strain-energy localization at the entrance and exit to the open trefoil knot. However, more recent studies by Uehara et al. [111] and Przybył and Pierański [112] have indicated that the ideal rope model may not be appropriate to describe the *mechanical* properties of *tight* physical knots. Whereas recent studies have addressed the mechanics of *loose* overhand knots [61, 63, 64], the mechanics of the corresponding *tight* configurations remains largely unexplored.

Research questions: Overall, we aim to answer the question if the ideal geometric model could act as a scaffold to (fully or partially) describe the shape of physical knots, including elasticity. In this context, we will answer the following questions:

- Which key features in simple knots are not captured by the purely geometric rods? And vice versa, which purely geometric characteristics are smoothed by the presence of elasticity?
- Are curvature peaks observed at the knot entrance (as reported by Pierański et al. [65]) of elastic knots? if not, in which rod segments does the curvature profile reach its maximum value in physical knots?
- How is the double-contact line feature from ideal knots translated in a purely elastic knot system?
- Beyond curvature, what could be the source of structural weakening at the entrance and exit points of the knot?

4.2 Physical Realization of Trefoil Knots

We have devised an experimental framework and performed FEM simulations to realize tight physical knots tied on homogeneous, intrinsically straight, elastic rods. In this section, we describe the methodology that we followed on both fronts.

4.2.1 Experimental Protocols

Fabrication of customized elastic rods: We fabricated composite elastomeric rods with the goal of making them compatible with μCT imaging and 3D image analysis to extract their centerline coordinates and self-contacting regions. We used the fabrication protocol described in Chapter 2, Section 2.2. The fabrication of composite elastomeric rods made out of vinyl polysiloxane, VPS32 were decorated with an elastomeric concentric physical fiber, an eccentric inset, and an elastomeric coating. In this Chapter, the inset fiber allowed us to match the twist of the glued extremities when fabricating the *closed* trefoil knot. Finally, the elastomeric rods of total diameter $D_0 = 8.5\,\mathrm{mm}$ were then cut to different values of their total length of L_0, depending on the system of interest.

Tying of open trefoil knots: We tied open trefoil knots on the fabricated rods. Any build-up of excess twist at the free ends was avoided by carefully aligning the eccentric fiber at the extremities during the manual tying process. The knot was progressively tightened by increasing the end-to-end distance while the sample was immersed in a container of soapy water (Palmolive Original) to ensure vanishing friction conditions. The limited size of the sample holders of the μCT apparatus required rods of different undeformed lengths: $L_0 = 185\,\mathrm{mm}$ or $125\,\mathrm{mm}$, respectively, for the looser or tighter open knot configurations detailed next. Pierański *et al.* [99] computed the normalized knot length, Λ_{OC} (the engaged knot length divided by the tube diameter), corresponding to the normalized difference between the arc lengths of the centerline associated to the first (entrance) and last (exit) contact points, s_2 and s_1, respectively. Both the μCT scanning and the FEM provide access to Λ_{OC}. We chose two elastic configurations, one looser ($L_0 = 185\,\mathrm{mm}$, $\Lambda_{\mathrm{OC}} = 127.5/D_0 = 15.0$) and the other tighter ($L_0 = 125\,\mathrm{mm}$, $\Lambda_{\mathrm{OC}} = 85.9/D_0 = 10.1$) than the tightest ideal open trefoil knot ($\Lambda_{\mathrm{OC}} = 12.4$) [99]. The elastic open trefoil knot with $\Lambda_{\mathrm{OC}} = 10.1$ is shown in Figure 4.2**b1**.

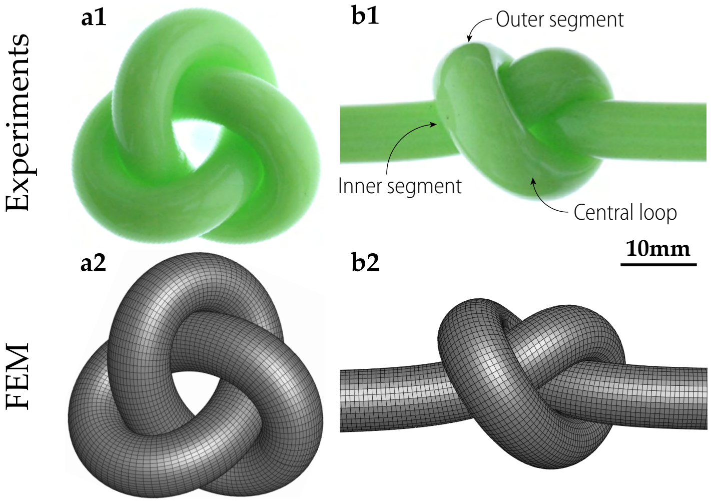

Figure 4.2: **Elastic *closed* and *open* trefoil knots in experiment and FEM. a1**, Experimental photograph of a closed trefoil knot tied on an elastomeric rod with length-to-diameter ratio $L_0/D_0 = 16.37$ ($L_0 = 139.1\,\mathrm{mm}$ and $D_0 = 8.5\,\mathrm{mm}$). **a2**, Numerical counterpart of **a1** computed from FEM. **b1**, Experimental photograph of a tight, open trefoil knot tied on an elastomeric rod. **b2**, Numerical counterpart of **b1** computed from FEM.

Tying of the closed trefoil knot: To compare the elastic closed trefoil knot and its ideal equivalent (results in Section 4.3), we trimmed the elastic rod according to the length-to-diameter ratio computed by *e.g.* Carlen *et al.* [100]. For these experiments, our undeformed elastic rod of diameter $D_0 = 8.5\,\mathrm{mm}$ had a length of $L_0 = 16.37 D_0 \approx 139.1\,\mathrm{mm}$ dictated from the geometric model. The physical closed trefoil knot was tied by first producing an open trefoil knot and then joining the two rod extremities using a silicone adhesive (Sil-Poxy, Smooth-On). During this closure procedure the eccentric fibers at each end were aligned at the joint location, which appeared to closely correspond to minimizing any additional, imposed, excess twist. Also, note that this tying procedure does not necessarily yield the lowest energy state, however, the determination of the relations between twist, Writhe and internal energy was outside of the scope of this study, and therefore not evaluated further. The closed knot was placed in an ultrasonic bath (VWR, USC1200TH) with a water-soap mixture (Palmolive Original, ≈20% in volume) for five minutes (at frequency 45 kHz and temperature 22 °C). The combination of the ultrasonic vibrations and lubrication by the soap minimized frictional effects in the regions of self-contact (ensuring the absence of tangential surface stresses there), in agreement with the assumption of frictionless self-contact of idealized rods. Figure 4.2**a1** shows an optical photograph of the final physical closed trefoil knot.

Post-processing of μCT images: We quantified the 3D geometry of the knotted rods using μCT imaging (μCT100, Scanco Medical), with spacial resolutions (voxel size) of 24.6 μm or 16.4 μm for the open or closed knot configurations, respectively (see Chapter 2, Section 2.3.1). The algorithm for subsequent post-processing of the tomographic images is described in detail in Chapter 2, Section 2.3.2 and Section 2.4.3. The computation of the discretized curvature of the rod centerline is according to Bergou et al. [39], and described in Chapter 1, Section 1.2.3. Further, the regions in the μCT images corresponding to the thin uniform outer coating layer of Solaris were segmented to reveal the regions of self-contact. The individual contact points on the rod surface are shown in Figure 4.3**a1** and **a2**.

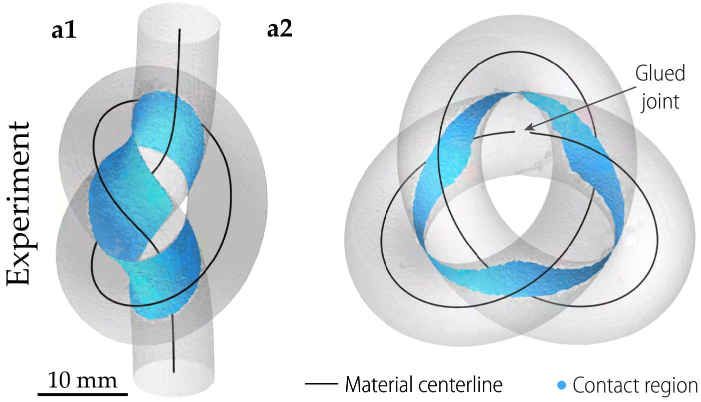

Figure 4.3: **Methods to realize and analyze the elastic *open* and *closed* trefoil knots. a1**, Rendering of the reconstructed μCT-data of an experimental open trefoil knot with a normalized knot length $\Lambda_{OC} = 85.9/D_0 = 10.1$. **a2**, Rendering of the reconstructed μCT-data of the elastic closed trefoil knot with a length-to-diameter ratio of $L_0/D_0 = 16.37$.

4.2.2 Finite Element Simulations

We used the finite element method (FEM, ABAQUS STANDARD 6.14-1, Simulia, Dassault Systems 2014) to simulate the tying of the same knots realized in the experiments. These experimentally validated simulations yield information that cannot be accessed directly through experiment; *e.g.*, the pressure field in the regions of self-contact. Contrariwise, the close agreement between the two (see results in Figure 4.4, 4.5, and 4.6) serves as a verification that the experimental configurations are, indeed, the equilibrium ones, with no additional significant experimental artifact.

The FEM computations were performed using the procedure described in Chapter 3, involving a dynamic-implicit analysis to capture the geometrically nonlinear deformation of the closed trefoil knot. The number of elements per cross-sectional area was 120 and 190 for the open and closed knots, respectively. The mesh size along the axial direction of the rod was chosen such that the aspect ratio of the elements was close to unity.

Firstly, we established a configuration of the open trefoil knot based on the knot-tying procedure described in Chapter 3, Section 3.2.1 (see Figure 3.2). Then, we gradually brought the extremities of the rods in contact to establish the closed configuration, as detailed in Chapter 3, Section 3.2.3 (see 3.4).

4.3 Ideal Versus Elastic *Closed* Trefoil Knots

We proceed by quantifying the similarities and dissimilarities between physical and ideal *closed* trefoil knots, with the analogous discussion of the *open* case appearing in the next section. A closed knot offers the advantage of having a closed centerline curve with matching periodic boundary conditions; its configuration is not subject to external factors such as applied external forces. As the experimental material is elastic, a trefoil knot can be tied in tubes with a wide range of aspect ratios of L_0/D_0 of undeformed centerline length to undeformed cross-section diameter. Cases with L_0/D_0 large would correspond to loose knots as considered in [61, 63, 64]. Cases with L_0/D_0 small would require large extension just to be able to close the centerline to form the knot, with associated large tensions, and presumably associated large cross-sectional deformation. A systematic study of dependence on a range of chosen values for L_0/D_0 is beyond the scope of the current work. Instead we chose the single critical value $L_0/D_0 = 16.37$, which is a good approximation to the smallest value known to be possible in the ideal geometric theory with an inextensible centerline and undeformable cross-section (and no bending stiffness). We would expect the resulting experimental equilibrium configuration to be relatively tight, and with relatively small centerline extension and cross-sectional deformation. After a closed trefoil is tied on the physical elastic rod (with undeformed rod length $L_0 = 139.1\,\mathrm{mm}$ and cross-section diameter $D_0 = 8.5\,\mathrm{mm}$), the observed stretch of its centerline is 1.070 in experiment and 1.082 in FEM-simulation. The overall length-to-diameter ratio of the stretched rod, L/D, was measured to be 18.12 and 18.53 in experiments and FEM-simulations, respectively. To further compare our results with those of the ideal geometric theory, we take the observed small axial strain into account by using the normalized and rescaled arc length $s = S/L \times L_0/D_0$, with the stretched rod length, L, and the ideal normalized rod length $L_0/D_0 = 16.37$, while also assuming that the axial strain is constant along S.

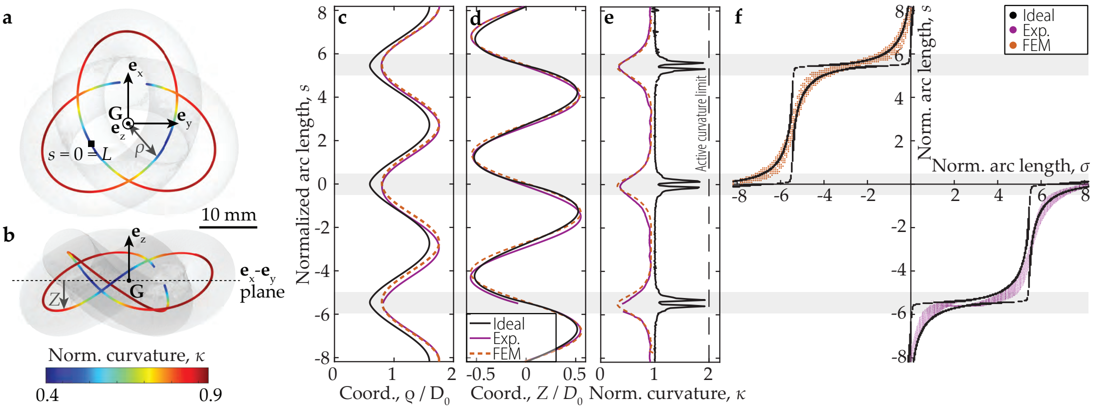

Figure 4.4: **Ideal versus elastic closed trefoil knots.** **a**, **b** Top and side views of the 3D reconstruction of the experimental closed trefoil knot, including the barycenter of the closed centerline curve, **G**, and the radial and vertical centerline coordinates, ρ and Z respectively. The normalized centerline curvature, $\kappa(s) = KD_0$, is represented by a color-map on the centerline curve. **c**, Comparison of the normalized radial centerline coordinate $\rho/D_0 \equiv \sqrt{X^2+Y^2}/D_0$. The three arc lengths S are individually normalized and rescaled such that $s = S/L \times L_0/D_0$. The shaded areas indicate the inner segments. **d**, Comparison of the normalized vertical centerline position $z = Z/D_0$. **e**, Normalized curvature profile for the ideal and elastic case, including the active curvature limit at $\kappa = KD_0 = 2$. The black solid line (ideal) data are reproduced from Ref. [100, 107]. **f**, Contact map showing the characteristic double contact in the ideal case, and the filled area of the equivalent elastic case (experiment and FEM).

To perform a comparison between the *centerline coordinates* $\mathbf{r}(s) = (X(s), Y(s), Z(s))$ of the elastic and the ideal closed trefoil knots, we introduce (following Ref. [100]) cylindrical coordinates in the Cartesian basis $\{\mathbf{e}_x, \mathbf{e}_y, \mathbf{e}_z\}$, as shown in Figure 4.4**a** and **b**. The knot lies flat on the $\mathbf{e}_x$-$\mathbf{e}_y$-plane, and the origin is chosen by the condition that the center of mass, or barycenter, of the centerline curve $\mathbf{G} = \sum_{i=1}^{N} \mathbf{r}(s_i)\delta s_i/L$ lies on the $\mathbf{e}_z$-axis. (Here, N is the number of discretization points, L is the stretched rod arc length, and δs_i is the length of the ith segment between two successive discretized centerline points.) In Figure 4.4**c**, we compare the radial distance between the centerline and the barycenter axis, quantified as $\rho(s) \equiv \sqrt{X^2(s)+Y^2(s)}$, for the experimental, FEM and ideal knot cases (with three individually scaled arc lengths on ordinate, but all plots with the same common length scale on abscissa). The experimental and FEM data are in excellent agreement. Compared to the ideal knot, the experimental and FEM closed knots exhibit a radial inflation, presumably due to elasticity effects, as evidenced by the horizontal offset of the ρ data. For example, ρ/D_0 differs by 0.20 and 0.16 in the inner segments (minima; shaded) and the outer segments (maxima of ρ/D_0 curves), respectively. Moreover, the effect of the cross-sectional deformation is reflected in the amplitude of ρ for the elastic knot which is $0.95\,D_0$ (D_0 for the ideal case). To complete the comparison of the cylindrical coordinates, in Figure 4.4**d**, we present the rescaled vertical centerline coordinate, $Z(s)/D_0$, for the three cases, which, interestingly, shows an excellent match between the ideal and the elastic closed knots, unlike the ρ data presented in Figure 4.4**c**.

Based on the μCT and FEM data, we construct a two-dimensional contact map; the projection of the contact surface onto the arc length s vs. arc length σ plane. To assemble this contact map, each point in the contact surface is assigned to the two closest centerline positions of the knotted rod, at arc lengths s and σ. In Figure 4.4**f**, we plot the contact map for the ideal case [108] (black solid lines), together with the corresponding data extracted from μCT and FEM. Note that by construction the arc length contact map is point-symmetric with respect to $s = \sigma = 0$ [108]. Consequently, due to this symmetry, we only present one half of the μCT and FEM contact data, respectively in the lower-right and upper-left quadrants of the $s-\sigma$ plot in Figure 4.4**e**. We observe that, whereas, for the ideal knot, there are precisely two contact points σ_1 σ_2 for each s value, the physical knots exhibit an extended contact region with a range of σ values for each s value. Moreover, we find that the contact set for the physical knot is a surface that lies fully inside the double contact lines (black lines) of the ideal closed trefoil knot; the geometric model acts as an outer outer skeleton for the elastic case. This filled (areal) contact region for the physical case, replaces the double-line contact in the ideal knot (see Section 4.1) due to cross-sectional deformation. The mismatch between the ideal and the elastic cases is particularly evident in the inner segments; there, the corners of the geometric contact set are not filled in the elastic case.

In Figure 4.4**e**, we plot the *curvature profiles* of the elastic and the ideal trefoil knots. The curvature data are also presented in Figure 4.4**a** (see color-map), along the centerline of the experimental case. The elastic knot exhibits plateaus in the three outer segments with average normalized curvatures of $\kappa = KD_0 \approx 0.93$ (whereas $\kappa \approx 1.00$ for the ideal knot). Despite these close values in the outer segments, the behavior in the inner segments is strikingly different between the elastic and ideal cases; the elastic knot exhibits clear curvature minima, whereas the ideal model predicts twin curvature peaks approaching the active curvature limit $\kappa = 2$, separated by a local minimum [100]. We hypothesize that this difference in curvature profiles between the two cases is rooted in the cross-section deformations allowed in 3D elasticity, which we address further in the next section, in the context of the *open* trefoil knot.

4.4 Ideal Versus Elastic *Open* Trefoil Knots

The *open* trefoil knot allows us to directly control the level of tightness by applying forces to the rod extremities, to study the role of elasticity more systematically. This feature is not possible in the closed case since the extremities are, naturally, '*glued*' together. We will employ the experimental and numerical toolbox that we developed for the *closed* trefoil knot to explore the similarities and dissimilarities between the elastic open trefoil knot and the corresponding ideal case [99, 65].

In Figure 4.5**a**, we present the 3D reconstruction of an experimental open trefoil knot (normalized knot length of $\Lambda_{\mathrm{OC}} = 10.1$), with the measured normalized curvature profile, $\kappa(s) = KD_0$ superposed onto the centerline. This curvature profile is qualitatively similar to what we observed in Section 4.3 for the physical, closed trefoils, with minima at the inner segments (region ② in Figure 4.5**a**). In Figure 4.5**b**, we plot the experimental and FEM-computed $\kappa(s)$ profiles for the two elastic knots that we investigated, with normalized knot lengths of $\Lambda_{\mathrm{OC}} = 10.1$ and 15.0. By way of example, we describe the physical knot with $\Lambda_{\mathrm{OC}} = 10.1$, referring to the features labeled in Figure 4.5**a** and **b** while traveling along arc length (increasing s). Soon after the knot entrance (① in Figure 4.5**a**), the vanishing curvature of the almost straight elastic rod rises to a local maximum, in the central region of the inner segment (② in Figure 4.5**a**). The transition of the rod from the inner to the outer segment has a curvature drop, followed by an abrupt rise. The normalized curvature then reaches its maximum value in the outer segment (③ in Figure 4.5**a**). In this high-curvature region, we find that $\kappa > 1$ over a wide range of s due to cross-sectional deformation of the elastic rod. Eventually, there is a local curvature minimum at the central part of the loop (④ in Figure 4.5**a**).

The curvature profile of the ideal open trefoil knot in its tightest configuration ($\Lambda_{\mathrm{OC}} = 12.4$) obtained by Pieranski *et al.* [99] is also shown in Figure 4.5**b**, superposed onto the elastic profiles for comparison. There are important qualitative differences between the ideal and elastic results. For example the prominent curvature peaks occur at different locations and with different shapes between the two cases, a difference that can be attributed to elastic deformation of the cross-sections and the centerline.

In Figure 4.5**c**, we map the contact region for elastic knots with $\Lambda_{\mathrm{OC}} = 10.1$ and 15.0 (blue and green regions, respectively), extracted from the μCT and FEM data. For the experiments, the full contact region in the $s - \sigma$ space is plotted, whereas, to aid comparison, only the outer boundaries of the contact regions are shown for the FEM data (dashed lines). Again, FEM and experiments are in excellent agreement. Naturally, the contact map of a self-contacting rod is symmetric with respect to the $s = \sigma$ axis. Indeed, if contact occurs at the centerline arc

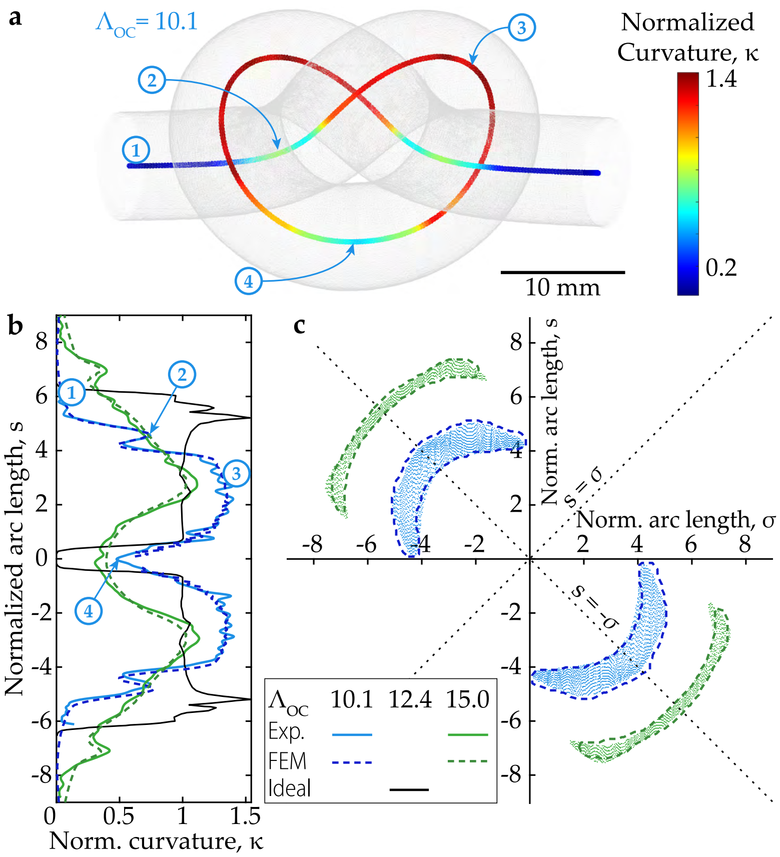

Figure 4.5: **Ideal versus elastic open trefoil knots. a**, Reconstruction of an experimental open trefoil knot with $\Lambda_{\mathrm{OC}} = 10.1$. The centerline of the knot is overlaid by the color-map of the normalized curvature profile $\kappa(s) = KD_0$. The following features are referred to in the text: (1) knot entrance, (2) inner segment, (3) outer segment, and (4) central loop. **b**, Normalized curvature profiles. Experimental (solid colored lines) and numerical data (dashed colored lines) for two normalized knot lengths Λ_{OC}={15; 10.1} compared to the geometric description according to Pierański *et al.* [99] (thin black line). The arc length S is normalized such that $s = S/D_0$ **c**, Contact regions mapped into the $s-\sigma$ space: μCT data (filled area) and FEM data (dashed lines, only the region boundaries are shown). The normalization of the arc length S is $s = S/D_0$ and $\sigma = S/D_0$.

length $s = a$ with the arc length $\sigma = b$, then it also occurs at $s = b$ with $\sigma = a$. Moreover, the symmetric nature of the overhand knot about $s = 0$ introduces the axis of symmetry $s = -\sigma$ on its contact map.

From the simulations, we extracted data for the contact pressure (normal traction) at the regions of self-contact. In Figure 4.6**a**, we present a snapshot of the elastic knot with $\Lambda_{\mathrm{OC}} = 10.1$, including the contact regions onto which we superpose the contact pressure (normalized by the Young's modulus E). The contact pressure map is shown in Figure 4.6**b**, using a similar representation (in the $s-\sigma$ space) used in Figure 4.5**c** for the contact map. The highest contact pressure is found along the entire central region of the contact set, with maximum characteristic normalized values of $p/E \approx 0.44$. Note that the knot entrance/exit (shaded regions in Figure 4.6**b**) correspond to regions of localized pressure, aligned perpendicularly to the rod centerline. To further quantify the localization of deformation along the knot, in Figure 4.6**c**, we present measurements of the circumferential contact set width profile $L_c(s)$, normalized by the total perimeter of a rod cross-section at arc length s. We observe sharp peaks of L_c at the inner segments ($-4.8 \lesssim s \lesssim -3.8$ and $3.8 \lesssim s \lesssim 4.8$), where up to 90% of the circumference of the cross-section is in self-contact. The regions of pronounced contact pressure (Figure 4.6**b**) in combination with the sharp circumferential contact width peaks (Figure 4.6**c**) lead to localization of high contact pressure in a narrow region with a small range of arc lengths. Consequently, as shown in Figure 4.6**d**, where we quantify the profile of deformed cross-sectional area as a function along the centerline of the rod, the cross-section of the inner rod segment is elastically constricted by up to ~ 63% compared to its rest cross-section area; such localized constrictions in knots are typically referred to as *nip* regions [22].

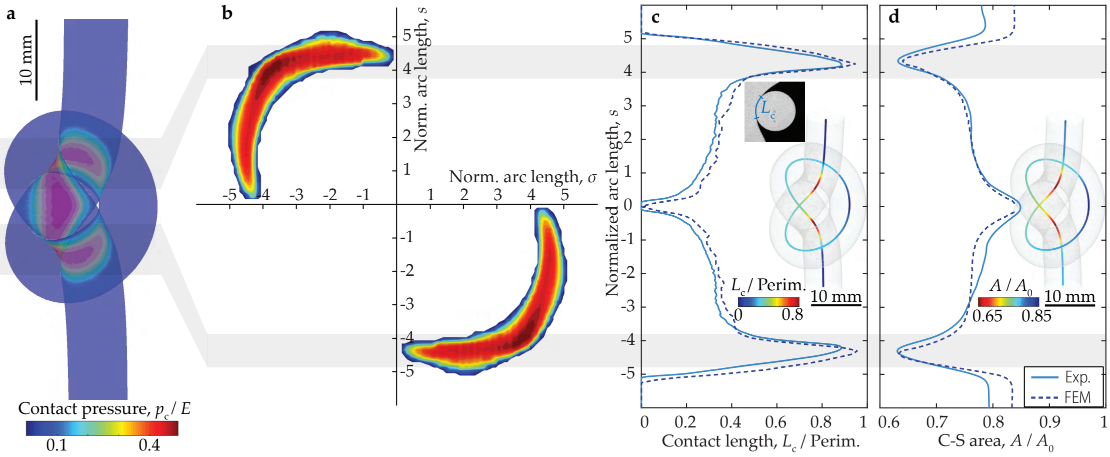

Figure 4.6: **Constriction at the entrance and exit of elastic tight open trefoil knots.** **a**, Numerical FEM contact pressure on the 3D knot of the tight configuration ($\Lambda_{OC} = 10.1$). The shaded regions indicate the inner segments at the knot entrance/exit. **b**, Numerical contact pressure map for tight configuration ($\Lambda_{OC} = 10.1$). The normalization of the arc length S is $s = S/D_0$ and $\sigma = S/D_0$. **c**, Circumferential (μCT- and FEM-data) contact set width L_c along the arc length, showing clear peaks at the entrance/exit of the knot. **d**, Cross-sectional area (μCT- and FEM-data) along the arc length, normalized by the cross-sectional area of the undeformed rod. The quantities plotted both in **c** and **d** are also represented on the respective insets, using a color-coded centerline of the 3D reconstruction of the knot.

4.5 Homotopy in the Physical Closed Trefoil Knot

Motivated by the known homotopy between the contact line and the knot centerline for numerically simulated, geometrically ideal, configurations of the closed trefoil knot (see Section 4.1 and Figure 4.1) we provide sequence of a three-dimensional rendering constructed from the μCT data for the physical closed trefoil knot in Figure 4.7. The knotted elastomeric rod (VPS32), shown in Figure 4.7**a** has a rest length $L_0 = 139.1$ mm and rest diameter $D_0 = 8.5$ mm ($D_0/L_0 = 16.37$). After locating the centerline of the knotted rod (black curve), as well as its self-contacting surface (blue surface), we extract the rim of the contact surface (red curve) in Figure 4.7**b**.

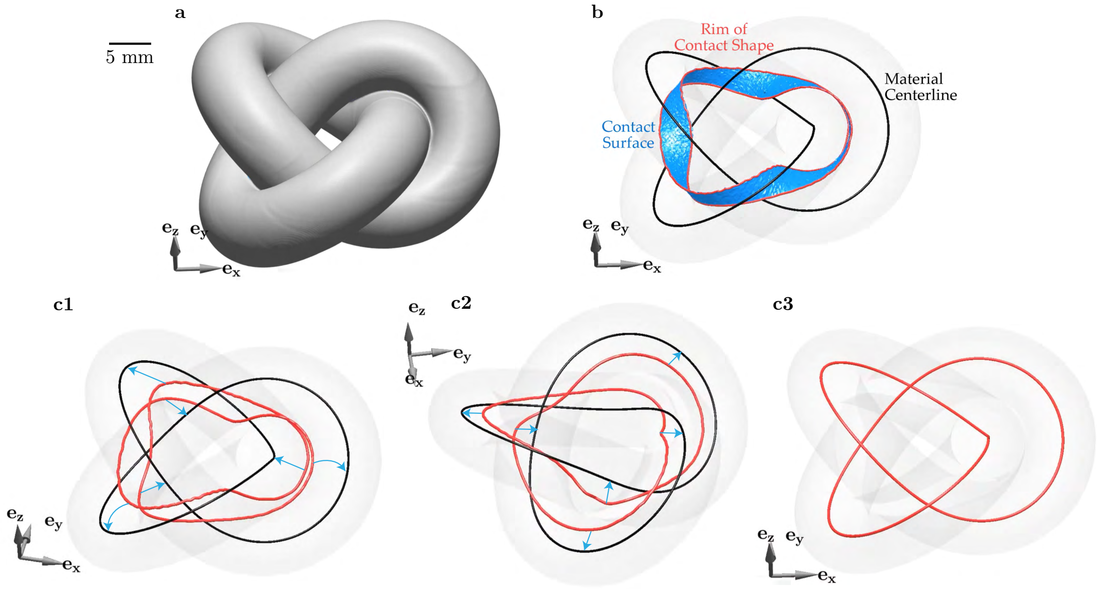

Figure 4.7: **Homotopy between the centerline of the physical closed trefoil knot and the rim of its contact shape.** **a**, 3D-visualization of the physical closed trefoil knot constructed from μCT data. **b**, Image-processing of the composite rod allows to get access to the material centerline (black curve) and the contact surface (blue region). Also, the rim (edge) of the contact shape is determined (red curve). **c1-c3**, Gradual morphing of the rim of the contact shape towards the material centerline reveals that the rim of the contact shape shares the same topology as the closed trefoil knot.

Without undergoing self-crossings (fixed topology), the rim of the contact surface is smoothly morphed into the rod centerline, thus revealing the homotopy between the rim of the contact shape and the rod centerline. To perform this morphing, we first parametrized the rim of the contact shape as $\mathbf{R}(s^*)$, where s^* is the arc length along the rim (of total length L_R). The intermediate morphing curve, $\mathbf{w}(s)$, ranges from the rim curve to the centerline curve (parametrized as $\mathbf{r}(s)$), following the parametrized deformation $\mathbf{w}(s) = (1-t)\,\mathbf{R}(s\,L_R/L) + t\,\mathbf{r}(s)$, where L is the total length of the centerline curve, and $0 \leq t \leq 1$ is the morphing parameter. The morphing sequence is presented in Figure 4.7**c1**-**c3** with the blue arrows visualizing the spacial displacement of the red (rim) onto the black curve (centerline).

Just as for the 2D arc length contact sets (cf. Figure 4.4), where the 2D contact region of the elastic configuration fills the outer skeleton provided by the double-contact line of the ideal geometric model when elastic deformation of the cross-section is allowed, the 3D ideal contact set curve acts as skeleton, which is fattened, or bridged, to arrive at a 3D physical contact surface strip, whose topology is inherited from the ideal case.

4.6 Summary and Outlook

We have systematically quantified the shapes of *physical* trefoil knots, in both *closed* and *open* configurations. Excellent agreement was found in all considered quantities between FEM and experiment. For the latter, we made extensive use of X-ray micro-computed tomography, gaining access to volumetric information, including centerline curvature and cross-sectional deformation profiles. In parallel, the experimentally validated FEM enabled us to quantify the contact pressure field, which is not available in experiment. Direct comparisons were also established between the experimental and FEM data for elastic trefoil knots and prior numerical computations of their (purely geometric) ideal shape counterparts.

For both open and closed physical trefoil knots the contact sets observed in both experiment and FEM were *smooth surfaces*, with a positive contact set width L_c, *i.e.* finite strips. For the closed trefoil, the physical contact surface is actually a closed strip, which, as an additional topological observation, we remark is a one and a half turn Möbius band (the more common Möbius band has only a single half turn) and so is non-orientable (it has only one face) and only one edge. Moreover for such 1.5-turn Möbius bands the single edge itself forms a trefoil knot. This is perhaps at first sight surprising, but the topology of the contact strip is inherited from the topology of the contact line of the ideal closed trefoil configuration, where it is already understood that the contact set in 3D is a closed curve that is itself a trefoil knot [100].

In the comparison between the elastic and ideal cases of trefoil knots, we found that their curvature profiles were not just quantitatively different, but also qualitatively different. In both open and closed cases, elasticity regularizes the curvature peaks within the inner segment that are predicted by the purely geometric model. To gain insight into the discrepancies between the elastic and the ideal systems, we focused on the open configuration, allowing us to systematically vary the knot tightness. The curvature peaks of the elastic system occur in the outer segment, for both looser and tight knots, contrary to the geometric counterpart, where they appear at the knot's entrance/exit regions. The contact pressure distribution extracted from FEM exhibited localized regions at the entrance of the knot (inner segments). This pressure localization leads to a prominent cross-sectional deformation in the inner segments, acting as local constrictions in these nip regions.

As reported by C.W. Ashley in his comprehensive reference manual on knots [22], "*a rope is weakest just outside of the entrance of the knot*"; a finding that is commonly confirmed by practical experience in knotted filaments. The significant reduction in the cross-sectional area reported in Figure 4.6**d** at the entrance/exit of tight elastic open knots could act as a precursor for weak spots on knotted filaments. Our interpretation is different from that of Pierański *et al.* [65], who attributed the onset of failure to regions of high centerline curvature, computed using their purely geometry model, which our results demonstrate to be in strong disagreement with the curvature profile of physical knots. Our investigation highlights that a mechanics-based approach, going beyond pure geometry, will be necessary to rationalize knot failure. Given the high level of tightening in functional knots tied onto elasto-plastic material filaments, these constriction regions are prone to local plastic deformation [111]. The effect of plasticity on the equilibrium shape of physical knots remains an open question, which we will address in Chapter 6 in the context of knot strength in surgical knots.

5 To Stop or Not to Stop: Capsizing Mechanism in Stopper Knots

In this Chapter, we investigate the stability of stopper knots using precision experiments and FEM simulations. We thread an elastic rod of diameter, D, through the hole of a stopper plate, tie a figure-eight knot at one of the rod's extremities and pull it against this plate (see Figure 5.1**a**). In this physical model system, the flat, rigid plate can represent the following objects in more applied scenarios: the belaying device in rock climbing, the needle's eye in sewing, or the sailor's feet sliding against bulky knots tied in a footrope when setting the sails. When the figure-eight knot is pulled against the plate, it converts a high pulling force on one extremity of the filament into a much smaller force at the other extremity before the knot capsizes. Experimentally validated FEM simulations (see Figure 5.1**b**) are employed to systematically investigate the effect of the frictional interactions on the capsizing mechanism. We quantify twist in a critical rod segment of the knot and demonstrate that friction-induced twist between self-contacting rods is at the source of capsizing. Increasing the friction coefficient between the rod and the stopper plate hampers the onset of capsizing. Whereas most of our investigation focuses on elastic rods, we note that differences of this mechanism are to be expected for braided ropes. Finally, we characterized several standard climbing and multi-functional (braided) ropes, all exhibiting a decoupling of the torsional and bending rigidities. Ropes are found to delay or even impede the capsizing mechanism due to their relatively higher twist energy penalty when compared with bending.

The text and figures in this Chapter are adapted from the unpublished manuscript, which is being finalized for submission to the journal *Extreme Mechanics Letters* in collaboration with Pedro M. Reis.

5.1 Literature Review and Motivation

Each knot has different topological and mechanical characteristics, enabling it to fulfill a specific task better than another one would (see Chapter 1, Section 1.1). Stability is key such that the function of applied physical knots is guaranteed, and filament breakage or knot unraveling is avoided. If a knot fails to fulfill its function, safety might be compromised. For instance, the consequences might be disastrous if a *hitch* attaching the mooring line of a boat to the dock unravels [37], a *bend* joining two ropes during rock climbing unties, or a *binding knot* in surgical suturing slides open [113, 114, 115, 116].

The need to evaluate knot stability has been recognized and addressed by Patil et al. [2] for common binding knots and bends. Unlike these 2-tangles, 1-tangles do not unravel by applying a tensile force on the extremities. Single-tangled knots, which are subjected to external loads and prevent a rope from escaping a device or block an object from slipping along a filament, are called *stopper knots*.

Stopper knots are ubiquitous across applications. In sewing, a knot prevents the filament to escape through the needle's eye. A figure-eight knot acts as a stopper knot in rock climbing, blocking the rope end to escape through the climber's belay device. In sailing, bulky knots in the 'footrope' allow to safely set the sails, while in tennis racket stringing, a set of half-hitches is tied at the string extremities against the frame, thus setting the string tension. This knot type is part of any comprehensive reference manual on knots [22, 1, 117, 118]. However, past studies evaluating their mechanical performance are limited to the risk of jamming and the knot bulkiness [22, 117]. The overhand knot is prone to jamming and injuring the rope [22]. The Stevedore and Ashley's stopper knots are bulkier [117], however, less applied due to their intricate topologies. The common stopper knots are the figure-eight and the double overhand knots, which are denoted in Alexander-Briggs notation as 4_1 and 5_1 [42], as introduced in Chapter 1, Section 1.3.

A recurrent and often undesired phenomenon in physical knots is called *capsizing*, which describes a mechanism involving the rearrangement of the knot configuration without altering its topology [22, 1]. On the one hand, intentional rearrangement of the rod segments can facilitate the untying of a jammed knot. However, on the other hand, capsizing constitutes a danger if the knot fails to resist an external load. While the phenomenon of capsizing is well-known amongst sailors, the underlying kinematics and mechanics has, to the best of our knowledge, never been addressed.

Research questions: In this Chapter, we aim to rationalize the mechanism of the capsizing failure mode in the common figure-eight knot. In this context, we will address the following questions:

- How do the rod segments rearrange when the knot is pushed against a blockage? Throughout the capsizing process, what is the maximal resistance the knot can provide, thereby preventing the end of a filament from passing through an orifice?
- What is the source of capsizing? How do the frictional interactions between self-contacting rods and between the rod and the rigid stopper plate affect the capsizing force?

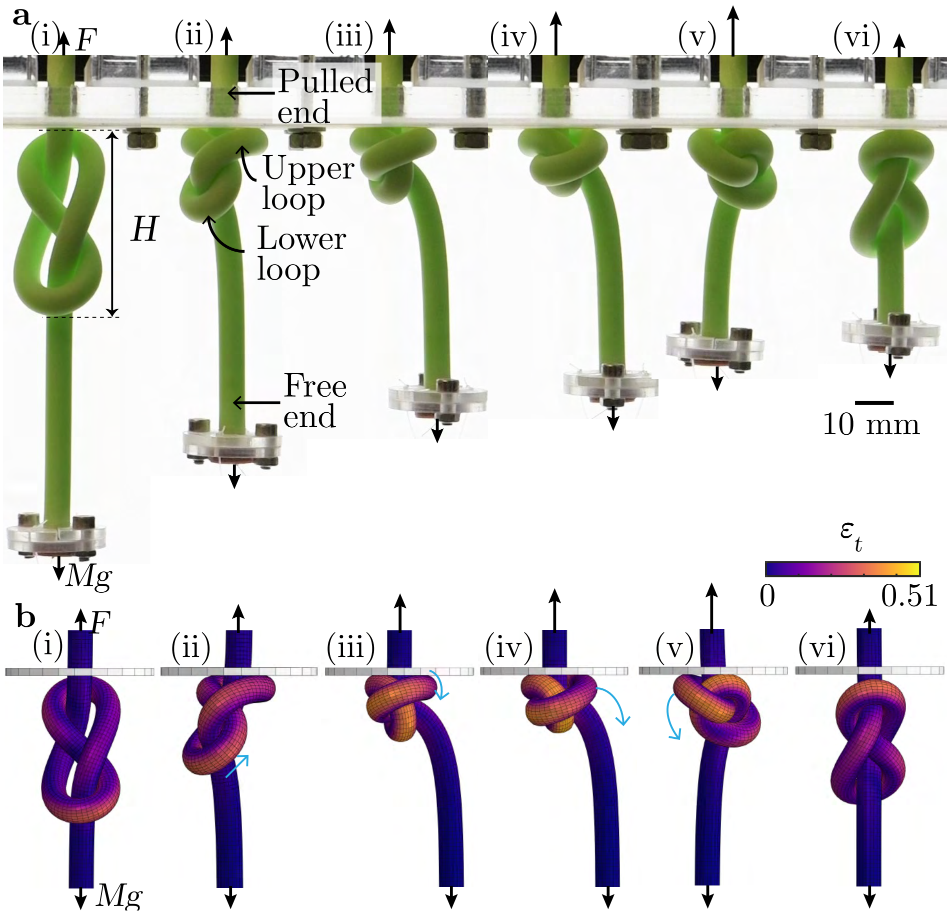

Figure 5.1: **Model system for a figure-eight stopper knot. a, b**, Sequence of experimental (**a**) and FEM (**b**) snapshots at different stages of the force-displacement curve. The sequence described by (i)-(vi) corresponds to the same loading level for the experiments and FEM. In panel **b**, the color map displays the true strains in the rod. The labels (i)-(vi), in both panels **a** (experiments) and **b** (FEM) correspond to the same points (i)-(vi) of the force-displacement curve in Figure 5.6**a**.

- Can we rationalize the failure mechanism and, consequently, tune geometric and mechanical properties (*e.g.* initial knot tightness and friction coefficients) to delay the capsizing event?

- How do elastic and braided systems compare in terms of capsizing? In case of dissimilar behavior, which properties could impede the failure of knots tied in ropes?

5.2 Experimental and Numerical Methodology

5.2.1 Fabrication of the Composite Rods

In studying the failure of stopper knots, we will focus on the capsizing mechanism (more details below) involving reconfigurations of the knot instead of other failure mechanisms such as fracture. For that purpose, we need to decouple the axial stretching of the rod caused by the pulling force from its bending and twisting strains. Moreover, minimizing axial stretching also reduces the effect of cross-sectional reduction during testing. We consider composite rods that are elastic in both bending and twisting but nearly inextensible in the axial direction. Therefore, our rods exhibit transversely isotropic behavior, a property that is observed in structured materials such as ropes, with an axial stiffness much larger than their bending stiffness.

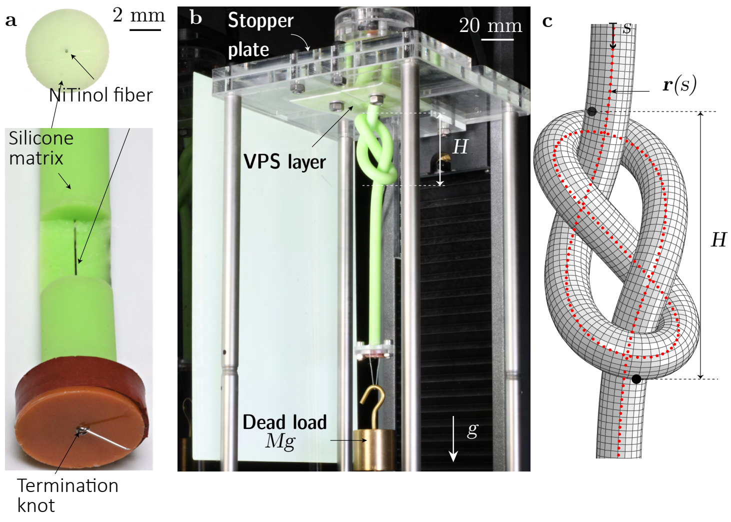

Figure 5.2: **Fabrication and preparation of a figure-eight stopper knot. a**, Composite rod, comprising an elastomeric matrix (VPS) and a slender fiber (Nitinol) located at the centerline. (left) A segment of the VPS matrix was cut out to reveal the Nitinol fiber. (right) Cross section of the composite rod. **b**, Photograph of the experimental setup. **c**, Knotted configuration used in FEM, showing the mesh and the beam reinforcement at the centerline location $\boldsymbol{r}(s)$ to emulate the composite rod with high axial stiffness.

The protocol described in Chapter 2, Section 2.2, served as a basis for the fabrication of elastic rods, but needed to be adapted for this Chapter to add the axial inextensibility property. We fabricated composite rods of diameter $D = 8.3\,\text{mm}$ and length, $L = 35\,\text{cm}$ made out of vinyl polysiloxane, VPS32 with a stiffer thin fiber embedded at the centerline, as shown in Figure 5.2**a**. For this fiber core, we used a slender Nitinol wire (Dynalloy, Inc.; diameter, $D_{\text{Nitinol}} = 0.25\,\text{mm}$, Young's modulus, $E_{\text{Nitinol}} = 79.5\,\text{GPa}$, Poisson's ratio, $\nu_{\text{Nitinol}} = 0.33$). The fiber is constrained at the rod extremities by a termination knot (overhand knot) against a circular, rigid Polyvinyl chloride (PVC) shim stock plate (thickness: 0.75 mm) with a central hole. Due to the significant difference in axial stiffness between the silicone matrix and the central fiber, the composite rods can be regarded as effectively inextensible. While the caps prevent global rod stretching, the composite rod design does not necessarily prevent local sliding and debonding between the VPS32 matrix and the Nitinol core, which needs to be verified with numerical results.

5.2.2 Characterization of Frictional Properties

To ensure reproducible frictional behavior, the rods were surface-treated with talcum powder (Milette, Migros). According to the experimental protocol introduced in Chapter 2, Section 2.5.2, the frictional relation between the tangential force, F_t, and the normal force, F_n, is used to characterize the contact behavior. In Figure 5.3, we present the results for the static and dynamic friction behavior over a wide range of normal loads, satisfying the Amontons-Coulomb friction law. The linear fits, $F_t = \mu_{\{s,t\}} F_n$, of the experimental data yield a static friction coefficient, $\mu_s = 0.41 \pm 0.04$, and a dynamic friction coefficient, $\mu_d = 0.35 \pm 0.02$.

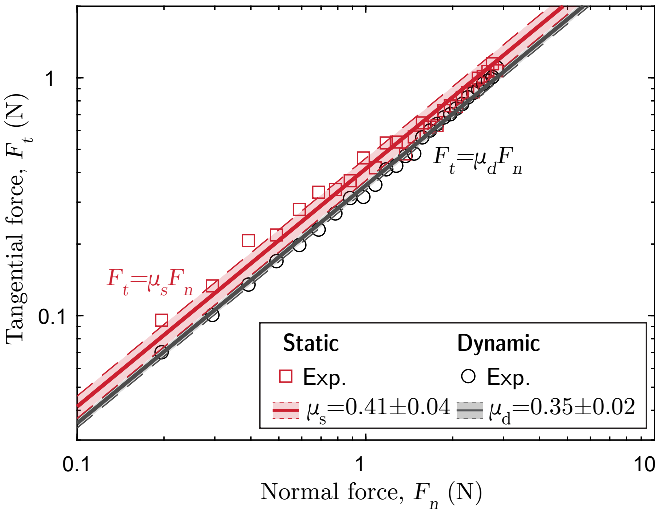

Figure 5.3: **Characterization of the static and dynamic friction coefficients** (μ_s and μ_d, respectively) between surface-treated rods over a wide range of normal contact loads, F_n. The solid line and shaded region represent the linear fit and the corresponding confidence interval.

5.2.3 Apparatus and Setting of the Initial Configuration

Developing a protocol to set the initial configuration of the stopper knot system is crucial for reproducibility due to the possibility of meta-configurations caused by rod-rod frictional self-interactions. This preparation protocol comprises two steps: (i) pre-tensioning of the knotted configuration, and (ii) loading of the lower extremity by a dead weight. (i) First, we tied a loose configuration of the figure-eight knot mid-way along the centerline of the composite rod and aligned the knotted rod vertically. The upper extremity of the rod was then passed through a horizontal acrylic plate (thickness: 10 mm), hereby referred to as the *stopper plate*, containing a circular clearance hole of diameter $d = 10\,\mathrm{mm}$ (slightly larger than the rod diameter, $D = 8.3\,\mathrm{mm}$), and clamped to the load cell of a universal testing machine (UTM, Instron 5943). Note that the lower surface of the stopper plate was coated by a thin film of VPS32 ($\approx 0.5\,\mathrm{mm}$ in thickness, talcum powder-treated surface) to have the same friction properties as the self-contacting rods. The lower extremity was first clamped, and the end-to-end distance of the knotted configuration was increased using the UTM to set the value of pre-tension, P, in the system. (ii) Then, the extremity of the lower rod was de-clamped and loaded by a weight (see Figure 5.2**b**) to induce a dead load, Mg, which kept the knot in place. The hanging mass was fixed at $M = 0.2\,\mathrm{kg}$ and g is the gravitational acceleration. The resulting knot shape constitutes the initial configuration for the experimental tests.

5.2.4 Protocol for the Experimental Mechanical Tests

The initial configuration can be quantified by the *knot size*, H, the defined shortest distance between the outer positions of the knot, as shown Figure 5.1**a** (i). The use of the geometric control parameter allows to accurately compare knots with different friction coefficients between the self-contacting rods. This comparison would not have been possible if the pre-tension, P, had been used directly.

Before the upper loop of the knot touches the stopper plate, an optical photograph is taken from a side-view (see Figure 5.4**a**). The use of a back-light enables sharp transitions for the image binarization in Matlab. Figure 5.4**b** shows the complement of the binary image with filled potential holes (Matlab function `imfill`).

Then, in Figure 5.4**c**, we plot the gradient of the intensity profile (`improfile`) along horizontal line segments of the binary image, *i.e.* the gradient of the number of white pixel-values for each horizontal line segment. Two distinct peaks in the gradient profile are recognized along the knot height. They are related to the sudden transitions between the straight, vertical rod and the bulk knot (upper and lower loop). A gradient threshold of ± 4 (vertical dashed lines)

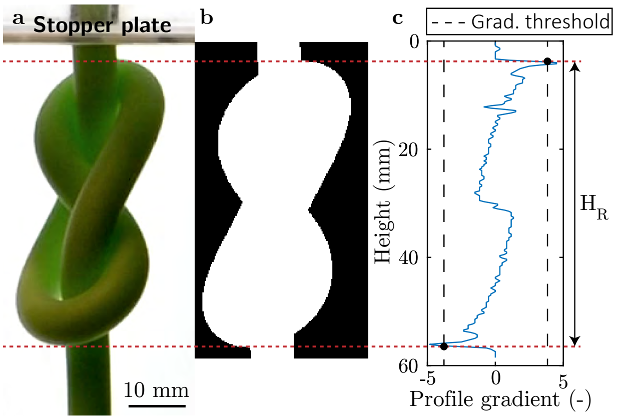

Figure 5.4: **Image analysis to determine knot size.** **a**, Optical photograph of the side view of the figure-eight knot in front of a back-light. **b** Image-processing on the captured side view image of the knot. **c** Profile gradient as a function of the captured height from **b**. The dashed vertical lines define the positive and negative gradient thresholds. The shortest distance between the intersections of the gradient thresholds with the plotted gradient profile yields the knot size, H.

allows to determine the shortest distance between the outer surface of the upper and lower loops (see horizontal dashed lines), which corresponds to the *knot size*, H.

The pre-tension was systematically varied in the range $1 \lesssim P/Mg \lesssim 3$ to obtain initial configurations with different values of H, as shown in Figure 5.5 (inset). The data evidences that higher values of pre-tension result in lower knot sizes. These results will be discussed in more detail in Section 5.3. Using the UTM, the rod containing a figure-eight knot and the dead load on the lower extremity was pulled by the upper extremity such that the knot was pushed against the (rigid) stopper plate. The tests were done under imposed displacement, at constant vertical velocity $v = 1\,\mathrm{mm/s}$. During testing, we recorded the traction force, F, measured by the UTM as a function of the displaced rod length, δ.

5.2.5 Finite Element Simulations

In parallel to the physical experiments, we performed numerical simulations using the finite element method (FEM, ABAQUS STANDARD 6.14-1, Simulia, Dassault Systems 2014) to probe quantities that cannot be readily varied in the experiments. Particular emphasis is given to systematically varying the values of the rod-rod and rod-plate friction coefficients. Moreover, FEM enables us to quantify the local twist of the rod during the capsizing mechanism.

The FEM simulations were conducted with a nonlinear dynamic-implicit analysis, as described in Chapter 3. An initially straight elastic rod was meshed with reduced hybrid 3D solid elements (`C3D8RH`). The number of elements was 270 along the axial rod direction and 44 on the cross section. The material was modeled as an incompressible neo-Hookean solid, with Young's modulus chosen to be the same as the experiments $E = 1.25\,\mathrm{MPa}$. Two other values $E = \{0.52, 0.98\}$ were also considered.

In addition to the method described in Chapter 3, 3.1, and to mimic the Nitinol fiber at the core of the experimental samples, a beam reinforcement was implemented at the centerline (see Figure 5.2**c**) with the experimental geometric and material properties, D_{Nitinol} and E_{Nitinol}. The corresponding Abaqus feature, `stringer element`, shares its nodes with the underlying mesh. Further, a node-set is defined along the axial direction (described by the arc length, s) at the outer rod surface. From the discrete coordinates $\boldsymbol{\xi}(s_i)$ along the axial nodes $i \in [1, 270]$, together with the material centerline nodes, $\boldsymbol{r}(s_i)$, we can define the director vector $\hat{\mathbf{d}}_1(s_i)$. As introduced in Chapter 1, Section 1.2.2., this director vector is orthogonal to the straight, undeformed centerline [36, 37]. The discrete form of $\hat{\mathbf{d}}_1(s_i)$ is given by Eq. (2.16) in Chapter 2, Section 2.4.1, and will be needed in Section 5.6 to quantify the evolution of twist in the rod between different loading levels of the knot (see Chapter 1, Section 1.2.2).

During testing, the stopper-knot system is subject to two types of contact interactions, both involving friction. First, there are regions of self-contact (labeled as $R-R$ for '*Rod vs. Rod*'), where the rod is in frictional contact with itself. Second, there are regions where segments of the knotted rod are in frictional contact with the stopper plate (labeled as $R-P$ for '*Rod vs. Plate*'). The rod-rod and rod-plate contacts were modeled using Amontons-Coulomb friction law. Similar to Chapter 4 and previous studies [62, 78, 90, 37], the frictional contact was enforced through normal penalty forces combined with tangential frictional forces, implemented by a single friction coefficient. Appropriately attributing the friction coefficient to the respective contact regions will be crucial in this Chapter and will be discussed in more detail in Section 5.5.

The computational procedure to tie a knot in a purely elastic rod, including validation of the figure-eight knot, was reported in Chapter 3, 3.2.4 [62]. In the present study, we followed the same knot-tying protocol for the composite, axially reinforced rod. The initial configuration is numerically set in the same way as in the experiments by tightening the figure-eight knot up to a pre-tension, P, which subsequently is released to the dead load, Mg. Finally, similarly to the experiments, the knot size, H, is determined as the shortest distance between the outer positions of the knot (see Figure 5.2**c**).

5.3 Initial Knotted Configuration Prior to Testing

As described in Section 5.2.3, prior to each experimental test, to ensure reproducibility, the initial configuration of the knotted rod needs to be prepared with a protocol involving pretensioning of the system, followed by the application of a dead load at the lower extremity of the rod to set the knot size. Figure 5.2**b** presents a photograph of the experimental system after the preparation steps and before testing.

In Figure 5.5 (inset), we plot the experimental results and the corresponding FEM simulations for the knot size, H, obtained after the preparation steps, as a function of the applied pretension, P, for the composite VPS32-Nitinol rod (reference system with $E = 1.25\,\text{MPa}$ for the elastomeric matrix and $M = 200\,\text{g}$ for the dead load). The experimental data (crosses; the error bars represent the standard deviation of 5 independent runs) are in satisfactory agreement with the FEM simulations. In the plot, we also present FEM simulation data for two other composite-rod systems with ($E = 0.98\,\text{MPa}$, $M = 157\,\text{g}$) and ($E = 0.52\,\text{MPa}$, $M = 83\,\text{g}$). We explore these three different cases so as to test that the general scaling laws valid for a homogeneous rod still hold for our composite rod. Specifically, the geometric properties (*e.g.*, knot size, H) for a knotted homogeneous rod are expected to scale with the rod diameter, D. In addition, the dead load, Mg, and the bending stiffness, $B = E\pi D^4/64$, are the primary ingredients setting the knot shape. Physical similarity between systems, that is with the same value of the dimensionless group $\mathscr{K} = ED^2/(Mg)$, with different material properties (E), requires the corresponding dead load to be adapted. The three data sets in Figure 5.5 (inset) all have the same value of $\mathscr{K} = 44$; the collapse of the three curves when plotted as H/D versus P/Mg confirms the physical similarity of the three systems. The change of the bending stiffness through the Young's modulus is fully compensated by the adapted dead load. Thus, incorporating the stiff, slender fiber does not affect the scaling of the elastic system, which deforms primarily through bending.

In Figure 5.5, even if the agreement between experiments and the collapsed simulation data is satisfactory, especially given the complex coupling between the underlying geometrically nonlinearities and the frictional contact, the FEM systematically under-predicts the experimental data. This mismatch suggests the likelihood that an additional quantity affects the knot shape. At this stage, we speculate that the reason for this offset can be attributed to the detailed treatment of friction; for the FEM data presented so far, we set both the rod-rod and rod-plate friction coefficients to $\mu = 0.33$ (lowest dynamic friction coefficient measured experimentally), which is over-simplistic, as we demonstrate next.

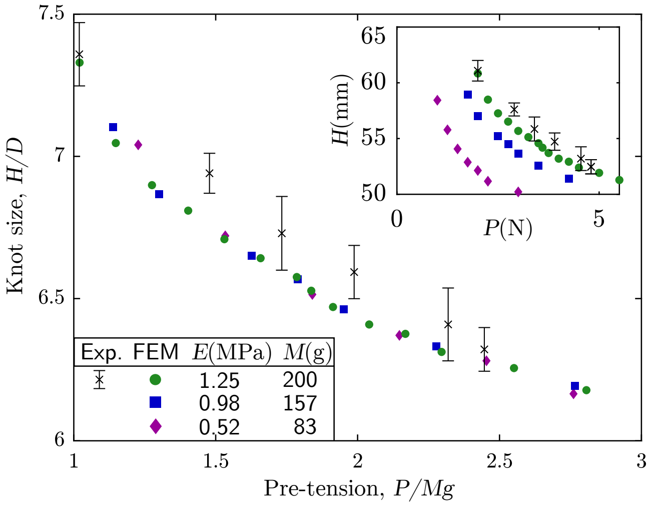

Figure 5.5: **Initial configuration of the figure-eight knot.** Normalized knot size, H/D, after preparation and before testing as a function of the applied pre-tension, P/Mg. The error bars in the experimental data (crosses) correspond to the standard deviation of 5 independent tests. FEM data is represented by the solid symbols (see legend for values of E and M) (inset) Corresponding dimensional version of the plot.

5.4 Mechanical Testing of the Figure-Eight Stopper Knots

The phenomenon of capsizing can be observed when a knot is subjected to an external force [22, 1]. Using the protocol described in Section 5.2.4, the figure-eight knot was tested by pulling it against the stopper plate containing a clearance hole. In Figure 5.1**a**, **b**, we had displayed a sequence of snapshots (i)-(vi) of the experimental and numerical model systems that we now describe in more detail. For clarity, we refer to the *pulled end* as the upper extremity of the rope clamped to the load cell of the UTM, whereas the *free end* is the extremity of the rod onto which the dead load is attached. Below the pulled end, the rod is passed through the clearance hold of the stopper plate, under which the figure-eight knot is located. To further simplify the discussion of the capsizing mechanism, we use the following designations: the upper bent rod segment touching the stopper plate is called the *upper loop*, and the lower one closer to the free end is referred to as the *lower loop*.

In the following description, the labels (i)-(vi) correspond to the panels in Figure 5.1**a**, **b**, which are at the same loading stages for the experiments and simulations. At (i), the upper loop first establishes contact with the stopper plate and is then compressed against it; (i)-(ii). Once the whole upper loop contacts the plate, the lower loop acts as a hook, lifting the free end; (ii)-(iii). Between (iii) and (iv), the lower loop opens the upper loop in a wedge-like mechanism. Consequently, as we quantify below, a friction-induced twist is accumulated in the upper loop. Both the wedging and the twisting mechanisms trigger the lower loop to overtake the upper one, with the latter rolling and snapping down towards the free end; (iv)-(v). In the final knot configuration (vi), the figure-eight knot reaches a new traveled position closer to the extremity of the free end. This *capsizing* mechanism was observed for all studied knot sizes in both experiments and simulations. Note that if the pulling process were to be continued, other capsizing cycles would repeat (with increasingly tighter initial configurations). After multiple capsizing events, the knot would eventually unravel at the extremity of the free end, which would then fully pass through the stopper plate. For the remainder of the study, we focus on a single (the first) capsize event.

In Figure 5.6**a**, we present a typical force-displacement curve for experiments and FEM for the knot size $H = 6.6 \pm 0.1$ (prepared with a dimensionless pre-tension of $P/Mg = 1.99$), the same as the knot in Figure 5.1. The normalized traction force, F/Mg, measured by the load cell increases monotonically, albeit nonlinearly, as a function of normalized displaced rod length, δ/D, then reaches a peak force, F_0, and, finally, drops close to zero. We shall refer to F_0 as the *capsizing force*: the maximum load-bearing capacity at capsizing. The points (i)-(vi) correspond to the loading sequence presented in Figure 5.1, with the capsizing event occurring between (iv) and (v).

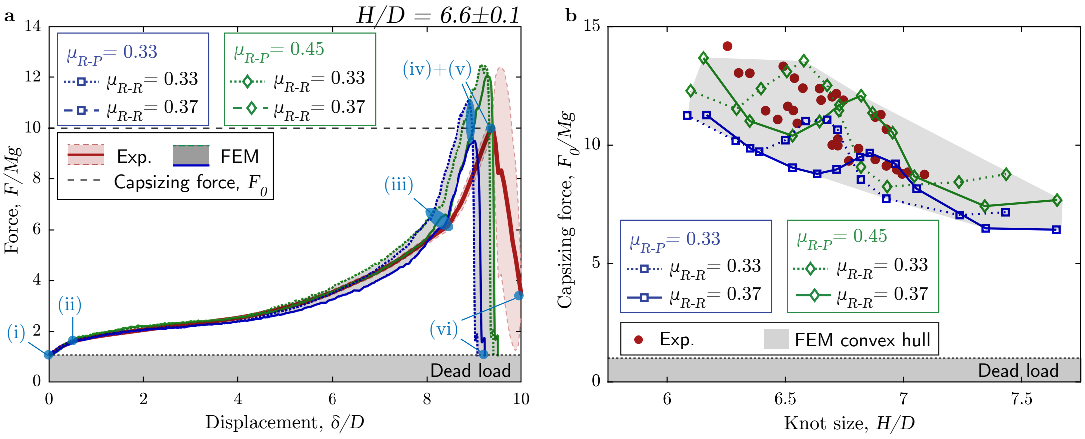

Figure 5.6: **Testing of a figure-eight stopper knot.** **a**, Mechanical testing of the stopper knot: force-displacement curve obtained when the knotted rod (including a dead weight) is pulled against the stopper plate. The solid (red) line corresponds to the experimental data; the shaded region represents the standard deviation of 4 runs. The blue and green curves correspond to the FEM data; the gray-shaded region corresponds to the interval associated with the full range of friction coefficients explored (μ_{R-R} and μ_{R-P}); see text for details on the parameters. The points (i)-(vi) correspond to the configurations in Figure 5.1 with the same labels. **b**, Normalized capsizing (peak) force, F_0/Mg, versus knot size, H/D. The experimental data is represented by the solid circles and the FEM data by the open symbols (see the legend for the corresponding values of μ_{R-R} and μ_{R-P} explored in the simulations.)

Note that the nonlinear behavior of the force-displacement curves in Figure 5.6**a** is not due to hyperelastic stretching since the Nitinol center fiber makes the system effectively inextensible. Previous studies [78, 62, 37, 33] showed that the *dynamic* friction coefficient is sufficient to reliably capture self-contacting rod interactions. Thus, the frictional rod-rod contact is described by the experimentally measured average and uncertainty of the average dynamic friction coefficient , $\mu_{R-R} = 0.35 \pm 0.02$, which yields the lower and upper bounds, $\mu_{R-R} \in [0.33, 0.37]$.

Since it is unclear how the rod-plate frictional properties affect the response of our system, we systematically consider the full range of relevant friction coefficients, $\mu_{R-P} \in [0.33\ 0.45]$, between the lowest dynamic friction coefficient and the highest static friction coefficient. The envelope of the FEM data in Figure 5.6**a** spans the four numerical force-displacement for the four limiting frictional-coefficient values: $\mu_{R-R} = \{0.33, 0.37\}$ and $\mu_{R-P} = \{0.33, 0.45\}$. We remark that the experimental and numerical response curves are similar, exhibiting the same events corresponding to the labels (i)-(vi) in Figure 5.1 at nearly the same loading levels, which partially validates the numerics within the considered range of friction coefficients.

The stopper knot system involves a nontrivial interplay between static and dynamic friction behavior. In Figure 5.5**b**, we plot the experimentally measured capsizing force, F_0/Mg, versus knot size, H/D, finding that F_0/Mg tends to decrease with increasing H, although there is some scatter in this experimental data. In other words, the tighter the initial configuration of the figure-eight knot, the higher the capsizing force is. Similar to the simulations data in Figure 5.5**a**, in Figure 5.6**b**, we present four FEM-computed datasets for the four limiting values of frictional-coefficient considering the Rod-Rod and Rod-Plate interactions: $\mu_{R-R} = \{0.33, 0.37\}$ and $\mu_{R-P} = \{0.33, 0.45\}$. The complex envelope of the FEM data (grey region in Figure 5.6**b**) encompasses the experimental data, serving as an additional validation of the simulations. Note that each of the FEM curves shows an overall decreasing trend of F_0/Mg versus H/D, albeit non-monotonically; there is a 'bump' in the data (at a characteristic knot size) H/D, the location of each depends on the combination of μ_{R-R} and μ_{R-P}. We have not been able to rationalize this feature of the FEM data, speculating that it is related to a complex interaction between geometry, contact pressure, and friction, calling for a more detailed future analysis.

5.5 The Role of Friction in Dictating Knot Performance

By surface-treating the composite rods in the same way as the thin-film coating of VPS on the underside of the stopper plate (see Section 5.2.2), the experimental system was designed to target values of rod-rod (μ_{R-R}) and rod-plate (μ_{R-P}) frictional properties that were as close as possible. Still, having validated the FEM simulations against experiments in the previous section, we now leverage the FEM to investigate in more detail the rod-rod and rod-plate (dynamic) frictional interactions affect the capsizing mechanism.

First, we perform FEM simulations with the following four values $\mu_{R-R} = \{0.32, 0.33, 0.35, 0.37\}$ of the rod-rod friction coefficient while fixing the rod-plate friction coefficient to $\mu_{R-P} = 0.45$. In Figure 5.7**a**, we plot the normalized pulling force, F/Mg as a function of the length of the displaced rod, δ/D, for the knot size, $H/D = 6.59 \pm 0.04$. We find that all four curves coincide, independently of μ_{R-R}, between the loading levels (i) and (iv) (same labels as in Figure 5.1). However, the portion of the curve with a final steep slope between the loading step (iv) and the triggering of capsizing at (v) is extended for lower values of μ_{R-R}, consequently, with higher capsizing (peak) forces. In Figure 5.7**b**, we plot the normalized peak force, F_0/Mg, as a function of knot size, H/D, for the same four values of μ_{R-R} explored in Figure 5.7**a**. The same qualitative behavior (non-monotonic decrease) is observed for the four cases of μ_{R-R}; from high capsizing forces for tight figure-eight knots ($H/D \lesssim 6.5$) to lower capsizing forces for looser configurations ($H/D \gtrsim 7$). Note that the curves shift progressively to higher values of H/D as μ_{R-R} increases. With decreased rod-rod friction, the knot needs to be tighter (smaller H) to attain a similar level of mechanical performance, as measured by the capsizing force.

Next, we fix the rod-rod friction to $\mu_{R-R} = 0.3$, and systematically vary the rod-plate friction with the values $\mu_{R-P} = \{0.20, 0.30, 0.40, 0.50\}$. In Figure 5.7**c**, we plot the corresponding force-displacement curves for the same knot size, $H/D = 6.41 \pm 0.004$. Similarly to Figure 5.7**a**, the curves coincide between loading levels (i) and (iv) but with a final extension, between (iv) and (v), with capsizing (peak) forces that increase with μ_{R-P}. In in Figure 5.7**c**, we plot F_0/Mg versus H/D for the four values of μ_{R-P}. For loose knots below $H/D \approx 6.5$, the approximately constant peak force level increases with μ_{R-P}. For $H/D \gtrsim 6.5$, after a transition region, the peak force is reduced significantly. Throughout, the mechanical performance of the knots as measured by its capsizing force increases substantially for higher values of μ_{R-P}. Take, for example, the figure-eight knot of size $H/D = 6.3$. For $\mu_{R-P} = 0.2$, the figure-eight knot achieves a peak force $F_0 \approx 15Mg$ and only $F_0 \approx 9Mg$ when $\mu_{R-P} = 0.5$.

Combining the data in Figure 5.7**b** and Figure 5.7**d**, we conclude that increasing the rod-plate friction has a more important effect in increasing the performance of the stopper knot than the rod-rod friction, especially for looser initial configuration. These findings could serve as valuable guidelines for practical applications of performant stopper knots.

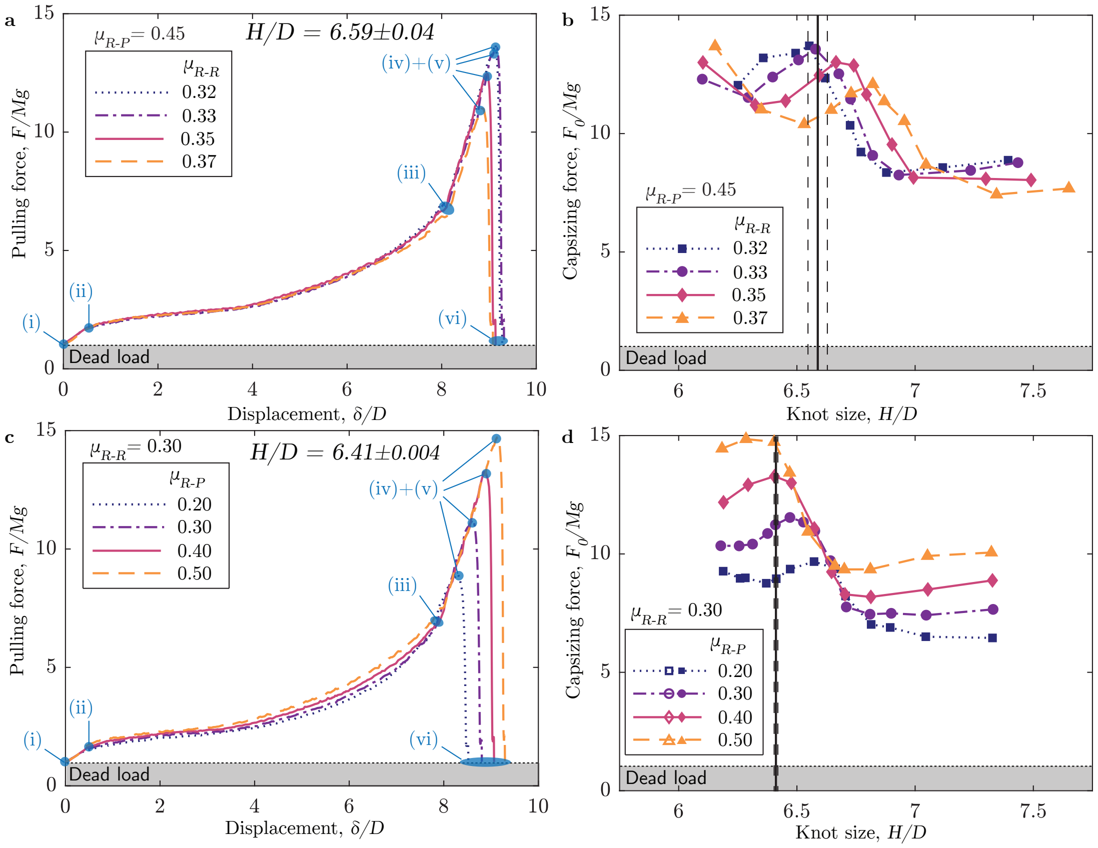

Figure 5.7: **Effect of the frictional interactions on the capsizing force. a, b**, Performance characterization for changes in the frictional behavior of the self-contact rods. The force-displacement curves in **a** correspond to the knot size, $H/D = 6.59 \pm 0.04$, in **b** (vertical lines). **c, d**, The effect of the surface roughness of the stopper plate on the capsizing force. The force-displacement curves in **c** correspond to the knot size, $H/D = 6.41 \pm 0.004$, in **d** (vertical lines).

5.6 Friction-Induced Twist Triggers Capsizing

We proceed by investigating the mechanism underlying the finding that the capsizing (peak) force, F_0, is strongly associated with the extent of the force-displacement curve, between loading levels (iii) and (iv), prior to capsizing, as described in the previous section (cf. Figure 5.7**a, d**). Moreover, from the data in Figure 5.7**b, c** we found that F_0 is directly related to the rod-rod and rod-plate frictional interactions, increasing with both μ_{R-R} and μ_{R-P}. Next, we use the experimentally validated FEM to quantify the extent of twisting of the upper loop. For this purpose, we will use information on the evolution of the director vector, $\hat{\boldsymbol{d}}_1(\tilde{s})$, as defined in Eq. (2.16), as a function of normalized arc length, $\tilde{s} = S/D$, and loading level. In Figure 5.8**a**, we show representative FEM-computed configurations of the stopper knot at four representative loading levels, (i)-(iv); the labels corresponding qualitatively to the configurations in

Figure 5.1. Note that the stopper plate is not shown for clarity of visualization. In these 3D representations, the centerline of the rod (thin solid line) is decorated with the $\hat{\boldsymbol{d}}_1(\tilde{s})$ director vector, only on the upper loop, defined in the segment with arc length $21 \leq \tilde{s} \leq 30$, with $\tilde{s} = 0$ at the pulling end. The director vector was defined in the straight, unknotted rod configuration (see Section 5.2.5).

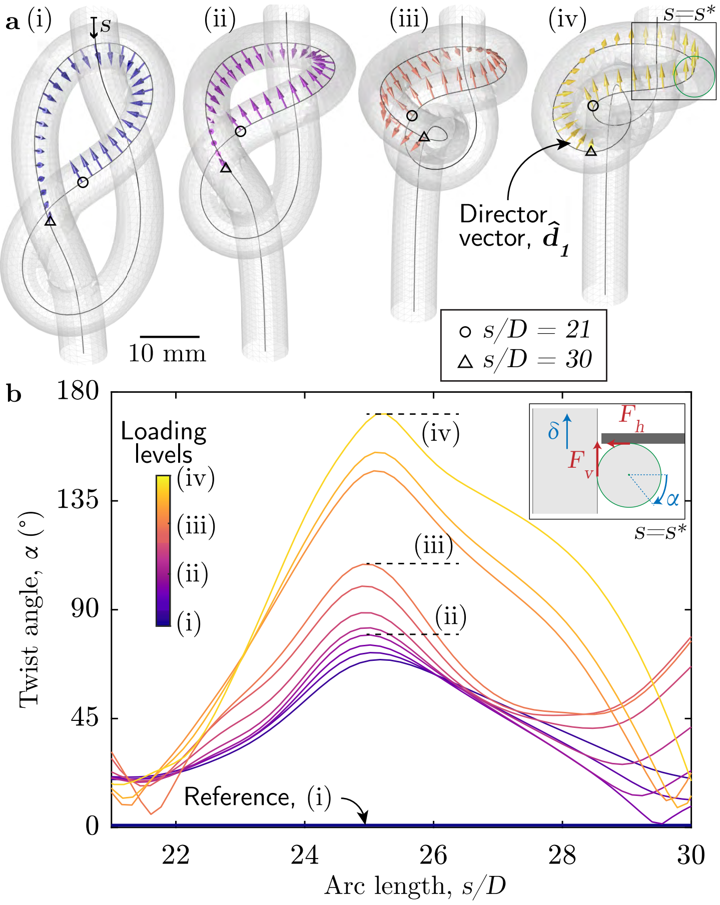

Figure 5.8: **Friction-induced twist in the upper loop segment.** **a**, 3D configurations from FEM for the loading levels, (i-iv), according to the number introduced in Figure 5.1, with (i), the reference configuration, and (iv), the knot shape at the onset of the capsizing event. The configuration corresponds to $H = 5.7$ with $\mu_s = \mu_d = 0.33$. The director vector, $\hat{\boldsymbol{d}}_1$, is represented in the upper loop, which is roughly defined by the arc length range, $21 \leq s/D \leq 30$. **b**, Twist angle, α, according to Eq. (5.1), as a function of the arc length, s/D. The capsizing mechanism is depicted in the schematic (inset) of a cross-sectional rod cut ($s = s^*$ in **a**(iv)).

To simplify the data interpretation, we define as the reference director vectors those of the initial *knotted* configuration in Figure 5.8**a**(i), $\hat{\boldsymbol{d}}_{1,\mathrm{Ref}}(\tilde{s})$. Then, we computed the twist angle on the upper loop, α, of subsequently deformed configurations, relative to that reference geometry, such that:

$$\alpha(\tilde{s}) = \arccos\left(\frac{\hat{\boldsymbol{d}}_1(\tilde{s}) \cdot \hat{\boldsymbol{d}}_{1,\mathrm{Ref}}(\tilde{s})}{||\hat{\boldsymbol{d}}_1(\tilde{s}) \cdot \hat{\boldsymbol{d}}_{1,\mathrm{Ref}(\tilde{s})}||}\right). \tag{5.1}$$

In Figure 5.8**b**, we plot $\alpha(\tilde{s})$ curves at different levels of loading, as indicated by the adjacent color bar. By definition, the reference (initial) configuration has $\alpha(\tilde{s}) = 0$. At each loading level, the twist angle profile is spatially heterogeneous and non-monotonic along $\tilde{s}$. Throughout the loading process, from level (i) to (iv), there is an overall increase of twist, with particular growth between loading levels (iii) and (iv). Near the two edges of the upper loop $\tilde{s} \approx 21$ and $\tilde{s} \approx 30$, the twist angle does not accumulate significantly; α is at most 80° at $\tilde{s} = 30$ for loading level (iii) but remain typically well below that value. This observation suggests that the accumulation of twist in the upper loop is induced primarily by rod-rod friction through the vertical rod displacement, δ.

The inset of Figure 5.8**b** illustrates our interpretation of the capsizing mechanism; the schematic shows the cross-sectional cut, highlighted in Figure 5.8**a**(iv), at the specific point where a nearly horizontal segment of the rod at $s = s^*$ is in contact with a nearly vertical segment earlier in s. The displacement, δ, of the pulled rod excites a vertical friction force, F_v, on the other contacting rod segment. The increase of the resulting twist, α, is impeded by the frictional interaction between the upper loop and the stopper plate, with a frictional force F_h, opposing the twisting direction of the rod. Moreover, the higher capsizing forces for tighter knots reported in Figure 5.6**b** and Figure 5.7**b, d**, can be attributed to the higher torsional stiffness of shorter upper-loop segments, L (torsional stiffness $\sim 1/L$), in addition to also higher normal contact forces. This qualitative interpretation of the capsizing mechanism is aligned with the results reported in Figure 5.7 and Figure 5.8.

5.7 Resistance to Capsizing in Braided Ropes

Thus far, our investigation of stopper knots, with an emphasis on the capsizing mechanism, made use of composite elastomeric rods, which were effectively inextensible along the axial direction (making them transversely isotropic) due to the stiff fiber located at the centerline. Still, the rod behaves elastically in bending and torsion, as supported by the scaled results in Figure 5.5**a**. Following classical procedures, one can define the bending and torsional stiffnesses of a rod as $B = EI$ and $C = GJ$, respectively, where E is the Young's modulus, G the shear modulus, I the second moment of area, and J the second polar moment of area. For an elastic rod, C and B are coupled as

$$\Gamma = \frac{B}{C} = (1+\nu) > 1, \tag{5.2}$$

where ν is the Poisson's ratio of the material. This result is expected to remain valid for an inextensible rod, as in our composite rods.

In Figure 5.9**a**, we plot experimental measurements of B versus C for two elastomeric composite rods (containing a Nitinol core fiber), with $E = 0.52\,\mathrm{MPa}$ and $E = 1.25\,\mathrm{MPa}$; square and diamond solid symbols in the plot. The data was obtained from the standard tests of three-point bending (for B) and torsion (for C), following Zou and Li [119] and ASTM E143-02 [120], respectively. Unsurprisingly, these two data points for elastic rods fall on the $\Gamma = 3/2$ line, as expected from Eq. (5.2) for the elastomeric materials we used, which are nearly incompressible ($\nu \approx 0.5$).

The ropes, yarns, and threads commonly used in climbing, sailing, or sewing, onto which stopper knots are regularly tied, are structured, anisotropic, and flexible structures comprising assemblies of braided filaments. As such, Eq. (5.2) is not valid for these braided structures, whose bending and torsion properties decouple, and we expect $\Gamma \neq 3/2$. For the remainder of this section, we will consider real (braided) ropes, in comparison to the elastic case.

In addition to the elastic rods mentioned above, we also measured B and C for eight static and dynamic climbing ropes as well as multi-functional ropes; the results are plotted in Figure 5.9**a**. For all the rope samples, the bending to torsional rigidity ratio is smaller than 1 ($\Gamma < 1$). This decoupling between B and C with $C > B$ results in a higher torsional energy penalty in ropes compared to bending, acting as an impediment to twisting deformation. More specifically, the B vs. D data for all the tested ropes lies within the shaded region of the plot in Figure 5.9**a**, with $0.18 \leq \Gamma \leq 0.67$.

The above results, especially the spread of the data in the B vs. C plot, convey the complexity of the mechanical properties of braided ropes compared to the (much) simpler case of elastic rods. As such, a comprehensive study of stopper knots tied onto braided ropes is beyond the scope of the present study, even if it certainly deserves attention in future work. Still, we can provide several qualitative observations based on the insight we have gained for elastic rods. For braided ropes, we expect that the higher energetic cost of torsion compared to bending will have a strong effect in delaying or even inhibiting capsizing of common stopper knots.

In Figure 5.9**b**, we show photograph of a the figure-eight knot (denoted 4_1 as introduced in Section 5.1), tied on a static rope ($D = 5.7\,\mathrm{mm}$) in its original configuration (left) and after it has been pushed against the stopper plate (right). Another, more complex, stopper knot that is commonly used in applications is the double overhand knot, 5_1, essentially part of the double fisherman's and the blood/barrel knot [22, 117, 118]. In Figure 5.9**c**, we present photographs for this 5_1 knot tied on the composite rods described in Section 5.2.1 in the initial (left) and

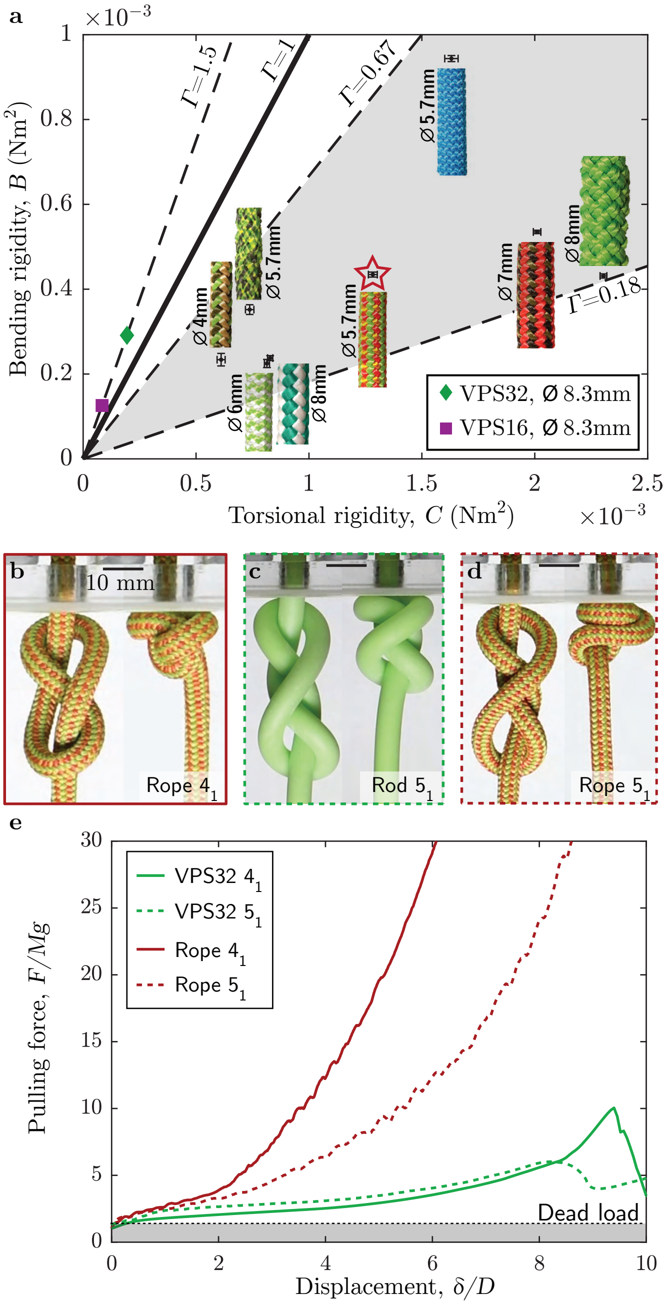

Figure 5.9: **Stopper knots tied in single-stranded rods vs. braided rope-systems. a**, Bending rigidity, B, as a function of the torsional rigidity, C, for incompressible isotropic materials (VPS) and numerous ropes. **b**, Photographs of a figure-eight knot (4_1) tied in a rope, before testing (left) and at locking (right). **c-d**, Photos of double overhand knots (5_1) tied in an inextensible elastomeric rod (**c**) and in a rope (**d**), before testing (left) and at capsizing or locking (right). **e**, Pulling force, F/Mg, as a function of displacement, δ/D, for the systems represented in **b**, **c-d**, and Figure 5.1.

loaded (right) configurations. Figure 5.9**c** shows the same 5_1 knot on the same rope used in Figure 5.9**b**. Similarly to the protocol introduced in Section 5.2.4, a dead weight of Mg with $M = 0.2\,\mathrm{Kg}$ is attached to the free end of the knotted system.

In Figure 5.9**e**, we present force-displacement curves (F/Mg vs. δ/D), analogous to Figure 5.6**a** obtained by pulling the above 4_1 and 5_1 knots for both the elastic rod and the braided rope, onto the stopper plate. For the knots tied on the braided ropes, we find sharp monotonically increasing pulling forces, without capsizing (up to the practical limit of our apparatus; $F = 30Mg$). By contrast, similar to the 4_1 knot studied in the previous sections, the 5_1 knot tied on the elastic rope capsizes (as evidenced by the undulations in the data), which we regard as failure. Overall, we observe that the mechanical behavior of stopper knots tied in braided ropes is qualitatively different than those on elastic rods. The absence of capsizing in the braided rope case may be attributed to the decoupling between C and B, with torsion being energetically more costly than bending.

5.8 Summary and Outlook

Stopper knots are typically used in applications where they should lock at a specific location of the filament, even when pushed against a blockage, thereby preventing the end of a rope from passing through an orifice. For instance, a stopper knot tied to the end of a climbing rope prevents it from retracing through a narrow passage in the climber's belay device. Numerous other applications of stopper knots are found in the stringing of tennis rackets, sailing, and sewing.

In this Chapter, we focused on the capsizing mechanism of stopper knots as their first mode of failure, without considering the possibility of fracture. We investigated the source of capsizing and how it can be delayed on the figure-eight knot by using model precision experiments and Finite Element simulations. We found that capsizing results from friction-induced rod twisting in the loop, as it is pressed against the stopper plate. The capsizing is therefore delayed for lower rod-rod friction coefficients and higher rod-plate friction coefficients. Since torsional stiffness is higher for shorter rod segments, tighter knots with a shorter total arc length of their upper loop yield higher peak forces at capsizing. Further, we quantified the decoupling of torsional and bending rigidities in climbing and multi-functional ropes, which typically have a higher torsional energy penalty. Given the variety of knot topologies, it is not obvious if the studied capsizing mechanism can be generalized to a whole subgroup of knot topologies, and should be tested case-by-case in future studies.

We showed that stopper knots, tied in isotropic rods, capsize for loose and tight configurations since low torsional rigidities facilitate rod twisting. For stopper knots tied on braided ropes, we did not observe capsizing when the knot size and the rope diameter were of the same order of magnitude, $H \sim D$. We recognize that the comparative observations between elastic and braided systems remained mostly qualitative and that a detailed quantitative comparison would be inappropriate since the two systems have different frictional properties. We hope that our observations will instigate future quantitative analysis of stopper knots in braided rope systems, taking the elastic case that we studied in detail as a starting point.

6 Strength of Surgical Knots

In this Chapter, we seek to establish operational and safety guidelines on the mechanical strength of surgical sliding knots. We develop a physical model system to study the knot strength by systematically varying the tying pre-tension to set distinctive levels of knot tightness. Throughout, we use commercial polypropylene suturing monofilaments that are common in surgical practice. The focus is put on *tight, sliding knots*, ranging from the simple sliding granny knot, S||S, to multiple-throw knots in their sliding conformation. We uncover power-law behavior for the untying strength of these knots as a function of the applied pre-tension. Next, we analyze knots from an experienced surgeon and find that they intuitively target the middle of this power-law region, leaving a safety clearance between the regime where the knot is too loose to be functional and the regime of filament fracture. Further, we explore the effects of the number of throws and the knot topology ('||' vs. 'S×S'-throws). To further gain insight into the key role of friction on knot safety, we performed FEM simulations of plastic knots with varying values of friction coefficient. The underlying elasto-plastic constitutive model was calibrated on experimental results from uni-axial and bending material responses. Tying, tightening and untying sliding knots with different frictional contact interactions allow us to relate the knot strength to the underlying normal contact forces in the knot. Finally, we propose a normalization that collapses all our experimental and numerical data onto a master curve predicting the knot strength of tight knots, covering all sliding knot conformations we investigated and a wide range of friction coefficients.

The text and figures in this Chapter are adapted from the unpublished manuscript that we are currently preparing for submission to a journal, in collaboration with Changyeob Baek, Paul Grandgeorge, Shawn A. Chester, and Pedro M. Reis, as well as Dr. Samia Guerid, an independent plastic surgeon in Lausanne, Switzerland.

6.1 Literature Review and Motivation

Surgery, a word rooted etymologically in “handwork" [121], is a delicate craft. Similarly to the precision of the applied incisions, high-quality suturing also requires optimal manual skills that are only mastered by surgeons after years of practice and experience. Knots are central to surgical procedures, where they are used as ligatures to bind and lock surgical threads during suturing [24, 25, 26]. Importantly, knots are the weakest link in a suture [26, 122, 123], with disastrous consequences if a knotted suture fails to perform its functions. For example, massive bleeding may occur when the suture loop surrounding a vessel becomes untied or breaks, leading to wound dehiscence [124], or an incisional hernia may follow knot disruption [125, 126]. Sugerman et al. [127] reported that incisional hernia can be as high as 20% within the first year following midline laparatomy, one of the most common surgical procedure [127]. When compared to braided filaments, monofilaments are more challenging to ensure mechanical knot safety while having the advantage of lower infection risks [128]. Besides unraveling, another common failure mode is suture rupture, which was studied for various filament materials and knot types [102, 123, 74, 129].

Surgeons tie sliding knots on a daily basis, consciously or unwittingly [130], and it was demonstrated that all intended flat knots tied in monofilaments capsize into sliding conformation in vivo [131]. Sliding knots consist of a series of half-hitches around a nearly straight segment of filament under tension. Depending on the direction of each throw, two different topologies are distinguished, acting as building blocks for other surgical knot configurations: (i) the sliding granny knot and (ii) the sliding square knot. A simple notation to describe these knot configurations was first introduced by Tera and Aberg [130] and developed subsequently [122, 132, 116, 74]: ‘S’ stands for sliding throws, ‘$||$’ indicates identical throws, and ‘$\times$’ refers to non-identical throws. As such, the sliding granny knot with two identical throws is represented as (S$||$S), and the sliding square knot with two non-identical as (S$\times$S). In a more complex example, the S$||$S$\times$S configuration describes a sliding granny knot followed by a sliding square knot. We will use this notation throughout the present Chapter.

Although a high variability of knot tying techniques has been reported between surgeons [133], Trimbos et al. [122], Ivy et al. [134], Silver et al. [135] showed that adding additional throws in a knot consistently decreases untying rates. Also, the tying pre-tension (i.e., the tension applied by the surgeon to tighten each throw) appears to rely more on individual perception than the level of experience [136]. Further, even if the importance of mechanical analysis of knots has long been recognized in the medical profession, existing guidelines for best practices rely primarily on empirical observations gathered from historical experience, not on a physics-based structural analysis [122]. Despite their broad and practical relevance, the predictive understanding of the underlying physical mechanisms in knots remains crude. On the one hand, the classic mathematical theory of knots involves the study of purely geometric models of filaments tied in their tightest knot shape [50, 97, 99, 65, 112, 100, 107, 108], as introduced in Chapter 1, Section 1.4 and covered in Chapter 4. However, localized elastic deformation and contact friction, which are essential in physical knots, are not captured by the purely geometric abstractions [78, 90]. On the other hand, elasticity and frictional interactions were considered (at least partially) in one-dimensional elastic rod models based on the theory of elastic Kirchhoff rods [61, 63, 64]. Still, and as mentioned throughout this Thesis, this framework is limited to loose knots, and cannot capture the mechanical behavior of tight elastic knots with their three-dimensional deformation [62]. Besides the challenges related to topology, tightness, 3D elasticity, contact shapes and frictional interactions between filaments in tight contact, surgical monofilaments undergo high plastic deformation [111, 137]. The consequences and potentials of *plasticity* in functional knots have, to the best of our knowledge, not been considered in knot mechanics to date.

Research questions: In this Chapter, we aim to establish operational and safety guidelines on the mechanical strength of surgical sliding knots. We will address the following research questions:

- How does the strength of surgical sliding knots depend on the applied tying pre-tension?
- Do additional sliding throws increase knot safety? If yes, what is the relationship between the number of applied throws and the knot strength?
- Is the direction of the sliding throw (sliding granny versus square knot) a factor in setting the sliding resistance of the knot?
- What is the range of tying pre-tension, and consequently the resulting range of knot strength, that an experienced surgeon targets intuitively?
- How does the strength of surgical knots tied by an experienced surgeon compare to those tied by a training (less experienced) surgeon?
- How does the self-contact friction coefficient of suturing filaments influence knot strength?
- What is the role of plastic deformation of the polymer filaments, in addition to topology, geometry, elasticity and friction, in setting normal contact forces, which in turn should relate to the strength of tight surgical knots?

6.2 Failure of Surgical Sliding Knots

In the photograph of Figure 6.1**A**, a surgeon ties a series of half-hitch throws in the common polypropylene suturing filament (Prolene, Ethicon Inc., Johnson & Johnson). Throughout this Chapter, we will use this monofilament of circular cross section and area, A, in the diameters of 0.25 or 0.49 mm (USP designation 3-0 and 1, respectively [138]). The yield strength of as-received Prolene was determined from uniaxial stress-strain measurements to be $\sigma_Y = 19.1\,\mathrm{MPa}$ (from the 0.1% offset yield point [139]).

Typically, multiple suturing knots allow to bind tissues together, sealing an accident tear or a surgical incision [102, 140, 128]. By way of example, in Figure 6.1**B1-B3**, we present a series of photographs of a suture system on a custom-fabricated surgical practice pad. The practice pad was fabricated in-house using the silicone-based vinyl polysiloxane, VPS32 (Elite Double 32, Zhermack) with two colored layers (each 2 mm in thickness) for visualization purposes. This suturing system consists of three stitches (S||S×S each) loaded by a gradually increasing far-field uniaxial stress field of magnitude σ_∞. To visualize a typical failure mode, the top and bottom knots (k_1 and k_3, respectively), were made tighter than the middle knot (k_2). At a sufficiently large stress-level, the filament of the knot, k_2, starts sliding (Figure 6.1**B2**), until it completely slips through and, therefore, no longer fulfills its binding function (Figure 6.1**B3**). In Figure 6.1**C1-C2**, we present an optical-microscope image of the two possible sliding knot topologies: the S||S (**C1**) and the S×S (**C2**) knots. The depicted knots were machine-tied using a Universal Testing Machine (UTM): Instron 5943 in its horizontal position. Below, we show the corresponding topological diagrams.

6.2.1 Procedure to Tie Surgical Knots

To achieve reproducible results on the knot strength, we developed a well-defined protocol to systematically tie and test surgical knots. In what follows, first, we describe the procedure to tie the various knot topologies on a rigid pin with the relevant mechanical and geometric parameters. Second, we detail the subsequent mechanical tests that enabled the measurements of the knot strength.

In Figure 6.1**C** and **D**, we present optical-microscope images (top) of S||S and the S×S knots, tightened using a UTM (universal testing machine, Instron 5943), along with their corresponding topological diagram (bottom). The knots (surgeon- and machine-tied) were tied around rigid 3D-printed pins (stereolithography 3D-printer: Form 2, Formlabs; Clear V4 resin), with a flat upper surface of width, $2L = 6\,\mathrm{mm}$ (Figure 6.1**E**). This pin geometry was chosen based on the common rule for skin closures [141], prescribing a distance between the entry point of the

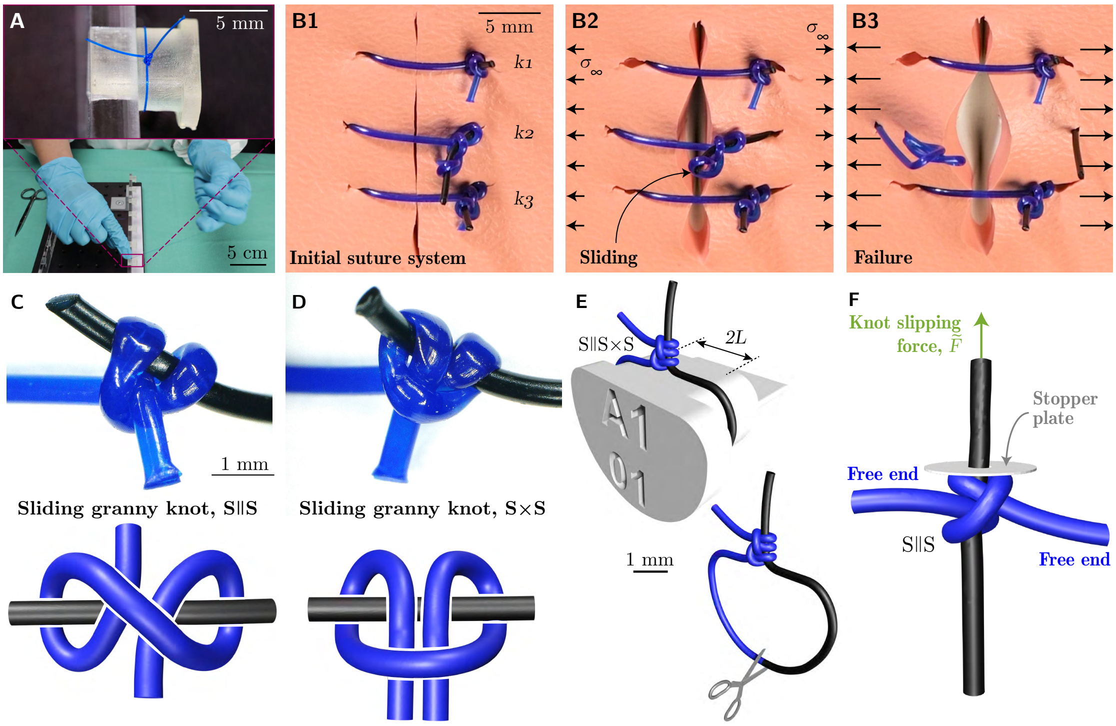
A
5 mm
5 cm
B1
5 mm
k_1
k_2
k_3
Initial suture system
B2
σ_∞
σ_∞
Sliding
B3
Failure
C
1 mm
Sliding granny knot, S||S
D
Sliding granny knot, S×S
E
S||S×S
$2L$
A1
01
1 mm
F
Knot slipping force, $\tilde{F}$
Stopper plate
Free end
S||S
Free end

Figure 6.1: **Failure of surgical sliding knots. A**, Photograph of the tying of a common sliding knot by an experienced surgeon in a Prolene polypropylene filament on a rigid support. **B1-B3**, Photographs illustrating knot safety and sliding for different tightness of the S||S×S knot in a suture system on a practice pad, at increasing levels of the far-field stress, σ_∞. The S||S×S knot is tied in a blue- and black-colored monofilaments (Prolene 1 and Ethilon 1, respectively). **C,D** Optical-microscope image (top) and topological diagram (bottom) of the S||S (C), and S×S (D) sliding-knot topologies. **E** Schematic of the S||S×S knot tied around a 3D-printed pin and visualization of the cutting location in the suture loop. **F** FEM-computed configuration for a S||S knot tied with a pre-tension of $\tilde{T} = 10.9$. The same configuration is implemented in the mechanical testing experiments to measure the slipping force, $\tilde{F}$, of the S||S knot.

needle and the wound edge, L, equal to the thickness of the tissue, ranging from 1 to 4 mm in the human body. After the half-hitch (identical or non-identical throw) was set manually in its loose configuration on the rigid pin, the two free extremities of the filament were clamped to the UTM. The tying protocol involved a displacement-controlled knot tightening followed by a load-controlled holding step to account for any viscous material effects. The knot was tightened with a pulling speed of 1 mm/s (constant engineering strain rate $\dot{\varepsilon} = 0.01/\text{s}$) up to the set tying pre-tension, which, subsequently, was held constant during 100 s. This protocol was repeated for any additional throw.

6.2.2 Mechanical Testing to Measure the Knot Strength

For the remainder of this Chapter, we will focus on the untying of surgical knots to extract information on the quality and safety of sliding surgical knots. To this end, the loop surrounding the pin was cut open (Figure 6.1**E**), and the protruding sliding strand (extremity of the black filament at the cutting location) was threaded through the hole of a stopper plate, as schematized in Figure 6.1**F** for the S||S knot. Then, the knotted configuration was pulled against this plate, enabling the measurement of the *knot slipping force*, $\tilde{F}$. In this model system, the rigid plate takes the role of the bound tissue in the suturing system, where tissue tractions on the suture could lead to wound dehiscence (Figure 6.1**B**).

In Figure 6.2**A1**, we present our experimental setup, where the protruding (sliding) strand, previously part of the loop, was first slid manually into a narrow clearance hole (0.30 mm diameter for 3-0 USP filament) in a flat, rigid acrylic plate (4 mm thickness). Using the UTM, the knot (S||S) is then pulled at the constant speed of 1 mm/s against the acrylic plate, which blocks the knot against vertical translation, leading to the sliding mechanism (Figure 6.2**A1**-**A4**). In Figure 6.2**B**, we plot the resulting dimensionless slipping force $\tilde{F} = F/(\sigma_Y A)$ as a function of normalized displacement $\tilde{\delta} = \delta/D$. Initially, the force increases as the vertical filament is pulled upward, and the knotted filament is pressed against the stopper plate (Figure 6.2**A2**). Past an initial transient, the force reaches a plateau, where the filament slides with a nearly constant slipping force (Figure 6.2**A3**). This characteristic force, denoted non-dimensionally as $\tilde{F}_0$, corresponds to the *knot strength* as it is ultimately responsible for the knot's untying (Figure 6.2**A4**). Note that we express dimensionless forces in units of $\sigma_Y A$ (σ_Y is the filament yield strength); applied dimensionless tensions greater than 1 involve plastic deformation of the straight filament strand.

6.3 Effect of Experience of the Surgeon on Strength of Knots

von Trotha et al. [136] conducted an extensive exploratory study to analyze whether surgical experience affects the reproducibility of the hand suturing tension. Against the author's expectations, no significant differences were detected between different subgroups based on surgical experience.

In our work work, we seek to contrast the knot strength quality between a surgeon with more than ten years of experience (S. Guerid, M.D., independent) versus the ones tied by a medical intern with less than one year of experience. Both were asked to tie 50 S||S×S knots with an adequate tying pre-tension on rigid pins. The specific goal of the study was not known by the subjects a priori so as not to bias the results. We disqualified samples that were accidentally

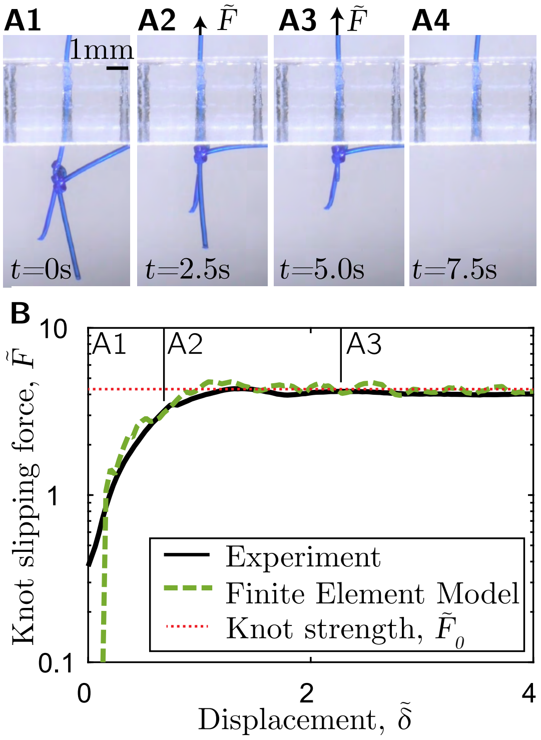

Figure 6.2: **Measuring the strength of a S||S knot. A1-A4**, Sequence of photographs during mechanical testing, visualizing the sliding process of a previously tied knot that is pulled against a stopper plate to measure the slipping force, $\tilde{F}$. **B**, Representative curves (experiments and FEM) of $\tilde{F}$ versus displacement, $\tilde{\delta} = \delta/D$. The plateau of the curves defines the knot strength, $\tilde{F}_0$. The points A1, A2, and A3 correspond to the photographs in (A1-A3). The S||S knot was tied to a pre-tension of $\tilde{T} = 10.9$.

tied with different knot topologies, leaving 38 valid surgeon-tied and 22 valid intern-tied knots. In Figure 6.3**A**, we plot the histogram of the untying knot strength, $\tilde{F}_0$, of S||S×S knots tied by the surgeon. Similarly, the results by the medical intern are presented in Figure 6.3**C**.

Even though both the surgeon and the intern span a similar range of knot strength, $1.5 < \tilde{F}_0 < 7.5$, the intern tends to tie knots with lower resistance to sliding. By contrast, the experienced surgeon achieves a quasi-uniform distribution of the knot strength (see Figure 6.3**A**). This observation is confirmed by the summarizing box plots in Figure 6.3**B**, showing a median knot strength of the surgeon of $\tilde{F}_{0,\,\text{surgeon}} = 3.2$ versus $\tilde{F}_{0,\,\text{intern}} = 2.5$ of the medical intern. Further, the highest knot strengths achieved by the intern are evaluated as outliers (more than 1.5 times the interquartile range away from the 75th percentile), which confirms their hesitant application of tying pre-tensions. Finally, the notched visualization of the box plots (Figure 6.3**B**) displays the variability of the medians between the surgeon and intern data sets. Overlapping notches reveal that the median knot strengths between the surgeon and the intern are not significantly different (at the 5% significance level).

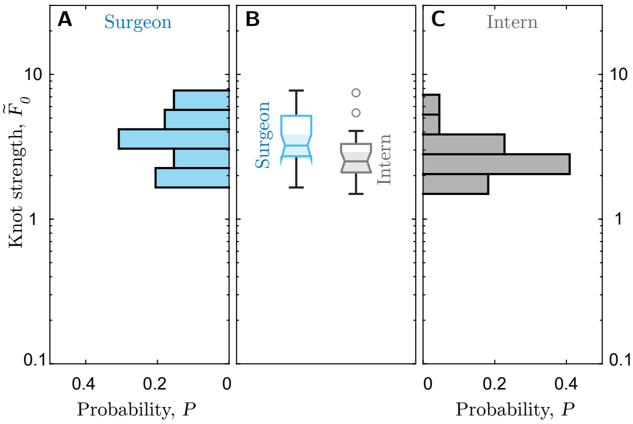

Figure 6.3: **Knot strength difference between an experienced surgeon and a medical intern.** **A**, Probability histogram showing knot strength distribution, $\tilde{F}_0$, of surgeon-tied S||S×S knots. **B**, Box plots summarizing the histogram representation of the knot strength, $\tilde{F}_0$, in **A** (surgeon) and **C** (intern). **C**, Probability histogram depicting the distribution of knot strength, $\tilde{F}_0$, of S||S×S knots tied by a medical intern.

6.4 Definition of a Tight Knot

A recurrent question when studying physical knots is the definition of their level of tightness. In Chapter 1, Section 1.5 we discussed the required separation of length scales between characteristic properties of a knotted rode to ensure the appropriateness of using the Kirchhoff rod model. Next, we take an alternative point of departure by adopting a definition of tightness that is more relevant in the context of surgical knots.

In general, the crossover between a loose and a tight physical knot is a continuous process without an abrupt change in geometry or mechanical behavior (see Figure 6.4**A**). Still, in this section, we will describe a method to define an approximate threshold for the separation between two regimes. This method combines a volumetric analysis based on X-ray micro-computed tomography (μCT), and a purely geometric rod model. We focus on the elementary, sliding granny knot, S||S, since knots with higher throw numbers are not necessary for the procedure described.

The notion of 'tightest knot' is well-defined in mathematical knot theory: a prescribed diameter and arc length of an *ideal* (perfectly flexible) filament allow to compute the tightest knot shape for the maximal end-to-end shortening [99, 90]. The filament is based on the ideality assumptions of an undeformable circular cross-section, inextensible centerline, and vanishing bending stiffness [100]. The centerline coordinates of the two filaments of a loose S||S knot tied in FEM served as an input into the software package, `Ridgerunner` by Ashton et al. [55]. The tightening program is based on a C-language code for tightening ideal knots [142], combining

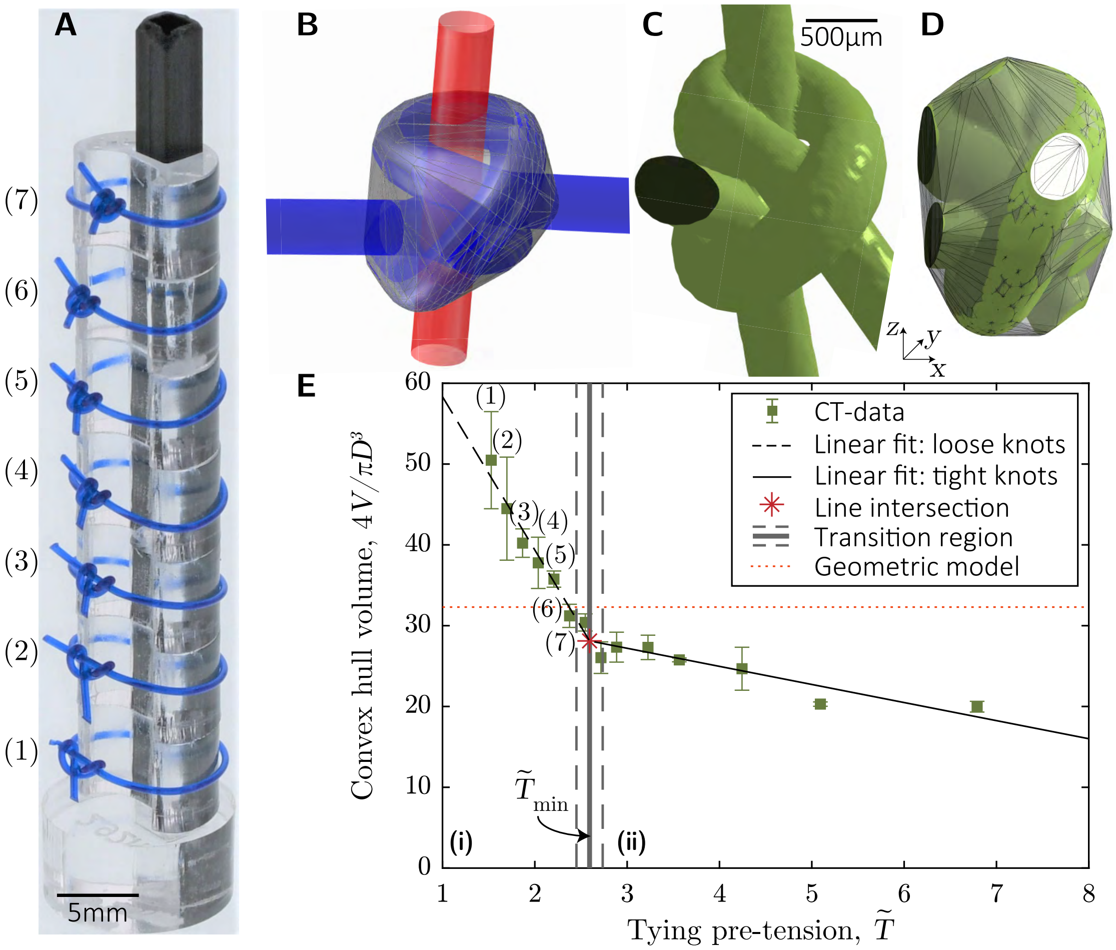

Figure 6.4: **Definition of the onset of tight knots.** **A**, Photograph of 7 sliding granny knots of different tightness (increasing from bottom to top) for μCT scanning. **B**, Tightest ideal S||S knot configuration. A convex hull is applied to the bulk knot, excluding the protruding strands. **C**,3D reconstructed S||S knot (7) with its four protruding strands. **D**, Bulk S||S knot after the protruding strands were removed by image processing. A convex hull is applied on the resulting volume. **E**, Normalized convex hull volume, $4V/\pi D^3$, as a function of the applied tying pre-tension, $\tilde{T}$, for experimental measurements. Two distinct slopes are described by linear fittings of seven consecutive data points; the first fit (dashed, black line) for low pre-tensions and the second one (continuous black line) for high pre-tensions. The intersection point with its uncertainty results from the best fits, and gives the transition region, $\tilde{T}_{\rm min} = 2.59 \pm 0.14$ (vertical line). The volume of the convex hull applied on the tightest, ideal S||S knot is shown by the dotted horizontal line.

a polygonal thickness version [143, 144, 54] with a Constrained Gradient Descent (CGD). In Figure 6.4**B**, we present the tightest S||S knot configuration, computed by Prof. Eric Rawdon (University of St. Thomas, USA). The compactness of the resulting knot was measured by applying a 3D convex hull (`convhulln` function in Matlab 2019, based on Qhull [145]), around the bulk knot, excluding the protruding filaments. The computed convex hull on the tightest sliding granny knot on an ideal rope is shown by the semi-transparent cover in Figure 6.4**B**, and has the dimensionless volume $4V_{\text{ideal}}/\pi D^3 \approx 32.3$.

Next, we apply a similar method to physical knots and quantify their compactness as a function of their tightness. First, the S||S knots were machine-tied on Prolene 1 USP (0.49 mm in diameter) monofilaments within the range of tying pre-tensions, $1.5 \leq \tilde{T} \leq 6.8$. Second, and as shown in the photograph in Figure 6.4**A**, the knot samples were mounted in an array, labeled (1)-(7), ordered from lower to higher tying pre-tensions, $\tilde{T}$. Then, the samples were slid into a narrow cylindrical sample holder (diameter 14 mm) and scanned with the maximum spatial resolution of 4.9 μm (voxel size) using μCT imaging (μCT100, Scanco Medical). In Figure 6.4**C**, we show the 3D reconstruction of the μCT-scanned tightest knot (7) with four protruding strands. To quantify only the volume of the knot, we excluded the four protruding strands by implementing the following strategy in Matlab (`Matlab 2019b, MathWorks`). The 3D image consisted of gray-scale values, representing the local material density of the voxels, ranging from 0 (non-occupied voxels outside filament) to 1 (occupied voxels inside filament). The data set was binarized using the voxel-value 0.5 as the threshold. The gradient profile (`gradient` function in Matlab), representing the change in the number of occupied voxels, was computed in each of the three spatial directions, $\{x, y, z\}$. The gradient profile (along each spatial direction) exhibits peaks (gradient values larger than 25) at the transition between the bulk knot and either surrounding air or a single protruding strand. Beyond each peak location, the voxel values were set to 0 (non-occupied voxels), such that the long protruding strands were cut off from the bulk knot, leaving a confined knot region. This technique was repeated by rotating the knot in each of the three spatial directions (incremental rotation angle: $\pi/4$ rad) and smoothly removing all protruding strands. Similar to the compactness measurement of the tightest ideal knot, we applied a 3D convex hull on the bulk physical knot, as shown by the semi-transparent cover in Figure 6.4**D**.

In Figure 6.4**E**, the measurements of the convex hull volume obtained from the μCT, $4V/\pi D^3$, are plotted against the tying pre-tension, $\tilde{T}$. Each experimental data point is based on three scanned knot samples. We observe two regimes with different slopes, whose transition was determined by performing a linear fit to each of the two regions and determining the intersect, fitting seven consecutive data points in each regime. The uncertainty of each best fit is at the basis for the error analysis on the intersection point. The resulting onset of tight knots is given by the tying pre-tension, $\tilde{T}_{\text{min}} = T_{\text{min}}/\sigma_Y A = 2.59 \pm 0.14$ (vertical line). At this tightness level, the experimental knot volume is $4V_0/\pi D^3 \approx 28.1$ and corresponds to knot (7) in Figure 6.4**A**. Interestingly, the transition between the two regimes is compatible with the result of the tightest knot volume from the purely geometric model, $4V_{\text{ideal}}/\pi D^3 \approx 32.3$, represented by the dotted horizontal line in Figure 6.4**E**. We conclude that the transition between the distinct behavior in volume reduction is an appropriate definition for the onset of tight knots. Note that the smaller volume of experimental knots at the transition is presumably due to cross-sectional deformations, which induce a decrease in volume for the same amount of confined arc length.

Note that since the knot tightness is dictated by the volume of each individual throw, the tight knot onset only depends on the applied tying pre-tension. In the main text, we report a change in the knot strength behavior between lower and higher tying pre-tensions, *i.e.*, between loose and tight knots. Remarkably, the transition between the two regimes corresponds to the transition tension determined using the critical knot volume described above, $\tilde{T}_{\text{min}}$, further confirming the validity of the knot volume method to describe the onset of tight knots.

6.5 Material Testing and Fracture

The operating conditions of a knot depend on the environmental conditions and on the detailed tying procedure of the surgeon. More specifically, the tying speed varies between individual surgeons, and the temperature of the operating room is often adapted to the type of surgery, the preferences of the surgeon, and the well-being of the patient. Polymeric suturing filaments typically exhibit viscoelastic and viscoplastic effects, and might behave differently under different temperature conditions. The described uncertainties in the surgical context call for a systematic investigation of the rate- and temperature-dependence on the mechanical response of Prolene monofilaments. Eventually, we aim to extract the typical upper limits for the tying force, $\tilde{T}_{\text{max}}$, at which filament fracture occurs.

Previous studies on the evaluation of the mechanical performance of surgical knots reported tying strain rates between $\dot{\varepsilon}_{\text{low}} = 0.0167/\text{s}$ and $\dot{\varepsilon}_{\text{rapid}} = 0.1667/\text{s}$, respectively [146, 132]. Moreover, the temperature in the operating room is adapted to the type of surgery and the well-being of the patient, avoiding intraoperative hypothermia (core temperature $< 35°\text{C}$) [147, 148]: in orthopedics, the room temperature is regulated to 16°C to reduce the infection risk [149]; in obstetrics, the well-being of the newborn requires a temperature of $20-21°\text{C}$ [150]; and in burn surgery, the operating room is heated to $30-40°\text{C}$ [151]. In addition to the room temperature, the suturing filaments are often in contact with body fluids, *e.g.* blood, which has the 37°C body temperature.

All the experiments presented later in this Chapter were performed at room temperature (21°C) and with constant engineering strain rate $\dot{\varepsilon} = 0.01/\text{s}$ for the knot tying and strength testing. In the next few paragraphs, we will perform mechanical tests on the material response and fracture force to evaluate the range of applicability of our results for different tying rates and operating room temperatures.

To achieve high strains in uniaxial tensile tests by avoiding the filament from breaking at the clamps, we used the standard ISO 11566 [152] to test the tensile properties of single-filament specimens. In Figure 6.5**A-B**, we present schematic diagrams illustrating the preparation of samples with either straight, un-knotted (**A**) or knotted (**B**) monofilaments. Since the knotted case is used for fracture tests, a S||S knot is manually tied on a rigid pin (see Section 6.2.1). For both cases, the Prolene 3-0 USP filament (straight or knotted) was glued with epoxy on a rectangular PVC shim stock frame (thickness: 0.1 mm, outer dimensions of the frame: 70x20 mm) with a gauge length of $L = 50\,\mathrm{mm}$. Besides the precise reference length, this technique also reinforces the filament at the ends by the epoxy layer, thus avoiding fracture at the clamping due to stress concentrations. Once the sample is clamped in a UTM, the frame is cut along the y-direction (orthogonal to the filament). Then, the mechanical response is measured by pulling along the axial direction of the filament (x-direction in Figure 6.5**A-B**) and recording the traction forces and the displacement.

Figure 6.5**C** plots the cyclic, engineering stress-strain behavior (maximum strain, $\varepsilon = 0.5$) of the straight Prolene 3-0 USP filament at room temperature (21°C) as a function of the applied strain rate, ranging from $\dot{\varepsilon} = 0.0025/\mathrm{s}$ to $\dot{\varepsilon} = 0.16/\mathrm{s}$. Each curve shows the mean (solid line) and standard deviation (shaded region) of three tests on five different Prolene 3-0 USP samples. We notice a slight increase in the stress quantities for higher strain rates. Given the explored range of strain rates (6300%), the relative change at $\varepsilon_{\mathrm{eng.}} = 0.5$ is 6.7% and, therefore, relatively small. The fracture strength is determined from the maximum recorded engineering tensile force on straight filaments and plotted by the blue box plots in Figure 6.5**D**. Similarly, the fracture strength remains nearly unchanged for different strain rates. Adding a S||S knot to the filament reduces the fracture strength by 40 – 50% (see gray box plots), in accordance to the observations reported by Pierański et al. [65]. Further, we observe that the fracture strength of a knotted filament decreases for higher strain rates.

In Figure 6.5**E**, we present results for the engineering stress-strain response of filaments under cyclically-loading (constant strain rate, $\dot{\varepsilon} = 0.01/\mathrm{s}$) while controlling the temperature. Tests were conducted at room temperature (21°C), at the human body temperature (37°C), and at a high temperature of 45°C. Three tests on three different Prolene 3-0 USP samples were performed for each curve in Figure 6.5**E**. High reproducibility was achieved and is visible by the small uncertainty interval (shaded region) around the average curve (solid curve). The Prolene filaments are clearly temperature-dependent, exhibiting softening in their mechanical response for higher temperatures. This trend is less visible in the fracture strength of S||S-

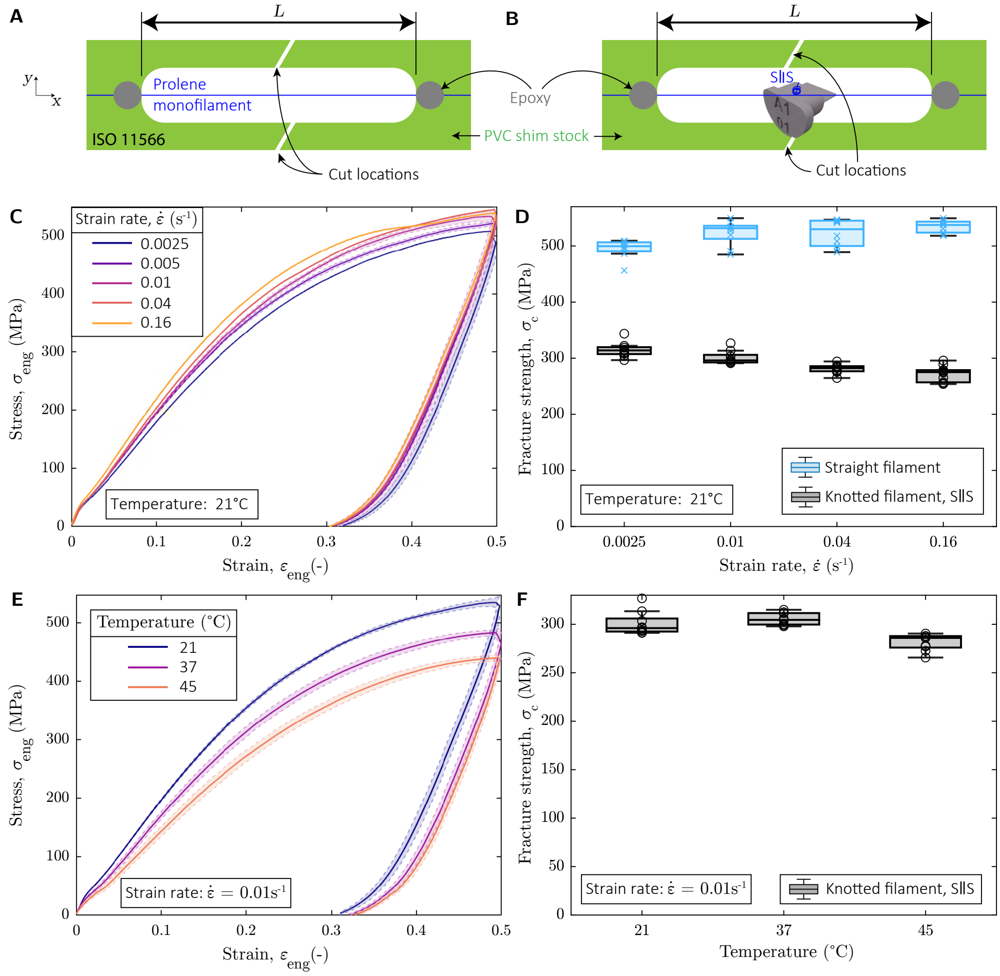

Figure 6.5: **Rate- and temperature-dependence of Prolene 3-0 USP monofilaments.** **A**, Schematic of a straight, unknotted Prolene monofilament glued with epoxy on a frame of PVC shim stock, setting the gauge length, L (following ISO 11566 [152]). **B**, The same testing technique as in **A**, with the addition of a S||S knot tied on a rigid pin. **C**, Rate-dependence on the engineering stress-strain behavior of straight filaments, recorded at room temperature (21°C). **D**, Rate-dependence on the fracture strength, σ_c, of straight and knotted (S||S) filaments, at room temperature (21°C). **E**, Temperature-dependence on the engineering stress-strain response of straight filaments, measured at a strain rate, $\dot{\varepsilon} = 0.01/\text{s}$. **F**, Temperature-dependence on the fracture strength, σ_c, of knotted (S||S) filaments, at a strain rate, $\dot{\varepsilon} = 0.01/\text{s}$.

knotted filaments, plotted in Figure 6.5**F** as a function of the three temperature-regulated environments. Still, the relative difference between the median values of the fracture strength at 21°C versus 45°C is only 3.6%.

As expected, the Prolene monofilaments show a rate- and temperature-dependence in the mechanical response of straight filaments. In the current case study, we are, however, largely concerned with the uncertainty of the fracture strength in knotted samples. Relative changes of 12.3% and 6.1% are to be expected for the whole range of explored strain rates ($\dot{\varepsilon} = [0.0025 - 0.16]/\mathrm{s}$) and temperature values ($21 - 45°\mathrm{C}$), respectively. Considering the vast range of parameters, we evaluate the rate- and temperature-dependence as small. Consequently, we will consider the mean fracture strength with its standard deviation, $\sigma_\mathrm{c} = 300.6\,\mathrm{MPa} \pm 12.1\,\mathrm{MPa}$, for the case of a strain rate, $\dot{\varepsilon} = 0.01/\mathrm{s}$, and at room temperature (21°C). Finally, the normalized tying tension, $\tilde{T}_\mathrm{max} = \sigma_\mathrm{c}/\sigma_Y = 15.74 \pm 0.63$, will be considered as the upper force limit for knotted Prolene monofilaments.

6.6 Dependence of the Knot Strength on Pre-Tension and Topology

From the mechanical tests introduced in Figure 6.1**F**, we characterize the untying knot strength, $\tilde{F}_0$, by systematically varying the tying pre-tension, $\tilde{T}$, and the number of throws in the knot, n; i.e., its topology. First, we focus on the S||S×S topology ($n = 3$), applying an equal tying pre-tension on each throw. Different levels of tying pre-tension in the knotting process can lead to the following three distinct regimes:

(i) Loose knots, for $\tilde{T} < \tilde{T}_\mathrm{min}$;

(ii) Tight knots, for $\tilde{T}_\mathrm{min} \leq \tilde{T} \leq \tilde{T}_\mathrm{max}$; and

(iii) Filament fracture, for $\tilde{T} > \tilde{T}_\mathrm{max}$.

Photographs of knots in these three regimes are presented in Figure 6.6**A** for: (i) loose knots ($\tilde{T} = 1.5$), (ii) tight knots ($\tilde{T} = 8.5$), and (iii) a broken filament at the last throw ($\tilde{T} = 20$). In the subsequent Sections, we will take a closer look at the relevant range of tying pre-tensions applied by surgeons and the corresponding knot strength as a function of the number of throws and knot topology.

6.6.1 Intermediate Tightness Regime

The volumetric study in Section 6.4 enabled us to define the minimum knot tying pre-tension, $\tilde{T}_\mathrm{min} = T_\mathrm{min}/\sigma_Y A = 2.59 \pm 0.14$, (represented in Figure 6.6**B** by the first vertical line), below which the knot is considered to be loose. Remarkably, the transition between the two regimes, (i) and (ii), corresponds to the determined critical knot volume, $\tilde{T}_\mathrm{min}$, which, therefore, can be considered as an appropriate quantity to describe the onset of tight knots. We focus on the intermediate region (ii) above the onset of tight knots, where the knot strength is consistent with a power-law increase:

$$\tilde{F}_0 = \tilde{K}\tilde{T}^{\alpha}, \tag{6.1}$$

which provides an excellent fit to the experimental data in Figure 6.6**B**, within the intermediate regime, up to filament fracture. The upper limit of the tying pre-tension is determined by the rate- and temperature-dependent fracture tests on knotted Prolene filaments, as described above, in Section 6.5, and represented by the vertical line at $\tilde{T}_{\mathrm{max}} = T_{\mathrm{max}}/\sigma_Y A = 15.74 \pm 0.63$.

6.6.2 Mapping the Operating range of the Surgeon

We will now map the strength of knots tied by a surgeon onto the results from model experiments described in the previous Section. We asked our collaborator Dr. Samia Guerid, who is an experienced independent plastic surgeon in Lausanne, Switzerland, to hand-tie 38 knots onto a rigid pin using the same Prolene filament and with the same ($\mathrm{S}||\mathrm{S}\times\mathrm{S}$) topology of the model experiments. The surgeon was instructed to tie each knot identically to what they would do their routine suturing procedures. Naturally, since these knot were tied by manually, the level of pre-tension was unknown. A photograph of a representative surgeon-tied knot is shown in Figure 6.6**C**).

Each of these 38 surgeon-tied knots was then tested mechanically by pushing them against a rigid stopper plate to measure the knot strength, $\tilde{F}_0$, using the same protocol of the model experiments described in the previous Section. The corresponding histogram of $\tilde{F}_0$ is presented in Figure 6.6**D**, exhibiting a nearly uniform distribution in the range, $1.7 < \tilde{F}_0 < 7.7$. Note that the data in Figure 6.6**D** is the same as in Figure 6.3**A**, which is repeated for convenience. This probability distribution of the surgeon-tied knots is summarized by the box plot with a median strength 3.2 and lower and upper quartiles at 2.7 and 5.2, respectively. Projecting the median knot strength as well as the interquartile ranges onto the empirically fitted knot strength of the $\mathrm{S}||\mathrm{S}\times\mathrm{S}$ knot (represented by blue shade from Figure 6.6**D** to Figure 6.6**B**) provides an estimation for the operating range of pre-tensions for surgeon-tied knots, $\tilde{T}_{\mathrm{surgeon}}$.

Interestingly, we find that $\tilde{T}_{\mathrm{surgeon}} \in [\tilde{T}_{\mathrm{min}}, \tilde{T}_{\mathrm{max}}]$. The surgeon is able to target in the middle of the intermediate regime (ii), for tight knots, identified by our model experiments, while leaving safety clearances between loose knot configurations, $\tilde{T}_{\mathrm{min}}$, and filament fracture, $\tilde{T}_{\mathrm{max}}$.

6.6.3 Enhancing Knot Safety with Additional Number of Throws

Thus far, we have focused on the $\mathrm{S}||\mathrm{S}\times\mathrm{S}$ knot since it represents the simplest configuration comprising both of the sliding topologies of interest; $\mathrm{S}||\mathrm{S}$ and $\mathrm{S}\times\mathrm{S}$. However, surgeons typically tie more than three half-hitches, with additional trows, to further increase knot safety.

To explore the effect of the number of throws, n, on the knot strength, we return to the model

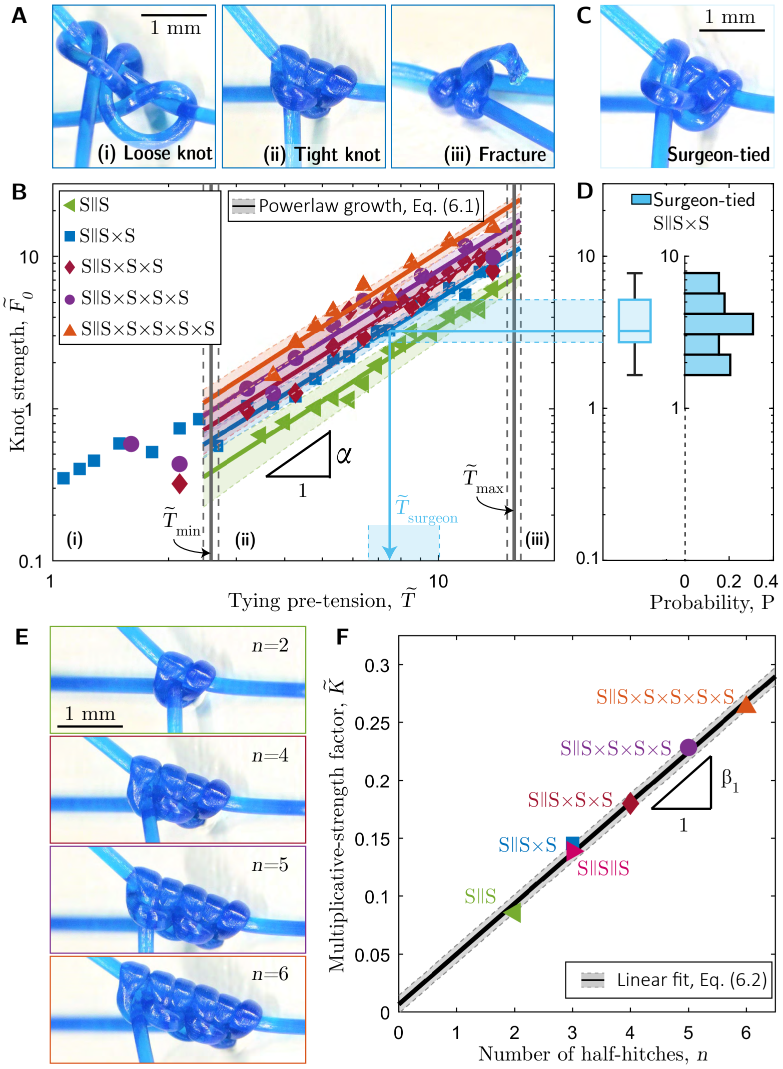

Figure 6.6: **Dependence of the knot strength on pre-tension and topology. A**, Photographs of representative S||S×S knots at different level of tightness: (i) loose knot, (ii) tight knot, (iii) fracture of the last throw. **B**, Normalized knot strength, $\tilde{F}_0$, as a function of the normalized tying pre-tension, $\tilde{T}$, for knot topologies ranging from 2-throw to 6-throw sliding knots. The bounds of the intermediate region (ii), $\tilde{T}_{\text{min}}$ and $\tilde{T}_{\text{max}}$, are represented by vertical lines, respectively, with their confidence interval. **C**, Photograph of a surgeon-tied S||S×S knot. **D**, Histogram and summarizing box-plot of knot strength measurements from surgeon-tied S||S×S knots. Since the tying pre-tension is unknown, the mapping on the experimental curve onto **B** (shaded region) shows the region of operation. **E**, Photographs of sliding knots with different number of throws, $n = \{2\,4\,5\,6\}$, tied with $\tilde{T} = 8.5$. **F**, Multiplicative-strength factor, $\tilde{K}$, of the fitted curves in **B** as a function of the number of throws, n, according to Eq. (6.2). The linear fit, $\tilde{K} = n\beta_1$, and the corresponding confidence interval are represented by the solid line and shaded region.

experiments and systematically investigate configurations with different numbers of throws $n = \{2, 4, 5, 6\}$. As shown in Figure 6.6**E**, all these configurations are realized by first tying a sliding granny knot, followed by a series of sliding square knots. In Figure 6.6**B**, their measured knot strength, $\tilde{F}_0$, is plotted as a function of the tying pre-tension, $\tilde{T}$. These more complex knots with additional throws exhibit the same power-law behavior – Eq. (6.1) – of the simpler S||S×S topology, with $\alpha = 1.59 \pm 0.03$ (with standard deviation lower than 2% of the average), albeit with different prefactors. This consistency of the exponent α across the different tested topologies is striking, considering the complexity of the geometries involved. With increasing number of throws, the untying knot strength is systematically increased by prefactor, which we denote the *multiplicative-strength factor*, $\tilde{K}$. In Figure 6.6**F**, we plot the fitted value of $\tilde{K}$ as a function of n, finding that, remarkably, the data follows the linear relation $\tilde{K} = \beta_1 n$, with $\beta_1 = 0.044 \pm 0.006$.

6.6.4 Effect of Topology on Knot Strength

In Figure 6.1**C**, we visualized the two topologies we considered for sliding knots, S||S and S×S, which are both based on two consecutive half-hitches. Although the topology differs for these two knots, we are interested in the resulting knot performance for a given tying pre-tension.

In Figure 6.7, we plot the knot strength, $\tilde{F}_0$, as a function of the applied tying pre-tension, $\tilde{T}$, for both the S||S×S and the S||S||S knot. Note that the first two throws are identical throws (same direction) for both knots to avoid contact effects from the underlying pin while tying. The final throw is then tied using a different topology. Here, we use a linear axis to better compare the response of the two knots, especially for higher tying pre-tensions. The knot strength data is consistent with a power-law increase, as described by Eq. (6.1). We find that the knot strength is equivalent for the two knot topologies throughout the whole range of tight knots.

We conclude that the resistance to sliding does not depend on the throw direction (identical vs. non-identical throws) in surgical sliding knots. In other words, the two topologies, S||S and S×S, are equivalent in terms of the untying knot strength. These observations suggest that our quest to understand the mechanical performance of complex surgical knots with various topological combinations of multiple throws can be reduced to rationalizing a single sliding knot ($n = 2$) with a single topology (*e.g.*, S||S).

Overall, combining the above observations, we have found that surgeon-tied sliding knots are in the tight knot regime, where the knot strength follows a power-law, Eq. (6.1), with a unique exponent, α, independently of the number of throws or the topological combination. Moreover, with each additional throw, the knot strength is described by a multiplicative-strength factor, $\tilde{K}$, which itself depends linearly on the number of throws, n, such that:

$$\tilde{F}_0 = \beta_1 n \tilde{T}^{\alpha}. \tag{6.2}$$

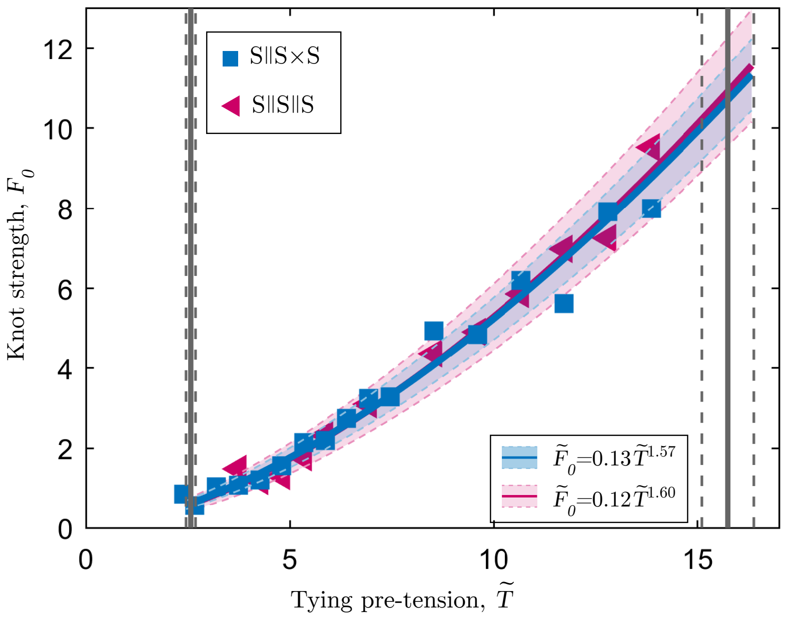

Figure 6.7: **Equivalence of knot topology.** Knot strength, $\tilde{F}_0$ as a function of applied tying pre-tension, $\tilde{T}$, comparing the performance between the S||S×S and the S||S||S knot.

6.7 Characterization of the Frictional-Contact Interactions

For the FEM simulations presented in the next Section 6.8, we will require an experimental measurement of the self-contacting friction coefficient of our Prolene filaments, which is tackled as described next.

Measuring the friction coefficient between two filaments in contact cannot be performed as described in Chapter 2, Section 2.5.2 since the polypropylene material with exactly the same surface finish as the suturing Prolene monofilaments is not commercially available in a flat sheet geometry. Therefore, we had to design a new experimental apparatus to measure the frictional properties of two *orthogonally-crossed* filaments in sliding contact. To this end, the upper end of the first filament (Prolene 1 USP) was attached to a 50-N load cell of the UTM while hanging a dead load of 100 g at the lower end straightens the intrinsically-curved filament. A second filament (Prolene 1 USP) was tightly coiled (10 windings) around a rigid acrylic post (20x20 mm with rounded corners), as shown in the photograph inset of Figure 6.8. Inspired by the apparatus reported in Grandgeorge et al. [33], the straight vertical filament was pressed by an annular ball bearing (external diameter: 30 mm) against the coiled filament with a normal load, F_n, using a mass–pulley system (not shown in the Figure). Next, the vertical filament was displaced upwards at a speed of 1 mm/s, which is the same displacement velocity imposed in the knot untying experiments.

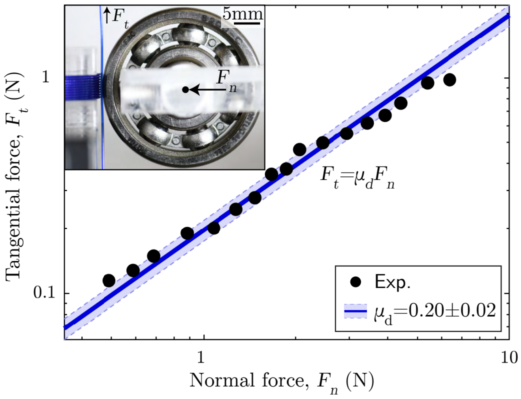

Figure 6.8: **Characterization of the kinematic friction coefficient between Prolene monofilaments.** Tangential force measurements, F_t, as a function of imposed normal force, F_n. The solid line and shaded region represent the linear fit and the corresponding confidence interval. The inset shows a photograph of the setup consisting of a vertical straight filament, which is pressed with the force, F_n, against a layer of coiled monofilaments by a ball bearing.

In Figure 6.8, we plot the measured tangential contact force, F_t, as a function of the imposed normal force, F_n. The relation between F_t and F_n is linear, as expected for Amontons-Coulomb friction behavior. The linear fit, $F_t = \mu_d F_n$ (solid line in Figure 6.8), of the experimental data over a wide range of normal loads, yields a dynamic friction coefficient, $\mu_d = 0.20 \pm 0.02$, which is in agreement with values reported in the literature for Prolene monofilaments [137], respectively. It is important to emphasize that the friction coefficient was measured in dry conditions, which, in a surgical environment, could correspond to dry skin operations. When surgery is executed in the presence of blood and other fluids, an even lower friction coefficient can be expected.

In this Section, we characterized the friction coefficient for self-contacting Prolene monofilaments, which will be important to validate our numerical simulations with experiments.

6.8 Modeling of Surgical Filaments

We proceed by combining the experimental results presented above with computer simulations performed using fully three-dimensional Finite Element Modeling (FEM). We seek to gain further physical insight into the underlying mechanism leading to the power-law growth of knot strength in the tight regime. Using the commercial package ABAQUS/EXPLICIT (Simulia, Dassault Systèmes), we simulated knotted filaments to probe physical quantities not readily available in experiments, especially the contact pressure field along the surface of the filament.

Along the way, to ensure accurate simulations of the physical knot using FEM, we will need to experimentally characterize the constitutive elasto-plastic behavior the Prolene filaments to calibrate the constitutive model, including fitting residual stresses.

6.8.1 Constitutive Elasto-Plastic Model

The 3D continuum-level constitutive model for elastic-viscoplastic mechanical behavior that we developed for the FEM simulations is based on Refs. [153, 154]. As such, only a summary of the relevant content is provided here. The implementation of the following framework into the Finite Element Model using a user-material was performed primarily by Prof. Shawn A. Chester (New Jersey Institute of Technology), who is also a co-author on the works in Ref. [153, 154], in the context of a collaboration with the author of this thesis.

Overall, the model includes isotropic hardening since the filaments only undergo one single loading cycle during the knot-tying and tightening process. Further, the model is rate-dependent, a choice that is supported by the data presented in Figure 6.5. The total deformation gradient is decomposed into elastic and plastic parts:

$$\mathbf{F} = \mathbf{F}^e \mathbf{F}^p. \tag{6.3}$$

We assume that plastic flow is incompressible, meaning that $\det \mathbf{F}^p = J^p = 1$, where $J = \det \mathbf{F}$. The evolution equation for $\mathbf{F}^p$ is

$$\frac{\mathrm{d}\mathbf{F}^p}{\mathrm{d}t} = \mathbf{D}^p \mathbf{F}^p. \tag{6.4}$$

The flow rule may be written in the form

$$\mathbf{D}^p = \sqrt{\frac{1}{2}} \nu^p \mathbf{N}^p, \tag{6.5}$$

where the equivalent plastic shear strain rate is

$$\nu^p = \nu_0 \left(\frac{\bar{\tau}}{S} \right)^{1/m}, \tag{6.6}$$

the equivalent shear stress is

$$\bar{\tau} = \sqrt{\frac{1}{2} (\mathbf{M}_0^e : \mathbf{M}_0^e)}, \tag{6.7}$$

and the direction of plastic flow is given by

$$\mathbf{N}^p = \frac{\mathbf{M}_0^e}{\sqrt{2}\bar{\tau}}. \tag{6.8}$$

In the expressions above, the notation $(\bullet)_0$ denotes the deviator of $(\bullet)$. The Mandel stress in Eq. (6.8) is given by the constitutive relation

$$\mathbf{M}^e = 2G\mathbf{E}^e + \lambda(\mathrm{Tr}\mathbf{E}^e)\mathbf{1} = 2G\mathbf{E}^e_0 + K(\mathrm{Tr}\mathbf{E}^e)\mathbf{1}, \tag{6.9}$$

where G, K, and $\lambda = K - (2/3)G$ are the shear modulus, bulk modulus, and Lamé parameter, respectively. It is important to note that the strain measure used is $\mathbf{E}^e = \ln \mathbf{U}^e$, where $\mathbf{U}^e$ is the elastic stretch, $\mathbf{F}^e = \mathbf{R}^e\mathbf{U}^e$, and accounts for large deformations. The Cauchy stress is related to the Mandel stress by

$$\mathbf{T} = J^{-1}\mathbf{R}^e\mathbf{M}^e\mathbf{R}^{e\top}. \tag{6.10}$$

The strength model is given by an evolution equation for the deformation resistance S, which enters in Eq. (6.6), taking the form

$$\dot{S} = h(S_{\mathrm{sat}} - S)\nu^p, \quad S(t=0) = S_0, \tag{6.11}$$

where S_{sat} is a saturation level for the deformation resistance, and h controls how quickly S approaches S_{sat}.

In summary, the elasto-viscoplastic model with isotropic hardening presented above involves the following material parameters, $(E, S_0, S_{\mathrm{sat}}, h)$.

6.8.2 Residual Stresses to Describe Unknown Deformation History

The Prolene filament used throughout the experiments came originally packaged in a stadium-shaped spool (with straight sides of length 55 mm and semi-circular caps of radius 10 mm) and exhibits natural curvature upon unpacking. As is common in plasticity problems, this prior loading history affects any subsequent material response. To account for this (unknown) deformation history in the FEM simulations, we consider the effective residual bending stress, σ_R, as a pre-defined stress field on the initially straight reference configuration of the filament and treat it as an additional fitting parameter. We specify σ_R by assuming elastic-perfectly plastic (small) deformation of a beam with a circular cross-section of diameter, D, with curvature $\kappa(x)$ along the axial direction, x, of the beam, the axial strain in the bending direction, y, can be expressed as $\varepsilon_{xx} = -\kappa(x)y$.

For a fully plastic beam with yield strength, σ_Y, the cross section consists of two regions: the lower half, $-D/2 \le y \le 0$, with $\sigma_{xx} = \sigma_Y$ and area, A_1; and the upper half, $0 \le y \le D/2$, with $\sigma_{xx} = -\sigma_Y$ and area, A_2. Thus, two regions of integration (A_1 and A_2) are considered to compute the bending moment:

$$M_p = -\int_{A_1} y\sigma_Y dA_1 - \int_{A_2} y(-\sigma_Y) dA_2 = \frac{D^3\sigma_Y}{6}. \tag{6.12}$$

The residual stress is then expressed as the difference between the fully loaded and the elastically unloaded case:

$$\sigma_{xx}(\text{unloaded}) = \sigma_{xx}(\text{loaded}) - \Delta\sigma_{xx}, \tag{6.13}$$

with the stress difference due to elastic spring-back:

$$\Delta\sigma_{xx} = E\Delta\varepsilon_{xx} = -E(\kappa_{\text{loaded}} - \kappa_{\text{unloaded}})y. \tag{6.14}$$

Further, from the moment-curvature relation, $M_{\text{loaded}} = EI(\kappa_{\text{loaded}} - \kappa_{\text{unloaded}})$, we get:

$$\kappa_{\text{loaded}} - \kappa_{\text{unloaded}} = \frac{M_{\text{loaded}}}{EI}. \tag{6.15}$$

Plugging Eq. (6.15) in Eq. (6.14), yields the axial stress difference:

$$\Delta\sigma_{xx} = -\frac{M_p y}{I}, \tag{6.16}$$

where we considered loading to the fully plastic state ($M_{\text{loaded}} \equiv M_p$). Thus, Eq. (6.13) is written in the form:

$$\sigma_{xx}(\text{unloaded}) = \sigma_{xx}(\text{loaded}) + \frac{M_p y}{I}. \tag{6.17}$$

Considering a fully plastic deformation ($\sigma_{xx}(\text{loaded}) = \pm\sigma_Y$), and plugging Eq. (6.12) into Eq. (6.17) gives the residual stress field as a function of the yield strength:

$$\sigma_R(y) = \begin{cases} \left(1 + \dfrac{32y}{3\pi D}\right)\sigma_Y & \text{for} \quad y < 0, \\ \left(-1 + \dfrac{32y}{3\pi D}\right)\sigma_Y & \text{for} \quad y > 0. \end{cases} \tag{6.18}$$

6.9 Calibration of the Material Model

The 3D continuum-level constitutive model for elastic-viscoplastic mechanical behavior presented in Section 6.8.1 needs to be calibrated against experimental measurements, which will be tackled below, in Section 6.9.1. Further, the residual stress formulation presented in Section 6.8.2 will require an additional calibration layer to account for unknown deformation history of the Prolene monofilaments, which will be tackled below, in Section 6.9.2.

In Figure 6.9**A**, we show characterization plots for the cyclic stress-strain behavior of a straight (un-knotted) Prolene monofilament (1 USP; gauge length, $L = 50\,\mathrm{mm}$; constant engineering strain rate $\dot{\varepsilon} = 0.01/\mathrm{s}$). We followed the ISO11566 protocol, which is appropriate for large strain measurements (see schematic inset in Figure 6.9**A**). The plot inset in Figure 6.9**A** quantifies the dissipated energy density, W, per cycle, which decreases by ≈ 500% between the first and the second cycle before reaching a steady-state. This seemingly large amount of dissipated energy, which is only observed in the first cycle and not in subsequent cycles, may be attributed to the unknown state of the material due to prior deformation history. Since the polymeric filaments can undergo plastic (irreversible) deformation for large strains, an appropriate plasticity (constitutive) model is required to reproduce the experimentally measured stress-strain curves in FEM. We interpret the straightening of the intrinsically-curved filament from the packaging and the preparation of the specimen for testing as the first loading cycle. To account for this first loading cycle, we apply the material parameter fitting on a cyclic uni-axial test of a pre-stretched filament ($\varepsilon_{\text{eng. pre-stretch}} = 25\%$).

In what follows, we will calibrate the material parameters of the model using the experimental data of uni-axial, cyclic tensile tests. Then, to account for the unknown deformation history of the filaments, the presence of residual stresses in bending is estimated by using a simple bending case.

6.9.1 Uniaxial tensile tests for Model Calibration

In summary, the elasto-viscoplastic model with isotropic hardening presented above involves the following material parameters, $(E, S_0, S_{\text{sat}}, h)$, which must be determined by fitting to the experimental data presented in Figure 6.9**B**, for the three consecutive loading and unloading cycles of a straight, un-knotted, and pre-stretched Prolene monofilament.

The 3D constitutive model has been specialized for uni-axial tension, and the reduced model is implemented into Matlab for the purpose of parameter calibration. These parameters are the Young's modulus, E, the initial yield strength, σ_0 (taken as the initial condition for S), the saturated yield strength, S_{sat}, and the initial hardening modulus, h. Based on the experimental data presented in Figure 6.9**B**, the built-in Matlab function `lsqnonlin` was used to perform a nonlinear least-square optimization of the four parameters with a prescribed initial guess and lower and upper bounds, as summarized in Table 6.1. The rate-sensitivity parameter was assumed as $m = 0.08$ in order to improve the numerical convergence of the optimization process, and the shear strain rate was set to $\nu_0 = 0.001$. Furthermore, we constrained the values of E using the initial slope of the test curves in the unloading region, which was measured to be $\approx 7000\,\mathrm{MPa}$. Assuming material incompressibility, the shear modulus is related to the Young's modulus by $G = E/3$. The optimization process yields the calibrated quantities presented in

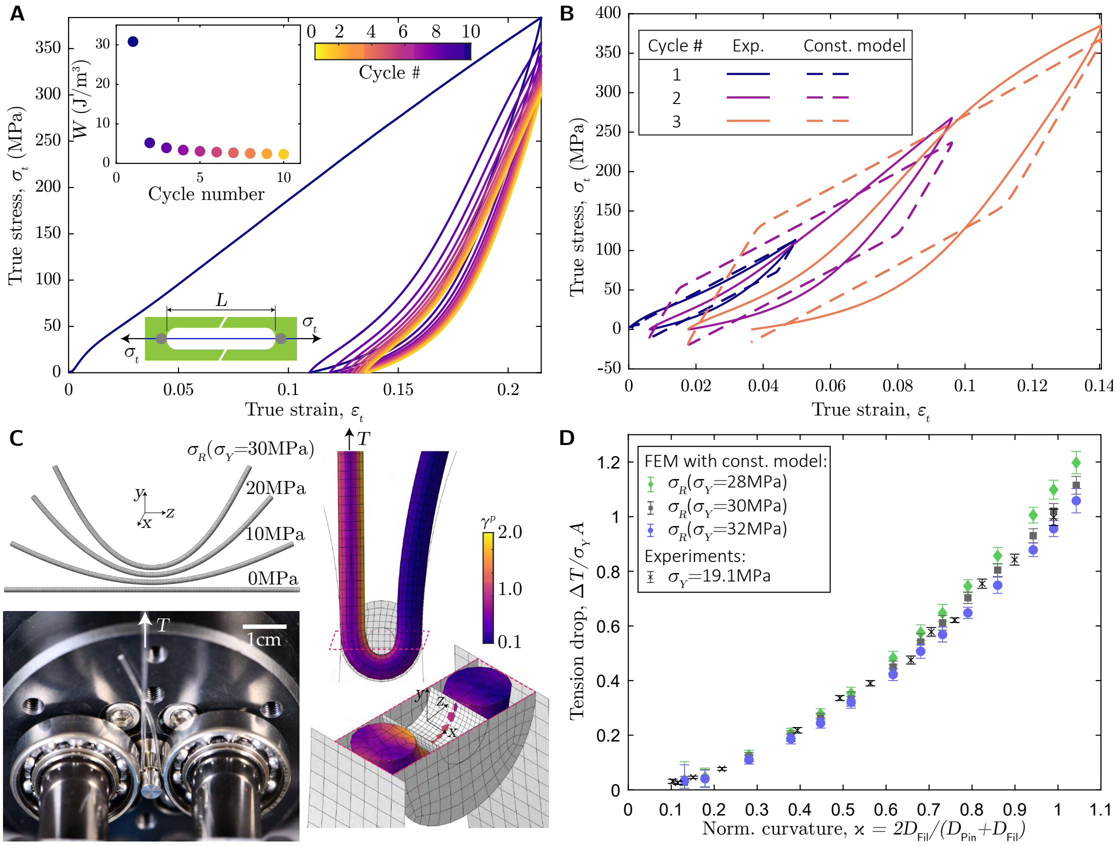

Figure 6.9: **Plasticity modeling of surgical filaments.** **A**, True stress, σ_t, as a function of true strain, ε_t, of Prolene 1 in a cyclic uniaxial tension test, for 10 cycles. The schematic (inset) illustrates the specimen preparation, and the inset quantifies the dissipated energy density, W, between 10 consecutive cycles. **B**, Cyclic tensile response of a pre-stretched filament with increasing maximum strain, plotted as true stress, σ_t, versus true strain, ε_t. A constitutive model for elastic-viscoplastic mechanical behavior is fit onto the experimental data. **C**, Deformed shape of the originally-straight filament in FEM before and after it has been subjected to residual bending stresses, $\sigma_R(\sigma_Y)$, with $\sigma_Y = \{10, 20, 30\}$ MPa, according to Eq. (6.18). *Bottom left:* close-up photo on the plastic capstan apparatus used to quantify plastic dissipation by measuring the tension drop, ΔT, across the two ends. *Right:* FEM snapshot of the plastic capstan system, visualizing equivalent plastic shear strain, γ^{p} in a side view and in the horizontal cutting plane (purple dashed line). **D**, Tension drop, $\Delta T/\sigma_Y A$, as a function of normalized curvature, $\kappa = 2D_{\mathrm{Fil}}/(D_{\mathrm{Pin}} + D_{\mathrm{Fil}})$. The plasticity material model is calibrated by tuning the residual stresses to match the experimental data by tuning the fitting parameter to $\sigma_Y = 30 \pm 2$ MPa.

Table 6.1, with the model fitted (dashed lines) to the experimental cyclic stress-strain curves (solid lines), as shown in Figure 6.9**B**.

Parameters:	E (MPa)	σ_0 (MPa)	σ_{Sat} (MPa)	h (MPa)
Initial guess	6000	5	50	2
Lower bound	5000	0.1	30	0.5
Upper bound	7000	30	450	20
Fitted param.	5060.9	1.25	137.5	0.5

$\rightarrow G{=}1687.0$ MPa

Table 6.1: **Calibration of material parameters using experimental data.**

6.9.2 Plastic Capstan Configuration to Calibrate the Residual Stress

The surgical filaments used throughout this study undergo unknown deformation during their manufacturing and packaging, leading to an intrinsic curvature. As is typical in plasticity problems, this prior loading history affects any subsequent material response. To account for this (unknown) deformation history in the FEM simulations, we consider the effective residual bending stress, σ_R, as a pre-defined stress field on the initially straight reference configuration of the filament and treat it as a fitting parameter. Since the true residual stress profile is unknown, we assume the perfectly plastic case in bending since the material is spooled for packaging and exhibits natural curvature upon unpacking. Following existing literature for elasto-plastic materials [155] for a fully plastic deformation, the residual stress field can be expressed as described by Eq. (6.18) in Section 6.8.2.

In Figure 6.9**C**, we show deformed filament configurations for different values of $\sigma_R(\sigma_Y)$, with $\sigma_Y = \{10, 20, 30\}$ MPa, applied on the initially-straight filament ($\sigma_R(\sigma_Y = 0\,\text{MPa})$). Note that different values of σ_R relate to different natural curvatures of the filament.

Our knotted monofilaments undergo significant plastic deformation in bending (see bent rest-shape of the untied knot, k_2, in Figure 6.1**B3**). Thus, we proceed by first testing the plasticity model for a filament in simple bending before applying it to simulate knotted configurations. In Figure 6.9**C** (bottom left), we show a photograph of the apparatus we developed to perform to calibrate the parameters of our plasticity model. We shall refer to this configuration as the *plastic capstan*. In this configuration, we quantify the tension drop, ΔT, between the free end and the pulled end of a Prolene monofilament (1 USP) passing through a grooved pin with the diameter in the range $0.5\,\text{mm} \leq D_{\text{Pin}} \leq 9\,\text{mm}$. Given that the pin is mounted on an air-bearing, and the two constraining ball-bearings minimize friction, the ensemble rotates as a frictionless gear when pulling the filament. As such, there are minimal sliding frictional dissipation effects; the dissipation is only due to plastic bending deformation of the filament around the pin, which causes the tension to drop between the two extremities. By contrast, in the classic capstan problem [28, 29], the tension drop is due to the friction interaction alone.

In FEM, we simulate this same plastic capstan configuration for filaments subjected to residual bending stresses. The pin of diameter, D_{Pin}, and the gap walls were simulated as rigid bodies according to the fabrication tolerances of the pins, leaving a groove of depth $D_{\text{Fil}} + 0.01\,\text{mm}$ and width $D_{\text{Fil}} + 0.11\,\text{mm}$. In Figure 6.9**C**, we present an FEM-computed configuration of the plastic capstan ($D_{\text{Pin}} = 0.5\,\text{mm}$), color-coded by the equivalent plastic shear strain, γ^p, which increases along the filament from the free end (right) to the pulled end (left) as a result of the plastic deformation accumulated. A horizontal cut (purple dashed line) at the height of the pin exposes the in-plane profile of γ^p. In Figure 6.9**D**, we plot experimental and FEM data for the normalized tension difference, $\Delta T/(\sigma_Y A)$, as a function of normalized curvature imposed by the pin of diameter D_{Pin} on the filament of diameter D_{Fil}: $\kappa = 2D_{\text{Fil}}/(D_{\text{Pin}} + D_{\text{Fil}})$. Tuning the residual stresses allows for the calibration of the numerical model by matching its results to the experimental data, thereby determining the fitting parameter. With the fitted value of $\sigma_R(\sigma_Y = 30 \pm 2\text{MPa})$, we find that the FEM simulations accurately represent the experimental data across the full range. Note that the fitted yield strength is of the same order as the experimentally-determined 0.1% offset yield strength, $\sigma_Y = 19.1\,\text{MPa}$ [139].

6.10 Knot Strength Established by Normal Contact Forces

Having validated and calibrated the FEM simulations using the plastic capstan system, we proceed to simulate S||S knots on a Prolene monofilament. In the commercial package ABAQUS/EXPLICIT (Simulia, Dassault Systèmes), two initially straight filaments were implemented, each with unit-diameter, $D_{\text{Fil}} = 1$. The filament (1) forming the two half-hitches was modeled with axial length, $L_1 = 35D_{\text{Fil}}$. The sliding filament (2) was chosen to be half as long. The two filaments were oriented such that their centerlines cross with a relative angle of 10°. Both filaments were meshed with 3D solid elements, enhanced with incompatible modes for bending (`C3D8I`). The number of elements along the axial direction was 230 for filament (1) and 115 for filament (2), with 40 elements per cross-section in both cases. Two circular plates ($5D_{\text{Fil}}$ in diameter, $0.1D_{\text{Fil}}$ in thickness) with a central clearance hole of diameter, $1.10D_{\text{Fil}}$, were modeled as rigid bodies and aligned with the centerline axis of filament (2), leaving a relative distance $7D_{\text{Fil}}$ between the two plates.

In an initial step, the central region of filament (1), $0.25L_1 < L_{\text{center}} < 0.75L_1$, was subject to the residual stress field $\sigma_R(\sigma_Y = 30 \pm 2\text{MPa})$ since the filament extremities are not part of the knot. Mimicking the tying procedure of the surgeon, a dead load ($Mg = 50\,\text{N}$) was applied to one of the extremities of filament (2), keeping the other end clamped. Next, by applying a sequence of prescribed displacements and rotations to control the nodes located at each end and the central coordinate of filament (1), two half-hitches were formed around filament

(2), corresponding to the sliding granny knot. A similar tying protocol has been introduced by Sano *et al.* [37], and described in Chapter 3, Section 3.2.5 in the context of the clove hitch knot. Both knots share the same topology but differentiate by their application: a clove hitch knot attaches a rod to a rigid cylinder (typically larger than the rod diameter), whereas the sliding granny knot is a binding knot, connecting two rods (of equal diameters). We made use of the tying algorithm used in Ref. [37], with minor adaptations to tie the S||S knots.

After the S||S topology was set, both rigid plates were displaced, leaving a relative distance of $6D_{\mathrm{Fil}}$, to help keep filament (2) in place (in addition to the applied dead load) during the subsequent tightening step. Then, the two extremities of filament (1) were gradually loaded by the tying pre-tension of the same magnitude, $\tilde{T}$, but in opposite directions to yield a symmetric knot. Next, the pre-tensions were released symmetrically to free the ends of filament (1), while one of the two plates was displaced along the centerline axis of filament (2), away from the actual system since, subsequently, it is no longer needed. Finally, the clamped boundary condition at the extremity of filament (2) was also released, such that the filament could be displaced with the constant unit-speed $1\,\mathrm{s}^{-1}$. Finally, the S||S knot was pulled against the rigid stopper plate, and the slipping force, $\tilde{F}$, was measured.

In Figure 6.1**D**, we presented a knotted configuration tied numerically by subjecting the horizontally-aligned filament strands to a tying pre-tension of $\tilde{T} = 10.9$. The corresponding force-displacement curve computed from FEM was presented in Figure 6.2**C** (dashed line), exhibiting excellent agreement against experiments, especially in the plateau region used to define the knot strength, $\tilde{F}_0$. Note that, at this stage, the FEM has no adjustable parameters with all model parameters and mechanical properties having been determined independently, including the calibration using the plastic capstan system.

As a final validation step of the numerical model, we compare the FEM-computed knot strength against experiments, over the full tightness range of the tight knots (ii) regime, $\tilde{T}_{\mathrm{min}} < \tilde{T} < \tilde{T}_{\mathrm{max}}$. In Figure 6.10**A**, we replot the experimental knot strength (solid line), $\tilde{F}_0$, as the fitted power-law extracted from Figure 6.6**B**, with the shaded region representing the experimental uncertainty. In the same plot, we plot FEM simulation results with the experimentally measured kinematic friction coefficient, $\mu = 0.2$. Excellent agreement is found between experiments and FEM, providing extra confidence on the high-fidelity of the simulations. Furthermore, we leverage the FEM to systematically vary the friction coefficient, μ, which cannot be readily changed experimentally; these simulation results are juxtaposed in Figure 6.10**A**, where we find that knot strength increases with μ. The excellent agreement between the FEM data (for the specific value of $\mu = 0.2$, the same as in experiments) and the experiments confirms that the non-dimensionalization of the forces by the diameter (in addition to σ_Y) was a valid choice.

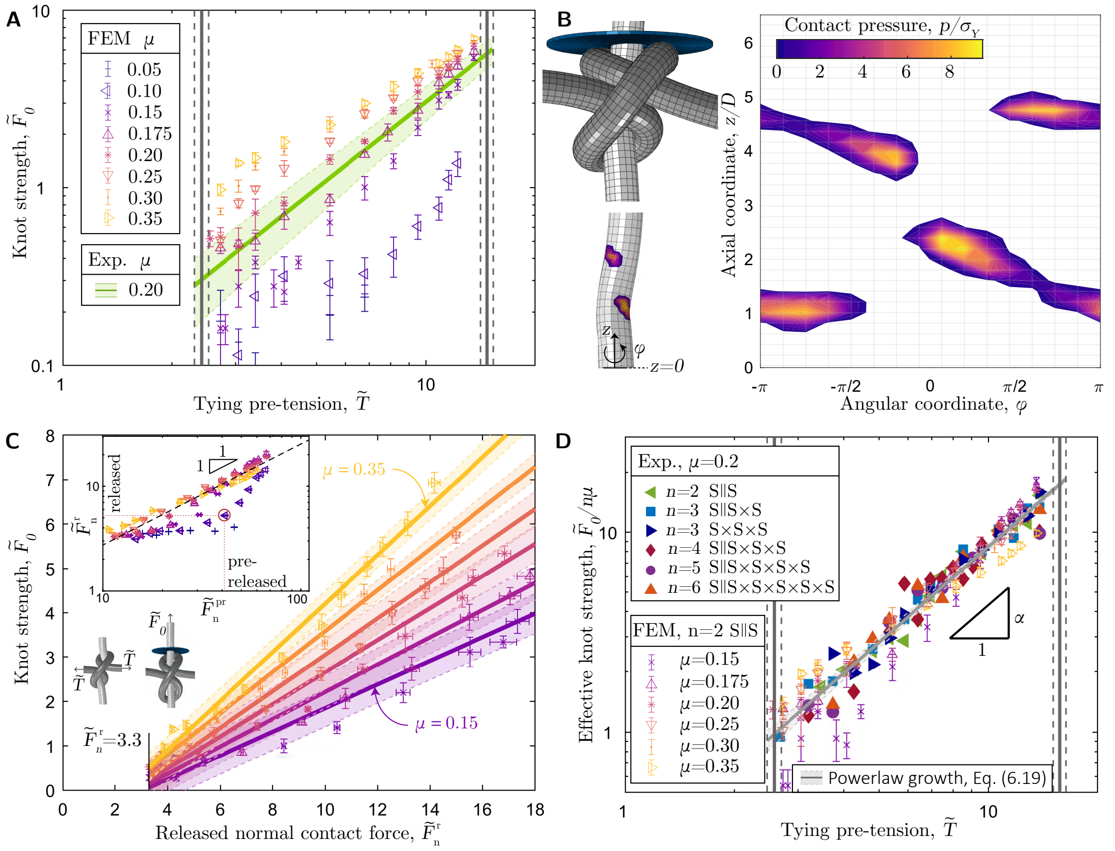

Figure 6.10: **Analysis of surface tractions and master curve for knot strength. A**, FEM-computed knot strength, $\tilde{F}_0$, versus tying pre-tension, $\tilde{T}$, for the S||S ($n = 2$) configuration, over a range of friction coefficients, $\mu \in [0.05-0.35]$. The green line corresponds to the experimental fit to Eq. (6.1), from Figure 6.6**B**, and the shaded region to the 65% confidence interval of the fit. The experimental value of the friction coefficient is $\mu = 0.2$. **B**, 3D-visualization of the S||S knot system ($\tilde{T} = 9.5$) simulated using FEM (top). Contact pressure, p/σ_Y, visualized on the pulled 3D rod (bottom) and mapped in 2D along the axial coordinate, z/D, and the angular coordinate, φ (right). **C**, Knot strength, $\tilde{F}_0$ versus the released integrated normal contact force, $\tilde{F}_{n2}$, for friction coefficients in the range, $\mu \in [0.15-0.35]$; see legend in (A). Linear fit of the data (lines) and 65% confidence interval (shaded regions). Inset: released normal contact force, $\tilde{F}_{n2}$ versus the pre-released normal contact force, $\tilde{F}_{n1}$, for all the simulated values of μ; see legend in (A). Springback (dilation) of the knots is observed for the datasets with $\mu = 0.05, 0.10$, an example of which is shown in the adjacent FEM configuration corresponding to the red-circled data point ($\mu = 0.10$, $\tilde{T} = 6.8$). **D**, Effective knot strength, $\tilde{F}_0/n\mu$, versus $\tilde{T}$, combining all the experimental and numerical results obtained in this study.

To explore the inner workings of the knot, we used the FEM to compute the normalized contact pressure, p/σ_Y, between the half-hitches and the quasi-straight sliding filament. For the representative case of an S||S knot ($n = 2$) with $\tilde{T} = 9.5$, Figure 6.10**B** shows a 3D visualization of p/σ_Y and its projected 2D map, the latter focusing only on the contacting regions. We distinguish two main contact regions related to the two half-hitches, with four distinct pressure hot spots. Integrating the local normal tractions over the entire surface of the knotted rod yields the integrated normal contact force, $\tilde{F}_\mathrm{n} = F_\mathrm{n}/\sigma_Y A$. It is useful to define the *pre-released configuration* as the state when the pre-tension is still applied before freeing the ends and the *released configuration* when the ends have been freed for testing; renderings in Figure 6.10**C**, left and right, respectively. The inset in Figure 6.10**C** plots the integrated normal contact forces of the released versus the pre-released configurations; *i.e.*, $\tilde{F}_\mathrm{n}^\mathrm{r}$ vs. $\tilde{F}_\mathrm{n}^\mathrm{pr}$. For $\mu \geq 0.15$, we find that $\tilde{F}_\mathrm{n}^\mathrm{r} \approx \tilde{F}_\mathrm{n}^\mathrm{pr}$ (dashed line), meaning that the released configuration maintains the normal contact force onto the sliding filament due to the plastic deformation accumulated during the pre-tensioning step. For $\mu < 0.15$, $\tilde{F}_\mathrm{n}^\mathrm{r} < \tilde{F}_\mathrm{n}^\mathrm{pr}$ as the knot dilates after the pre-tension is released (elastic springback) with an insufficient level of plastic deformation (rendering in Figure 6.10**C**, right). In these low-friction cases, the desired constricting geometry around the sliding filament is not provided, and consequently, the normal tractions in the released configuration ($\tilde{F}_\mathrm{n}^\mathrm{r}$) are low. Thus, plasticity turns out to be crucial to prevent the complete unraveling of the knot; even for vanishing friction coefficients ($\mu = 0.05$); the plastically bent filament guarantees the knot topology, while the same knots on a purely elastic rod would unravel.

Focusing on the tight, non-dilated configurations ($\mu \geq 0.15$), the data in Figure 6.10**A** evidence that the global knot strength depends linearly on the integrated local normal force; $\tilde{F}_0 \propto \tilde{F}_\mathrm{n}^\mathrm{r}$. Therefore, despite the strong underlying geometric nonlinearities, the Amontons-Coulomb friction law is at the source of this proportionality (as implemented in the FEM model), relating the total integrating tangential force, $\tilde{F}_\mathrm{t}$, and hence the knot strength, to $\tilde{F}_\mathrm{n}^\mathrm{r}$. Combining the friction-related dependence with Eq. (6.2), the knot strength is expected to behave as

$$\tilde{F}_0 = \beta_2 n \mu \tilde{T}^\alpha, \tag{6.19}$$

with the prefactor $\beta_2 = \tilde{K}/(n\mu) = 0.21 \pm 0.07$ measured by fitting. In Figure 6.10**D**, we plot $\tilde{F}_0/(n\mu)$ versus $\tilde{T}$ for the experimental data ($n \in [2, 6]$, from Figure 6.6) together with the FEM data ($n = 2$ and $\mu \in [0.15, 0.35]$). The data collapse onto a master curve, consistently with Eq. (6.19), with $\alpha = 1.56 \pm 0.23$. These results confirm that the frictional interactions dictate the knot strength with the required normal contact forces ensured by the plastic deformation pre-tensioning. Note that the power-law in Eq. (6.19), as evidenced in Figure 6.10**C**, is valid only for tight knots (above T_min), and does not hold for loose knots ($\tilde{F}_\mathrm{n}^\mathrm{r} < 3.3$), presumably due to the dilation of the released configurations. These findings call for future theoretical work to rationalize the measured values of α and β_2, which were found to be independent of the filament diameter, the number of throws, and the friction coefficient (for $\mu \geq 0.15$), in the whole tension range of the tight-knots regime.

6.11 Summary and Outlook

Our results from both surgeon-tied knots and model experiments, combined with FEM simulations, enabled us to identify the primary ingredients dictating the mechanical performance of surgical sliding knots. In addition to topology, geometry, and elasticity, the interplay between plastic deformation and frictional interactions is crucial in monofilament sutures. We propose that our findings be translated into practical guidelines on how to tie a safe surgical knot into a given suturing monofilament with friction coefficient, $\mu \geq 0.15$, and yield strength, σ_Y. The surgeon can adapt the filament caliber (cross-sectional area) and the number of throws, as well as control the tying pre-tension to induce an appropriate level of plastic deformation and hence normal-contact pressures, which, through friction, establish an appropriate knot strength. Since we only considered dry conditions, the master curve of the effective knot strength is applicable for dry suturing environments, *e.g.* dry skin operations. In the presence of blood and other fluids in surgical procedures, lower friction coefficients and, consequently, lower knot strengths are to be expected, which can be compensated by $\tilde{T}$ and n.

We hope that the know-how gained from our investigation raises awareness of the physical ingredients in surgical knots to experienced surgeons and will be valuable in the training of entry-level surgeons. Further, our quantitative description of the mechanism underlying sliding knots could be implemented into emerging robotic-assisted surgical devices containing haptic feedback to target effective knot-tying at a level similar to an experienced surgeon [156].

7 Conclusion and Perspectives

In this concluding chapter, we first summarize our key findings in Section 7.1. Then, in Section 7.2, we describe a few directions of ongoing work, which was motivated by the experimental and numerical techniques developed in this thesis, especially, in Chapters 2 and 3, respectively. Finally, in Section 7.3, we identify possible avenues for future research opened by the present results of this thesis.

7.1 Summary of Findings

In this thesis, we have studied several configurations of physical knots, in their tight and functional configurations. The importance of tightness and the three-dimensional nature of tight contacts were highlighted throughout. The use of mechanical testing and volumetric imaging, combined with Finite Element Modeling, enabled us to study the intricate interplay between topology, geometry, friction, and elasto-plastic constitutive behaviors of knotted structures, ranging from model systems of filaments in tight contact to realistic knots in surgical sutures. In general, the use of model systems enabled us to rationalize the underlying mechanisms and physical principles, which were then contrasted against theoretical frameworks. We also established comparisons with real-life applications, including stopper knots in ropes or surgical knots tied by an experienced surgeon.

In **Chapter 1**, we performed a literature review of the existing tools and models to study knots. We considered topological knot theory and the geometry of the tightest knot configurations tied on ideal (perfectly flexible and slippery) ropes. Beyond topology and geometry, for physical knots tied in elastic filaments, analytic models based on the Kirchhoff theory of rods incorporate the minimal physical ingredients, including resistance to bending and torsion, as well as frictional contact interactions. Further, the discrete elastic rod theory was recognized as a powerful tool to describe knots if the deformations of the cross-section of the rod and the contact interactions can be neglected or approximated. Also, a few studies used Finite Element Modeling to simulate knotted rods, although with simplifying assumptions to describe contact or the underlying constitutive models. Finally, we summarized relevant studies that characterize the quality and stability of physical knots but are not able to provide analytical predictions for their performance. From all of this existing body of literature, we identified the timely and relevant research niche for our work to provide much-needed physical insight into the nontrivial behavior of tight, physical knots.

In **Chapter 2**, we described the experimental toolbox and protocols that we have developed to study physical knots. The fabrication of composite rods was required to extract useful information from subsequent X-ray μCT imaging. A physical fiber was incorporated at the rod centerline, together with an eccentric inset. In addition, a thin and uniform outer rod coating was applied by dip-coating the elastomeric rods. Differences in material densities in knotted composite rods enabled us to extract fundamental geometric information from non-destructive X-ray tomographic imaging data. A sophisticated image analysis toolbox was developed to access the material centerline with its curvature, compute the director vectors of the Cosserat frame, and gain access to contact regions as well as cross-sectional deformation of knotted rods. Lastly, we characterized the material properties of elastomeric materials and described the protocol to determine the friction behavior of powder-treated elastomeric surfaces, which were essential in the subsequent chapters.

In **Chapter 3**, we developed a computational framework to enable systematic investigations of tight elastic knots based on a fully 3D finite element method (FEM). Depending on the specific problem at hand (addressed in subsequent chapters), the rods were modeled as solid rods or tubes, isotropic or transversely-isotropic. Numerical tying algorithms were presented to tie open and closed trefoil knots, the figure-eight, and the sliding granny knot (equivalent to the clove hitch knot). Moreover, the coupling between geometric features and the applied tension from the numerical results was compared to the corresponding experimental data for validation purposes. Finally, the experimentally validated computational framework was used to quantify the accurateness between the geometric centerline definition *minCS* (introduced in Chapter 2) and the well-defined material centerline.

In **Chapter 4**, empowered by the experimental and numerical toolbox presented in Chapters 2 and 3, we performed a compare-and-contrast investigation between the equilibrium shapes of physical and ideal trefoil knots, both in *closed* and *open* configurations. Physical realizations of tight trefoil knots were tied in an elastomeric rod, and X-ray tomography and 3D finite element simulation allowed a detailed characterization of the geometry of these knots.

Specifically, we evaluated the role of elasticity in dictating the overall shape of these physical knot, including their curvature profile, self-contact regions, and cross-section deformation. We compared the shape of our elastic knots to prior computations of the corresponding geometric configurations for the same knot tied on ideal ropes. Our results on tight physical knots exhibited many similarities to their purely geometric counterparts but also some striking dissimilarities that we examined in detail. These observations raised the hypothesis that regions of localized elastic deformation, not captured by the geometric models, could act as precursors for the weak spots that compromise the strength of knotted filaments.

In **Chapter 5**, we investigated the stability of stopper knots, again using a combination of experiments and FEM simulations. In a physical model system, we threaded an elastic rod through the clearance hole of a stopper plate and tied a figure-eight knot at one of the rod's extremities. When pulled against the plate, the figure-eight knot converts a high pulling force into a much smaller force at the other extremity before the knot capsizes. Leveraging experimentally validated simulations, we employed FEM to systematically study the effect of the frictional interactions on the capsizing mechanism. We quantified twist in a critical rod segment and demonstrated that friction-induced twist between self-contacting rods is at the source of the capsizing mechanism. An increase in the friction coefficient between the rod and the stopper plate hampered the onset of capsizing. Finally, we characterized several standard climbing and multi-functional ropes (braided), all of which showed a decoupling between their torsional and bending rigidities ought to their braided sub-structure. Whereas most of our investigation focused on elastic rods, our results suggests an explanation for why a difference in the capsizing mechanism is to be expected between elastic rods and braided ropes. Ropes were found to delay or even impede the capsizing mechanism due to their relatively higher twist energy penalty when compared with bending.

In **Chapter 6**, aimed to establish physics-based operational and safety guidelines on the mechanical strength of surgical sliding knots. We developed a physical model system to study the untying knot strength by systematically varying the tying pre-tension, leading to distinctive levels of knot tightness. Throughout this chapter, we focused exclusively on commercial polypropylene suturing monofilaments, which are common in surgical practice. We focused on tight, sliding knots, ranging from the simple sliding granny knot (S||S), to multiple-throw knots in their sliding conformation (*e.g.*, the 6-throw S||S×S×S×S×S knot). We uncovered power-law behavior for the untying strength of these knots as a function of the applied pre-tension. Next, we analyzed knots from an experienced surgeon, finding that they intuitively target the middle of this power-law region, leaving a safety clearance between the limiting regime where the knot is too loose to be functional and the limiting regime of filament fracture. Further, we explored the effects of the number of throws and the knot topology ('||' vs. '×'-throws, using a notation that is common in the surgical knots literature). Our results uncovered a strikingly simple linear relation between the knot strength and the number of throws. To further understand the key role of friction on knot safety, we simulated plastic knots with varying filament friction coefficient using the FEM. For these simulations, we had to develop a plasticity model, which was calibrated and validated against experimental results from uni-axial and bending material responses. Tying, tightening, and untying sliding knots with different frictional contact interactions allowed us to relate knot strength to the underlying normal contact forces present in the knot. Finally, we proposed a general scaling law that collapses all our experimental and numerical data onto a master curve, quantitatively describing the strength of tight knots for all the sliding knot conformations we investigated and a wide range of friction coefficients. Despite the complex constitutive behavior of filaments, intricate contact geometry, and knot topology, we were able quantitatively rationalized the underlying mechanism dictating knot strength. An aspect of particular novelty of the work presented in this chapter was the recognition of the previously overlooked but critical effect of plastic deformation in this class of knotted structures on polymeric monofilaments. These findings could have potential applications in the training of surgeons and in the control of robotic-assisted surgical devices.

7.2 Opportunities for Future Works

We explored the three-dimensional shapes and failure mechanisms of capsizing and sliding in a few relevant physical knot topologies tied in circular, solid rods. However, each knot topology has its own strength and weakness when applied in various physical contexts. In addition, knots can be tied in tubes or hollow rods (*e.g.*, a garden hose or the neck of a plastic bag), in rectangular beams (*e.g.*, flat shoelaces), or in complex-structured and braided filaments (*e.g.*, surgical thread or climbing ropes). Hereafter, we summarize several ongoing research efforts that have stemmed from the collaborative works of the author or that are based on similar investigations of complex knots using the tools developed by the author that are currently being investigated further at EPFL's Flexible Structures Laboratory.

7.2.1 Mechanics of the Bowline Knot

The bowline knot provides a stationary loop, typically at the end of a rope, and is one of the most common knots employed by sailors (see Figure 7.1**a**). More specifically, this knot is commonly used to attach the 'bow line' of a square sail to prevent it from being filled by the wind on the wrong side of the sail [117, 118]. The bowline knot is based on the classic sheet bend and therefore regarded as relatively secure. Still, in some circumstances, the knot can slip or capsize (see inset in Figure 7.1**a**), as the mechanism described in Chapter 5.

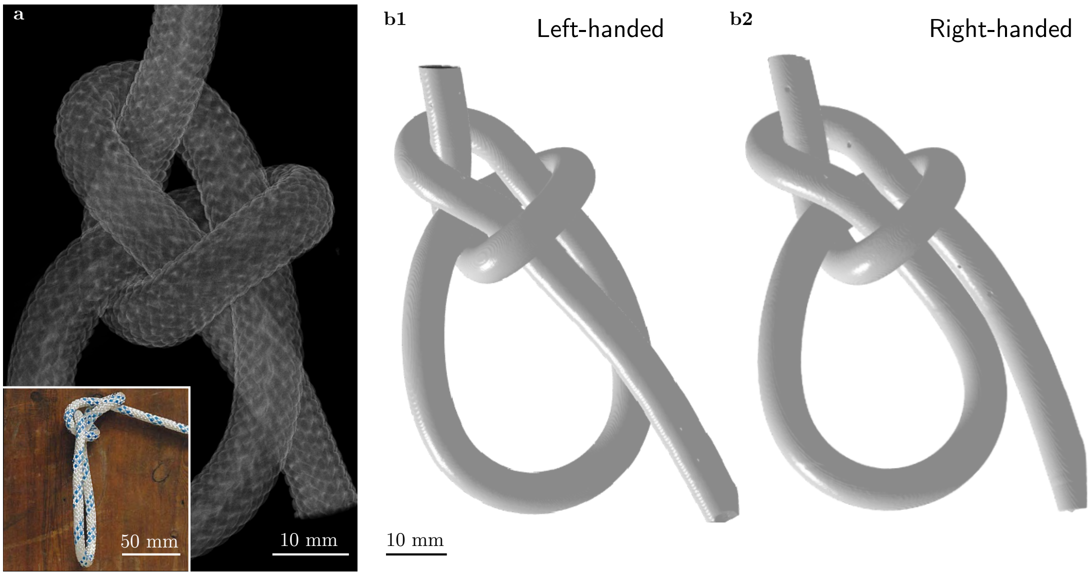

Figure 7.1: **Variations of the bowline knot. a**, X-ray scan of a left-handed bowline knot tied in a climbing rope. The inset depicts the capsizing, useful to untie the knot, and is adapted from Bloomsbury Publishing Plc [117]. **b1-b2**, CT-scans of bowline knots tied in elastomeric VPS32 rods in their left-handed (**b1**) and right-handed (**b2**) variations. Image credits for **b1** and **b2**: Mr. Bastien Aymon, Dr. Michael Gomez, and Dr. Fani Derveni (FLEXLAB, EPFL).

By cutting the leg of the loop, the basic bowline knot essentially becomes the sheet bend knot. Since there are numerous variations of the sheet bend knot, at least as many types of bowline knots can be formed: the true bowline, hitched bowline, tucked bowline, bowline in the bight, three legs bowline, Ontario bowline, Algonquin bowline, brummycham bowline, Spanish bowline, water bowline, amongst others [22, 1, 118].

This ongoing project, which is currently being undertaken by Mr. Bastien Aymon, Dr. Michael Gomez, and Dr. Fani Derveni, involves a detailed investigation of the stability of the simple bowline tied in the left-handed and right-handed configurations. Preliminary μCT scans were performed on a model system consisting of composite elastomeric rods tied in the two configurations, as shown in Figure 7.1**b1-b2**. The rods were fabricated according to the protocols described in Chapter 2, Section 2.2. Using the versatile image-processing algorithm presented in Chapter 2, Section 2.3.2, the material centerline coordinates, curvature and twist profiles, as well as the contact regions, can be readily extracted from the reconstructed volumetric data (Chapter 2, Section 2.4).

Beyond the volumetric imaging of bowline knots, mechanical tests are being performed to evaluate the resistance against untying as a function of tightness and knot configuration (left- vs. right-handed). In addition, the experimental data will be accompanied by numerical simulations (similar to the described procedure, presented in Chapter 3), which will hopefully yield further insight into the local kinematics and mechanics of the knotted rod. Finally, the topological fact that the bowline knot includes the sheet bend could be interesting to generalize findings on stability between these two knot types.

7.2.2 Mechanics of Knotted Umbilical Cords

In mammals, the umbilical cord plays a key role in the prenatal development of the fetus by enabling fluid exchanges with the maternal placenta [157]. As shown in the schematics in Figure 7.2**a**, the umbilical cord consists of a single vein that carries oxygen and nutrient-rich blood from the placenta to the fetus, together with two arteries that carry deoxygenated blood and waste back to the placenta [158]. These three blood vessels are twisted around each other, forming a triple helix that is embedded in a gel-like structure called Wharton's jelly [157]. During pregnancy, fetal activity can spontaneously lead to knotting of the umbilical cord (see Figure 7.2**b**). Even though Wharton's jelly provides a thick protective wall around the vein and arteries, the formation of knots can result in constrictions of the blood vessels and, in some cases, asphyxia of the fetus [16]. Knotted umbilical cords are observed only in around 1% of pregnancies, but have been shown to increase the probability of fetal death by almost a factor of four [17]. The conditions leading to such a catastrophic vessel constriction are still poorly understood.

In this research project, in collaboration with Dr. Michael Gomez (FLEXLAB, EPFL), and former collaborators, Mr. Nicolas Minazzo and Dr. Paul Grandgeorge, we have been studying the elasto-hydrodynamics of a knotted tube as a reduced model of the umbilical cord under different knotting conditions (see Figure 7.2**c1**). Specifically, we focus on the drop in flow rate of a pressure-driven viscous flow along a knotted elastomeric tube containing a single concentric vessel (lumen). By combining precision experiments and numerical computations (Figure 7.2**c2**), we observed that, at low tensions, T, the knot has a negligible effect on the flow rate (dictated by the Poiseuille flow in a straight tube). However, beyond a critical tightening tension, T^*, the flow rate rapidly decreases to zero. We make use of μCT imaging and FEM simulations to rationalize the highly non-linear relationship between flow rate and knot tension. In particular, as the knot tension increases, we observe that the lumen cross-section adopts a quasi-elliptical shape that rapidly closes beyond the critical knot tension T^*.

Next, to highlight the interplay between tube curvature and tension that leads to normal contact forces during knotting, we study the hydrodynamics of a simplified system comprising a tensioned tube wrapped around a rigid cylinder. The numerical tightening visualization of this configuration is shown in its loose state in Figure 7.2**d**. A displacement, δ, of the rigid

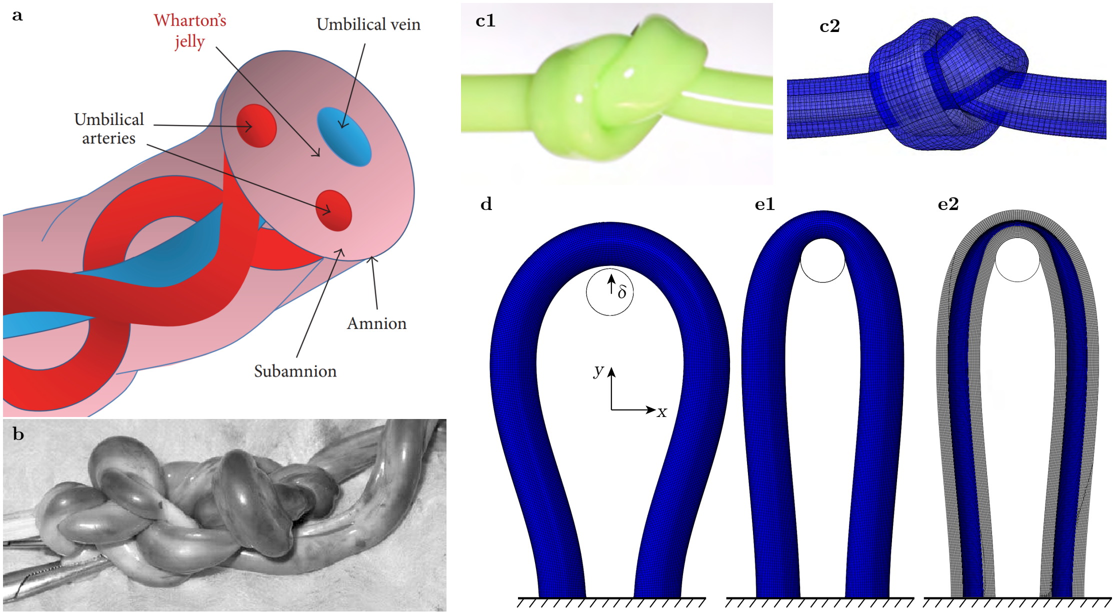

Figure 7.2: **Model-system experiments and simulations on the umbilical cord.** **a**, Schematics of the biological umbilical cord consisting of twisted arteries and a vein, embedded in the Wharton's jelly. Schematics adapted from Szepesi et al. [158]. **b**, photograph of a knotted umbilical cord. Image adapted from Omari [159]. **c1-c2**, Tight overhand knot tied in a tube in experiments (**c1**) and FEM (**c2**). Image credits of **c1**: Mr. Nicolas Minazzo. **d**, Bent elastic tube in FEM before the rigid cylinder moves in the positive y-direction. **e1-e2**, Numerical visualization of tensioned tube in an outer view (**e1**), and with a cross-sectional cut (**e2**.)

cylinder against the elastic tube results in the configuration shown in Figure 7.2**e1**, with the cross-sectional cut, displayed in Figure 7.2**e2**. Again, we observe similar phenomenology to a knotted tube: the flow rate undergoes a drastic drop beyond a critical value of the applied tension.

Finally, to gain a deeper understanding of the effect of contact forces on lumen deformation, we further simplify the problem by analyzing the flow through a straight tube compressed between two parallel plates. Despite the geometrical difference, we leverage the results of this final experiment to rationalize the load-deformation behavior in more complex configurations. By assuming that a knot is a sequence of tube portions wrapped around cylinders, our analysis enables us to provide a prediction of the hydrodynamic response of the intricate knotted tube.

Despite the differences between our model elastomeric tube and the triple-helix structure of an umbilical cord, we are confident that our results should enable a better understanding of the disastrous consequences of vessel constriction. By shining light on the underlying mechanisms leading to drops in flow rate, we hope that our findings could eventually enable novel obstetric evaluationg procedures in cases of tight, knotted umbilical cords.

7.3 Final Remarks

In the past few decades, advances in material science and engineering found alternatives to knots in everyday life. For instance, Velcro strips replace the binding of shoelaces, and tissue adhesive can be used instead of suturing a wound in low-tension surgeries. Further, zippers, glue, adhesive tape, staplers, magnets, and rubber bands reduce the application of knots in our everyday life [118]. Nevertheless, knots remain omnipresent, and in applications like sailing, climbing, and surgery, they remain the most secure and reliable solution.

In closing, the work performed throughout this thesis demonstrates the importance of each underlying geometric and mechanical property in dictating the performance of physical knots. We hope that our systematic exploration of knotted structures, and the physical insight into the nontrivial behavior of these systems can be used to motivate and validate accurate predictive models and computational tools.

Ultimately, the new reality of robot-assisted surgery raises questions about the quality of the knots produced by medical devices and how the sutures compare to those performed directly by a human surgeon [160, 161, 162]. As such, a new level of predictive models for knot tying, which considers all the underlying variables, will become increasingly essential to ensure reliable, strong, and secure sutures.

Bibliography

[1] J. C. Turner and P. C. van de Griend. *History and science of knots*. World Scientific, 1996. ISBN 9810224699.

[2] Vishal P. Patil, Joseph D. Sandt, Mathias Kolle, and Jörn Dunkel. Topological mechanics of knots and tangles. *Science*, 367(6473):71–75, jan 2020. doi: 10.1126/science.aaz0135.

[3] URL https://www.worldhistory.org.

[4] URL https://www.harvardmagazine.com.

[5] URL https://historyplex.com.

[6] URL https://www.christies.com.

[7] Nathaniel Bowditch. *American Practical Navigator Bowditch 1984 Edition Vol1 Part 2*. PARADISE CAY PUBN INC, 2015. ISBN 193719647X.

[8] Samuel Poincloux, Mokhtar Adda-Bedia, and Frédéric Lechenault. Geometry and elasticity of a knitted fabric. *Physical Review X*, 8(2), jun 2018. doi: 10.1103/physrevx.8.021075.

[9] Dorian M. Raymer and Douglas E. Smith. Spontaneous knotting of an agitated string. *Proceedings of the National Academy of Sciences*, 104(42):16432–16437, oct 2007. doi: 10.1073/pnas.0611320104.

[10] A. Marco Saitta, Paul D. Soper, E. Wasserman, and Michael L. Klein. Influence of a knot on the strength of a polymer strand. *Nature*, 399(6731):46–48, may 1999. doi: 10.1038/19935.

[11] Yasuharu Arai, Ryohei Yasuda, Ken-ichirou Akashi, Yoshie Harada, Hidetake Miyata, Kazuhiko Kinosita Jr, and Hiroyasu Itoh. Tying a molecular knot with optical tweezers. *Nature (London)*, pages 399, 446–448, 1999.

[12] V. V. Rybenkov, N. R. Cozzarelli, and A. V. Vologodskii. Probability of DNA knotting and the effective diameter of the DNA double helix. *Proceedings of the National Academy of Sciences*, 90(11):5307–5311, jun 1993. doi: 10.1073/pnas.90.11.5307.

[13] Dustin Kleckner and William T. M. Irvine. Creation and dynamics of knotted vortices. *Nature Physics*, 9(4):253–258, mar 2013. doi: 10.1038/nphys2560.

[14] Dustin Kleckner, Louis H. Kauffman, and William T. M. Irvine. How superfluid vortex knots untie. *Nature Physics*, 12(7):650–655, mar 2016. doi: 10.1038/nphys3679.

[15] J. W. Cirtain, L. Golub, A. R. Winebarger, B. De Pontieu, K. Kobayashi, R. L. Moore, R. W. Walsh, K. E. Korreck, M. Weber, P. McCauley, A. Title, S. Kuzin, and C. E. DeForest. Energy release in the solar corona from spatially resolved magnetic braids. *Nature*, 493(7433): 501–503, jan 2013. doi: 10.1038/nature11772.

[16] Alain Goriely. Knotted umbilical cords. In *Physical and Numerical Models in Knot Theory*, pages 109–126. World Scientific, sep 2005. doi: 10.1142/9789812703460/0006.

[17] Urpu Airas and Seppo Heinonen. Clinical significance of true umbilical knots: A population-based analysis. *American Journal of Perinatology*, 19(3):127–132, 2002. doi: 10.1055/s-2002-25311.

[18] URL https://www.bebeautiful.in.

[19] URL https://actu.epfl.ch/news.

[20] URL https://www.youtube.com/c/tenniswarehouse.

[21] URL https://www.intuitive.com/.

[22] C. W. Ashley. *The Ashley Book of Knots.* New York: Doubleday, 1944. ISBN 978-0821836781.

[23] Lindsey Philpott. *Complete Book of Fishing Knots, Leaders, and Lines: How to Tie the Perfect Knot for Every Fishing Situation.* SKYHORSE PUB, 2015. ISBN 163220536X.

[24] Richard F. Edlich. Surgical knot tying manual. In A. G. Covidien, editor, *Surgical Knot Tying Manual*, Third Edition, 150 Glover Avenue Norwalk, CT 06856, 2008.

[25] Frédéric Dubrana and Philippe Pasquier. Ligatures et sutures chirurgicales. In *Springer-Verlag, France*, 2011.

[26] P. Calhoun. Advanced surgical knot tying. *Independently Published*, 2nd Edition, 2016.

[27] Christopher A. Daily-Diamond, Christine E. Gregg, and Oliver M. O'Reilly. The roles of impact and inertia in the failure of a shoelace knot. *Proceedings of the Royal Society A: Mathematical, Physical and Engineering Science*, 473(2200):20160770, apr 2017. doi: 10.1098/rspa.2016.0770.

[28] Leonhard Euler. Remarques sur l'effet du frottement dans l'equilibre. *Memoires de l'academie des sciences de Berlin*, 1769.

[29] Johann Albert Eytelwein. *Handbuch der Mechanik fester Körper und der Hydraulik: mit vorzüglicher Rücksicht auf ihre Anwendung in der Architektur aufgesetzt.* Fleischer, 1842.

[30] URL https://manthecapstan.wordpress.com/.

[31] I M Stuart. Capstan equation for strings with rigidity. *British Journal of Applied Physics*, 12(10):559–562, oct 1961. doi: 10.1088/0508-3443/12/10/309.

[32] Jae Ho Jung, Ning Pan, and Tae Jin Kang. Capstan equation including bending rigidity and non-linear frictional behavior. *Mechanism and Machine Theory*, 43(6):661–675, jun 2008. doi: 10.1016/j.mechmachtheory.2007.06.002.

[33] Paul Grandgeorge, Tomohiko G. Sano, and Pedro M. Reis. An elastic rod in frictional contact with a rigid cylinder. *Journal of the Mechanics and Physics of Solids*, 164:104885, jul 2022. doi: 10.1016/j.jmps.2022.104885.

[34] Jae Ho Jung, Ning Pan, and Tae Jin Kang. Generalized capstan problem: Bending rigidity, nonlinear friction, and extensibility effect. *Tribology International*, 41(6):524–534, jun 2008. doi: 10.1016/j.triboint.2007.11.005.

[35] Oliver M. O'Reilly. *Modeling Nonlinear Problems in the Mechanics of Strings and Rods.* Springer International Publishing, 2017. doi: 10.1007/978-3-319-50598-5.

[36] B. Audoly and Y. Pomeau. *Elasticity and Geometry.* Oxford Univ. Press, 2010.

[37] Tomohiko G. Sano, Paul Johanns, Paul Grandgeorge, Changyeob Baek, and Pedro M. Reis. Exploring the inner workings of the clove hitch knot. *Extreme Mechanics Letters*, 55:101788, aug 2022. doi: 10.1016/j.eml.2022.101788.

[38] Eitan Grinspun and Adrian Secord. Introduction to discrete differential geometry. In *ACM SIGGRAPH 2005 Courses on - SIGGRAPH '05.* ACM Press, 2005. doi: 10.1145/1198555.1198660.

[39] Miklós Bergou, Max Wardetzky, Stephen Robinson, Basile Audoly, and Eitan Grinspun. Discrete elastic rods. In *ACM SIGGRAPH 2008 papers on - SIGGRAPH '08.* ACM Press, 2008. doi: 10.1145/1399504.1360662.

[40] Miklós Bergou, Basile Audoly, Etienne Vouga, Max Wardetzky, and Eitan Grinspun. Discrete viscous threads. *ACM Transactions on Graphics*, 29(4):1–10, jul 2010. doi: 10.1145/1778765.1778853.

[41] M. Khalid Jawed, Alyssa Novelia, and Oliver M. O'Reilly. *A Primer on the Kinematics of Discrete Elastic Rods*. Springer International Publishing, 2018. doi: 10.1007/978-3-319-76965-3.

[42] Colin C. Adams. *The Knot Book: An Elementary Introduction to the Mathematical Theory of Knots*. AMS Bookstore, Providence, RI, 2004. ISBN ISBN 978-0821836781.

[43] William F. Pohl. DNA and differential geometry. *The Mathematical Intelligencer*, 3(1): 20–27, mar 1980. doi: 10.1007/bf03023391.

[44] Steven A. Wasserman, Jan M. Dungan, and Nicholas R. Cozzarelli. Discovery of a predicted dna knot substantiates a model for site-specific recombination. *Science*, 229 (4709):171–174, 1985. doi: 10.1126/science.2990045. URL https://www.science.org/doi/abs/10.1126/science.2990045.

[45] R. Lavery, M. Moakher, J. H. Maddocks, D. Petkeviciute, and K. Zakrzewska. Conformational analysis of nucleic acids revisited: Curves+. *Nucleic Acids Research*, 37(17): 5917–5929, jul 2009. doi: 10.1093/nar/gkp608.

[46] Richard Lavery, Krystyna Zakrzewska, David Beveridge, Thomas C. Bishop, David A. Case, Thomas Cheatham, Surjit Dixit, B. Jayaram, Filip Lankas, Charles Laughton, John H. Maddocks, Alexis Michon, Roman Osman, Modesto Orozco, Alberto Perez, Tanya Singh, Nada Spackova, and Jiri Sponer. A systematic molecular dynamics study of nearest-neighbor effects on base pair and base pair step conformations and fluctuations in b-DNA. *Nucleic Acids Research*, 38(1):299–313, nov 2009. doi: 10.1093/nar/gkp834.

[47] J. W. Alexander and G. B. Briggs. On types of knotted curves. *The Annals of Mathematics*, 28(1/4):562, 1926. doi: 10.2307/1968399.

[48] William P. Thurston. Three dimensional manifolds, kleinian groups and hyperbolic geometry, 1983.

[49] O. Gonzalez, J. H. Maddocks, F. Schuricht, and H. von der Mosel. Global curvature and self-contact of nonlinearly elastic curves and rods. *Calculus of Variations and Partial Differential Equations*, 14(1):29–68, jan 2002. doi: 10.1007/s005260100089.

[50] J. A. Calvo. *Physical and Numerical Models in Knot Theory: Including Applications to the Life Sciences*. K & E series on knots and everything. World Scientific, 2005. ISBN 9789812561879.

[51] Jason Cantarella, Robert B. Kusner, and John M. Sullivan. On the minimum ropelength of knots and links. *Inventiones mathematicae*, 150(2):257–286, nov 2002. doi: 10.1007/s00222-002-0234-y.

[52] Piotr Pierański. In search of ideal knots. *Computational Methods in Science and Technology*, 4(1):9–23, 1998. doi: 10.12921/cmst.1998.04.01.09-23.

[53] R.A. Litherland, J. Simon, O. Durumeric, and E. Rawdon. Thickness of knots. *Topology and its Applications*, 91(3):233–244, feb 1999. doi: 10.1016/s0166-8641(97)00210-1.

[54] Eric J. Rawdon. Can Computers Discover Ideal Knots? *Experimental Mathematics*, 12 (3):287 – 302, 2003. doi: em/1087329232. URL https://doi.org/.

[55] Ted Ashton, Jason Cantarella, Michael Piatek, and Eric J. Rawdon. Knot tightening by constrained gradient descent. *Experimental Mathematics*, 20(1):57–90, mar 2011. doi: 10.1080/10586458.2011.544581.

[56] J. Baranska, S. Przybyl, and P. Pieranski. Curvature and torsion of the tight closed trefoil knot. *The European Physical Journal B*, 66(4):547–556, dec 2008. doi: 10.1140/epjb/e2008-00443-y.

[57] Smutny, Jana. Global radii of curvature, and the biarc approximation of space curves:in pursuit of ideal knot shapes. 2005. doi: 10.5075/EPFL-THESIS-2981.

[58] E. L. Starostin. A constructive approach to modelling the tight shapes of some linked structures. *PAMM*, 3(1):479–480, dec 2003. doi: 10.1002/pamm.200310509.

[59] John H. Maddocks Oscar Gonzalez and Jana Smutny. Curves, circles, and spheres. *Contemporary Mathematics*, pages 304:195–216, 2002.

[60] Ted Ashton, Jason Cantarella, Michael Piatek, and Eric Rawdon. Self-contact sets for 50 tightly knotted and linked tubes, 2005.

[61] B. Audoly, N. Clauvelin, and S. Neukirch. Elastic knots. *Physical Review Letters*, 99(16), oct 2007. doi: 10.1103/physrevlett.99.164301.

[62] Changyeob Baek, Paul Johanns, Tomohiko G. Sano, Paul Grandgeorge, and Pedro M. Reis. Finite element modeling of tight elastic knots. *Journal of Applied Mechanics*, 88(2), 2021. doi: 10.1115/1.4049023.

[63] N. Clauvelin, B. Audoly, and S. Neukirch. Matched asymptotic expansions for twisted elastic knots: A self-contact problem with non-trivial contact topology. *Journal of the Mechanics and Physics of Solids*, 57(9):1623–1656, sep 2009. doi: 10.1016/j.jmps.2009.05.004.

[64] M. K. Jawed, P. Dieleman, B. Audoly, and P. M. Reis. Untangling the mechanics and topology in the frictional response of long overhand elastic knots. *Physical Review Letters*, 115(11), sep 2015. doi: 10.1103/physrevlett.115.118302.

[65] Piotr Pierański, Sandor Kasas, Giovanni Dietler, Jacques Dubochet, and Andrzej Stasiak. Localization of breakage points in knotted strings. *New Journal of Physics*, 3:10–10, jun 2001. doi: 10.1088/1367-2630/3/1/310.

[66] Dezhong Tong, Mohammad Khalid Jawed, and Jungseock Joo Team Andrew Choi. Snap buckling in overhand knots. In *APS March Meeting Abstracts*, volume 2021 of *APS Meeting Abstracts*, page F16.009, January 2021.

[67] Andrew Choi, Dezhong Tong, Mohammad K. Jawed, and Jungseock Joo. Implicit contact model for discrete elastic rods in knot tying. *Journal of Applied Mechanics*, 88(5), mar 2021. doi: 10.1115/1.4050238.

[68] Dezhong Tong, Andrew Choi, Jungseock Joo, and M. Khalid Jawed. A fully implicit method for robust frictional contact handling in elastic rods, 2022.

[69] Xuanhe Li, Weicheng Huang, and M. Khalid Jawed. Discrete elasto-plastic rods. *Extreme Mechanics Letters*, 38:100767, jul 2020. doi: 10.1016/j.eml.2020.100767.

[70] Damien Durville. Contact-friction modeling within elastic beam assemblies: an application to knot tightening. *Computational Mechanics*, 49(6):687–707, 2012. doi: 10.1007/s00466-012-0683-0.

[71] Przemysław Litewka. Enhanced multiple-point beam-to-beam frictionless contact finite element. *Computational Mechanics*, 52(6):1365–1380, jun 2013. doi: 10.1007/s00466-013-0881-4.

[72] Arz Y. Qwam Alden, Andrew G. Geeslin, Jeffrey C. King, and Peter A. Gustafson. A finite element model of a surgical knot. In *Volume 3: Biomedical and Biotechnology Engineering*. ASME, nov 2017. doi: 10.1115/imece2017-72201.

[73] George B. Hanna, Tim G. Frank, and Alfred Cuschieri. Objective assessment of endoscopic knot quality. *The American Journal of Surgery*, 174(4):410–413, oct 1997. doi: 10.1016/s0002-9610(97)00129-3.

[74] Alex C. H. Lee, Ramy R. R. Fahmy, and George B. Hanna. Objective evidence for optimum knot configuration. *World Journal of Surgery*, 32(12):2736–2741, oct 2008. doi: 10.1007/s00268-008-9764-9.

[75] Elie A Goldenberg and Abhishek Chatterjee. Towards a better laparoscopic knot: using knot quality scores to evaluate three laparoscopic knot-tying techniques. *Journal of the Society of Laparoendoscopic Surgeons*, 13(3):416, 2009.

[76] John H. Maddocks and Joseph B. Keller. Ropes in equilibrium. *SIAM Journal on Applied Mathematics*, 47(6):1185–1200, dec 1987. doi: 10.1137/0147080.

[77] Widianto P. Moestopo, Arturo J. Mateos, Ritchie M. Fuller, Julia R. Greer, and Carlos M. Portela. Pushing and pulling on ropes: Hierarchical woven materials. *Advanced Science*, 7(20):2001271, aug 2020. doi: 10.1002/advs.202001271.

[78] Paul Grandgeorge, Changyeob Baek, Harmeet Singh, Paul Johanns, Tomohiko G. Sano, Alastair Flynn, John H. Maddocks, and Pedro M. Reis. Mechanics of two filaments in tight orthogonal contact. *Proceedings of the National Academy of Sciences*, 118(15): e2021684118, apr 2021. doi: 10.1073/pnas.2021684118.

[79] L. Landau and B. Levich. Dragging of a liquid by a moving plate. In *Dynamics of Curved Fronts*, pages 141–153. Elsevier, 1988. doi: 10.1016/b978-0-08-092523-3.50016-2.

[80] H. C. Mayer and R. Krechetnikov. Landau-levich flow visualization: Revealing the flow topology responsible for the film thickening phenomena. *Physics of Fluids*, 24(5):052103, may 2012. doi: 10.1063/1.4703924.

[81] G. I. Taylor. Deposition of a viscous fluid on the wall of a tube. *Journal of Fluid Mechanics*, 10(02):161, mar 1961. doi: 10.1017/s0022112061000159.

[82] David A. White and John A. Tallmadge. A gravity corrected theory for cylinder withdrawal. *AIChE Journal*, 13(4):745–750, jul 1967. doi: 10.1002/aic.690130428.

[83] J. A. Tallmadge and D. A. White. Film properties and design procedures in cylinder withdrawal. *Industrial & Engineering Chemistry Process Design and Development*, 7(4): 503–508, oct 1968. doi: 10.1021/i260028a004.

[84] Pascale Aussillous and David Quéré. Quick deposition of a fluid on the wall of a tube. *Physics of Fluids*, 12(10):2367, 2000. doi: 10.1063/1.1289396.

[85] Emmanuelle Rio and François Boulogne. Withdrawing a solid from a bath: How much liquid is coated? *Advances in Colloid and Interface Science*, 247:100–114, sep 2017. doi: 10.1016/j.cis.2017.01.006.

[86] K. Grundke, S. Michel, G. Knispel, and A. Grundler. Wettability of silicone and polyether impression materials: Characterization by surface tension and contact angle measure-

ments. *Colloids and Surfaces A: Physicochemical and Engineering Aspects*, 317(1-3): 598–609, mar 2008. doi: 10.1016/j.colsurfa.2007.11.046.

[87] Gabor T. Herman. *Fundamentals of Computerized Tomography*. Springer London, 2009. doi: 10.1007/978-1-84628-723-7.

[88] B. P. Flannery, H. W. Deckman, W. G. Roberge, and K. L. D'AMICO. Three-dimensional x-ray microtomography. *Science*, 237(4821):1439–1444, sep 1987. doi: 10.1126/science.237.4821.1439.

[89] Johannes Schindelin, Ignacio Arganda-Carreras, Erwin Frise, Verena Kaynig, Mark Longair, Tobias Pietzsch, Stephan Preibisch, Curtis Rueden, Stephan Saalfeld, Benjamin Schmid, Jean-Yves Tinevez, Daniel James White, Volker Hartenstein, Kevin Eliceiri, Pavel Tomancak, and Albert Cardona. Fiji: an open-source platform for biological-image analysis. *Nature Methods*, 9(7):676–682, jun 2012. doi: 10.1038/nmeth.2019.

[90] Paul Johanns, Paul Grandgeorge, Changyeob Baek, Tomohiko G. Sano, John H. Maddocks, and Pedro M. Reis. The shapes of physical trefoil knots. *Extreme Mechanics Letters*, 43:101172, feb 2021. doi: 10.1016/j.eml.2021.101172.

[91] Alan N. Gent. *Engineering with rubber*. Carl Hanser Verlag, Munich, 2001. ISBN 978-1569902998.

[92] Bo N. J. Persson. *Sliding Friction*. Springer Berlin Heidelberg, 2013. ISBN 9783662042830.

[93] ASTM D1894-14. Standard test method for static and kinetic coefficients of friction of plastic film and sheeting.

[94] Marcus J. Goudie, Jitendra Pant, and Hitesh Handa. Liquid-infused nitric oxide-releasing (LINORel) silicone for decreased fouling, thrombosis, and infection of medical devices. *Scientific Reports*, 7(1), oct 2017. doi: 10.1038/s41598-017-14012-9.

[95] ABAQUS 6.19. *Abaqus theory guide*. USA: Dassault Systems Simulia Corp., 2019.

[96] H. D. Hibbitt and B. I. Karlsson. Analysis of pipe whip. Technical report, nov 1979.

[97] Sylwester Przybył and Piotr Pierański. High resolution portrait of the ideal trefoil knot. *Journal of Physics A: Mathematical and Theoretical*, 47(28):285201, jun 2014. doi: 10.1088/1751-8113/47/28/285201.

[98] Md Ibrahim Khalil, Dezhong Tong, Guanjin Wang, Mohammad Khalid Jawed, and Bashir Khoda. Systematic variation of friction of rods. *Journal of Applied Mechanics*, 89(11), sep 2022. doi: 10.1115/1.4055544.

[99] P. Pierański, S. Przybył, and A. Stasiak. Tight open knots. *The European Physical Journal E*, 6(2):123–128, oct 2001. doi: 10.1007/s101890170012.

[100] M. Carlen, B. Laurie, J. H. Maddocks, and J. Smutny. Biarcs, global radius of curvature, and the computation of ideal knot shapes. In *Physical and Numerical Models in Knot Theory*, pages 75–108. World Scientific, sep 2005. doi: 10.1142/9789812703460/0005.

[101] C. E. I. Wright and J. E. Magowan. Knots for climbers. *Alpine Journal*, 1928.

[102] F. W. Taylor. Surgical knots. In *Ann Surg.*, volume 107(3), pages 458–68, 1938.

[103] H Taylor and AW Grogono. The constrictor knot is the best ligature. *The Annals of The Royal College of Surgeons of England*, 96(2):101–105, mar 2014. doi: 10.1308/003588414x13814021677638.

[104] Der-Lin Chow and Wyatt Newman. Trajectory optimization of robotic suturing. In *2015 IEEE International Conference on Technologies for Practical Robot Applications (TePRA)*. IEEE, may 2015. doi: 10.1109/tepra.2015.7219672.

[105] O. Gonzalez and J. H. Maddocks. Global curvature, thickness, and the ideal shapes of knots. *Proceedings of the National Academy of Sciences*, 96(9):4769–4773, apr 1999. doi: 10.1073/pnas.96.9.4769.

[106] Friedemann Schuricht and Heiko von der Mosel. Euler-lagrange equations for nonlinearly elastic rods with self-contact. *Archive for Rational Mechanics and Analysis*, 168(1): 35–82, jun 2003. doi: 10.1007/s00205-003-0253-x.

[107] Henryk Gerlach. *Ideal Knots and Other Packing Problems of Tubes*. PhD thesis, EPFL, 2010. Additional Data: http://lcvmwww.epfl.ch/ lcvm/articles/T10/data/.

[108] Mathias Carlen. Computation and visualization of ideal knot shapes. 2010. doi: 10.5075/epfl-thesis-4621.

[109] Andrzej Stasiak and John H. Maddocks. Best packing in proteins and DNA. *Nature*, 406 (6793):251–252, jul 2000. doi: 10.1038/35018674.

[110] Amos Maritan, Cristian Micheletti, Antonio Trovato, and Jayanth R. Banavar. Optimal shapes of compact strings. *Nature*, 406(6793):287–290, jul 2000. doi: 10.1038/35018538.

[111] Hiroki Uehara, Hiroyuki Kimura, Asami Aoyama, Takeshi Yamanobe, and Tadashi Komoto. Effects of knot characteristics on tensile breaking of a polymeric monofilament. *New Journal of Physics*, 9(3):65–65, mar 2007. doi: 10.1088/1367-2630/9/3/065.

[112] Sylwester Przybył and Piotr Pierański. Tightening of the elastic overhand knot. *Physical Review E*, 79(3), mar 2009. doi: 10.1103/physreve.79.031801.

[113] Thanapong Waitayawinyu, Paul A. Martineau, Shai Luria, Douglas P. Hanel, and Thomas E. Trumble. Comparative biomechanic study of flexor tendon repair using FiberWire. *The Journal of Hand Surgery*, 33(5):701–708, may 2008. doi: 10.1016/j.jhsa.2008.01.010.

[114] Anthony Nigliazzo, Rodrigo Arrangoiz, Richard Hutchison, Marc Basson, and Andrew Saxe. Surgical knot strength in continuous wound closures. *Surgical Science*, 02(04): 195–197, 2011. doi: 10.4236/ss.2011.24043.

[115] Evert J.C. van Rijssel, J. Baptist Trimbos, and Maurits H. Booster. Mechanical performance of square knots and sliding knots in surgery: A comparative study. *American Journal of Obstetrics and Gynecology*, 162(1):93–97, jan 1990. doi: 10.1016/0002-9378(90)90828-u.

[116] Daniel C. Schubert, James B. Unger, Debi Mukherjee, and Jack F. Perrone. Mechanical performance of knots using braided and monofilament absorbable sutures. *American Journal of Obstetrics and Gynecology*, 187(6):1438–1442, dec 2002. doi: 10.1067/mob.2002.129156.

[117] Nic Compton Bloomsbury Publishing Plc. *The Knot Bible: The Complete Guide to Knots and Their Uses.* ADLARD COLES NAUTICAL PR, 2013. ISBN 1408154765.

[118] Philippe Petit. *Why Knot?* Abrams Image, 2013. ISBN 978-1419706769.

[119] Wenyao Zou and Xiaoyang Li. Mechanical properties of steel wire rope under combination of stretch and bending state. *DEStech Transactions on Engineering and Technology Research*, 2017. doi: 10.12783/dtetr/mime2016/10198.

[120] ASTM E143-02. Standard test method for shear modulus at room temperature.

[121] URL https://en.wiktionary.org/wiki/surgery.

[122] J. B. Trimbos, E. J. C. Van Rijssel, and P. J. Klopper. Performance of sliding knots in monofilament and multifilament suture material. *Obstetrics & Gynecology*, 68(3):425–430, sep 1986. doi: 10.1097/00006250-198609000-00029.

[123] J.A. von Fraunhofer, R.J. Storey, and B.J. Masterson. Tensile properties of suture materials. *Biomaterials*, 9(4):324–327, jul 1988. doi: 10.1016/0142-9612(88)90027-0.

[124] Nicholas J. Slater, Robert P. Bleichrodt, and Harry van Goor. Wound dehiscence and incisional hernia. *Surgery (Oxford)*, 30(6):282–289, jun 2012. doi: 10.1016/j.mpsur.2012.03.001.

[125] M B Myers and G Cherry. Functional and angiographic vasculature in healing wounds. *The American surgeon*, 36:750–756, December 1970. ISSN 0003-1348. URL https://europepmc.org/article/med/4923803.

[126] L C Bartlett. Pressure necrosis is the primary cause of wound dehiscence. *Canadian journal of surgery. Journal canadien de chirurgie*, 28:27–30, January 1985. ISSN 0008-428X. URL https://europepmc.org/article/med/3882201.

[127] Harvey J. Sugerman, John M. Kellum, H. David Reines, Eric J. DeMaria, Heber H. Newsome, and James W. Lowry. Greater risk of incisional hernia with morbidly obese than steroid-dependent patients and low recurrence with prefascial polypropylene mesh. *The American Journal of Surgery*, 171(1):80–84, jan 1996. doi: 10.1016/s0002-9610(99)80078-6.

[128] Rishabh Singh and William Hawkins. Sutures, ligatures and knots. *Surgery (Oxford)*, 38(3):123–127, mar 2020. doi: 10.1016/j.mpsur.2020.01.003.

[129] Tyler M. Muffly, Jamie Boyce, Sarah L. Kieweg, and Aaron J. Bonham. Tensile strength of a surgeon's or a square knot. *Journal of Surgical Education*, 67(4):222–226, jul 2010. doi: 10.1016/j.jsurg.2010.06.007.

[130] H Tera and C Aberg. Tensile strengths of twelve types of knot employed in surgery, using different suture materials. *Acta chirurgica Scandinavica*, 142:1–7, 1976. ISSN 0001-5482.

[131] Daniel A. Davis, Donna M. Pellowski, and Eric J. Rawdon. All monofilament knots assume sliding conformation in vivo. *Dermatologic Surgery*, 39(5):729–733, may 2013. doi: 10.1111/dsu.12112.

[132] Christopher A. Zimmer, John G. Thacker, David M. Powell, Kenneth T. Bellian, Daniel G. Becker, George T. Rodeheaver, and Richard F. Edlich. Influence of knot configuration and tying technique on the mechanical performance of sutures. *The Journal of Emergency Medicine*, 9(3):107–113, may 1991. doi: 10.1016/0736-4679(91)90313-5.

[133] Lars Fischer, Thomas Bruckner, Beat P. Müller-Stich, Jörg Höer, Hanns-Peter Knaebel, Markus W. Büchler, and Christoph M. Seiler. Variability of surgical knot tying techniques: do we need to standardize? *Langenbeck's Archives of Surgery*, 395(4):445–450, dec 2009. doi: 10.1007/s00423-009-0575-8.

[134] Joseph J. Ivy, James B. Unger, Jason Hurt, and Debi Mukherjee. The effect of number of throws on knot security with nonidentical sliding knots. *American Journal of Obstetrics and Gynecology*, 191(5):1618–1620, nov 2004. doi: 10.1016/j.ajog.2004.05.029.

[135] Eric Silver, Rong Wu, James Grady, and Liansheng Song. Knot security- how is it affected by suture technique, material, size, and number of throws? *Journal of Oral and Maxillofacial Surgery*, 74(7):1304–1312, jul 2016. doi: 10.1016/j.joms.2016.02.004.

[136] K.-T. von Trotha, J. Grommes, N. Butz, A. Lambertz, C. D. Klink, U. P. Neumann, M. Jacobs, and M. Binnebösel. Surgical sutures: coincidence or experience? *Hernia*, 21(4): 505–508, apr 2017. doi: 10.1007/s10029-017-1597-8.

[137] B.S. Gupta. Surgical knot performance in sutures. In *Biotextiles as Medical Implants*, pages 335–365. Elsevier, 2013. doi: 10.1533/9780857095602.2.335.

[138] The United States pharmacopeia. The National formulary, 1979. URL http://ftp.uspbpep.com/v29240/usp29nf24s0_m80200.html.

[139] ASTM D0638-14. Test method for tensile properties of plastics.

[140] P.B. Price. Stress, strain and sutures. *Ann. Surg.*, 128(3):408–20, 1948.

[141] Jon Armitage and Sonia Lockwood. Skin incisions and wound closure. *Surgery (Oxford)*, 29(10):496–501, 2011. ISSN 0263-9319. doi: https://doi.org/10.1016/j.mpsur.2011.06.022. URL https://www.sciencedirect.com/science/article/pii/S0263931911001542. Wound Management.

[142] J. Cantarella, M. Piatek, and E. Rawdon. Visualizing the tightening of knots. In *VIS 05. IEEE Visualization*. IEEE, 2005. doi: 10.1109/visual.2005.1532844.

[143] A Stasiak, V Katritch, and L H Kauffman. *Ideal Knots*. World Scientific, nov 1998. doi: 10.1142/3843.

[144] Eric J. Rawdon. Approximating smooth thickness. *Journal of Knot Theory and Its Ramifications*, 09(01):113–145, feb 2000. doi: 10.1142/s0218216500000062.

[145] C. Bradford Barber, David P. Dobkin, and Hannu Huhdanpaa. The quickhull algorithm for convex hulls. *ACM Transactions on Mathematical Software*, 22(4):469–483, dec 1996. doi: 10.1145/235815.235821.

[146] John G. Thacker, George Rodeheaver, James W. Moore, James J. Kauzlarich, Leonard Kurtz, Milton T. Edgerton, and Richard F. Edlich. Mechanical performance of surgical sutures. *The American Journal of Surgery*, 130(3):374–380, sep 1975. doi: 10.1016/0002-9610(75)90408-0.

[147] M. John, D. Crook, K. Dasari, F. Eljelani, A. El-Haboby, and C.M. Harper. Comparison of resistive heating and forced-air warming to prevent inadvertent perioperative hypothermia. *British Journal of Anaesthesia*, 116(2):249–254, feb 2016. doi: 10.1093/bja/aev412.

[148] Jie Yi, Yongjing Lei, Shiyuan Xu, Yongyu Si, Shiyang Li, Zhongyuan Xia, Yisa Shi, Xiaoping Gu, Jianshe Yu, Guohai Xu, Erwei Gu, Yonghao Yu, Yanqing Chen, Hequn Jia, Yinglin Wang, Xiuli Wang, Xiaoqing Chai, Xiaoju Jin, Junping Chen, Meiying Xu, Junyu Xiong, Guonian Wang, Kaizhi Lu, Wenli Yu, Weifu Lei, Zaisheng Qin, Jingguo Xiang, Longyun Li, Ziyong Xiang, Shuang Pan, Lujing Zhan, Kai Qiu, Min Yao, and Yuguang Huang. Intraoperative hypothermia and its clinical outcomes in patients undergoing general anesthesia: National study in china. *PLOS ONE*, 12(6):e0177221, jun 2017. doi: 10.1371/journal.pone.0177221.

[149] Merrill A. Ritter, Emily M. Olberding, and Robert A. Malinzak. Ultraviolet lighting during orthopaedic surgery and the rate of infection. *The Journal of Bone & Joint Surgery*, 89(9): 1935–1940, sep 2007. doi: 10.2106/jbjs.f.01037.

[150] S. Aluri and I.J. Wrench. Enhanced recovery from obstetric surgery: a UK survey of practice. *International Journal of Obstetric Anesthesia*, 23(2):157–160, may 2014. doi: 10.1016/j.ijoa.2013.11.006.

[151] Julie A. Rizzo, Matthew P. Rowan, Ian R. Driscoll, Rodney K. Chan, and Kevin K. Chung. Perioperative temperature management during burn care. *Journal of Burn Care & Research*, 38(1):e277–e283, 2017. doi: 10.1097/bcr.0000000000000371.

[152] ISO 11566. Carbon fibre — determination of the tensile properties of single-filament specimens, 1996. URL https://www.iso.org/standard/19518.html.

[153] Lallit Anand, Nicoli M. Ames, Vikas Srivastava, and Shawn A. Chester. A thermo-mechanically coupled theory for large deformations of amorphous polymers. part i: Formulation. *International Journal of Plasticity*, 25(8):1474–1494, aug 2009. doi: 10.1016/j.ijplas.2008.11.004.

[154] Nicoli M. Ames, Vikas Srivastava, Shawn A. Chester, and Lallit Anand. A thermo-mechanically coupled theory for large deformations of amorphous polymers. part II: Applications. *International Journal of Plasticity*, 25(8):1495–1539, aug 2009. doi: 10.1016/j.ijplas.2008.11.005.

[155] Lallit Anand and Sanjay Govindjee. *Continuum Mechanics of Solids*. Oxford University Press, 2020. ISBN 0198864728.

[156] Frank Tendick, Michael Downes, Tolga Goktekin, Murat Cenk Cavusoglu, David Feygin, Xunlei Wu, Roy Eyal, Mary Hegarty, and Lawrence W. Way. A virtual environment testbed for training laparoscopic surgical skills. *Presence: Teleoperators and Virtual Environments*, 9(3):236–255, jun 2000. doi: 10.1162/105474600566772.

[157] Giancarlo Pennati. Biomechanical properties of the human umbilical cord. *Biorheology*, 38:355–66, 02 2001.

[158] Áron Szepesi, Zsolt Matula, Anna Szigeti, György Várady, József Szalma, Gyula Szabó, Ferenc Uher, Balázs Sarkadi, and Katalin Német. In vitro characterization of human mesenchymal stem cells isolated from different tissues with a potential to promote complex bone regeneration. *Stem Cells International*, 2016:1–9, 2016. doi: 10.1155/2016/3595941.

[159] AA Omari. Getting knotted: umbilical knots in a monochorionic monoamniotic twin pregnancy. *Archives of Disease in Childhood - Fetal and Neonatal Edition*, 90(1):F24–F24, jan 2005. doi: 10.1136/adc.2004.061812.

[160] Sergio Maeso, Mercedes Reza, Julio A. Mayol, Juan A. Blasco, Mercedes Guerra, Elena Andradas, and María N. Plana. Efficacy of the da vinci surgical system in abdominal surgery compared with that of laparoscopy. *Annals of Surgery*, 252(2):254–262, aug 2010. doi: 10.1097/sla.0b013e3181e6239e.

[161] David Escobar-Castillejos, Julieta Noguez, Luis Neri, Alejandra Magana, and Bedrich Benes. A review of simulators with haptic devices for medical training. *Journal of Medical Systems*, 40(4), feb 2016. doi: 10.1007/s10916-016-0459-8.

[162] François Jourdes, Brice Valentin, Jérémie Allard, Christian Duriez, and Barbara Seeliger. Visual haptic feedback for training of robotic suturing. *Frontiers in Robotics and AI*, 9, feb 2022. doi: 10.3389/frobt.2022.800232.

Paul Johanns

Mechanics Experimentalist

Personal Information

Address: EPFL STI IGM FLEXLAB
MED 0 1326, Station 9
CH-1015 Lausanne
Switzerland
Phone: +41 21 693 38 94
Email: paul.johanns@outlook.com
Place of Birth: Wiltz, Luxembourg
Date of Birth: 25 October 1992
Marital Status: Single
Citizenship: Luxembourg

Summary of Qualifications & Assets

I am a doctoral candidate at the fleXLab – Flexible Structures Laboratory – at EPFL. My current research involves **experiments** and **modelisation** of the mechanics of soft matter, ranging from elastic rods and ropes to plasticity in surgical knots.

I am passionate about **understanding** and **predicting** the behavior of physical systems around me. More specifically, I love studying the mechanics of **thin deformable structures** interacting with their environment through precision experiments and analytical modeling.

Education

2018 - 2022

Ph.D. Student in Mechanics, fleXLab, EPFL, Switzerland
Focus area: solid mechanics and slender structures
During my Ph.D., I have participated in several international conferences, supervised Bachelor and Master students in the laboratory and gave several classes as a Teaching Assistant.
Project title: *Mechanics of Physical Knots: From Filaments in Contact to Surgical Suturing*
Supported by the Fonds National de la Recherche (FNR), Luxembourg 12439430
Supervisor: Prof. Pedro M. Reis

2015 - 2017

Master of Science in Mechanical Engineering, ETH Zurich, Switzerland
Focus area: Mechanics and Metamaterials
Advisor: Prof. Chiara Daraio
Semester project with publication: *Characterization of vertically aligned carbon nanotube forests grown on stainless steel surfaces*
Carbon nanotube synthesis using chemical vapor deposition
Wet bench work in the cleanrooms of the Nano-Technology Center at IBM Zurich Research Laboratory.
Impact tests to quantify energy absorption

Master Thesis, California Institute of Technology, USA
In collaboration with the Jet Propulsion Laboratory (JPL)
Publication: *Design and impact response of 3D-printable tensegrity-inspired structures*
Advisor: Prof. Jürg Dual, Co-Advisor: Prof. Chiara Daraio
Acquired skills: experimental setup development, 3D-printing capabilities, micro-structure testing (FEMTO-tools), in depth Finite Element Modelling

2012 - 2015

Bachelor of Science in Mechanical Engineering, ETH Zurich, Switzerland
Focus area: Biomedical Engineering and Mechatronics
Title of Bachelor Thesis: *Study of Biaxial Strain Field: Simulation and Experimental Validation*
In the context of the Zurich Heart - Hybrid Membrane project
Advisor: Prof. Edoardo Mazza

2005 - 2012

Education in Enseignement Secondaire, Lycée du Nord Wiltz, Luxembourg
Branch of study: Mathematics and Informatics
Degree: Fin d'études secondaires moderne, section B

Work and Research Experience

2018 - 2022

Graduate Research Assistant (Ph.D.), flexLab, EPFL, Switzerland

Setting-up research labs – 2018, 2019
Testing lab: universal testing machine (Instron), sensors, actuators, linear stages
Fabrication lab: 3D printers, laser-cutter, water-jet cutter, milling machine, lathe
Chemical lab: polymer synthesis, spin-coating, scientific oven
Imaging lab: X-ray micro-CT scanner, optical microscopes, profilometer, 3D-scanner

Experimental and numerical toolbox development
Fabrication of composite rods for micro-CT imaging,
involving injection molding, fiber insets, dip-coating.
Elasto-plastic material modelling and study of frictional interactions.
Development of automated image-processing algorithm for volumetric micro-CT data.
Finite Element simulations (Python scripting for Abaqus CAE) of knotted filaments.

Compare-and-contrast study between ideal and physical knots
Collaboration with the department of mathematics at EPFL: Prof. John Maddocks.
Evaluation of the role of elasticity in dictating the physical knot's overall shape,
self-contact regions, curvature profile, and cross-section deformation.
Publication: *The shapes of physical trefoil knots* (see publication section below).

Capsizing due to friction-induced twist in the failure of stopper knots
We investigated the mechanical performance of the figure-eight knot tied onto elastic ropes as a stopper knot, using precision model experiment and high-fidelity Finite Element Modeling.
Friction-induced twist is at the source of knot capsizing in stopper knots.
Capsizing is delayed in elastic rods for tighter configurations and a rougher stopper plate surface, or in ropes with high torsional rigidity.

Strength of surgical knots: an interplay between plasticity and friction
Investigation on surgical knots" operational and safety limits.
Collaboration with independent plastic surgeon: Dr. Samia Guerid.
Development of 1D plasticity model to describe suturing monofilament,
collaborating with expert in polymer plasticity modelling: Prof. Shawn Chester.
Finite element modelling with user-defined material and residual stresses.
Rationalizing primary ingredients dictating the mechanical performance of surgical knots.
Findings could have potential applications in the training of surgeons and control robotic-assisted surgical devices.

2016 - 2017	**Industrial Internship** (3 months) Pilatus Aircraft Ltd, Stans, Switzerland Department: Structural Analysis Fatigue and Damage Tolerance (F&DT) group Fatigue analysis: validation of chemical milling process for aluminium skins of PC-24 Development of new software tool for data evaluation of fatigue and static component tests
2005 - 2017	Active Collaboration at **Family Farm** Handling and repairing of agricultural machinery
2012	**Factory Internship** (3 months) CTI Systems S.A., Lentzweiler, Luxembourg Acquisition of machining procedures: assembling, milling, metal forming, rotary drilling
2011	**Engineering Trainee Days** Gradel Services S.A., Steinfort, Luxembourg Insights into engineering activities for prototype construction in nuclear and aerospace domain

Teaching Experience

Mechanics of Slender Structures (Master) — Fall 2019, Fall 2020, Fall 2021
Professor: Pedro M. Reis (ref. EPFL – ME-411) – *Flexible Structures Laboratory, EPFL*

Introduction to Structural Mechanics (Bachelor) — Spring 2019, Spring 2020, Spring 2021, Spring 2022
Professor: Pedro M. Reis (ref. EPFL – ME-104) – *Flexible Structures Laboratory, EPFL*

Oscillation of Continuous and Discrete Systems (Bachelor) — Spring 2016, Fall 2016
Professor: Jürg Dual – *IMES (Institute for Mechanical Systems), ETH Zurich*

Innovation project – Team coaching in the context of product development (Bachelor) — Spring 2014
Professor: Mirko Meboldt – *pdz (product development zurich), ETH Zurich*

Student Research Projects Supervision

Nicolas Minazzo – Master thesis – 2021
Mechanics of knotted umbilical cords – experiments and simulations

Arthur Serres – Semester project – 2020
Exploratory work in the project on the role of plastic deformation in surgical knots

Caroline Gay — ESPCI internship — 2019
Volumetric imaging of elastic knots through X-ray tomography

Bartosz Karczmarski – Princeton university internship – 2018
Uniform rod coating using the dip-coating technique: development of an empirical model describing coating thickness

Articles in Peer Reviewed International Journals

- P. Johanns, C. Baek, P. Grandgeorge, S. Guerid, S. A. Chester, and P. M. Reis,
  Strength of Surgical Knots: an interplay between throw number, friction, and plasticity
  Unpublished manuscript in preparation (2022).

- P. Johanns, and P. M. Reis,
  Capsizing due to friction-induced twist in the failure of stopper knots
  Unpublished manuscript in preparation (2022).

- T. G. Sano, P. Johanns, P. Grandgeorge, C. Baek, and P. M. Reis,
  Exploring the inner workings of the clove hitch knot
  Extreme Mechanics Letters, 101788 (2022).

- P. Grandgeorge, C. Baek, H. Singh, **P. Johanns**, T. G. Sano, A. Flynn, J. H. Maddocks, and P. M. Reis,
  Mechanics of two filaments in tight orthogonal contact
  Proceedings of the National Academy of Science U.S.A., **118**, e2021684118 (2021).

- **P. Johanns**, P. Grandgeorge, C. Baek, T. G. Sano, J. H. Maddocks, and P. M. Reis,
  The shapes of physical trefoil knots
  Extreme Mechanics Letter, **43**, 101172 (2021).

- C. Baek, **P. Johanns**, T. G. Sano, P. Grandgeorge, and P. M. Reis,
  Finite element modeling of tight elastic knots
  Journal of Applied Mechanics, **88**, 024501 (2021).

- E. Roumeli, M. Diamantopoulou, M. Serra-Garcia, **P. Johanns**, G. Parcianello, C. Daraio,
  Characterization of Vertically Aligned Carbon Nanotube Forests Grown on Stainless Steel Surfaces
  Nanomaterials, **9(3)**, 444 (2019).

- K. Pajunen, **P. Johanns**, R. K. Pal, J. Rimoli, C. Daraio,
  Design and impact response of 3D-printable tensegrity-inspired structures
  Materials & Design, **182**, 107966 (2019).

CONTRIBUTED SEMINARS

European Solid Mechanics Conference (ESMC), Galway, Ireland – 2022
Major event for the solids mechanics community in Europe
Talk title: *Why do surgeons sleep better with plasticity in their knots?*

MEGA.Seminar (Mechanics Gathering Seminar Series), EPFL – 2021
Weekly seminar series with a focus on the local community in Mechanics at EPFL
Talk title: *Why do surgeons sleep better with plasticity in their knots?*
Memento of talk: here

American Physical Society March Meeting, Virtual conference – 2021
Global audience of physicists and scientists meeting on an annual basis
Talk title: *Physical trefoil knots: elastic deformation and failure*

Society of Engineering Science (SES) 56th Annual Technical Meeting, Virtual conference – 2018
Conference focusing on engineering, physical and life sciences as well as mathematics
Talk title: *The mechanics of trefoil knots in both closed and open configurations*

American Physical Society March Meeting, Denver, USA – 2020
Due to the COVID-19 outbreak the conference was canceled but replaced by virtual sessions organized by the DSOFT (Division of Soft Matter) community.
Talk title: *To stop or not to stop: the stopper knot as a friction device*

American Physical Society March Meeting, Boston, USA — 2019
Talk title: *Untangling the mechanics of elastic knots*

MEGA.Seminar (Mechanics Gathering Seminar Series), EPFL – 2018
Talk title: *Untangling the mechanics of elastic knots and not-knots*
Memento of talk: here

Society of Engineering Science (SES) 55th Annual Technical Meeting, Madrid, Spain — 2018
Talk title: *Untangling the influence of topology on the mechanics of knots*

PUBLIC OUTREACH AND SCIENTIFIC VULGARIZATION

Spotlight on young researchers – 2020
Being supported by the AFR funding scheme by the Luxembourg National Research Fund (FNR), I was featured in the FNR initiative Spotlight on Young Researchers. There article can be found here.

Public relations officer – 2019, 2020
Executive committee of the Luxembourgish student's association in Lausanne

Invited talk by the Young Entrepreneurs Luxembourg association – 2019
Closing event of the Engineering Trainee Days, with leading national companies in industry

EPFL open days — 2019
Presentation of the Flexible Structure Laboratory's research activities
Event organized for families and high school students

Engineering Class Lessons in Secondary School at the Lycée du Nord Wiltz (Luxembourg) – 2014, 2016
Objective: create enthusiasm among pupils to study science

FELLOWSHIP AWARD

Successful application for a grant awarded by the NATIONAL RESEARCH FUND (FNR), Luxembourg

> providing funding for my Ph.D. research project (12439430)
> under the **AFR Ph.D. funding scheme**; employment contract with the host institution

SKILLS

Languages
Fluently spoken: Luxembourgish (mother tongue), (Swiss-)German, French, English
Basic skills: Spanish, Chinese
Safety trainings
Radioprotection officer at EPFL
Nanoparticle safety in the Nano-technology Center at IBM Zurich Research Laboratory
Experimental skills
Rapid prototyping, mechanical testing, laser cutting, milling, lathing
3D X-ray tomography, fast imaging techniques
Polymer synthesis, wet bench work in cleanrooms
Informatics skills
3D/CAD-programs: Abaqus FEA, Siemens NX, SolidWorks, Rhino/Grasshopper, Blender
Other softwares: Matlab, Illustrator, imageJ, ffmpeg, imc FAMOS, GitHub, Mathematica, LabView, LaTeX
Programming languages: C, C++, Python, Pascal, Delphi
Driver's Licenses: B & F

HOBBIES

Organ, trumpet, paragliding, salsa dancing